ISBN 978-82-326-4294-6 (printed ver.)
ISBN 978-82-326-4295-3 (electronic ver.)
ISSN 1503-8181

Elias Bjørne

Doctoral thesis

Doctoral theses at NTNU, 2019:349

Elias Bjørne

Globally Stable Observers for Simultaneous Localization and Mapping

Doctoral theses at NTNU, 2019:349

NTNU
Norwegian University of Science and Technology
Thesis for the Degree of
Philosophiae Doctor
Faculty of Information Technology and
Electrical Engineering
Department of Engineering Cybernetics

NTNU

NTNU
Norwegian University of
Science and Technology

NTNU
Norwegian University of
Science and Technology

Elias Bjørne

Globally Stable Observers for Simultaneous Localization and Mapping

Thesis for the Degree of Philosophiae Doctor

Trondheim, November 2019

Norwegian University of Science and Technology
Faculty of Information Technology and Electrical Engineering
Department of Engineering Cybernetics

NTNU
Norwegian University of
Science and Technology

NTNU
Norwegian University of Science and Technology

Thesis for the Degree of Philosophiae Doctor

Faculty of Information Technology and Electrical Engineering
Department of Engineering Cybernetics

ISBN 978-82-326-4294-6 (printed ver.)
ISBN 978-82-326-4295-3 (electronic ver.)
ISSN 1503-8181

Doctoral theses at NTNU, 2019:349

Printed by NTNU Grafisk senter

To Emilie
Love makes people do stupid stuff
I ended up taking a PhD

Summary

This thesis focuses on developing observers that can be applied to simultaneous localization and mapping (SLAM), with an emphasis on developing observers that has theoretical proof of convergence. The motivation for this research has been to develop robust navigation methods, that can apply information from the surroundings through on-board sensors, mainly cameras. Applying nonlinear system theory, all the observers have proof of semi global or global asymptotic stability; while globally exponential stability and exponential stability in the large is also shown for some of the observers.

Conversely to the main practice in the literature, the observers have been designed on the bearing measurements being represented as unit vector measurements. Two different techniques are applied in the design of the observers or filters. The first technique was based on having an attitude heading reference system available and rearrange the system as a linear time varying system. A standard Kalman filter could thus be used, and globally exponential stability achieved. A setup where the Kalman filter was combined with a nonlinear observer was also tested, and the combination was able to improve both the accuracy and robustness of the filtering.

The second design method, utilized the kinematics of the unit vector pointing at landmarks, and filtered directly the bearing measurements. Inspired by the literature on nonlinear observers, the cross product was used as an innovation term involving the bearing vectors. This proved to give the observer semi-global stability. Through the filtering, it was proved that gyro bias and distance to the landmark could be estimated separately, with the same semi global asymptotic stability, and exponential stability in the large.

The fact that the observer designed around unit vector measurements also opened other applications which are highly relevant to visual navigation. A well known fact when performing navigation only based on camera, is that the depth of the scene is ambiguous. This means that all the structure from motion that is estimated from the camera is relative, in fact, the absolute depth in the scene or scale between the camera and real world is unobservable without external information. By normalizing the velocity measured by the camera, similar kinematics as used for the landmark measurements could be applied, and by assuming that a self calibrating IMU with gravity estimate was available, the observer could fuse normalized velocity with the sensor values from the IMU and estimate the metric velocity of the vehicle. This setup also worked with other observers and filters from the literature, and a thorough comparative study was made in simulations and with experimental data, confirming that the velocity estimation was possible.

Finally, an observer was expanded to estimate both distance to the landmark and gyro bias simultaneously. With the same global asymptotic stability and exponentially stability in the large. With verifiable conditions for convergence. This

made it possible to apply a camera to both gyro bias estimation and estimating distance to the landmark without dealing with problems of initialization or divergence. The setup was verified both in simulations and on a UAV flight experiment, where the combination of a GNSS, IMU and camera, could perform estimation both of gyro bias and depth in the camera. Further it was shown how heading and altitude could be estimated or derived from the measurements, such that with the sensor setup proposed, both an altimeter and magnetometer were redundant sensors.

There is some work left to prove that camera navigation based on the presented observers is feasible in closed loop or in an industrial setting. Never the less, the thesis has been able to address two important topics in camera aided navigation, namely having a observer using monocular camera handling gyro-bias, and having a setup for velocity estimation provided only a monocular camera and a tactical self calibrating IMU; all with proof of semi-global stability.

Preface

This thesis is submitted in partial fulfillment of the requirements of the degree of philosophiae doctor (Ph.D.) at the Norwegian University of Science and Technology (NTNU). Thework presented in this thesis is the results of the doctoral studies carried out at the Centre for Autonomous Marine Operations and Systems (NTNU AMOS), Department of Engineering Cybernetics, NTNU under supervision of Professors Tor Arne Johansen, Thor I. Fossen and Edmund Førland Brekke. I was employed as a Ph.D. candidates by the knowledge building project "Multi-stage Global Sensor Fusion for Navigation using Nonlinear Observers and eXogeneous Kalman Filter". The project was financed by the Research Council of Norway through the Centres of Excellence funding scheme and AMOS (Autonomus Marine Operations and Systems) programme, grant numbers, 250725 and 223254. In addition, part of the research for the thesis was carried out at Jet Propulsion Laboratory, California Institute of Technology, under a contract with National Aeronautics and Space Administration.

Acknowledgments

First I would like to thank Professor Johansen for giving me this opportunity to peruse the Ph.D. degree on a topic of great personal interest. I would also like to thank him for introducing me to Associate Professor Brekke. It has been a great privilege to be a Ph.D. candidate under your supervision. Thank for all the interesting discussion, and the patience with regards to my writing, I am utter great-full. I have also appreciated the autonomy I have been able to enjoy and the opportunity to shape my own working days and do the research on topics of my own choosing. It has been an honor and a privileged to work with one of Norway's most distinguished researchers within the field of control systems. I also had the pleasure to be a exchange research fellow at Jet Propulsion Laboratory, and I want to give a special thanks to Jeff Delaune, for inviting me over and being a mentor while I was visiting. Also a big thanks to the rest of the people at the micro UAV lab for making the visiting research both a great learning experience as well as an enjoyable time. It was also very inspirational working along the people who is sending a helicopter to Mars next year.

I also have had the pleasure to work with great colleagues at the Department of Engineering Cybernetics. Thanks, goes out to Pål Kvaløy, Lars Semb, Terje Haugen, Glenn Angel for technical assistance with the experiments. I would also give a thanks to all my colleges at the department who sported me with with help and knowledge, including Robert Rogne, João Fortuna, Fredrik Leira, Håkon Helgesen, Kristoffer Gryte and thanks to Torleiv Bryne who helped me with the GNSS processing. I would also like to thank Tove Kristin Blomset Johnsen, Head of administration at the department, for help with administrative tasks during

my Ph.D. research fellowship. I also want to thank Dr Antonio Loria and Anton Shiriaev for theoretical discussions. I have also had the privilege of working along many great fellow Ph.D. candidates and Postdoc fellows, which have provided a prosperous working environment, both at AMOS and at the department, including discussions and insight in both academic and non-academic topics. And thanks for all the chess games I was able to lose, and all the banana walks giving me a break during the day. There are so many of you, and you know who you are. Thank you all for both interesting working days and a nice spare time as well. I also want to give a thanks to my new working place Cognite, and the people there, for giving me time to finish my thesis and making me look forward to my career.

Finally I would like to thank friend and family. Always paying interest to my work and always supporting me. Dad, thanks for showing me that you are proud of me, and mom thanks for giving me great advise and help. And Emilie, thanks for being patient and always making my day shine.

Contents

1 Introduction

1.1 Context and background

Robust navigation and positioning are a fundamental part for achieving autonomous missions. A possible scenario is the use of autonomous vehicles for inspection of structures such as bridges, power lines and wind turbines. For such tasks, the need of high accuracy in position and attitude estimates is essential, as the vehicles will have to operate near the inspection target. The motivation for researching SLAM is the necessity for high quality and robust navigation for an autonomous systems. Usually a global navigation satelite system (GNSS) is used for navigation in combination with an inertial measurement unit (IMU). However, the satellite technology has limitations. This is especially experienced close to large structures that can shadow the signals, or reflect the GNSS signals. In addition, as safety and security is an important part of the developments and usage of autonomous systems, there will be a higher demand for redundant navigation systems, thus there will be need for other navigation systems to work alongside GNSS. On top of that, GNSS is not applicable for indoor navigation, where there is usually some infrastructure installation needed for a positioning system. In addition the ability of the autonomous system to perceive its surrounding is essential for safe autonomous operations in unpredictable environments. Further, the price of cameras, LIDAR and other sensors have decreased significantly the latter years. Parallel to an increase in both the quality of these sensors and computational power available. Applying these types of sensors for navigation has been of increase interest both in industry and in the scientific community. This challenge, often refereed to as the SLAM problem, was considered one of the fundamental problems in robotics from as far back as the 1986 IEEE Robotics and Automation Conference [28][6]. The readers are refereed to these articles for an introduction to classical SLAM, but a more modern introduction and overview is [21].

It is important to clarify some terminology, which also can be different depending on the scientist, and in which scientific community the communication is done. As noted above SLAM consists of the problem of fusing on-board sensor data on a vehicle to estimate its position and map its surrounding. It is often divided into range and bearing SLAM, bearing only SLAM and Range Only SLAM. Range is then the relative distance between the vehicle and a landmark, while bearing information is in which direction the landmark is observed. What is performed is dependent on the sensors available on the vehicle. Range and Bearing SLAM can for instance be performed with a LIDAR, Radar or stereo camera. Range SLAM can be performed with either acoustic beacons. Bearing only SLAM is often performed with a monocular camera. When a camera is used in SLAM, it can also be refereed to as visual SLAM. Lately, there has been a distinction between whats been referred to as visual SLAM and visual odometry (VO). The difference is illustrated

in Figure 1.1, where we see that SLAM preforms loop closure, while VO only use visual information which is currently in the view for dead reckoning. The error will therefore always drift in time and will eventually be unbounded. In addition, a VO system may neglect the mapping part of SLAM. Visual inertial odometry (VIO) is when the visual information is fused with an IMU, both for higher accuracy and to acquire a bounded scale error. Other terms that comes up in the computer vision literature is structure from motion (SFM) and photogrammetry. Photogrammetry refers to the extraction of three-dimensional measurements from two-dimensional images, where SFM refers to the part where the relative poses of the camera images along with position of features and camera parameters are estimated.

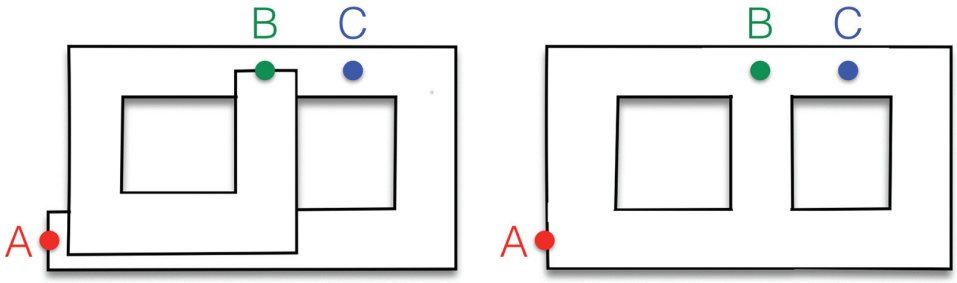

Figure 1.1: Left: map built from odometry. The map is homotopic to a long corridor that goes from the starting position A to the final position B. Points that are close in reality (e.g., B and C) may be arbitrarily far in the odometric map. Right: map build from SLAM. By leveraging loop closures, SLAM estimates the actual topology of the environment, and âĂIJdiscoversâĂİ shortcuts in the map. [21]

In addition there are two main setups for solving SLAM, graph SLAM and SLAM filtering. The main difference is that in graph SLAM all the measurements are included in the estimation for every iteration, while in SLAM filtering only the last measurements are used at every update in a recursive algorithm. The difference between these fundamental setups are discussed in [104]. The most successful visual SLAM methods developed lately, are based on the key-frame bundle adjustment [89, 30]. The key frames are chosen so that the optimization is sparse, and hence the optimization is possible to perform in real time. The various setups are illustrated in Figure 1.2.

The combination of the non linearity of SLAM combined with the fundamental uncertainty between the unknown position of the vehicle and the map, makes the problem difficult. In addition, as SLAM requires a map to be estimated, the complexity of the problem increase, often polynomial with the size of the map. Thus when dealing with SLAM, challenges with regards to accuracy, consistency, scalability, robustness, loop closure, computational load, scale ambiguity and drift have to be considered. This means that the SLAM problem can be highly difficult depending on the requirements and the sensor setup of the system. Below is a short overview of the different challenges that one is faced with when building a

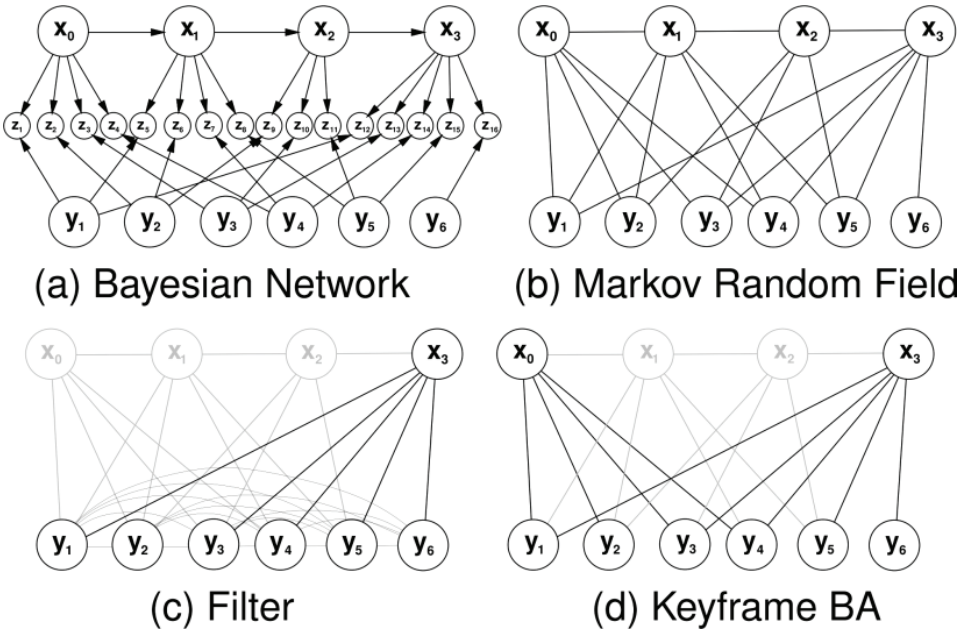

Figure 1.2: (a) Bayesian network for SLAM/SFM. (b) SLAM/SFM as markov random field without representing the measurements explicitly. (c) and (d) visualise how inference progressed in a filter and with keyframe-based optimisation. [104]

SLAM system, especially when designing a monocular visual SLAM system.

Accuracy The accuracy of the SLAM estimation means the accuracy of both the pose estimate of the vehicle, and the accuracy of the estimated map. This can often be measured by the root mean square error (RMSE). For experiments only the RMSE of the pose of the vehicle is often given, as the map RMSE is more difficult to acquire. High accuracy can be viewed as the ultimate goal of the SLAM estimation, however other features such as robustness and consistency can be viewed as even more important.

Consistency The consistency of the estimation is a measure of how well the estimation procedure is able to estimate the uncertainty of the acquired estimates. For an extended Kalman filter (EKF) or Kalman Filter (KF), the uncertainty is reflected in the covariance matrices returned from the filters. The consistency can then be measured by comparing the actual estimation error to the covariance estimate through calculating the normalized estimation error squared (NEES) and preforming a Chi squared test [7]. The EKF often provides estimates that are too optimistic with regards to the uncertainty. The relation between the observability of the system and the consistency of the EKF filters has been extensively studied in the literature [22, 109, 56], and has resulted in methods developed to maintain

consistency like Multi-State Constraint Kalman Filter (MSCKF) [74] and Invariane EKF (IEKF) [9, 52]. SLAM systems based on nonlinear optimization, or graph SLAM, can have global uncertainty as the inverse of the hessian matrix. which means that the uncertainty of the estimates has to be determined explicitly or empirically. The same applies to most of the deterministic observers including most nonlinear observers.

Robustness Achieving robust visual SLAM and visual inertial odometry (VIO) setups is still considered an open problem in many scenarios [21]. A common problem is not only to have algorithms that converge regardless of model error, noise and initialization, a question often asked, but more seldom answered, is for which conditions will the SLAM methods converge. For example, how close to the true value does the estimates need to be initialized for the system to converge, and under which maneuvers is the algorithm guaranteed to converge. Some work has been done in this regard, for instance there is a well known fact that the relative depth of a scene is unobservable for a monocular camera if the camera does not move [67]. For some instances, the unknowns can be found by solving a linear system, where a condition number would determine if the problem is well posed. However, relating this to an automatic criterion to guarantee convergence has yet to be demonstrated [91]. In control theory stability analysis are used to determine the robustness of a system. Having a system which is uniformly globally asymptotically stable (UGAS), uniformly globally exponentially stable (UGES) or have similar stability properties means that for all initial states of the system, the states will converge. As SLAM is a nonlinear problem, a SLAM system is often based on a EKF, nonlinear optimization or other nonlinear estimation schemes. Many of these methods can not have their stability analyzed. However, there are some results in the literature of SLAM and visual odometry methods that are UGAS and UGES [77, 71, 49, 27, 101, 58], including several methods developed throughout this thesis. The benefit of the stability results are two fold, it guarantees that the estimates will converge regardless of how bad they are initialized, but it also gives an insight into how the sensors need to be excited to be able to guarantee uniform observability and convergence. In addition, if a system is UGES it is input to state stable (ISS) [64, Lemma 4.6], which means that if a bounded error is introduced, the error of the states will also be bounded. This then leads to a strong robustness property that can be proven analytically. Never the less, UGES is not a guarantee for having a well preforming observer, especially when high noise values are present.

Scalability Scalability of a SLAM system, is related to its ability to handle a map which is growing, which ideally would result in the computational cost would increase logarithmic to the size of the map. For many SLAM systems this is far from the case. An EKF implementation of SLAM will have n states, which

would lead to a covariance matrix that has n^2 elements, thus the computational cost increases $O(n^3)$ with the number of map elements [96], however reducing how often the global map needs to be updated the computational complexity can be suppressed. For nonlinear optimization, a naive implementation methods based on direct linear solvers increases memory quadratic with the number of landmarks [21], however, in recent years there have been a set of examples where by maintaining the optimization graph sparse, real time performance for large maps can be accomplished [89], [30], by using solvers that exploit the sparsity of the optimization [69].

Loop closure Loop closure is the ability of the system to realize that the scene has been visited before. This information is important in two ways, one it can be used to reduce the drift due to dead reckoning, thus keeping the error bounded in time. In addition, a loop closure detection is essential to get a good topology of the map that is created. This is illustrated in Figure 1.1. This information can then be utilized to keep the error bounded. Historically, this has been viewed as part of the data association problem which is solved through gating, a classical technique in tracking problems [92][7]. However this has not proven to be a robust approach. In [113] several loop closure strategies were compared: map to map, image to image and image to map comparisons. The image to image approach has been shown to be the most popular, because of its robustness and availability. The loop closure is done by sorting features by their descriptor into categories called visual words. An image can thus be represented by a relative histogram of the words presented in the image, which is called the bag of words (BoW) vector of the image. The images can therefore be sorted, indexed and inverse indexed by the BOW, and comparing a newly acquired image to the collected image database can be done in logarithmic time [24, 39, 90]. A benefit of image to image loop closure is that it also enables relocalization.

The similarity between relocalization and loop closure is that in both the current images are compared to an image database and it is tested if the scene being viewed has been visited before. The difference is that in relocalization the track of the vehicle is lost so that the new position of the vehicle is relocalized. On the other hand, in a loop closure the track has not been lost, but there has been accumulated error that can be measured when a place is revisited. This error is then used to update the map, and thus reduce the accumulated drift to zero where the loop is closed.

Scale ambiguity and drift For monocular SLAM, a problem is that the scale of the world is ambiguous. This means that when a depth scene is calculated, only the relative depths within the image are observable, while the absolute depth is unobservable. This means that if it is desirable to know how a camera has moved by comparing images, the images have to be fused with other sensors such as laser

scanner, altimeter, IMU or sonar. Alternatively if the camera observe features with known relative distance, such as a checkerboard or a tag [94] a metric relative pose can be calculated by solving the perspective n-point problem [72]. A scale can also be found by fusing the camera with an IMU (VIO). In VIO loop closure is often neglected in order to have a computationally simple system. Several VIO methods have been developed to be able to run on a small computer, mobile phone or onboard a UAV [111, 80, 73]. In addition, a velocity observer able to estimate the velocity with UGES was also presented in [41]. In ORB-SLAM [91], the scale is initialized through an optimization scheme combining IMU and camera information. In addition, the global optimization is done on the sim(3) group introduced in [103] which has the scale as a degree of freedom (DOF) resulting in the bundle adjustment (BA) having 7 degree of freedom and can account for scale drift when closing the loops. However there is no guarantee that the scale error will be bounded with regards to the distance to the initial camera pose.

In this thesis, the focus has been on the challenge of having robust SLAM methods, where the goal of the research has been to develop SLAM methods based on nonlinear observer theory, thus providing observers with some kind of global stability.

1.2 Nonlinear stability theory for SLAM

As mentioned, a challenging problems within SLAM is having robust estimation. Some recent work has addressed this by developing SLAM methods using nonlinear observer theory, thus acquiring SLAM observers with proof of certain stability properties. In this section we discuss different nonlinear observers that can be applied to SLAM or VIO, and how the stability property is acquired. This is both to give the reader an overview of the state of the art of these types of observers, and illustrate how this thesis has positioned itself with regards to the rest of the literature. It will also be noted how the references have been influential with regards to the work in this thesis. The author also wishes to highlight some more general work that has been influential to the theory part of this thesis.

We are all standing on the shoulders of giants, where a vast amount of theory and practice has been produced and re-used for other applications. Arguably the most influential work the last century is the work of Kalman [63, 62], which in essence made a recipe of how to make an observer for a linear time-varying system. Moreover, conditions for controllable and observable systems were presented, which made it possible to determine whether a KF and/or an optimal controller could be applied to a linear system. In [3], it was proven that a KF or the Riccati equations can provide UGAS or UGES error dynamics when applied to linear system.

With regards to nonlinear systems, some nonlinear systems can be transformed

to linear time-varying systems. This is possible by inserting measured input or state values into the system matrices. If these measurements are accurate enough, the nonlinear system can be analyzed as a time-varying system with the following stability properties. Such schemes are discussed in [10, 11, 13], and have also been applied to SLAM and position observers such as [12, 47, 77, 50, 58]. This was also applied in the stability proof of the Riccati observer presented in Chapter 6. On the other hand, this approach renders the process and measurement noise to be non-additive and and non-white, compromising the optimality of the KF.

However, in general, proving stability for nonlinear systems is not simple. Nonlinear systems are all systems that are not linear, which means that they are a highly diverse group. Never the less, some theory is general enough to be applicable to many systems. Lypaunov theory falls into that category, and can be utilized to prove stability for a vast amount of systems. However, the catch with Lyapunov theory is that there is a requirement of finding a Lyapunov function. Finding a suitable Lyapunov function for a system is not a trivial task, where experience and guessing is often how it is found. In addition, for some systems, especially where parameter estimation is performed, the Lypunov analysis falls short and more specialized theory needs to be applied. This was the case for the first article in Chapter 3, where Matrosov's theorem [86] was used to prove that all states estimates of the observer converged to their true values.

As mentioned, a Lyapunov function can be difficult to find, however, systems with a certain structure will tend to have a Lyapunov function candidate that can be constructed based on the system. Such a family of nonlinear systems is the skew-symetric systems. This structure often arrive when there are unknown states or parameters that depend linearly on a state that is measured, and hence often appears in adaptive control and parameter estimation. The skew symmetric systems have been investigated extensively in different forms including in [4, 87, 95, 75, 35]. Skew symetric systems have also been found when working with camera systems, most notably [57][27][40][101][41]. In addition it has been applied in both Chapter 3 and 4, when finding state estimation laws and Lyapunov candidate functions for the observers presented.

Other inspirational work was the nonlinear attitude observer [48, 82, 42], where it is shown how the cross product can be used as an innovation for a nonlinear observer on the special orthogonal group, which is the innovation used for the nonlinear observers with bearing measurement in chapters 3 and 4. The cascade structure from [12] was also influential when designing the attitude estimation in Chapter 3.

Other important observers which were not visited in this thesis were the symmetry preserving observers [83], such as [81] and [107], and invariant observers such as [8].

1.3 Scope, objective and contribution

In this thesis the focus has been on developing observers that are applicable to the SLAM or VIO scenario, and that have their stability analyzed. The goal was to develop observers that were computationally simple and robust enough to be applicable on an UAV. The sensor suite that is most sought after in GNSS denied navigation is having a low-cost MEMS IMU and a monocular camera. Lowcost IMU, means that the observer should ideally handle slowly varying bias in the gyro and acceleration measurements. In addition having only a monocular camera means that only the bearing measurements are available from the camera. Most of the nonlinear observers with global convergence have assumptions that make them difficult to apply to an UAV flight. A common assumption is that a velocity measurement is present. This is a reasonable assumption when performing SLAM on a wheeled robot or a surface vessel. For an UAV however, it can be a limiting assumption, which requires an altimeter or altitude laser combined with a camera to estimate the velocity. Note that airspeed measurements are of limited use due to significant and unknown winds. There are VIO algorithms that can fuse IMU and camera to acquire velocity, however they lack the robustness or stability that is desired. Another assumption is that there is a gyro measurement without bias. This can be a limiting factor as a MEMS IMU with small gyro bias tends to have a high cost.

What we have not focused on in this thesis is the front end part of SLAM, this means feature extraction, data association and loop closure. The only focus with regards to these has been to develop filters with consistency properties in the case of the SLAM filters in Chapter 6, and when making simple feature extractors and matchers as part of the experimental setup.

1.3.1 Main Contributions

- A cascade structure for gyro bias and attitude estimation was presented. The gyro bias observer presented is able to estimate the bias using landmarks with unknown position and velocity. In addition it was shown that having the separation of the gyro bias estimation and attitude estimation could lead to a higher robustness when the gyro is corrupted with a large bias. A proof of the USGAS of the observer was also presented.

- The gyro bias observer was expanded to handle bearing only measurements. With the result that both the gyro bias and range to the landmarks can be estimated when velocity measurements are available. Included was a proof of USGAS and UES. A scenario where an UAV equipped with a camera, GNSS and IMU, the observer could estimate both altitude/proximity and gyro bias was presented. In addition, how the gyro bias in yaw could be estimated while hovering was also shown.

- An observer filtering a calibrated gyro, velocity and normalized vector measurement to estimate the vector magnitude was presented. Included was a proof of USGAS and UES. A setup was presented, in which an UAV equipped with a high grade AHRS/IMU could estimate its velocity by fusing these sensor values with a normalized velocity measurement. In addition, a cascade structure was also proposed so that USGAS bearing only filtering can be performed with a monocular camera and a high grade IMU, without any velocity measurement.
- A thorough experimental verification of the velocity estimation setup was performed, where a comparison of the novel observer to similar observers for velocity estimation was performed. The robustness of the nonlinear observers compared to an EKF implementation was shown.
- A bearing only SLAM system based on an AHRS was presented. The availability of the attitude from the AHRS made it possible to reorganize SLAM into a linear system. The observability of the system was analyzed, where its dependence on the excitation of the bearing measurements is proven. The PE condition for uniformly observability and thus UGES KF is that the bearing measurements are non stationary in the inertia frame. In addition the design of the co-variance matrices was performed and the consistent behavior of the KF was shown.
- The nonlinear observer and Kalman based SLAM method was combined into a cascade observer. It was shown how this setup was more robust and accurate than the observers separately.

The contributions in this thesis are listed chronologically, where the content of the thesis is organized as follows with the articles related:

Chapter 3), Cascade Attitude Observers Using Landmark Measurements

Part 1: Applying Landmark measurements

- Bjørne, E., Brekke, E. F. and Johansen, T. A., *Cascade Attitude Observer for the SLAM filtering problem*, Control Technology and Applications (CCTA), 2017 IEEE Conference on, p.945–952, 2017

Contribution

The main contribution of this research was the design of a new gyro bias estimator which applied measurements from landmarks with unknown position. This

makes it possible to estimate gyro bias in yaw, without magnetometer measurments, if velocity, range and bearing measurements from landmarks are available. In addition, The idea of separating gyro bias estimation from attitude estimation was shown to increase robustness.

Part 2: Applying Bearing Only Landmark measurements

- Bjørne, E., Brekke, E. F., Bryne, T. H. and Johansen, T. A., *Semi-globally Asymptotically Stable Nonlinear Observer for Camera Aided Navigation*, IEEE Transactions on Control Systems Technology, submitted as a brief paper,2019

Contribution

In this research we presented a novel observer, where we combined the ideas from [16, 19] and designed an observer that estimates distance to a landmark in addition to the gyro bias. It filters the velocity and bearing measurements from landmarks, to estimate the range to the landmark as well as gyro-bias. It can also be used for bearing only SLAM if it is combined with a loop closing front end system. It was presented with a proof of semi-globally asymptotically stability and exponentially stability in the large. The observer was also demonstrated in simulations, both in a generic form as well as for a sensor setup with a camera, GNSS and IMU for a UAV, where the observer was able to both provide range/altitude estimate as well as estimating the gyro-bias. The later setup was verified experimentally, and the gyro bias observer was used in a cascade in an attitude estimator as in [16]. The attitude observer was compared to a more straight forward velocity aided attitude observer based on a nonlinear complimentary filter [43].

Chapter 4), Nonlinear observers for estimating vector magnitude from its direction and derivative

- Bjørne, Delaune, J. and Johansen, T. A., *Estimating vector magnitude from its direction and derivative, with application to bearing-only SLAM filter problem*, IEEE Conference on Decision and Control (CDC), p.1353–1360, 2018

Contribution

In this research we presented a novel observer for estimating the magnitude of a time varying vector. We proved that if we assume a lower bound on the magnitude of the vector, and a PE unit vector measurement, the vector magnitude observer is USGAS and UES and will estimate the magnitude of the vector. We employed the vector magnitude observer to the bearing-only SLAM problem with AHRS measurements, and this also demonstrates two instances of the vector magnitude observer working in cascade; once for velocity and once for range to landmark

estimation. In addition it was shown that estimating the distance to a landmark using bearing measurements and velocity, is equivalent to estimating velocity using a normalized velocity and acceleration measurements is available.

Chapter 5), , Globally Stable Velocity Estimation Using Normalized Velocity Measurement

Contribution

- Bjørne, E., Brekke, E. F., Bryne, T. H., Delaune, J. and Johansen, T. A., , *Globally Stable Velocity Estimation Using Normalized Velocity Measurement*, International Journal of Robotics Research, submitted,2019

Contribution

A comparative study of globally stable observers applied to the ego motion estimation is presented. The solution can give globally stable velocity estimates provided that a camera and an IMU with pitch and roll estimates are available. The comparison was shown both in simulations and using experimental data. The tuning of the different observers was discussed and performed, both by estimating the measurement and process noise of selected observers and using Monte Carlo simulations. In simulations the magnitude observer (MO) performed the best, followed by the exogenous Kalman filter (XKF) [59], where it was also shown how the MO observer could filter the unit vector measurements. Also on experimental data, the MO observer was shown to have the best overall performance of the velocity direction observers, with fast convergence and small RMSE in steady state. The nonlinear observers were also compared to an EKF, and the observers were shown to have a more robust performance than the EKF. The results of the chapter confirmed that ego-motion estimation with global convergence using camera is possible, provided that an IMU, with pitch/roll estimates, is also available.

Chapter 6), Linear Time varying SLAM filtering using Kalman Filter

Part 1: Observability analysis and covariance matrix design

- Bjørne, E., Johansen, T. A. and Brekke, E. F., *Redesign and analysis of globally asymptotically stable bearing only SLAM*, 20th International Conference on Information Fusion (Fusion),2017

Contribution

The main contribution was the redesign of the bearing only SLAM, previously presented in [58]. The new design requires less sensors as it uses neither gyro nor bearing derivative. In addition, a novel design of the tuning covariance matrices using linearisation was proposed and analysed. Simulations were done in 2D, and Monte Carlo (MC) simulations were used to investigate the performance and consistency of the KF.

Part 2: eXogenus Kalman Filter

- Bjørne, E., Johansen, T. A. and Brekke, E. F., *Cascaded Bearing Only SLAM with Uniform Semi-Global Asymptotic Stability*, 22th International Conference on Information Fusion (Fusion),2019 submitted

Contribution

In this research we took inspiration from the XKF setup, introduced in [59]. We used the nonlinear filter [19] as a first-stage filter on the bearing measurements and feed these to the system matrices in the KF from the previous part of the chapter. We proved that the setup is USGAS, and simulations demonstrated that the cascade setup is more robust against large measurement noise, than the filters are individually. In addition we investigated how the novel nonlinear observer [19] preformed against the KF [17].

2 Notation, theory and kinematics

2.1 Notation

Scalars are in lower case a, x, ω, vectors are lower case bold $\boldsymbol{a}, \boldsymbol{x}, \boldsymbol{\omega}$, sets are upper case A, X, Ω, and matrices are bold upper case $\boldsymbol{A}, \boldsymbol{X}, \boldsymbol{\Omega}$. The 0 denotes the scalar zero, while $\mathbf{0}$ is the matrix zero where dimensions are implicitly given by the context. The accents $\hat{\bullet}, \tilde{\bullet}, \dot{\bullet}, \bar{\bullet}, \underline{\bullet}$, denotes estimate, estimate error, time derivative, upper and lower bound. The subscript $\bullet_{(m)}$ denotes the measured value. Some common mathematical expressions which will be used are: The Euclidean norm for vectors and Frobenius norm for matrices, denoted $\|\bullet\|$, absolute value , denoted $|\bullet|$ and the transpose, denoted $\bullet^\top$. The representation of index sets is $\{1, ..., n\} = \{x \in \mathbb{Z} | x \leq n\}$.
A vector can be represented in different coordinate systems. The representation is denoted with the superscripts $\bullet^b, \bullet^n$ which represents the body-fixed and earth-fixed (inertial) coordinate systems, and will be called body-frame and inertial-frame. Lower case will denote the indices of a landmark, vector or matrix $\bullet_i$ and $\bullet_{i,j}$.

2.1.1 Rotation representation

Rotation is the attitude change between two coordinate systems, and a rotation from coordinate system b to n is denoted with subscript $\bullet_{nb}$. This can be represented as:
angle-axis
$\boldsymbol{\Phi}_{nb} = \theta \boldsymbol{u} \in \{\mathbb{R}^3 | \, |\theta| \leq \pi, \|u\| = 1\}$,
Euler angles
$\boldsymbol{\theta}_{nb} = [\phi, \theta, \psi]^\top \in \{\mathbb{R}^3 | \, |\phi| \leq \pi, \, |\theta| \leq \pi, \, |\psi| \leq \pi\}$,
quaternions
$\boldsymbol{q}_{nb} = [s, \boldsymbol{r}^\top]^\top \in \{\boldsymbol{R}^4 | s \in \mathbb{R}, \boldsymbol{r} \in \mathbb{R}^3, \|\boldsymbol{q}\| = 1\}$
rotation matrix
$\boldsymbol{\mathcal{R}}_{nb} \in \{\mathbb{R}^{3\times3} | \, \boldsymbol{\mathcal{R}}_{nb}\boldsymbol{\mathcal{R}}_{nb}^\top = \boldsymbol{I}, \; det(\boldsymbol{\mathcal{R}}_{nb}) = 1\} = SO(3)$. The rotational vector transformation is calculated with the rotation matrix $\boldsymbol{x}^n = \boldsymbol{\mathcal{R}}_{nb}\boldsymbol{x}^b$.

The dynamics of the rotation matrix is described by

$$\dot{\boldsymbol{\mathcal{R}}}_{nb} = \boldsymbol{\mathcal{R}}_{nb}\boldsymbol{S}(\boldsymbol{\omega}) \tag{2.1}$$

where $\boldsymbol{\omega} = \boldsymbol{\omega}_{nb}^b$ is the angular velocity of the frame b relative to n decomposed in b. The matrix $\boldsymbol{S}(\boldsymbol{\omega})$, is the skew-symmetric matrix, representing the cross product in matrix form $\boldsymbol{S}(\boldsymbol{x})\boldsymbol{y} = \boldsymbol{x} \times \boldsymbol{y}$, where $\boldsymbol{S}(\bullet)$ is a skew-symmetric matrix

$$\boldsymbol{S}(\boldsymbol{x}) = \begin{bmatrix} 0 & -x_3 & x_2 \\ x_3 & 0 & -x_1 \\ -x_2 & x_1 & 0 \end{bmatrix} \tag{2.2}$$

which gives $\boldsymbol{S}(\bullet) = -\boldsymbol{S}(\bullet)^\top, \boldsymbol{x}^\top \boldsymbol{S}(\bullet)\boldsymbol{x} = \boldsymbol{0},\ \forall \boldsymbol{x},\ \boldsymbol{S}(\boldsymbol{x})\boldsymbol{y} = -\boldsymbol{S}(\boldsymbol{y})\boldsymbol{x}$ and $\boldsymbol{\mathcal{R}}\boldsymbol{S}(\boldsymbol{x})\boldsymbol{\mathcal{R}}^\top = \boldsymbol{S}(\boldsymbol{\mathcal{R}}\boldsymbol{x}),\ \forall \boldsymbol{\mathcal{R}} \in SO(3)$. Other identities of the $\boldsymbol{S}(\bullet)$ when used with a unit vector $\boldsymbol{u}_x$ are

$$\begin{aligned}
\boldsymbol{S}^2(\boldsymbol{u}_x) &= \boldsymbol{u}_x(\boldsymbol{u}_x)^\top - \boldsymbol{I} \\
\boldsymbol{S}^3(\boldsymbol{u}_x) &= -\boldsymbol{S}(\boldsymbol{u}_x) \\
\boldsymbol{S}^4(\boldsymbol{u}_x) &= -\boldsymbol{S}^2(\boldsymbol{u}_x) \\
\boldsymbol{S}^5(\boldsymbol{u}_x) &= \boldsymbol{S}(\boldsymbol{u}_x) \\
\boldsymbol{S}^6(\boldsymbol{u}_x) &= \boldsymbol{S}^2(\boldsymbol{u}_x)
\end{aligned}$$

Moreover, the cross-product gives the difference in angle-axis between two vectors

$$\boldsymbol{S}(\boldsymbol{x})\boldsymbol{y} = \|\boldsymbol{x}\|\|\boldsymbol{y}\| \sin(\theta)\boldsymbol{u} \tag{2.3}$$

where θ is the angle between the vectors, and $\boldsymbol{u}$ is the unit vector of the axis of the rotation, defined by the right hand rule, and is orthogonal to the two vectors. For the $\boldsymbol{S}$ matrix in 2D

$$\boldsymbol{S}(x) = \begin{bmatrix} 0 & -x \\ x & 0 \end{bmatrix} \tag{2.4}$$

the the cross product is between $[0,\ 0,\ x] \times [y_1,\ y_2,\ 0]$. Commonly x represents rotation rate ω for a vehicle in a 2-D scenario.

More detailed information can be found in Sola [100] and Fossen [34]. Let the rotation matrix denote the rotation from the body-fixed frame to the inertial-frame. The dynamics of the of the rotation matrix is described by

$$\dot{\boldsymbol{\mathcal{R}}}_{nb} = \boldsymbol{\mathcal{R}}_{nb}\boldsymbol{S}(\boldsymbol{\omega}) \tag{2.5}$$

where $\boldsymbol{\omega} = \boldsymbol{\omega}_{nb}^b$ is the angular velocity of the frame b relative to n decomposed in b. For discrete propagation, the Rodriguez formula can be applied to aproximate the rotation [46]

$$\breve{\boldsymbol{\omega}} = \int_t^{t+\Delta t} \boldsymbol{\omega}(t)dt, \quad \bar{\omega} = \|\breve{\boldsymbol{\omega}}\|, \quad \boldsymbol{u}_\omega^b = \frac{\breve{\boldsymbol{\omega}}}{\|\breve{\boldsymbol{\omega}}\|} \tag{2.6}$$

$$\boldsymbol{\mathcal{R}}_{nb}(t + \Delta t) = \boldsymbol{\mathcal{R}}_{nb}\boldsymbol{\mathcal{R}}_{\Delta t} \tag{2.7}$$

$$\boldsymbol{\mathcal{R}}_{\Delta t} = \boldsymbol{I} + \sin(\bar{\omega})\boldsymbol{S}(\boldsymbol{u}_\omega^b) + (1 - \cos(\bar{\omega}))\boldsymbol{S}(\boldsymbol{u}_\omega^b)^2 \tag{2.8}$$

Usually the gyro measurement $\boldsymbol{\omega}_m$ is assumed corrupted by a constant gyro bias

$$\boldsymbol{\omega}_m = \boldsymbol{\omega} + \boldsymbol{b}_\omega \tag{2.9}$$

The estimate of the rotation matrix is denoted $\hat{\boldsymbol{\mathcal{R}}}_{nb}$, and will have the error defined $\tilde{\boldsymbol{\mathcal{R}}}_{nb} = \hat{\boldsymbol{\mathcal{R}}}_{nb}\boldsymbol{\mathcal{R}}_{nb}^\top$ as in [48]. This means the error is a rotation matrix in itself. The gyro-bias error is defined normally $\tilde{\boldsymbol{b}}_\omega = \boldsymbol{b}_\omega - \hat{\boldsymbol{b}}_\omega$

2.2 Projection

It can often be useful to project vector into parallel and orthogonal spaces to certain vectors. This can be done using the unit vector $\boldsymbol{u}_x^n = \frac{x}{\|x\|}$ and skew symmetric matrices. We can define the parallel and orthogonal projection operator or matrices

$$\boldsymbol{U}_x^{\perp} = -\boldsymbol{S}(\boldsymbol{u}_x^n)^2 = (\boldsymbol{I} - \boldsymbol{u}_x^n(\boldsymbol{u}_x^n)^{\top}) \tag{2.10}$$

$$\boldsymbol{U}_x^{\parallel} = \boldsymbol{u}_x^n(\boldsymbol{u}_x^n)^{\top} \tag{2.11}$$

where the projection is preformed by multiplying these matrices with vector

$$\boldsymbol{y} = \boldsymbol{U}_x^{\perp}\boldsymbol{y} + \boldsymbol{U}_x^{\parallel}\boldsymbol{y} \tag{2.12}$$

$$(\boldsymbol{U}_x^{\perp}\boldsymbol{y})^{\top}\boldsymbol{x} = 0 \tag{2.13}$$

$$\boldsymbol{S}(\boldsymbol{U}_x^{\parallel}\boldsymbol{y})\boldsymbol{x} = \boldsymbol{0} \tag{2.14}$$

2.2.1 Parameter projection

Projection also comes opp in parameter projection, which is used when it is desirable to bound the parameter parameter estimates. Details about the parameter projection can be seen in [68, E.1]. It works as a Lipschitz continuous saturation which enables the parameters or state estimates to be bounded. Let the set of possible parameters for state $\boldsymbol{y}$ be defined by $\mathcal{B}_y := y \in \mathbf{R}^n | \mathcal{P}(\boldsymbol{y}) \leq 0$, where $\mathcal{P} : \mathbf{R}^n \to \mathbb{R}$ is a smooth and convex function. For the states estimated in this thesis, the estimates are bounded by the following equations

$$\mathcal{P}_d(\hat{d}_i) = (\hat{d}_i - \bar{d})(\hat{d}_i - \underline{d}) < 0$$
$$\mathcal{P}_b(\hat{b}_\omega) = \boldsymbol{b}_\omega^{\top}\boldsymbol{b}_\omega - \bar{b}^2 < 0$$

which has the following gradients

$$\nabla\mathcal{P}_d = 2\hat{d}_i - (\bar{d} + \underline{d})$$
$$\nabla\mathcal{P}_b = \boldsymbol{b}_\omega^{\top}$$

The projection is then

$$\text{Proj}_{di}(z) = \tag{2.15}$$

$$\begin{cases} z & \mathcal{P}_d(\hat{d}_i) < \delta_d \text{ or } \nabla\mathcal{P}_d z \leq 0 \\ (1 - \min\{1, \frac{\mathcal{P}_d(\hat{d}_i)}{\delta_d}\})z & \mathcal{P}_d(\hat{d}_i) > \delta_d \text{ and } \nabla\mathcal{P}_d z > 0 \end{cases} \tag{2.16}$$

and

$$\text{Proj}_b(z) = \tag{2.17}$$

$$\begin{cases} z & \mathcal{P}_b(\hat{\boldsymbol{b}}_\omega) < \delta_b \text{ or } \nabla\mathcal{P}_b z \leq 0 \\ \boldsymbol{U}^\perp(\hat{\boldsymbol{b}}_\omega, \nabla\mathcal{P}_b)z & \mathcal{P}_b(\hat{\boldsymbol{b}}_\omega) > \delta_b \text{ and } \nabla\mathcal{P}_b z > 0 \end{cases} \tag{2.18}$$

$$\boldsymbol{U}^\perp(\hat{\boldsymbol{b}}_\omega, \nabla\mathcal{P}_b) = (\boldsymbol{I} - \frac{1}{\|\nabla\mathcal{P}_b\|^2}\min\{1, \frac{\mathcal{P}_b(\hat{b}_\omega)}{\delta_b}\}\nabla\mathcal{P}_b\nabla\mathcal{P}_b^\top) \tag{2.19}$$

and will keep the estimates bounded so that $\underline{d} \leq \hat{d}_i < \bar{d}$ and $\|\hat{\boldsymbol{b}}_\omega\| < \bar{b}$. Where δ_d and δ_b are tuning parameters to make the smoother and continuous.

2.3 Landmark and vehicle kinematics

We assume that there is a vehicle with position $\boldsymbol{p}^n$ and m stationary landmarks where the ith landmark has position $\boldsymbol{p}_i^n$. The vectors to the landmarks are the $\boldsymbol{\delta}_i^n = \boldsymbol{p}_i^n - \boldsymbol{p}^n$. These vectors can be represented by their range and bearing,

$$\varrho_i = \|\boldsymbol{\delta}_i^n\| \ , \ \boldsymbol{u}_{\delta i}^n = \boldsymbol{\delta}_i^n / \|\boldsymbol{\delta}_i^n\| \tag{2.20}$$

where the range ϱ_i is the geometric distance, while the bearing $\boldsymbol{u}_{\delta i}^n$ is the unit vector pointing at the landmark. These can also be represented in the body-frame

$$\boldsymbol{\delta}_i^b = \boldsymbol{\mathcal{R}}_{nb}^\top \boldsymbol{\delta}_i^n, \ \ \boldsymbol{u}_{\delta i}^b = \boldsymbol{\mathcal{R}}_{nb}^\top \boldsymbol{u}_{\delta i}^n \tag{2.21}$$

The kinematics of the position of the vehicle is

$$\dot{\boldsymbol{p}^n} = \boldsymbol{v}^n = \boldsymbol{\mathcal{R}}_{nb}\boldsymbol{v}^b \tag{2.22}$$

which results in the time derivative of the distance vector to be

$$\dot{\boldsymbol{\delta}_i^n} = -\boldsymbol{v}^n \tag{2.23}$$

To find the dynamics of the distance vector in body-frame, (2.5) and (2.21)-(2.23) was used with the product rule

$$\begin{aligned} \dot{\boldsymbol{\delta}_i^b} &= \dot{\boldsymbol{\mathcal{R}}}_{nb}^\top \boldsymbol{\delta}_i^n + \boldsymbol{\mathcal{R}}_{nb}^\top \dot{\boldsymbol{\delta}_i^n} \\ &= (\boldsymbol{\mathcal{R}}_{nb}\boldsymbol{S}(\boldsymbol{\omega}))^\top \boldsymbol{\delta}_i^n + \boldsymbol{\mathcal{R}}_{nb}^\top(-\boldsymbol{v}^n) \\ &= -\boldsymbol{S}(\boldsymbol{\omega})\boldsymbol{\delta}_i^b - \boldsymbol{v}^b \end{aligned} \tag{2.24}$$

From this, the dynamics of the range and bearing can be found

$$2\dot{\varrho}_i\varrho_i = 2(\boldsymbol{\delta}_i^n)^\top \dot{\boldsymbol{\delta}}_i^n \tag{2.25}$$

$$\dot{\varrho}_i = (\boldsymbol{u}_{\delta i}^n)^\top(-\boldsymbol{v}^n) = -(\boldsymbol{u}_{\delta i}^n)^\top \boldsymbol{v}^n = -(\boldsymbol{u}_{\delta i}^b)^\top \boldsymbol{v}^b \tag{2.26}$$

$$\begin{aligned}\dot{\boldsymbol{u}}^n_{\delta i} &= \boldsymbol{\delta}^n_i(\frac{\dot{1}}{\varrho_i}) + \frac{\dot{\boldsymbol{\delta}}^n_i}{\varrho_i} = \boldsymbol{\delta}^n_i\frac{-1}{\varrho_i^2}\dot{\varrho}_i + \frac{-\boldsymbol{v}^n}{\varrho_i} \\ &= \boldsymbol{u}^n_{\delta i}\frac{1}{\varrho_i}(\boldsymbol{u}^n_{\delta i})^\top\boldsymbol{v}^n - \frac{\boldsymbol{v}^n}{\varrho_i} \\ &= \frac{1}{\varrho_i}(\boldsymbol{u}^n_{\delta i}(\boldsymbol{u}^n_{\delta i})^\top - \boldsymbol{I})\boldsymbol{v}^n = \frac{1}{\varrho_i}\boldsymbol{S}(\boldsymbol{u}^n_{\delta i})^2\boldsymbol{v}^n \end{aligned} \tag{2.27}$$

$$\begin{aligned}\dot{\boldsymbol{u}}^b_{\delta i} &= \boldsymbol{\delta}^b_i(\frac{\dot{1}}{\varrho_i}) + \frac{\dot{\boldsymbol{\delta}}^b_i}{\varrho_i} = \boldsymbol{\delta}^b_i\frac{-1}{\varrho^2}\dot{\varrho}_i + \frac{-\boldsymbol{S}(\boldsymbol{\omega})\boldsymbol{\delta}^b_i - \boldsymbol{v}^b}{\varrho_i} \\ &= -\frac{\boldsymbol{S}(\boldsymbol{\omega})\boldsymbol{\delta}^b_i}{\varrho_i} + \boldsymbol{u}^b_{\delta i}\frac{1}{\varrho_i}(\boldsymbol{u}^b_{\delta i})^\top\boldsymbol{v}^b + \frac{-\boldsymbol{v}^b}{\varrho_i} \\ \dot{\boldsymbol{u}}^b_{\delta i} &= -\boldsymbol{S}(\boldsymbol{\omega})\boldsymbol{u}^b_{\delta i} + \frac{1}{\varrho_i}(\boldsymbol{u}^b_{\delta i}(\boldsymbol{u}^b_{\delta i})^\top - \boldsymbol{I})\boldsymbol{v}^b \\ &= -\boldsymbol{S}(\boldsymbol{\omega})\boldsymbol{u}^b_{\delta i} + \frac{1}{\varrho_i}\boldsymbol{S}(\boldsymbol{u}^b_{\delta i})^2\boldsymbol{v}^b \end{aligned} \tag{2.28}$$

where we have used that $\boldsymbol{S}(\boldsymbol{u}^b_{\delta i})^2 = (\boldsymbol{u}^b_{\delta i}(\boldsymbol{u}^b_{\delta i})^\top - \boldsymbol{I})$. For mathematical convenience, the inverse range $d_i = \frac{1}{\varrho_i}$ is introduced. Equation (2.26) leads to the time derivative

$$\dot{d}_i = -\frac{1}{\varrho_i^2}\dot{\varrho}_i = d_i^2(\boldsymbol{u}^n_{\delta i})^\top\boldsymbol{v}^n = d_i^2(\boldsymbol{u}^b_{\delta i})^\top\boldsymbol{v}^b \tag{2.29}$$

$$\tag{2.30}$$

which gives the unit vector dynamics

$$\dot{\boldsymbol{u}}^b_{\delta i} = -\boldsymbol{S}(\boldsymbol{\omega})\boldsymbol{u}^b_{\delta i} - d_i(\boldsymbol{u}^b_{\delta i}(\boldsymbol{u}^b_{\delta i})^\top - \boldsymbol{I})\boldsymbol{v}^b \tag{2.31}$$

$$= -\boldsymbol{S}(\boldsymbol{\omega})\boldsymbol{u}^b_{\delta i} + d_i\boldsymbol{S}(\boldsymbol{u}^b_{\delta i})^2\boldsymbol{v}^b \tag{2.32}$$

2.4 Unit vector error and propagation

First, we reorganize the unit vector dynamic (2.32) into

$$\dot{\boldsymbol{u}}^b_{\delta i} = -\boldsymbol{S}(\boldsymbol{\omega})\boldsymbol{u}^b_{\delta i} - d_i\boldsymbol{S}(\boldsymbol{S}(\boldsymbol{u}^b_{\delta i})\boldsymbol{v}^b)\boldsymbol{u}^b_{\delta i} \tag{2.33}$$

$$= -\boldsymbol{S}(\boldsymbol{\omega} + d_i\boldsymbol{S}(\boldsymbol{u}^b_{\delta i})\boldsymbol{v}^b)\boldsymbol{u}^b_{\delta i} \tag{2.34}$$

We then see that we also can use Rodriguez formula (2.8) to propagate the unit vector, by integrating

$$\breve{\boldsymbol{\omega}} = \int_t^{t+\Delta t}(\boldsymbol{\omega} + d_i\boldsymbol{S}(\boldsymbol{u}^b_{\delta i})\boldsymbol{v}^b)\,dt \tag{2.35}$$

$$\boldsymbol{u}^b_{\delta i}(t+\Delta t) = \boldsymbol{\mathcal{R}}^\top_{dt}\boldsymbol{u}^b_{\delta i} \tag{2.36}$$

It was also seen from the (2.3) that the cross-product contains the angle between two vectors. In fact the rotation matrix rotating a unit vector $\hat{\boldsymbol{u}}^b_{\delta i}$ to $\boldsymbol{u}^b_{\delta i}$ can be found by the closed form formula, derived from the Rodriguez formula

$$\boldsymbol{u}^b_{\delta i} = \tilde{\boldsymbol{\mathcal{R}}}\hat{\boldsymbol{u}}^b_{\delta i} \tag{2.37}$$

$$\tilde{\boldsymbol{u}}^b_{\delta i} = \boldsymbol{S}(\boldsymbol{u}^b_{\delta i})\hat{\boldsymbol{u}}^b_{\delta i},\ \check{\boldsymbol{u}}^b = (\hat{\boldsymbol{u}}^b_{\delta i})^\top \boldsymbol{u}^b_{\delta i} \tag{2.38}$$

$$\tilde{\boldsymbol{\mathcal{R}}} = \boldsymbol{I} + \boldsymbol{S}(\tilde{\boldsymbol{u}}^b_{\delta i}) + \frac{1}{1+\check{\boldsymbol{u}}^b}\boldsymbol{S}(\tilde{\boldsymbol{u}}^b_{\delta i})^2 \tag{2.39}$$

It should be noted that the rotation matrix rotating $\hat{\boldsymbol{u}}^b_{\delta i}$ to $\boldsymbol{u}^b_{\delta i}$ is not unique, and has one degree of freedom. The rotation matrix found with formula (2.39) is, however, the matrix with minimal rotation. We also see that the first term in the Taylor expatiation of this rotation is

$$\boldsymbol{u}^b_{\delta i} \approx (\boldsymbol{I} + \boldsymbol{S}(\tilde{\boldsymbol{u}}^b_{\delta i}))\hat{\boldsymbol{u}}^b_{\delta i} \tag{2.40}$$

2.5 Sensor model 2-D special case

In the last part of this thesis, an example of bearing only SLAM will be in the 2-D case will be used for experiments. Where the assumed measurements are: bearing, heading, velocity and acceleration. Their sensor models are summarized in Table 2.1. We will assume that a heading reference system is available, for instance [44], utilizing a magnetometer and accelerometer. This will be able to feed heading estimate $\psi^m = \psi + w_\psi$ from which the rotation matrix estimate can be built

$$\boldsymbol{\mathcal{R}}^m_{nb} = \begin{bmatrix} \cos(\psi + w_\psi) & -\sin(\psi + w_\psi) \\ \sin(\psi + w_\psi) & \cos(\psi + w_\psi) \end{bmatrix} \tag{2.41}$$

Where we see that the rotation matrix is nonlinear with respect to $\psi + w_\psi$, and produces noise that is affected by the nonlinear transformations.This is similar for the bearing measurement from landmarks, which in 2-D with an angle β_i, can be represented as the vector

$$\boldsymbol{u}^{bm}_{\delta i} = \begin{bmatrix} \cos(\beta_i + w_{\beta i}) \\ \sin(\beta_i + w_{\beta i}) \end{bmatrix} \tag{2.42}$$

Table 2.1: Overview of the measurements used in SLAM in 2-D

Measurments	
Measurments	Noise
Bearing: $\boldsymbol{u}_{\delta i}^{bm} = [\cos(\beta_i + w_\beta),\ \sin(\beta_i + w_\beta)]^\top$	$w_\beta = \mathcal{N}(0, \sigma_\beta)$
Heading: $\boldsymbol{\mathcal{R}}_{nb}^{m} = \begin{bmatrix} \cos(\psi + w_\psi) & -\sin(\psi + w_\psi) \\ \sin(\psi + w_\psi) & \cos(\psi + w_\psi) \end{bmatrix}$	$w_\psi = \mathcal{N}(0, \sigma_\psi)$
Acceleration: $f^{bm} = f^b + w_f$	$w_f = \mathcal{N}(0, \sigma_f I_2)$
Velocity: $\boldsymbol{v}^{bm} + w_v$	$w_v = \mathcal{N}(0, \sigma_v I_2)$

2.6 Model Linearization

The system which will be investigated is structured so that the system matrices are time varying; with sensor models having auxiliary measurements as time varying terms. This leads to a non-trivial noise characteristic for the KF, as discussed. Never the less we can approximate the covariance matrices $\boldsymbol{Q}$ and $\boldsymbol{R}$ for the plant noise $\boldsymbol{w}_x$ and output noise $\boldsymbol{w}_y$, respectively and use these in the KF. In addition, if the noises are small perturbations, linearization can give good approximation of the noise characteristics.

The linearization will be on the sensor models in Table 2.1, with respect to the measurements noise w_ψ, $w_{\beta i}$, $\boldsymbol{w}_v$ and $\boldsymbol{w}_f$. We stack all the sensor and sensor noise variables in the vectors $\boldsymbol{z}(t) = [\psi,\ \beta_1,\ \cdots,\ \beta_m,\ (\boldsymbol{v}^b)^\top,\ (\boldsymbol{f}^\top)^\top]^\top$, $\boldsymbol{w} = [w_\psi,\ w_{\beta 1},\ \cdots,\ w_{\beta m},\ \boldsymbol{w}_v^\top,\ \boldsymbol{w}_{fb}^\top]^\top$, respectively, where the multivariate random variable $\boldsymbol{w}$ has the covariance matrix $\boldsymbol{S}$. To then approximate the noise that is introduced by these sensor inputs we linearize the system matrices with respect to the measurement vector $\boldsymbol{z}_m(t) = \boldsymbol{z}(t) + \boldsymbol{w}$

$$\hat{\boldsymbol{F}}(t) = \frac{\partial \boldsymbol{A}(\boldsymbol{z}_m(t), t)\hat{\boldsymbol{x}}(t) + \boldsymbol{B}(\boldsymbol{z}_m(t), t)\boldsymbol{u}(t)}{\partial \boldsymbol{z}_m}$$
$$\hat{\boldsymbol{Y}}(t) = \frac{\partial \boldsymbol{C}(\boldsymbol{z}_m(t), t)\hat{\boldsymbol{x}}(t)}{\partial \boldsymbol{z}_m}$$

Then the covariance of the process noise and measurement noise can be approximated by

$$\hat{\boldsymbol{Q}} = \hat{\boldsymbol{F}}\boldsymbol{S}\hat{\boldsymbol{F}}^\top + \boldsymbol{G}_Q \tag{2.43}$$
$$\hat{\boldsymbol{R}} = \hat{\boldsymbol{Y}}\boldsymbol{S}\hat{\boldsymbol{Y}}^\top + \boldsymbol{H}_R \tag{2.44}$$

where $\boldsymbol{G}_Q$ and $\boldsymbol{H}_R$ are used as tuning/regularization matrices, which also guarantee that the matrices are positive definite. For further details on the linearization for approximating the nonlinear noise, see [17].

2.7 Kalman Filter

Consider the LTV system

$$\dot{\boldsymbol{x}}(t) = \boldsymbol{A}(t)\boldsymbol{x}(t) + \boldsymbol{B}(t)\boldsymbol{u}(t) + \boldsymbol{w}_x \tag{2.45}$$
$$\boldsymbol{y}(t) = \boldsymbol{C}(t)\boldsymbol{x}(t) + \boldsymbol{w}_y \tag{2.46}$$

with states $\boldsymbol{x}$ and output $\boldsymbol{y}$, where $(A(t),\ C(t))$ is Uniformly Completely Observable (UCO). Then a KF can be used as an observer with UGAS error dynamics [99] [62]. The continuous-time KF is,

$$\dot{\hat{\boldsymbol{x}}} = \boldsymbol{A}(t)\hat{\boldsymbol{x}} + \boldsymbol{B}(t)\boldsymbol{u}(t) + \boldsymbol{K}(\boldsymbol{y} - \boldsymbol{C}(t)\hat{\boldsymbol{x}}) \tag{2.47}$$
$$\boldsymbol{K} = \boldsymbol{P}\boldsymbol{C}(t)^\top \mathbf{R}(t)^{-1} \tag{2.48}$$
$$\dot{\boldsymbol{P}} = \boldsymbol{A}(t)\boldsymbol{P} + \boldsymbol{P}\boldsymbol{A}(t) + \boldsymbol{Q}(t) - \boldsymbol{P}\boldsymbol{C}^\top(t)\mathbf{R}(t)^{-1}\boldsymbol{C}(t)\boldsymbol{P} \tag{2.49}$$

where $\boldsymbol{R}$ is the positive definite covariance matrix of the measurement noise $\boldsymbol{w}_y$, and $\boldsymbol{Q}$ is a positive semi-definite matrix of the process noise $\boldsymbol{w}_x$. It should also be noted that sub-optimal covariance matrices $\boldsymbol{Q}$ and $\boldsymbol{R}$ will not damage the global stability property of the observer [3]. In fact, it was shown that symmetry, positive definiteness and boundedness are sufficient conditions on $\boldsymbol{Q}$ and $\boldsymbol{R}^{-1}$. If in addition, the covariance matrix $\boldsymbol{Q}$ is such that $(\boldsymbol{A}(t), \sqrt{\boldsymbol{Q}})$ is controllable, $\boldsymbol{P(0)}$ is symmetric positive definite, the error dynamic is uniformly globally exponentially stable (UGES) stable, and $\boldsymbol{P}$ is uniformly bounded [3]. Here we have reviewed the continuous-time KF, for convenience, and note that its discrete-time version should be used in implementations.

2.8 Observability theory

As mentioned, a Kalman filter can be used on a LTV systems to get a GES observer. Consider the LTV system

$$\dot{\boldsymbol{x}}(t) = \boldsymbol{A}(t)\boldsymbol{x}(t) + \boldsymbol{B}(t)\boldsymbol{u}(t) + \boldsymbol{w}_x \tag{2.50}$$

$$\boldsymbol{y}(t) = \boldsymbol{C}(t)\boldsymbol{x}(t) + \boldsymbol{w}_y \tag{2.51}$$

with the state transition matrix $\boldsymbol{\Phi}(t, t_0)$ satisfying

$$\frac{d}{dt}\boldsymbol{\Phi}(t, t_0) = \boldsymbol{A}(t)\boldsymbol{\Phi}(t, t_0) \tag{2.52}$$

Then the observability can be characterized by the observability Gramian [60]

$$\boldsymbol{\mathcal{W}}_O(t, t+T) = \int_t^{t+T} (\boldsymbol{C}(\tau)\boldsymbol{\Phi}(\tau, t))^\top (\boldsymbol{C}(\tau)\boldsymbol{\Phi}(\tau, t)) d\tau \tag{2.53}$$

If there is a $T > 0$ such that the Gramian is positive definite for any t, the system $(A(t),\ C(t))$ is Uniformly Completely Observable (UCO) [99] [62]. The KF is then,

$$\dot{\hat{\boldsymbol{x}}} = \boldsymbol{A}(t)\hat{\boldsymbol{x}} + \boldsymbol{B}(t)\boldsymbol{u}(t) + \boldsymbol{K}(\boldsymbol{y} - \boldsymbol{C}(t)\hat{\boldsymbol{x}}) \tag{2.54}$$

$$\boldsymbol{K} = \boldsymbol{P}\boldsymbol{C}(t)^\top \mathbf{R}(t)^{-1} \tag{2.55}$$

$$\dot{\boldsymbol{P}} = \boldsymbol{A}(t)\boldsymbol{P} + \boldsymbol{P}\boldsymbol{A}(t) + \boldsymbol{Q}(t) - \boldsymbol{P}\boldsymbol{C}^\top(t)\mathbf{R}(t)^{-1}\boldsymbol{C}(t)\boldsymbol{P} \tag{2.56}$$

where $\boldsymbol{R}$ is the positive definite covariance matrix of the measurment noise $\boldsymbol{w}_y$, and $\boldsymbol{Q}$ is a possitive semi-definite matrix of the prosess noise $\boldsymbol{w}_x$. If in addition, the covariance martix $\boldsymbol{Q}$ is such that $(\boldsymbol{A}(t), \sqrt{\boldsymbol{Q}})$ is controlable, $\boldsymbol{P(0)}$ is symetric positive definite, and $\boldsymbol{C}(t)$ is bounded, the dynamic $\tilde{\boldsymbol{x}}$ is globally exponetially stable, and $\boldsymbol{P}$ is uniformally bounded [3]. Here we have reviewed the continuous-time KF, for convenience, and note that its discrete-time version should be used in implementations.

3 *Cascade Attitude Observers Part 1: Applying Landmark measurements*

3.1 Introduction

Robust navigation and positioning of autonomous vehicles are fundamental for any autonomous mission. A possible scenario is the use of autonomous vehicles for inspection of structures such as bridges, power lines, windmills etc., raising the need of high accuracy in position and attitude estimates, as the vehicles will have to work closely to the inspection target. In this case, the electromagnetic interference and the existence of ferromagnetic materials may degrade any magnetometer to the point of becoming unusable.

Attitude estimation is central to the navigation problem. A common approach for attitude estimation is the use of reference vectors that can among others, come from a magnetometer and accelerometer measuring the earth's gravity. The attitude is then determined by finding the rotation matrix that maps the measured reference vectors in body coordinate system to the known or measured reference vectors in an earth-fixed coordinate system. A computationally efficient complimentary filter was presented in [48, 83], which was proven to have almost global stability for constant reference vectors. Grip [42] proved that with a minor modification, semi-global exponentially stability for time varying reference vectors by could be achieved. An attitude and gyro bias estimation scheme is presented in Batista [14], where the dynamics are given as an LTV system and solved with a Kalman filter. A more computational efficient gyro bias attitude observer is also presented by Batista [13], where the gyro bias is in cascade with the attitude estimation. The mentioned methods use reference vectors from global phenomena. As these observers often rely on magnetometer as heading reference vector, applications where a magnetometer is degenerated can cause compromised results, such as drift in yaw. Several methods use measurements from known landmarks local surroundings. An example is shown by Vasconcelos [108], and Hua [55]. Since these methods require prior knowledge of the landmarks position they fall short when the landmarks are unknown. Lastly, in [47] a UGAS range and bearing SLAM was presented, with filtering preformed in body frame, by posing the SLAM as a linear time varying system.

The structure of the following sections are as follows: Section 3.2 presents the novel estimator and proof of its stability properties; while Section 3.3 shows simulation results. Finally Section 3.4 concludes the part of the chapter, and connects it with the second part of the chapter.

3.2 SLAM Atittude Observer

The attitude and gyro bias estimator in this paper is based on the intuition that the dynamics of the bearing measurement is closely related to the angle rates $\boldsymbol{\omega}$, and thus will be useful for estimating the gyro bias. This will also make it possible to decouple the bias estimation and attitude estimation so that an erroneous attitude estimate does not interfere with the bias estimation. The gyro bias estimator for a vehicle with m landmark observations is

$$\dot{\hat{\boldsymbol{u}}}_i^b = -S(\boldsymbol{\omega}_m - \hat{\boldsymbol{b}}_\omega + \boldsymbol{\sigma}_{ui})\hat{\boldsymbol{u}}_i^b + \frac{1}{\varrho_{im}} S(\hat{\boldsymbol{u}}_i^b) S(\boldsymbol{u}_{im}^b) \boldsymbol{v}_m^b \tag{3.1}$$

$$\boldsymbol{\sigma}_{ui} = k_i S(\boldsymbol{u}_{im}^b)\hat{\boldsymbol{u}}_i^b \tag{3.2}$$

$$\dot{\hat{\boldsymbol{b}}}_\omega = -\sum_{i=1}^{m} \boldsymbol{\sigma}_{ui} \tag{3.3}$$

We see that $(\hat{\boldsymbol{u}}_i^b)^\top \dot{\hat{\boldsymbol{u}}}_i^b = 0$, because $(\hat{\boldsymbol{u}}_i^b)^\top S(\hat{\boldsymbol{u}}_i^b) = \mathbf{0}$, which ensures that $\hat{\boldsymbol{u}}_i^b$ is maintained on the unit ball.

Theorem 1. *Consider the dynamics of a vehicle with bearing and range measurements of landmarks, in addition to velocity measurement, and gyro measurements with a bias* (2.9). *If we choose a k_i large enough, then the observer* (3.14)-(3.16) *is semi-globally asymptotically stable for all trajectories, and constant values of $\boldsymbol{b}_\omega$*

Proof. First comparing the vehicle dynamics to the estimator dynamics,

$$\dot{\boldsymbol{u}}_i^b = -S(\boldsymbol{\omega})\boldsymbol{u}_i^b + \frac{1}{\varrho_i} S(\boldsymbol{u}_i^b) S(\boldsymbol{u}_i^b) \boldsymbol{v}^b \tag{3.4}$$

$$\dot{\hat{\boldsymbol{u}}}_i^b = -S(\boldsymbol{\omega} + \tilde{\boldsymbol{b}}_\omega + \boldsymbol{\sigma}_{ui})\hat{\boldsymbol{u}}_i^b + \frac{1}{\varrho_i} S(\hat{\boldsymbol{u}}_i^b) S(\boldsymbol{u}_i^b) \boldsymbol{v}^b \tag{3.5}$$

the error dynamics of $\tilde{\boldsymbol{u}}_i^b = S(\boldsymbol{u}_i^b)\hat{\boldsymbol{u}}_i^b = \boldsymbol{\sigma}_{ui}$ and $\tilde{\boldsymbol{b}}_\omega = \boldsymbol{b}_\omega - \hat{\boldsymbol{b}}_\omega$ is then

$$\begin{aligned}
\dot{\tilde{\boldsymbol{u}}}_i^b &= S(\boldsymbol{u}_i^b)\dot{\hat{\boldsymbol{u}}}_i^b - S(\hat{\boldsymbol{u}}_i^b)\dot{\boldsymbol{u}}_i^b \\
\dot{\tilde{\boldsymbol{u}}}_i^b &= (S(\boldsymbol{u}_i^b)S(\hat{\boldsymbol{u}}_i^b) - S(\hat{\boldsymbol{u}}_i^b)S(\boldsymbol{u}_i^b))\boldsymbol{\omega} - S(\boldsymbol{u}_i^b)S(\tilde{\boldsymbol{b}}_\omega + \boldsymbol{\sigma}_{ui})\hat{\boldsymbol{u}}_i^b \\
&\quad \frac{1}{\varrho_i}(S(\boldsymbol{u}_i^b)S(\hat{\boldsymbol{u}}_i^b) - S(\hat{\boldsymbol{u}}_i^b)S(\boldsymbol{u}_i^b))S(\boldsymbol{u}_i^b)\boldsymbol{v}^b) \\
\dot{\tilde{\boldsymbol{u}}}_i^b &= S(\tilde{\boldsymbol{u}}_i^b)\boldsymbol{\omega} + \frac{1}{\varrho_i} S(\tilde{\boldsymbol{u}}_i^b) S(\boldsymbol{u}_i^b)\boldsymbol{v}^b - S(\boldsymbol{u}_i^b)S(\tilde{\boldsymbol{b}}_\omega + k_i\tilde{\boldsymbol{u}}_i^b)\hat{\boldsymbol{u}}_i^b \\
\dot{\tilde{\boldsymbol{b}}}_\omega &= \sum_{i=1}^{m} k_i \tilde{\boldsymbol{u}}_i^b
\end{aligned}$$

where we have used that $(S(\boldsymbol{u}_i^b)S(\hat{\boldsymbol{u}}_i^b) - S(\hat{\boldsymbol{u}}_i^b)S(\boldsymbol{u}_i^b)) = S(\tilde{\boldsymbol{u}}_i^b)$ and that the bias is constant $\dot{\boldsymbol{b}}_\omega = \mathbf{0}$. We then see that this system has an equilibrium point when

$\tilde{\boldsymbol{u}}_i^b = \mathbf{0}$ and $\tilde{\boldsymbol{b}}_\omega = \mathbf{0}$. We want to show that for any $0 < \epsilon < \pi$, a solution starting in $\tilde{\theta}_{ui} \in [-\pi + \epsilon, \pi - \epsilon] \forall i \in \{1, m\}$ will stay in the set for gain k_i large enough. We choose a Lyapunov function for every bearing measurment, $V_i = 1 - (\hat{\boldsymbol{u}}_i^b)^\top \boldsymbol{u}_i^b = 1 - \cos(\tilde{\theta}_{ui})$, which is positive definite and increasing for $\tilde{\theta}_{ui} \in (-\pi, \pi)$. It will have the derivative

$$\dot{V}_i = \tilde{\boldsymbol{b}}_\omega^\top \tilde{\boldsymbol{u}}_i^b - k_i \|\tilde{\boldsymbol{u}}_i^b\|^2 \leq -\|\tilde{\boldsymbol{u}}_i^b\|(k_i \|\tilde{\boldsymbol{u}}_i^b\| - \bar{b}_\omega)$$

where we recall that there is a bound on the bias $\bar{b}_\omega$ and that $\|\tilde{\boldsymbol{u}}_i^b\| = |\sin(\tilde{\theta}_{ui})|$. We see that we can choose a k_i large enough $k_i > \frac{\bar{b}_\omega}{|\sin(\epsilon)|}$, so that for $|\tilde{\theta}_{ui}| = \pi - \epsilon \Rightarrow \|\tilde{\boldsymbol{u}}_i^b\| = |\sin(\epsilon)|$ we will have $\dot{V}_i < 0$, which implies that $\tilde{\theta}_{ui}$ is strictly decreasing. Then $\|\tilde{\boldsymbol{u}}_i^b(0)\|$ can easily be chosen so that $|\tilde{\theta}_{ui}(0)| < \pi - \epsilon$, and by the continuity of the solution we can guarantee that the solution will never exceed $|\tilde{\theta}_{ui}| > \pi - \epsilon$, and will therefore utilize that this holds for the rest of our analysis. We choose the Lyapunov function candidate

$$V_b(\boldsymbol{u}_i^b, \hat{\boldsymbol{u}}_i^b, \tilde{\boldsymbol{b}}_\omega) = \sum_{i=1}^{m} k_i (1 - (\boldsymbol{u}_i^b)^\top \hat{\boldsymbol{u}}_i^b) + \frac{1}{2} \tilde{\boldsymbol{b}}_\omega^\top \tilde{\boldsymbol{b}}_\omega \tag{3.6}$$

First, we see that V_b can be rewritten as

$$V_b(\boldsymbol{u}_i^b, \hat{\boldsymbol{u}}_i^b, \tilde{\boldsymbol{b}}_\omega) = \sum_{i=1}^{m} k_i (1 - \cos(\tilde{\theta}_{ui})) + \frac{1}{2} \tilde{\boldsymbol{b}}_\omega^\top \tilde{\boldsymbol{b}}_\omega \tag{3.7}$$

where $\tilde{\theta}_{ui} = ||\tilde{\boldsymbol{\Phi}}_{li}||$ is the magnitude of the angle-axis between the LOS vector and its estimate, this makes V_b positive definite for $\tilde{\theta}_{ui} \in [-\pi, \pi]$. We calculate

$$\begin{aligned}
((\dot{\boldsymbol{u}}_i^b)^\top \hat{\boldsymbol{u}}_i^b + (\boldsymbol{u}_i^b)^\top \dot{\hat{\boldsymbol{u}}}_i^b) &= (-\boldsymbol{S}(\boldsymbol{\omega}) \boldsymbol{u}_i^b + \frac{1}{\varrho_i} \boldsymbol{S}(\boldsymbol{u}_i^b) \boldsymbol{S}(\boldsymbol{u}_i^b) \boldsymbol{v}^b)^\top \hat{\boldsymbol{u}}_i^b \\
&\quad + (\boldsymbol{u}_i^b)^\top (-\boldsymbol{S}(\boldsymbol{\omega} + \tilde{\boldsymbol{b}}_\omega + \boldsymbol{\sigma}_{ui}) \hat{\boldsymbol{u}}_i^b + \frac{1}{\varrho_i} \boldsymbol{S}(\hat{\boldsymbol{u}}_i^b) \boldsymbol{S}(\boldsymbol{u}_i^b) \boldsymbol{v}^b) \\
&= -(\boldsymbol{u}_i^b)^\top \boldsymbol{S}(\tilde{\boldsymbol{b}}_\omega + \boldsymbol{\sigma}_{ui}) \hat{\boldsymbol{u}}_i^b)
\end{aligned}$$

where we used that $(\frac{1}{\varrho_i} \boldsymbol{S}(\boldsymbol{u}_i^b) \boldsymbol{S}(\boldsymbol{u}_i^b) \boldsymbol{v}^b)^\top \hat{\boldsymbol{u}}_i^b + (\boldsymbol{u}_i^b)^\top \frac{1}{\varrho_i} \boldsymbol{S}(\hat{\boldsymbol{u}}_i^b) \boldsymbol{S}(\boldsymbol{u}_i^b) \boldsymbol{v}^b = 0$. The time derivative of V_b is then

$$\begin{aligned}
\dot{V}_b(\boldsymbol{u}_i^b, \hat{\boldsymbol{u}}_i^b, \tilde{\boldsymbol{b}}_\omega)) &= -\sum_{i=1}^{m} k_i ((\dot{\boldsymbol{u}}_i^b)^\top \hat{\boldsymbol{u}}_i^b + (\boldsymbol{u}_i^b)^\top \dot{\hat{\boldsymbol{u}}}_i^b) + \tilde{\boldsymbol{b}}_\omega^\top \dot{\tilde{\boldsymbol{b}}}_\omega \\
&= \sum_{i=1}^{m} [k_i (\boldsymbol{u}_i^b)^\top \boldsymbol{S}(\boldsymbol{\sigma}_{ui}) \hat{\boldsymbol{u}}_i^b + k_i (\boldsymbol{u}_i^b)^\top \boldsymbol{S}(\tilde{\boldsymbol{b}}_\omega) \hat{\boldsymbol{u}}_i^b] + \tilde{\boldsymbol{b}}_\omega^\top \sum_{i=1}^{m} k_i (\boldsymbol{S}(\boldsymbol{u}_i^b) \hat{\boldsymbol{u}}_i^b) \\
&= \sum_{i=1}^{m} k_i^2 (\boldsymbol{u}_i^b)^\top \boldsymbol{S}(\boldsymbol{S}(\boldsymbol{u}_i^b) \hat{\boldsymbol{u}}_i^b) \hat{\boldsymbol{u}}_i^b = -\sum_{i=1}^{m} k_i^2 (\hat{\boldsymbol{u}}_i^b)^\top \boldsymbol{S}(\boldsymbol{u}_i^b)^\top \boldsymbol{S}(\boldsymbol{u}_i^b) \hat{\boldsymbol{u}}_i^b
\end{aligned}$$

which is equal to

$$\dot{V}_b = -\sum_{i=1}^{m} k_i^2 \|\tilde{\boldsymbol{u}}_i^b\|^2 = -\sum_{i=1}^{m} k_i^2 \sin(\tilde{\theta}_{ui})^2 < 0, \;\; \tilde{\theta}_{ui} \neq 0 \text{ or } \pm\pi$$

Hence $\dot{V}_b$ is negative definite on the open set $\tilde{\theta}_{ui} \in (-\pi, \pi)$. We can conclude that the system is stable, and that the Lyapunov function will converge to $\dot{V}_b = 0$, hence the trajectories will converge to the set $E(\dot{V}_b = 0) = \{\tilde{\boldsymbol{u}}_i^b | \; \|\tilde{\theta}_{ui}\| = 0 \forall i \in \{1, m\}\}$, since $|\tilde{\theta}_{ui}| \neq \pi$. We can also conclude that the Lyapunov function V_b converges to a constant, thus $\|\tilde{\boldsymbol{b}}_\omega\|$ will also converge to a constant.

What is left is to show that the states will be in the set $E(\dot{V}_b = 0)$ in finite time, when $\|\tilde{\boldsymbol{b}}_\omega\| \neq 0$, which means $\|\tilde{\boldsymbol{b}}_\omega\|$ has to converge to zero. For this, Matrosov theorem will be utilized [86]. We choose the auxiliary function

$$W = \sum_{i=1}^{m} \tilde{\boldsymbol{b}}_\omega^\top \tilde{\boldsymbol{u}}_i^b = \sum_{i=1}^{m} (\boldsymbol{u}_i^b)^\top \boldsymbol{S}(\tilde{\boldsymbol{b}}_\omega) \hat{\boldsymbol{u}}_i^b \tag{3.8}$$

First we see that W is bounded by the states. To find the derivative of $\dot{W}$ we use

$$\begin{aligned}
(\dot{\boldsymbol{u}}_i^b)^\top \boldsymbol{S}(\tilde{\boldsymbol{b}}_\omega)\hat{\boldsymbol{u}}_i^b &= (\boldsymbol{u}_i^b)^\top \boldsymbol{S}(\boldsymbol{\omega})\boldsymbol{S}(\tilde{\boldsymbol{b}}_\omega)\hat{\boldsymbol{u}}_i^b + \frac{1}{\varrho_i}(\boldsymbol{v}^b)^\top \boldsymbol{S}(\boldsymbol{u}_i^b)\boldsymbol{S}(\boldsymbol{u}_i^b)\boldsymbol{S}(\tilde{\boldsymbol{b}}_\omega)\hat{\boldsymbol{u}}_i^b \\
(\boldsymbol{u}_i^b)^\top \boldsymbol{S}(\dot{\tilde{\boldsymbol{b}}}_\omega)\hat{\boldsymbol{u}}_i^b &= (\boldsymbol{u}_i^b)^\top \boldsymbol{S}(\sum_{i=1}^{m} k_i \tilde{\boldsymbol{u}}_i^b)\hat{\boldsymbol{u}}_i^b = -(\tilde{\boldsymbol{u}}_i^b)^\top \sum_{i=1}^{m} k_i \tilde{\boldsymbol{u}}_i^b \\
(\boldsymbol{u}_i^b)^\top \boldsymbol{S}(\tilde{\boldsymbol{b}}_\omega)\dot{\hat{\boldsymbol{u}}}_i^b) &= -(\boldsymbol{u}_i^b)^\top \boldsymbol{S}(\tilde{\boldsymbol{b}}_\omega)\boldsymbol{S}(\boldsymbol{\omega})\hat{\boldsymbol{u}}_i^b + (\boldsymbol{u}_i^b)^\top \boldsymbol{S}(\tilde{\boldsymbol{b}}_\omega)\boldsymbol{S}(\tilde{\boldsymbol{b}}_\omega)\hat{\boldsymbol{u}}_i^b \cdots \\
&\quad + (\boldsymbol{u}_i^b)^\top \boldsymbol{S}(\tilde{\boldsymbol{b}}_\omega)\boldsymbol{S}(\sigma_{ui})\hat{\boldsymbol{u}}_i^b + \frac{1}{\varrho_i}(\boldsymbol{u}_i^b)^\top \boldsymbol{S}(\tilde{\boldsymbol{b}}_\omega)\boldsymbol{S}(\hat{\boldsymbol{u}}_i^b)\boldsymbol{S}(\boldsymbol{u}_i^b)\boldsymbol{v}^b
\end{aligned}$$

Adding these together, along with some algebra gives

$$\begin{aligned}
\dot{W} = \sum_{i=1}^{m} [&(\tilde{\boldsymbol{b}}_\omega)^\top \boldsymbol{S}(\boldsymbol{\omega})\tilde{\boldsymbol{u}}_i^b + (\boldsymbol{v}^b)^\top \boldsymbol{S}(\boldsymbol{u}_i^b)\boldsymbol{S}(\tilde{\boldsymbol{b}}_\omega)\tilde{\boldsymbol{u}}_i^b \cdots \\
&- (\tilde{\boldsymbol{u}}_i^b)^\top \sum_{i=1}^{m} k_i \tilde{\boldsymbol{u}}_i^b + (\boldsymbol{u}_i^b)^\top \boldsymbol{S}(\tilde{\boldsymbol{b}}_\omega)\boldsymbol{S}(\tilde{\boldsymbol{b}}_\omega)\hat{\boldsymbol{u}}_i^b \cdots \\
&+ (\boldsymbol{u}_i^b)^\top \boldsymbol{S}(\tilde{\boldsymbol{b}}_\omega)\boldsymbol{S}(k_i \tilde{\boldsymbol{u}}_i^b)\hat{\boldsymbol{u}}_i^b]
\end{aligned}$$

Where we see that as $\|\tilde{\boldsymbol{u}}_i^b\| \to 0$, the term left is

$$\begin{aligned}
\lim_{\|\tilde{\boldsymbol{u}}_i^b\| \to 0} \dot{W} &= \sum_{i=1}^{m} (\boldsymbol{u}_i^b)^\top \boldsymbol{S}(\tilde{\boldsymbol{b}}_\omega)\boldsymbol{S}(\tilde{\boldsymbol{b}}_\omega)\hat{\boldsymbol{u}}_i^b = \sum_{i=1}^{m} (\tilde{\boldsymbol{b}}_\omega)^\top \boldsymbol{S}(\boldsymbol{u}_i^b)\boldsymbol{S}(\hat{\boldsymbol{u}}_i^b)\tilde{\boldsymbol{b}}_\omega \\
&= -c\|\tilde{\boldsymbol{b}}_\omega\|
\end{aligned}$$

where c is a positive constant. We have used that the eigenvalue of the matrix $\boldsymbol{S}(\hat{\boldsymbol{u}}_i^b)\boldsymbol{S}(\boldsymbol{u}_i^b)$ are $\boldsymbol{\lambda} = [0, \; -(\boldsymbol{u}_i^b)^\top \hat{\boldsymbol{u}}_i^b, \; -(\boldsymbol{u}_i^b)^\top \hat{\boldsymbol{u}}_i^b]$ which for $\|\tilde{\boldsymbol{u}}_i^b\| \to 0$ the matrix has

eigenvalues $\boldsymbol{\lambda} = [0, -1, -1]$ with the zero vector $\boldsymbol{u}_i^b$. The matrix $\sum_{i=1}^{m} \boldsymbol{S}(\boldsymbol{u}_i^b)\boldsymbol{S}(\hat{\boldsymbol{u}}_i^b)$ is therefore negative definite because there are at least two $\boldsymbol{u}_i^b$ that are not parallel so that the matrix is full rank, negative definite. Hence $\dot{W}$ is definitely not equal to zero when $\|\tilde{\boldsymbol{u}}_i^b\| = 0$ and $\|\tilde{\boldsymbol{b}}_\omega\| > 0$. Since we know that W is bounded by the states, we know that W converges to a constant. We therefore know that $\dot{W} \to 0$ as $t \to \infty$, which implies that $\tilde{\boldsymbol{b}}_\omega \to 0$ as $t \to \infty$. Hence we can conclude from Matrosov's theorem that the system will converge to $\|\tilde{\boldsymbol{b}}_\omega\| \to 0$ and $\|\tilde{\boldsymbol{u}}_i^b\| \to 0,\ \forall i \in \{1, m\}$ as $t \to \infty$, for almost all trajectories, since $\epsilon > 0$ can be chosen arbitrary small.

□

In practice, the estimate $\hat{l}_i^b$ can be chosen from its direct measurment in the initialization, so that k_i easier to furfill. In simmulations the observer has been tested with initialization $\tilde{\theta}_{ui} = \pi$ without any convergance problem. The bias estimated can then be used in cascade with the simplified complimentary filter from [55]

$$\dot{\hat{\boldsymbol{\mathcal{R}}}}_{nb} = \hat{\boldsymbol{\mathcal{R}}}_{nb}\boldsymbol{S}(\boldsymbol{\omega_m} - \hat{\boldsymbol{b}}_\omega + \sigma_{\mathcal{R}}) \tag{3.9}$$

$$\sigma_{\mathcal{R}} = \sum_{i=1}^{n} c_i \boldsymbol{S}(\boldsymbol{r}_i^b)\hat{\boldsymbol{\mathcal{R}}}_{nb}^\top \boldsymbol{r}_i^n \tag{3.10}$$

were semi-globally stability can be achieved. First however, an assumption is needed

Assumption 1. *there exists a constant $c_{obs} > 0$ so as, for each $t \geq 0$, the inequality $\|\boldsymbol{r}_j^b \times \boldsymbol{r}_k^b\| > c_{obs}$ holds for at least two of the indices $j, k \in \{1, ..., n\}$*

Theorem 2. *Consider the dynamics of a vehicle with bearing and range measurements of landmarks, in addition to velocity measurement, and gyro measurements with a bias* (2.9)*. Under the conditions of Theorem 3 and Assumption 1 satisfied, and for c_i large enough, the observer with* (3.14)-(3.16) *in cascade with* (3.101)-(3.102)*, will be semi-globally asymptotically stable for time varying reference vectors.*

Proof. From *Theorem 3*, and since the gyro bias estimator is independent of the attitude estimates, we know that the gyro bias estimate error $\tilde{\boldsymbol{b}}_\omega$ is bounded and converges $\|\tilde{\boldsymbol{b}}_\omega\| \to 0$ as $t \to \infty$. We also know that the Lyapunov function bounds the gyro bias error from the gyro bias observer $V_b(t) > \|\boldsymbol{b}_\omega(t)\|^2 \forall (t)$ that goes to zero monotonicly. What is left to show is that the system (3.101)-(3.102) is kept bounded for gyro bias error $\tilde{\boldsymbol{b}}_\omega$, and that for $\|\tilde{\boldsymbol{b}}_\omega\| \to 0$, the attitude estimate $\tilde{\boldsymbol{\mathcal{R}}}_{nb} \to I$. First we recall that the observer (3.101)-(3.102) with zero gyro bias, is shown in Mahony [82] and Hua [54] to have almost globally asymptotically stabilety properties for constant reference vectors and semi-globally exponentially stabilety propeties for time-varying reference vectors. This gives $\tilde{\boldsymbol{\mathcal{R}}}_{nb} \to I$ for $\|\tilde{\boldsymbol{b}}_\omega\| = 0$ for all trajectories starting with $|\tilde{\boldsymbol{\Phi}}_{nb}(0)| < \pi - \epsilon$. In addition, Grip showed in the start of the proof of Theorem 1 in appendix B [42]; that if the gyro

bias error is bounded, then an c_i can be chosen for system (3.101)-(3.102) so that the attitude estimate is bounded away from $|\mathbf{\Phi}_{nb}| < \pi - \epsilon$, which means an error from the gyro bias estimator below the bound will not destabilize the attitude estimate. The proof is in quaternions, where the attitude error is $\tilde{\boldsymbol{q}} = [\tilde{s}, \tilde{\boldsymbol{r}}^\top]^\top$, and we recall that $\tilde{s} = 1 \Leftrightarrow \tilde{\boldsymbol{\mathcal{R}}}_{nb} = I$. The Lyapunov function is chosen $V_R(\tilde{s}) = 1 - \tilde{s}^2$, which for system system (3.101)-(3.102) with a gyro bias error $\tilde{\boldsymbol{b}}_\omega$ has the derivative (from [42] appendix B)

$$\dot{V}_R \leq -\tilde{s}\tilde{\boldsymbol{r}}^\top \boldsymbol{\mathcal{R}}_{nb}\tilde{\boldsymbol{b}}_\omega - k_p c_{obs}^2 \tilde{s}^2(1-\tilde{s}^2) \leq \sqrt{V_b} - k_p c_{obs}^2 \tilde{s}^2(1-\tilde{s}^2)$$

where c_p is a lower bound on the c_i gains, and c_{obs} comes from the assumption on the reference vectors. For a given bound $V_b(0)$ on the gyro bias at the initialization, k_p can be chosen $k_p >= \bar{b}_\omega/(c_{obs}^2\epsilon^2(1-\epsilon^2))$ so that $\dot{V}_R < 0$ for $|\tilde{s}| = \epsilon$. Which implies that $\tilde{s}$ is increasing if $|\tilde{s}| = \epsilon$ and because of continuity of $\dot{V}_R$ and the solutions $\tilde{s}(0) \geq \epsilon$ then $\tilde{s}(t) > \epsilon \ \forall t > 0$. Further on, there is a γ so that for $\epsilon < |\tilde{s}| < \gamma$ the $\dot{V}_R < 0$, which by the ultimate boundedness Theorem 4.18 [64] ensures that $|\tilde{s}| > \gamma$, $t \geq \tau + T$ in finite time. In addition, we see that as $V_b \to 0$ the bound $\gamma \to 1$ which implies that $\tilde{\boldsymbol{\mathcal{R}}}_{nb} \to I$ as $t \to \infty$. Thus we can conclude that (3.14)-(3.16) in cascade with (3.101)-(3.102) is semi-globally asymptotically stable, making the estimates converge to $\tilde{\boldsymbol{\mathcal{R}}}_{nb} \to I$, $\tilde{\boldsymbol{b}}_\omega \to 0$ as $t \to \infty$ because ϵ can be arbitrary small. □

Remark 1. *It should be noted that the global reference vectors can also be used in the gyro bias observer, for* $\boldsymbol{u}_i^b = \boldsymbol{r}_i^b$ *and* $\varrho_i \to \infty$

The total observer is summarized in Table 3.2

Table 3.1: Summary of the SLAM Attitude Observer

SLAM ATTITUDE OBSERVER	
Measurements: $\boldsymbol{\omega}_m$, ϱ_{im}, $\boldsymbol{v}_m^b$, $\boldsymbol{u}_i^b$, $\boldsymbol{v}_i^b$, $(\boldsymbol{v}_i^n)$	
$\dot{\hat{\boldsymbol{u}}}_i^b = -\boldsymbol{S}(\boldsymbol{\omega}_m - \hat{\boldsymbol{b}}_\omega + \boldsymbol{\sigma}_{ui})\hat{\boldsymbol{u}}_i^b + \frac{1}{\varrho_{im}}\boldsymbol{S}(\hat{\boldsymbol{u}}_i^b)\boldsymbol{S}(\boldsymbol{u}_{im}^b)\boldsymbol{v}_m^b$	(3.14)
$\boldsymbol{\sigma}_{ui} = k_i \boldsymbol{S}(\boldsymbol{u}_{im}^b)\hat{\boldsymbol{u}}_i^b$	(3.15)
$\dot{\hat{\boldsymbol{b}}}_\omega = -\sum_{i=1}^{m} \boldsymbol{\sigma}_{ui}$	(3.16)
$\dot{\hat{\boldsymbol{\mathcal{R}}}}_{nb} = \hat{\boldsymbol{\mathcal{R}}}_{nb}\boldsymbol{S}(\boldsymbol{\omega_m} - \hat{\boldsymbol{b}}_\omega + \boldsymbol{\sigma}_{\mathcal{R}})$	(3.101)
$\boldsymbol{\sigma}_{\mathcal{R}} = \sum_{i=1}^{n} c_i \boldsymbol{S}(\boldsymbol{r}_i^b)\hat{\boldsymbol{\mathcal{R}}}_{nb}^\top \boldsymbol{r}_i^n$	(3.102)

3.3 Simulation Results and Performance Evaluation

The observer was tested with simulations, and compared to the complimentary filter. A vessel travelling in a 3D-space described by the dynamics of (2.5) and

(2.22), with changing angular velocity
$\boldsymbol{\omega}(t) = [r_1 \cos(f_1 t),\ r_2 \sin(f_2 t),\ r_3 \log(1 + f_3 t)]^\top$ and constant speed $\boldsymbol{v}^b = [v_1,\ 0,\ 0]$. The trajectory of the vessel, with the landmarks positions can be seen in Figure 5.9.

Three landmarks are placed randomly in a box $50m$ from the start point of the vessel. The $\boldsymbol{\omega}_m$ has a bias $\boldsymbol{b}_\omega = [0.8,\ 0.1,\ -0.5]^\top$, and is corrupted with a white noise with standard deviation $\boldsymbol{\sigma}_\omega = \boldsymbol{I}0.001$. The noise in the bearing and range measurements are $\boldsymbol{\sigma}_u = \boldsymbol{I}0.01$ and $\sigma_\varrho = 0.005$. The bearing noise is orthogonal to the bearing $\boldsymbol{u}_n = \boldsymbol{S}(\boldsymbol{u}^b_{\delta i})\boldsymbol{w}_u$, where the noise $\boldsymbol{w}_u$ was a white noise vector $\boldsymbol{w}_u = \mathcal{N}(0, \boldsymbol{\sigma}_u)$. The reference-vectors chosen were the normalized magnetometer and gravity.

$$\boldsymbol{r}^n_1 = [1,\ 0,\ 0]^\top,\ \boldsymbol{r}^b_1 = \boldsymbol{\mathcal{R}}^\top \boldsymbol{r}^n_1 \tag{3.11}$$

$$\boldsymbol{r}^n_2 = [0,\ 0,\ -1]^\top,\ \boldsymbol{r}^b_2 = \boldsymbol{\mathcal{R}}^\top([0, 0, -1]^\top + \boldsymbol{a}^n/g) \tag{3.12}$$

$$\boldsymbol{r}^n_3 = \boldsymbol{S}(\boldsymbol{r}^n_1)\boldsymbol{r}^n_2,\ \boldsymbol{r}^b_3 = \boldsymbol{S}(\boldsymbol{r}^b_1)\boldsymbol{r}^b_2 \tag{3.13}$$

The LOS observer was tuned with $k_i = \frac{1}{m} = \frac{1}{3}$. The SLAM attitude observer in cascade with the LOS observer, was tuned as the complimentary filter: $k_1 = 0.2,\ k_2 = 0.5,\ k_3 = 0.3$. Where the weights k_i are weighted according quality of the measurements and gave the best results for both observers. The bias estimation gain of the complimentary filter was $k_I = 0.15$, which gave the best trade-off between the transient performance and variance of the ω output. The starting attitude was $\boldsymbol{\theta}_{nb}(0) = \mathbf{0}$, while the start estimate was $\hat{\boldsymbol{\theta}}_{nb}(0) = [\frac{5}{6}\pi,\ 0,\ \frac{3}{4}\pi]$ The results can be seen in Figures, 3.2-3.4.

From the figures it is apparent that the SLAM observer has a faster convergence in both attitude and bias estimation, with no overshoots. This is a result of the decoupling of the estimation, so the bad attitude estimate does not affect the gyro bias estimation, as can happen with the complementary filter. It should be noted that this is the case if the gyro-bias is significant and there is a bad initial guess of the attitude estimate.

Another simulation was done for double gyro bias $\mathbf{b}_\omega = [1.6\ , 0.2\ , -1]$, and the results can be seen in figures 3.5-3.6. From these simulations it is apparent that the SLAM attitude observer is more robust against high gyro bias and bad attitude initialization, which again is the result of the decoupled system.

3.3.1 Magnetometer failure

A substantial goal for the SLAM attitude observer, is to make it less dependent on magnetometer measurements. To test if this is achieved, a scenario where the magnetometer is turned off is demonstrated. The compass reference vector is set to the zero after $t = 3000$, leaving the gravity as the only reference vector left. The results can be seen in figures 3.7 and 3.8. The bias estimation of the complimentary filter starts being irregular, resulting in a drift in the attitude estimates with axis parallel to the gravity vector. The SLAM attitude observer still manages to estimate

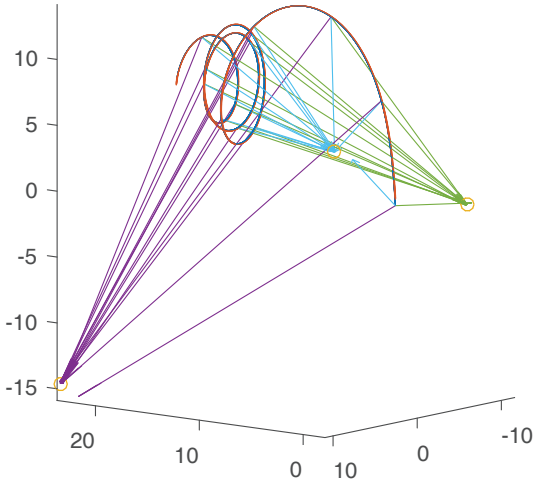

Figure 3.1: The figure shows the trajectory of the vehicle, and the landmarks. The arrows represent the estimated distance vectors using $\hat{\boldsymbol{l}}_i^n$

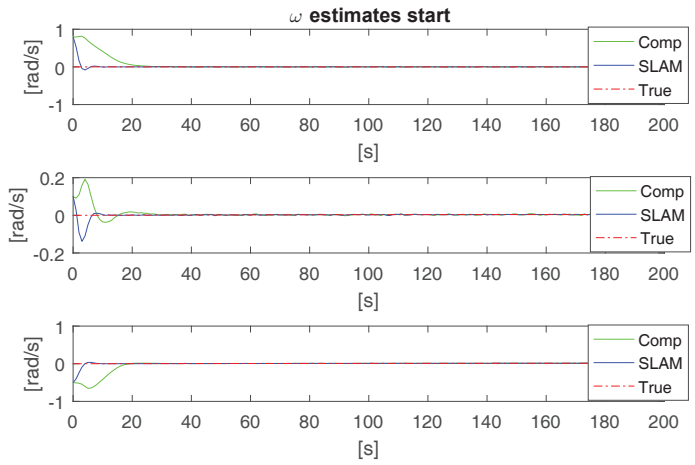

Figure 3.2: The resulting ω estimates transients from the complimentary filter and SLAM attitude observer

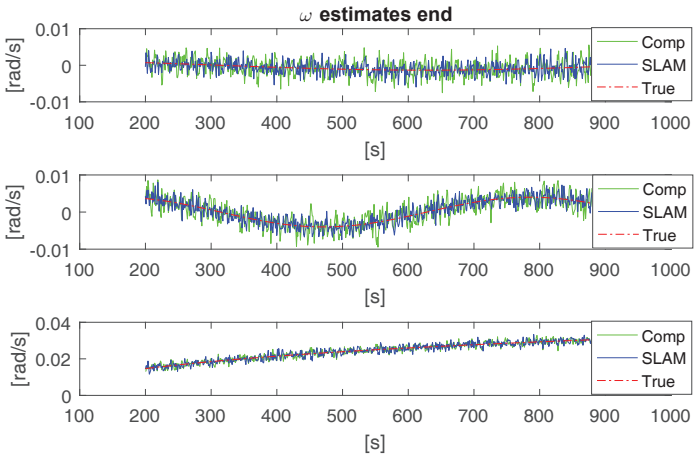

Figure 3.3: The resulting ω estimates from the complimentary filter and SLAM attitude observer, this shows the result for the steady state bias estimates

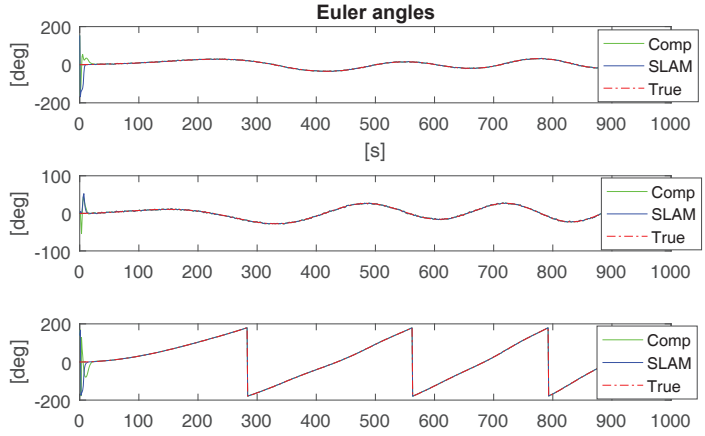

Figure 3.4: The figure shows the attitude from the complimentary filter and SLAM observer. Both gets good estimated, but SLAM observer demonstrates less overshoot

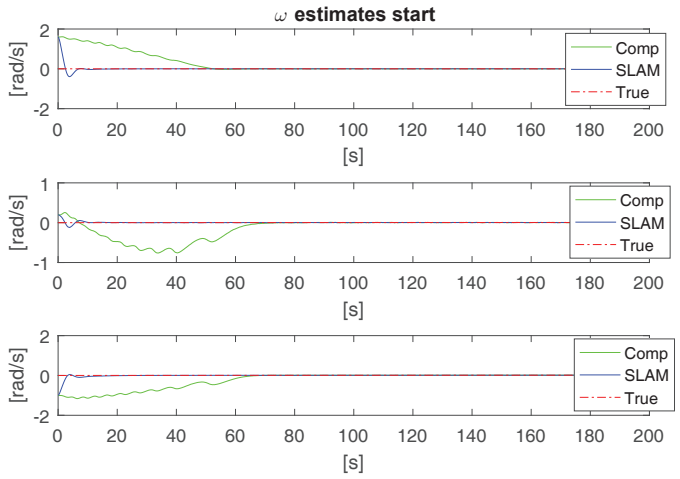

Figure 3.5: The resulting ω estimates transient from the complimentary filter and SLAM attitude observer for increased gyro bias

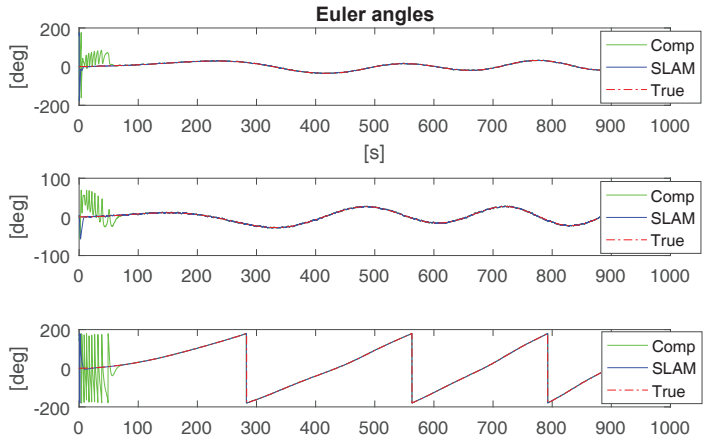

Figure 3.6: The figure shows the attitude from the complimentary filter and SLAM observer for increased gyro bias. The SLAM observer demonstrates faster and smoother convergence

the bias, and thus the estimated attitude is hardly affected by the loss of the magnetometer reference vector, although it has some minor drift in the yaw axis, which is expected.

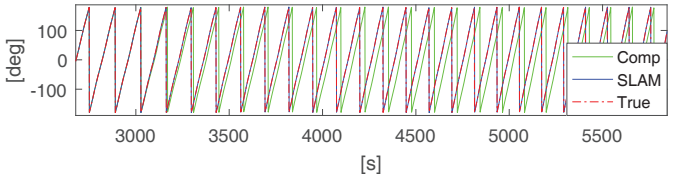

Figure 3.7: The figure shows the yaw angle from the complimentary filter and SLAM attitude observer. A compass failure is introduced in $t = 3000$ and the result is a drift in the yaw estimates for the complimentary filter, while the SLAM attitude observer does not get affected.

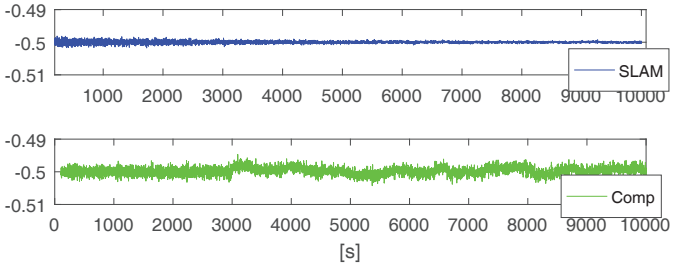

Figure 3.8: The resulting gyro bias estimates from the complimentary filter and SLAM attitude observer in yaw. A compass failure is introduced in $t = 3000$ and the result is oscillations for the complimentary filter

3.4 Conclusion

In this paper, we have discussed the SLAM problem, in addition to attitude and gyro bias estimation. We presented an observer that has decoupled the gyro bias and the attitude estimation to avoid that bad initialization interfere with the bias estimations. It applies bearing and range measurements of unknown landmarks for the bias estimation, in addition to reference vectors measurements. The performance of the observer is compared to the complimentary filter, where the advantageous behaviour of the observer is seen. A scenario in which there is a failure in the magnetometer has been demonstrated, and thus also the benefits of redundant measurements are shown.

A natural improvement of the setup, would be to relax the necessity of range measurements, which would allow the observer to work with a monocular camera. For a UAV flight this is important, as stereo camera and Liadar has more weight and power consumption. In part 2 of this chapter, an observer only requiring bearing measurements from landmarks is developed. The proof of its stability

is organized somewhat differently, and shows exponential stability in the large. Some parts, however, are clearly inspired from the proof in this part of the chapter. It also be noted that using similar steps as in the next chapter, it would be possible to prove that the observer presented in this part of the chapter has exponential stability in the large.

Cascade Attitude Observers Part 2: Bearing only Landmark measurements

3.5 Introduction

As mentioned previous in the chapter, having a robust heading estimate can be challenging with of the shelf sensors, especially when navigating in areas where a magnetometer is degenerated by electromagnetic fields. Also when navigating close to the poles the small heading component of the magnetic field can make a robust heading estimate even more challenging to acquire.

However, if a camera is available and it is observing enough features, a velocity in the body frame can be estimated as shown in [38], and yaw can hence be found by comparing the GNSS velocity to the camera velocity. However in a hovering scenario, as there is no velocity, the yaw is no longer observable for this setup.

Camera aided inertial navigation has been extensively studied. Some setups rely on having landmarks with known position, which is refereed to as the perspective n point (PnP) problem [50]. When assuming unknown landmarks many of the solutions are based either on some form of extended Kalman filter (EKF) [88, 20, 9]. There has recently been an increasing effort to investigate solutions to bearing only navigation with global convergence that are mentioned previous in the thesis, however, these observers are unable to estimate and compensate for any gyro bias.

In this part of the chapter, the gyro bias observer have been expanded to also handle bearing only measurements. It filters the velocity and bearing measurements from landmarks, to estimate the range to the landmark as well as gyro-bias. It will be presented with a proof of semi-global asymptotically stability and exponential stability in the large. The observer is also demonstrated in simulations, both in a generic form and in a sensor setup with a camera, GNSS and IMU for a UAV, where the observer is is used in a cascade as in the previous chapter. In addition the observer is able to provide range/altitude estimate for the presented scenario. The latter setup is also verified experimentally, where the attitude observer is compared to a simpler velocity aided attitude observer based on a nonlinear complimentary filter [43]. The observer can also be used for bearing only SLAM if it is combined with a landmark optimization and loop closing front end system.

The structure of this paper is as follows: Section 3.6 presents the novel estimator and proof of its stability properties; while Section 3.7 shows simulation results. In 3.8 the results of the experimental verification are shown and finally, Section 3.9 concludes the paper.

3.6 Observer Design

The observer is a high gain observer resembling the dynamics of the unit vector measurements. It uses the velocity and gyro measurements to propagate and filter the unit vector estimates while estimating both the inverted range to the landmarks and the gyro bias. The observer will use the measurements: Body velocity $\boldsymbol{v}^b$, bearing measurement $\boldsymbol{u}^b_{\delta i}$ and biased gyro measurement $\boldsymbol{\omega}_m$. The states to be estimated are the bearing $\hat{\boldsymbol{u}}^b_{\delta i}$, inverted range to landmark $\hat{d}_i$ and gyro bias $\hat{\boldsymbol{b}}_\omega$

$$\dot{\hat{\boldsymbol{u}}}^b_{\delta i} = -\boldsymbol{S}(\boldsymbol{\omega}_m - \hat{\boldsymbol{b}}_\omega + k_i\boldsymbol{\sigma}_i + \hat{d}_i\boldsymbol{S}(\boldsymbol{u}^b_{\delta i})\boldsymbol{v}^b)\hat{\boldsymbol{u}}^b_{\delta i} \tag{3.14}$$

$$\begin{aligned}\dot{\hat{d}}_i &= \mathrm{Proj}_{di}(\hat{d}_i^2(\boldsymbol{u}^b_{\delta i})^\top\boldsymbol{v}^b) \\ &\quad + k_{di}\mathrm{Proj}_{di}((\boldsymbol{v}^b)^\top\boldsymbol{S}(\boldsymbol{u}^b_{\delta i})^2\boldsymbol{S}(\hat{\boldsymbol{u}}^b_{\delta i})\boldsymbol{\sigma}_i))\end{aligned} \tag{3.15}$$

$$\dot{\hat{\boldsymbol{b}}}_\omega = \boldsymbol{K}_b\mathrm{Proj}_b(\sum_{i=1}^{m}\boldsymbol{S}(\hat{\boldsymbol{u}}^b_{\delta i})\boldsymbol{S}(\boldsymbol{u}^b_{\delta i})\boldsymbol{\sigma}_i) \tag{3.16}$$

$$\boldsymbol{\sigma}_i = \boldsymbol{S}(\boldsymbol{u}^b_{\delta i})\hat{\boldsymbol{u}}^b_{\delta i} \tag{3.17}$$

Where $k_i > 0$, $k_{di} > 0$ and $\boldsymbol{K}_b > 0$ are gains. The $\mathrm{Proj}_\bullet$ operator is presented in the Appendix, and ensures that the bias estimate is maintained in a ball which is predefined, and that the inverse range estimates are kept between $\underline{d} < \hat{d}_i < \bar{d}$. We see that $(\hat{\boldsymbol{u}}^b_{\delta i})^\top\dot{\hat{\boldsymbol{u}}}^b_{\delta i} = 0$, because $(\hat{\boldsymbol{u}}^b_{\delta i})^\top\boldsymbol{S}(\hat{\boldsymbol{u}}^b_{\delta i}) = \boldsymbol{0}$, which ensures that $\hat{\boldsymbol{u}}^b_{\delta i}$ is maintained on the unit ball.

Firsts the error dynamics of $\tilde{\boldsymbol{u}}^b_{\delta i} = \boldsymbol{S}(\boldsymbol{u}^b_{\delta i})\hat{\boldsymbol{u}}^b_{\delta i} = \boldsymbol{\sigma}_i$, $\tilde{d}_i = d_i - \hat{d}_i$ and $\tilde{\boldsymbol{b}}_\omega = \boldsymbol{b}_\omega - \hat{\boldsymbol{b}}_\omega$ are derived:

$$\dot{\tilde{\boldsymbol{u}}}^b_{\delta i} = \boldsymbol{S}(\boldsymbol{u}^b_{\delta i})\dot{\hat{\boldsymbol{u}}}^b_{\delta i} - \boldsymbol{S}(\hat{\boldsymbol{u}}^b_{\delta i})\dot{\boldsymbol{u}}^b_{\delta i} \tag{3.18}$$

$$\begin{aligned}\dot{\tilde{\boldsymbol{u}}}^b_{\delta i} &= \boldsymbol{S}(\boldsymbol{u}^b_{\delta i})(-\boldsymbol{S}(\boldsymbol{\omega} + \tilde{\boldsymbol{b}}_\omega + \tilde{\boldsymbol{u}}^b_{\delta i})\hat{\boldsymbol{u}}^b_{\delta i} + \hat{d}_i\boldsymbol{S}(\hat{\boldsymbol{u}}^b_{\delta i})\boldsymbol{S}(\boldsymbol{u}^b_{\delta i})\boldsymbol{v}^b) \\ &\quad - \boldsymbol{S}(\hat{\boldsymbol{u}}^b_{\delta i})(-\boldsymbol{S}(\boldsymbol{\omega})\boldsymbol{u}^b_{\delta i} + d_i\boldsymbol{S}(\boldsymbol{u}^b_{\delta i})\boldsymbol{S}(\boldsymbol{u}^b_{\delta i})\boldsymbol{v}^b)\end{aligned} \tag{3.19}$$

$$\begin{aligned}\dot{\tilde{\boldsymbol{u}}}^b_{\delta i} &= (\boldsymbol{S}(\boldsymbol{u}^b_{\delta i})\boldsymbol{S}(\hat{\boldsymbol{u}}^b_{\delta i}) - \boldsymbol{S}(\hat{\boldsymbol{u}}^b_{\delta i})\boldsymbol{S}(\boldsymbol{u}^b_{\delta i}))\boldsymbol{\omega} \\ &\quad -\boldsymbol{S}(\boldsymbol{u}^b_{\delta i})\boldsymbol{S}(\tilde{\boldsymbol{b}}_\omega + \boldsymbol{\sigma}_i)\hat{\boldsymbol{u}}^b_{\delta i} \\ &\quad + (\hat{d}_i\boldsymbol{S}(\boldsymbol{u}^b_{\delta i})\boldsymbol{S}(\hat{\boldsymbol{u}}^b_{\delta i}) - d_i\boldsymbol{S}(\hat{\boldsymbol{u}}^b_{\delta i})\boldsymbol{S}(\boldsymbol{u}^b_{\delta i}))\boldsymbol{S}(\boldsymbol{u}^b_{\delta i})\boldsymbol{v}^b)\end{aligned} \tag{3.20}$$

$$\begin{aligned}\dot{\tilde{\boldsymbol{u}}}^b_{\delta i} &= \boldsymbol{S}(\tilde{\boldsymbol{u}}^b_{\delta i})\boldsymbol{\omega} + k_i\boldsymbol{S}(\boldsymbol{u}^b_{\delta i})\boldsymbol{S}(\hat{\boldsymbol{u}}^b_{\delta i})\tilde{\boldsymbol{u}}^b_{\delta i} + \boldsymbol{S}(\boldsymbol{u}^b_{\delta i})\boldsymbol{S}(\hat{\boldsymbol{u}}^b_{\delta i})\tilde{\boldsymbol{b}}_\omega \\ &\quad + (\hat{d}_i\boldsymbol{S}(\boldsymbol{u}^b_{\delta i})\boldsymbol{S}(\hat{\boldsymbol{u}}^b_{\delta i}) - (\hat{d}_i + \tilde{d}_i)\boldsymbol{S}(\hat{\boldsymbol{u}}^b_{\delta i})\boldsymbol{S}(\boldsymbol{u}^b_{\delta i}))\boldsymbol{S}(\boldsymbol{u}^b_{\delta i})\boldsymbol{v}^b)\end{aligned} \tag{3.21}$$

$$\begin{aligned}\dot{\tilde{\boldsymbol{u}}}^b_{\delta i} &= \boldsymbol{S}(\tilde{\boldsymbol{u}}^b_{\delta i})\boldsymbol{\omega} + k_i\boldsymbol{S}(\boldsymbol{u}^b_{\delta i})\boldsymbol{S}(\hat{\boldsymbol{u}}^b_{\delta i})\tilde{\boldsymbol{u}}^b_{\delta i} + \boldsymbol{S}(\boldsymbol{u}^b_{\delta i})\boldsymbol{S}(\hat{\boldsymbol{u}}^b_{\delta i})\tilde{\boldsymbol{b}}_\omega \\ &\quad - \tilde{d}_i\boldsymbol{S}(\hat{\boldsymbol{u}}^b_{\delta i})\boldsymbol{S}(\boldsymbol{u}^b_{\delta i})\boldsymbol{S}(\boldsymbol{u}^b_{\delta i})\boldsymbol{v}^b + \hat{d}_i\boldsymbol{S}(\tilde{\boldsymbol{u}}^b_{\delta i})\boldsymbol{S}(\boldsymbol{u}^b_{\delta i})\boldsymbol{v}^b\end{aligned} \tag{3.22}$$

where we have used that $(\boldsymbol{S}(\boldsymbol{u}^b_{\delta i})\boldsymbol{S}(\hat{\boldsymbol{u}}^b_{\delta i}) - \boldsymbol{S}(\hat{\boldsymbol{u}}^b_{\delta i})\boldsymbol{S}(\boldsymbol{u}^b_{\delta i})) = \boldsymbol{S}(\tilde{\boldsymbol{u}}^b_{\delta i})$. From $\hat{d}_i\boldsymbol{S}(\tilde{\boldsymbol{u}}^b_{\delta i})\boldsymbol{S}(\boldsymbol{u}^b_{\delta i})\boldsymbol{v}^b =$

$-\hat{d}_i \boldsymbol{S}(\boldsymbol{S}(\boldsymbol{u}^b_{\delta i})\boldsymbol{v}^b)\tilde{\boldsymbol{u}}^b_{\delta i}$, we end up with the error dynamics

$$\begin{aligned}\dot{\tilde{\boldsymbol{u}}}^b_{\delta i} &= [-\boldsymbol{S}(\hat{d}_i \boldsymbol{S}(\boldsymbol{u}^b_{\delta i})\boldsymbol{v}^b + \boldsymbol{\omega}) + k_i \boldsymbol{S}(\boldsymbol{u}^b_{\delta i})\boldsymbol{S}(\hat{\boldsymbol{u}}^b_{\delta i})]\tilde{\boldsymbol{u}}^b_{\delta i} \\ &\quad \boldsymbol{S}(\boldsymbol{u}^b_{\delta i})\boldsymbol{S}(\hat{\boldsymbol{u}}^b_{\delta i})\tilde{\boldsymbol{b}}_\omega - \boldsymbol{S}(\hat{\boldsymbol{u}}^b_{\delta i})\boldsymbol{S}(\boldsymbol{u}^b_{\delta i})^2 \boldsymbol{v}^b \tilde{d}_i \qquad (3.23)\\ \dot{\tilde{d}}_i &= k_{di}\text{Proj}_{di}\left((\boldsymbol{v}^b)^\top \boldsymbol{S}(\boldsymbol{u}^b_{\delta i})^2 \boldsymbol{S}(\hat{\boldsymbol{u}}^b_{\delta i})\tilde{\boldsymbol{u}}^{\boldsymbol{b}}_{\boldsymbol{\delta i}}\right) \\ &\quad + d_i^2 (\boldsymbol{u}^b_{\delta i})^\top \boldsymbol{v}^b + \text{Proj}_{di}\left(-\hat{d}^2 (\boldsymbol{u}^b_{\delta i})^\top \boldsymbol{v}^b\right) \qquad (3.24)\\ \dot{\tilde{\boldsymbol{b}}}_\omega &= -\boldsymbol{K}_b \text{Proj}_b(\sum_{i=1}^m \boldsymbol{S}(\hat{\boldsymbol{u}}^b_{\delta i})\boldsymbol{S}(\boldsymbol{u}^b_{\delta i})\tilde{\boldsymbol{u}}^b_{\delta i}) \qquad (3.25)\end{aligned}$$

by assuming that the bias is constant $\dot{\boldsymbol{b}}_\omega = \boldsymbol{0}$. We see that the error dynamics has an equilibrium for $\tilde{\boldsymbol{u}}^b_{\delta i} = \boldsymbol{0}$, $\tilde{d}_i = 0$ and $\tilde{\boldsymbol{b}}_\omega = \boldsymbol{0}$. In addition, we stack the bearing errors in the vector $\boldsymbol{x} = [(\tilde{\boldsymbol{u}}^b_1)^\top, \cdots, (\tilde{\boldsymbol{u}}^b_m)^\top]^\top$, and the inverted range estimate errors and gyro bias error in vector $\boldsymbol{y} = [\tilde{d}_1, \cdots, \tilde{d}_m, (\tilde{\boldsymbol{b}}_\omega)^\top]^\top$. We see that the structure of the error dynamics can be represented as the system (3.26)-(3.27)

$$\dot{\boldsymbol{x}} = \boldsymbol{\mathcal{A}}(t)\boldsymbol{x} + \boldsymbol{\mathcal{B}}(t)\boldsymbol{y} \qquad (3.26)$$

$$\dot{\boldsymbol{y}} = -\boldsymbol{\Gamma}\boldsymbol{\mathcal{B}}_p(t,\boldsymbol{x})^\top + \boldsymbol{g}(t,\boldsymbol{y}) \qquad (3.27)$$

where the matrices are as follows

$$\begin{aligned}&\boldsymbol{\mathcal{A}}(t) = \\ &\text{diag}(\{-\boldsymbol{S}(\hat{d}_i \boldsymbol{S}(\boldsymbol{u}^b_{\delta i})\boldsymbol{v}^b + \boldsymbol{\omega}) + k_i \boldsymbol{S}(\boldsymbol{u}^b_{\delta i})\boldsymbol{S}(\hat{\boldsymbol{u}}^b_{\delta i})\}_{i=1}^m) \\ &\boldsymbol{\mathcal{B}}(t) = \\ &\begin{bmatrix}\text{diag}(\{-\boldsymbol{S}(\hat{\boldsymbol{u}}^b_{\delta i})\boldsymbol{S}(\boldsymbol{u}^b_{\delta i})^2 \boldsymbol{v}^b\}_{i=1}^m) & \{\boldsymbol{S}(\boldsymbol{u}^b_{\delta i})\boldsymbol{S}(\hat{\boldsymbol{u}}^b_{\delta i})\}_{i=1}^m\end{bmatrix} \\ &\boldsymbol{\mathcal{B}}_p(t,\boldsymbol{x})^\top = \begin{bmatrix}\left\{\text{Proj}_{di}\left((\boldsymbol{v}^b)^\top \boldsymbol{S}(\boldsymbol{u}^b_{\delta i})^2 \boldsymbol{S}(\hat{\boldsymbol{u}}^b_{\delta i})\tilde{\boldsymbol{u}}^b_{\delta i}\right)\right\}_{i=1}^m \\ \text{Proj}_b\left(\sum_{i=1}^m \boldsymbol{S}(\hat{\boldsymbol{u}}^b_{\delta i})\boldsymbol{S}(\boldsymbol{u}^b_{\delta i})\tilde{\boldsymbol{u}}^b_{\delta i}\right)\end{bmatrix}\end{aligned}$$

where $\{\bullet_i\}_1^m = [(\bullet_i|_{i=1})^\top, \cdots, (\bullet_i|_{i=m})^\top]^\top$ is a column vector or a matrix, where the entries $\bullet_i$ are stacked above each-other. The gains are in

$$\boldsymbol{\Gamma} = \begin{bmatrix}\text{diag}(k_{d1}, \cdots, k_{dm}) & \boldsymbol{0} \\ \boldsymbol{0} & \boldsymbol{K}_b\end{bmatrix} \qquad (3.28)$$

where we see that $\boldsymbol{\Gamma}$ is a positive definite matrix with a smallest and largest eigenvalues $\bar{\gamma}, \underline{\gamma}$, which also gives bounds on the observer gains. Finally $\boldsymbol{g}(t,\boldsymbol{y}) : \mathbb{R} \times \mathbb{R}^{m+3} \to \mathbb{R}^{m+3}$

$$\boldsymbol{g}(t,\boldsymbol{y}) = \begin{bmatrix}\left\{d_i^2 (\boldsymbol{u}^b_{\delta i})^\top \boldsymbol{v}^b + \text{Proj}_{di}\left(-\hat{d}^2 (\boldsymbol{u}^b_{\delta i})^\top \boldsymbol{v}^b\right)\right\}_1^m \\ \boldsymbol{0}\end{bmatrix}$$

We use this notation to highlight the similarities between $\mathcal{B}_p(t,\boldsymbol{x})^\top$ and $\mathcal{B}(t)^\top\boldsymbol{x}$ which in fact are identical $\mathcal{B}_p(t,\boldsymbol{x})^\top = \mathcal{B}(t)^\top\boldsymbol{x}$ when there are no projections activated. Nevertheless the set-up helps the reader to see why the adaptation law of the inverted range and gyro bias were chosen; to relate the system to the family of skew-symmetric systems. These systems have been investigated extensively in many forms including in [87, 75, 35, 57] where all the the systems either assume that the $\mathcal{A}(t)$ matrix is constant and negative definite, or that the vector function $g(t,\boldsymbol{y}) = \boldsymbol{0}$ is zero. All these systems have in common that they rely on some persistence of excitation (PE) like condition related to the skew symmetric part of the system and/or high gain. In the first lemma we show that the PE condition of this system related to the skew-symmetric part can be checked with a simpler matrix inequality. It is later discussed how this condition relates to the bearing measurements and the vehicle velocity.

Lemma 1. *Consider the matrix $\mathcal{B}(t)$, representing the part of the dynamic* (3.26) *that is linearly dependent on $\boldsymbol{y}$. Assume velocity of the vehicle is non-zero, $\|\boldsymbol{v}^b\| > 0$, not parallel to the bearing measurements, and there are at least three bearing measurements that are linearly independent so that the following inequalities hold*

$$-(\boldsymbol{v}^b)^\top S(\boldsymbol{u}^b_{\delta i})^2 S(\hat{\boldsymbol{u}}^b_{\delta i})^2 S(\boldsymbol{u}^b_{\delta i})^2 \boldsymbol{v}^b > \underline{a}\,,\ \forall i \tag{3.29}$$

$$-\sum_{i=1}^{m} \frac{1}{\boldsymbol{\xi_i}^\top \boldsymbol{\xi_i}} S(\hat{\boldsymbol{u}}^b_{\delta i}) S(\boldsymbol{u}^b_{\delta i}) S(\boldsymbol{\xi_i}) S(\boldsymbol{\xi_i}) S(\boldsymbol{u}^b_{\delta i}) S(\hat{\boldsymbol{u}}^b_{\delta i}) > \underline{b} \tag{3.30}$$

$$\boldsymbol{\xi_i} = -S(\hat{\boldsymbol{u}}^b_{\delta i}) S(\boldsymbol{u}^b_{\delta i})^2 \boldsymbol{v}^b \tag{3.31}$$

where $\underline{a} > 0$ and $\underline{b} > 0$ are positive lower bounds. Then the matrix

$$\mathcal{B}(t)^\top \mathcal{B}(t) > \mu \boldsymbol{I} \tag{3.32}$$

is positive definite, where $\mu > 0$ is a positive lower bound

Proof. If we calculate (3.32) we get the matrix

$$\mathcal{B}(t)^\top \mathcal{B}(\boldsymbol{t}) = \begin{bmatrix} \mathrm{diag}(\{a_i\}_{i=1}^m) & \{\boldsymbol{b}_i\}_{i=1}^m \\ (\{\boldsymbol{b}_i\}_{i=1}^m)^\top & \boldsymbol{C} \end{bmatrix} \tag{3.33}$$

where we note that $\{\boldsymbol{b}_i\}_{i=1}^m$ is the matrix with rows $\boldsymbol{b}_i$, and

$$a_i = -(\boldsymbol{v}^b)^\top S(\boldsymbol{u}^b_{\delta i})^2 S(\hat{\boldsymbol{u}}^b_{\delta i})^2 S(\boldsymbol{u}^b_{\delta i})^2 \boldsymbol{v}^b \tag{3.34}$$

$$\boldsymbol{b}_i = -(\boldsymbol{v}^b)^\top S(\boldsymbol{u}^b_{\delta i})^2 S(\hat{\boldsymbol{u}}^b_{\delta i}) S(\boldsymbol{u}^b_{\delta i}) S(\hat{\boldsymbol{u}}^b_{\delta i}) \tag{3.35}$$

$$\boldsymbol{C} = \sum_{i=1}^{m} S(\hat{\boldsymbol{u}}^b_{\delta i}) S(\boldsymbol{u}^b_{\delta i})^2 S(\hat{\boldsymbol{u}}^b_{\delta i}) \tag{3.36}$$

We then want to examine when this matrix is positive definite by examining its Schur complement. Since we know that for a block symmetric matrix to be positive definite

$$\begin{bmatrix} \boldsymbol{A} & \boldsymbol{B} \\ \boldsymbol{B}^\top & \boldsymbol{C} \end{bmatrix} > 0 \tag{3.37}$$

the inequalities

$$\boldsymbol{A} > 0 \tag{3.38}$$

$$\boldsymbol{C} - \boldsymbol{B}^\top \boldsymbol{A}^{-1} \boldsymbol{B} > 0 \tag{3.39}$$

need to hold. For (3.33), the first inequality would be

$$a_i > 0, \ \forall i \tag{3.40}$$

This is ensured since the bearings are not parallel to the velocity, and that the velocity is non zero. The second inequality is that the Schur compliment of the matrix is positive definite, which can be formulated as

$$\begin{aligned} &\sum_{i=1}^{m} \boldsymbol{S}(\hat{\boldsymbol{u}}_{\delta i}^b)\boldsymbol{S}(\boldsymbol{u}_{\delta i}^b)^2\boldsymbol{S}(\hat{\boldsymbol{u}}_{\delta i}^b) \\ &- \sum_{i=1}^{m} \boldsymbol{S}(\hat{\boldsymbol{u}}_{\delta i}^b)\boldsymbol{S}(\boldsymbol{u}_{\delta i}^b)\boldsymbol{\xi}_i(\boldsymbol{\xi}_i{}^\top \boldsymbol{\xi}_i)^{-1}\boldsymbol{\xi}_i{}^\top \boldsymbol{S}(\boldsymbol{u}_{\delta i}^b)\boldsymbol{S}(\hat{\boldsymbol{u}}_{\delta i}^b) \qquad (3.41) \\ &= \sum_{i=1}^{m} \boldsymbol{S}(\hat{\boldsymbol{u}}_{\delta i}^b)\boldsymbol{S}(\boldsymbol{u}_{\delta i}^b)[\boldsymbol{I} - \boldsymbol{\xi}_i(\boldsymbol{\xi}_i{}^\top \boldsymbol{\xi}_i)^{-1}\boldsymbol{\xi}_i{}^\top]\boldsymbol{S}(\boldsymbol{u}_{\delta i}^b)\boldsymbol{S}(\hat{\boldsymbol{u}}_{\delta i}^b) \qquad (3.42) \\ &= -\sum_{i=1}^{m} \frac{1}{\boldsymbol{\xi}_i{}^\top \boldsymbol{\xi}_i}\boldsymbol{S}(\hat{\boldsymbol{u}}_{\delta i}^b)\boldsymbol{S}(\boldsymbol{u}_{\delta i}^b)\boldsymbol{S}(\boldsymbol{\xi}_i)\boldsymbol{S}(\boldsymbol{\xi}_i)\boldsymbol{S}(\boldsymbol{u}_{\delta i}^b)\boldsymbol{S}(\hat{\boldsymbol{u}}_{\delta i}^b) \end{aligned}$$

where $\boldsymbol{\xi}_i = -\boldsymbol{S}(\hat{\boldsymbol{u}}_{\delta i}^b)\boldsymbol{S}(\boldsymbol{u}_{\delta i}^b)^2\boldsymbol{v}^b$, and we have used that $\boldsymbol{I} - \boldsymbol{\xi}_i(\boldsymbol{\xi}_i{}^\top \boldsymbol{\xi}_i)^{-1}\boldsymbol{\xi}_i{}^\top = -\frac{1}{\boldsymbol{\xi}_i{}^\top \boldsymbol{\xi}_i}\boldsymbol{S}(\boldsymbol{\xi}_i)\boldsymbol{S}(\boldsymbol{\xi}_i)$. Since this matrix is positive definite the Schur complement of matrix $\boldsymbol{\mathcal{B}}^\top \boldsymbol{\mathcal{B}}$ is positive definite and hence will be positive definite and inequality (3.32) will hold. □

The first inequality requirement (3.29) intuitively makes sense, since the range to the landmark is unobservable if the bearing is parallel to the velocity, hence constant. This is similar to what is found in [77, 49, 17, 19], where the derivative of the bearing vector being nonzero is a necessary condition for PE and observability. What distinguishes the presented observer to these, is that gyro bias estimation is also performed. In addition, the landmark positions are estimated, which is not done in [49, 71].

The condition of having (3.29) satisfied for every bearing is to guarantee that all distance estimates converge. In simulations, violating this condition for some

time or initializing the bearing estimate parallel to the velocity did not cause any problem for the observer. In addition, as we will see in experiments, this condition will not be necessary to make the gyro-bias estimation converge.

To understand the second inequality (3.30), which is related to the gyro-bias estimate, we will look at the special case when $\boldsymbol{u}_{\delta i}^b = \hat{\boldsymbol{u}}_{\delta i}^b$, which gives the matrix

$$-\sum_{i=1}^{m} \frac{1}{\boldsymbol{\xi_i}^\top \boldsymbol{\xi_i}} \boldsymbol{S}(\boldsymbol{u}_{\delta i}^b)^2 \boldsymbol{S}(\boldsymbol{\xi_i}) \boldsymbol{S}(\boldsymbol{\xi_i}) \boldsymbol{S}(\boldsymbol{u}_{\delta i}^b)^2 \tag{3.43}$$

where $\boldsymbol{\xi_i} = -\boldsymbol{S}(\boldsymbol{u}_{\delta i}^b)^3 \boldsymbol{v}^b = \boldsymbol{S}(\boldsymbol{u}_{\delta i}^b) \boldsymbol{v}^b$. This matrix has two eigenvectors with eigenvalue zero and one eigenvector with negative eigenvalue. We see that the first zero valued eigenvector is $\boldsymbol{v}_1 = \boldsymbol{u}_{\delta i}^b$. The second eigenvector $\boldsymbol{v}_2$ is found by solving the following equation

$$\boldsymbol{S}(\boldsymbol{\xi_i}) \boldsymbol{S}(\boldsymbol{u}_{\delta i}^b)^2 \boldsymbol{v}_2 = \boldsymbol{0} \tag{3.44}$$

$$\Updownarrow$$

$$S(\boldsymbol{u}_{\delta i}^b)^2 \boldsymbol{v}_2 - \lambda \boldsymbol{S}(\boldsymbol{u}_{\delta i}^b) \boldsymbol{v}^b = \boldsymbol{0} \tag{3.45}$$

$$S(\boldsymbol{u}_{\delta i}^b)(S(\boldsymbol{u}_{\delta i}^b) \boldsymbol{v}_2 - \lambda \boldsymbol{v}^b) = \boldsymbol{0} \tag{3.46}$$

where we see that if $\boldsymbol{v}_2$ is parallel to the cross product $\boldsymbol{S}(\boldsymbol{u}_{\delta i}^b) \boldsymbol{v}^b$ then this equation holds. The third eigenvector thus has to be orthogonal to the two previous eigenvectors, which makes it parallel to the vector $\boldsymbol{v}_3 = -\boldsymbol{S}(\boldsymbol{u}_{\delta i}^b) \boldsymbol{S}(\boldsymbol{u}_{\delta i}^b) \boldsymbol{v}^b = \boldsymbol{U}_{\delta i}^\perp \boldsymbol{v}^b$, which is the orthogonal projection of the velocity onto the space orthogonal to the bearing vector. We then see that for the matrix to be positive definite, we need that at least three bearing vectors exist, in which the projection of the velocity onto their orthogonal space spans $\mathbf{R}^3$

$$\exists i, j, k \in \{1, m\} | \text{span}([\boldsymbol{U}_{\delta i}^\perp \boldsymbol{v}^b,\ \boldsymbol{U}_{\delta j}^\perp \boldsymbol{v}^b,\ \boldsymbol{U}_{\delta k}^\perp \boldsymbol{v}^b]) = \mathbb{R}^3 \tag{3.47}$$

This gives us the intuition that the value μ will be related to how different the bearing vectors are, and how aligned they are to the velocity. The next theorem shows that a high gain can be chosen so that the system is uniformly semi-globally asymptotically stable, and exponentially stable in the large.

Theorem 3. *Consider the kinematic of a vehicle where bearing of landmarks $\boldsymbol{u}_{\delta i}^b$, velocity $\boldsymbol{v}^b$, and gyro with a bias* (2.9) *$\boldsymbol{\omega}_m$ are available, and assume that all input and system functions are Lipschitz and bounded. Further we assume that the landmarks are a minimum distance away from the vehicle so that the inverted ranges are also bounded. If we choose gains k_i large enough, then there exist gains k_{di} and $\boldsymbol{K}_b$ such that the observer* (3.14)-(3.16) *has an error dynamic that converges in finite time from initial estimates $\hat{\boldsymbol{u}}_{\delta i}^n$ satisfying $(\hat{\boldsymbol{u}}_{\delta i}^b)^\top \boldsymbol{u}_{\delta i}^b > \cos(\pi - \epsilon)$, and is exponentially stable for $(\hat{\boldsymbol{u}}_{\delta i}^b)^\top \boldsymbol{u}_{\delta i}^b > \cos(\epsilon)$ as long as the assumptions of Lemma 1 are fulfilled, and $\epsilon > 0$ is an arbitrary small constant.*

Outline of the proof

A) First prove that the the system (3.14)-(3.16) is Uniformly Bounded (UB), and the error states converges to an open set.

B) Define a Lyapunov function candidate for the error dynamics (3.23)-(3.25) and find its time derivative. And derive bounds on the terms of the time derivative

C) Handle the projection related to the perturbation terms, and derive a bound on the perturbation.

D) Using bounds B) ans C), to show that there exist gains that yields exponential stability in the large.

E) Combine A), D) to conclude that the observer is semi-globally asymptotically stable.

Proof. **A) Uniform Boundedness of the system** To show that the error of the observer is bounded we first employ the traits of the projection to conclude that the error of the inverted range estimates $\hat{d}_i$ and gyro bias estimate $\hat{\boldsymbol{b}}_\omega$ are uniformly bounded. To show that the unit vector estimation error is semi-globally bounded, we show that for any bearing angle error $\tilde{\theta}_{ui} : \{\tilde{\theta}_{ui} \in \mathbb{R} | (\boldsymbol{u}^n_{\delta i})^\top \hat{\boldsymbol{u}}^n_{\delta i} = \cos(\tilde{\theta}_i)\}$ starting an angle $\epsilon > 0$ close to the unstable equilibrium point $|\tilde{\theta}| = \pi$, so that the angle error is $|\tilde{\theta}_{ui}| < \pi - \epsilon$, then a k_ϵ exists, where $k_i > k_\epsilon$ for all $i \in \{1, m\}$; so that that the error is kept away from the unstable equilibrium point. We will use a Lyapunov-like function for each bearing measurement and its estimate

$$V_i(\tilde{\boldsymbol{u}}^b_{\delta i}) = 1 - (\hat{\boldsymbol{u}}^b_{\delta i})^\top \boldsymbol{u}^b_{\delta i} = 1 - \cos(\tilde{\theta}_{ui}) \tag{3.48}$$

which is clearly positive definite and $\|V_i\|$ increases as $|\tilde{\theta}_{ui}|$ increase for $|\tilde{\theta}_{ui}| < \pi$. It has the time derivative in the trajectory of the error dynamics given by

$$\dot{V}_i = -(\hat{\boldsymbol{u}}^b_{\delta i})^\top \dot{\boldsymbol{u}}^b_{\delta i} - (\boldsymbol{u}^b_{\delta i})^\top \dot{\hat{\boldsymbol{u}}}^b_{\delta i} \tag{3.49}$$

$$= -(\hat{\boldsymbol{u}}^b_{\delta i})^\top(-\boldsymbol{S}(\boldsymbol{\omega})\boldsymbol{u}^b_{\delta i} + d_i \boldsymbol{S}(\boldsymbol{u}^b_{\delta i})\boldsymbol{S}(\boldsymbol{u}^b_{\delta i})\boldsymbol{v}^b)$$

$$- (\boldsymbol{u}^b_{\delta i})^\top(-\boldsymbol{S}(\boldsymbol{\omega} + \tilde{\boldsymbol{b}}_\omega + \boldsymbol{\sigma}_i)\hat{\boldsymbol{u}}^b_{\delta i} + \hat{d}_i \boldsymbol{S}(\hat{\boldsymbol{u}}^b_{\delta i})\boldsymbol{S}(\boldsymbol{u}^b_{\delta i})\boldsymbol{v}^b) \tag{3.50}$$

$$= -(\hat{\boldsymbol{u}}^b_{\delta i})^\top \boldsymbol{S}(\boldsymbol{u}^b_{\delta i})\boldsymbol{S}(\boldsymbol{u}^b_{\delta i})\boldsymbol{v}^b d_i + (\boldsymbol{u}^b_{\delta i})^\top \boldsymbol{S}(\tilde{\boldsymbol{b}}_\omega)\hat{\boldsymbol{u}}^b_{\delta i}$$

$$+ (\boldsymbol{u}^b_{\delta i})^\top \boldsymbol{S}(k_i \boldsymbol{S}(\boldsymbol{u}^b_{\delta i})\hat{\boldsymbol{u}}^b_{\delta i})\hat{\boldsymbol{u}}^b_{\delta i} - (\boldsymbol{u}^b_{\delta i})^\top \boldsymbol{S}(\hat{\boldsymbol{u}}^b_{\delta i})\boldsymbol{S}(\boldsymbol{u}^b_{\delta i})\boldsymbol{v}^b \hat{d}_i \tag{3.51}$$

$$= (\boldsymbol{u}^b_{\delta i})^\top \boldsymbol{S}(\hat{\boldsymbol{u}}^b_{\delta i})\boldsymbol{S}(\boldsymbol{u}^b_{\delta i})\boldsymbol{v}^b d_i - (\boldsymbol{u}^b_{\delta i})^\top \boldsymbol{S}(\hat{\boldsymbol{u}}^b_{\delta i})\boldsymbol{S}(\boldsymbol{u}^b_{\delta i})\boldsymbol{v}^b \hat{d}_i$$

$$- (\tilde{\boldsymbol{b}}_\omega)^\top \boldsymbol{S}(\boldsymbol{u}^b_{\delta i})\hat{\boldsymbol{u}}^b_{\delta i} - k_i(\hat{\boldsymbol{u}}^b_{\delta i})^\top \boldsymbol{S}(\boldsymbol{u}^b_{\delta i})^\top \boldsymbol{S}(\boldsymbol{u}^b_{\delta i})\hat{\boldsymbol{u}}^b_{\delta i} \tag{3.52}$$

$$= -(\tilde{\boldsymbol{u}}^b_{\delta i})^\top \boldsymbol{S}(\boldsymbol{u}^b_{\delta i})\boldsymbol{v}^b \tilde{d}_i - (\tilde{\boldsymbol{b}}_\omega)^\top \tilde{\boldsymbol{u}}^b_{\delta i} - k_i \|\tilde{\boldsymbol{u}}^b_{\delta i}\|^2 \tag{3.53}$$

$$\leq -k_i \|\tilde{\boldsymbol{u}}^b_{\delta i}\|^2 + \|\tilde{\boldsymbol{u}}^b_{\delta i}\|\|\boldsymbol{v}^b\|\tilde{d}_i + \|\tilde{\boldsymbol{b}}_\omega\|\|\tilde{\boldsymbol{u}}^b_{\delta i}\| \tag{3.54}$$

$$\leq -\|\tilde{\boldsymbol{u}}^b_{\delta i}\|(k_i\|\tilde{\boldsymbol{u}}^b_{\delta i}\| - \|\boldsymbol{v}^b\|\|\tilde{d}_i\| - \|\tilde{\boldsymbol{b}}_\omega\|) \tag{3.55}$$

$$\leq -\|\tilde{\boldsymbol{u}}^b_{\delta i}\|(k_i\|\tilde{\boldsymbol{u}}^b_{\delta i}\| - \bar{v}\bar{d} - \bar{b}_\omega) \tag{3.56}$$

were we have used the boundedness of the inverted range, velocity and gyro, $|\tilde{d}_i| < \bar{d}$, $\|\boldsymbol{S}(\boldsymbol{u}^b_{\delta i})\boldsymbol{v}^b\| \leq \|\boldsymbol{v}^b\| < \bar{v}$ and $\|\tilde{\boldsymbol{b}}_\omega\| < \bar{b}_\omega$. We see that $|\tilde{\theta}_{ui}| < \pi - \epsilon$ implies that $\|\tilde{\boldsymbol{u}}^b_{\delta i}\| > \sin(\epsilon)$ as long as $|\tilde{\theta}_{ui}| > \epsilon$. So clearly a k_ϵ exists

$$k_\epsilon > \frac{\bar{v}\bar{d} + \bar{b}_\omega}{\sin(\epsilon)} \tag{3.57}$$

so that a $k_i > k_\epsilon$ will ensure that $\dot{V}_i < 0$; hence we can conclude that the bearing error is bounded away from the set $|\tilde{\theta}_{ui}| > \pi - \epsilon$ and that the bearing will converge to the set $|\tilde{\theta}_{ui}| \leq \epsilon$ in finite time [64, Theorem 3.18]. The boundedness is semi-global since ϵ can be chosen arbitrary small and the projection deals with the other states. This means that for the rest of this proof we can assume that the bound on the bearing estimate will hold.

A) Lyapunov function and its derivative

As a Lyapunov candidate for the entire system

$$V_2(t, \boldsymbol{x}, \boldsymbol{y}) = \frac{1}{2}\boldsymbol{x}^\top \boldsymbol{x} + \frac{1}{2}\boldsymbol{y}^\top \boldsymbol{\Gamma}^{-1}\boldsymbol{y} - \delta \boldsymbol{x}^\top \boldsymbol{\mathcal{B}}(t)\boldsymbol{y}, \tag{3.58}$$

where $\boldsymbol{x} = [(\tilde{\boldsymbol{u}}^b_1)^\top, \cdots, (\tilde{\boldsymbol{u}}^b_m)^\top]^\top$ and $\boldsymbol{y} = [\tilde{d}_1, \cdots, \tilde{d}_m, (\tilde{\boldsymbol{b}}_\omega)^\top]^\top$. Utilizing that $\|\boldsymbol{x}^\top \boldsymbol{\mathcal{B}}(t)\boldsymbol{y}\| \leq (\bar{v} + m)\|\boldsymbol{x}\|\|\boldsymbol{y}\|$ and $\bar{\gamma} = \|\Gamma\|$, we see that the parameter $\delta > 0$ has to abide the following inequality

$$\frac{1}{\bar{\gamma}(\bar{v} + m)^2} > \delta^2 \tag{3.59}$$

in order to make the Lyapunov function is positive definite, where we also recall that $\frac{1}{\|\bar{\gamma}\|} \leq \|\Gamma^{-1}\|$. The time derivative of the Lyapunov function along the trajectories of the error dynamics is

$$\begin{aligned}\dot{V}_2(t,\boldsymbol{x},\boldsymbol{y}) &= \boldsymbol{x}^\top\dot{\boldsymbol{x}} + \boldsymbol{y}^\top\boldsymbol{\Gamma}^{-1}\dot{\boldsymbol{y}} \\ &\quad - \delta\dot{\boldsymbol{x}}^\top\boldsymbol{\mathcal{B}}(t)\boldsymbol{y} - \delta\boldsymbol{x}^\top\dot{\boldsymbol{\mathcal{B}}}(t)\boldsymbol{y} - \delta\boldsymbol{x}^\top\boldsymbol{\mathcal{B}}(t)\dot{\boldsymbol{y}}\end{aligned} \tag{3.60}$$

in which we insert the error dynamics from (3.23)-(3.25) and get

$$\begin{aligned}\dot{V}_2(t,\boldsymbol{x},\boldsymbol{y}) &= \boldsymbol{x}^\top(\boldsymbol{\mathcal{A}}(t)\boldsymbol{x} + \boldsymbol{\mathcal{B}}(t)\boldsymbol{y}) \\ &\quad - \boldsymbol{y}^\top\boldsymbol{\Gamma}^{-1}(\boldsymbol{\Gamma}\boldsymbol{\mathcal{B}}_p(t,\boldsymbol{x})^\top - \boldsymbol{g}(t,\boldsymbol{y})) \\ &\quad - \delta(\boldsymbol{\mathcal{A}}(t)\boldsymbol{x} + \boldsymbol{\mathcal{B}}(t)\boldsymbol{y})^\top\boldsymbol{\mathcal{B}}(t)\boldsymbol{y} \\ &\quad - \delta\boldsymbol{x}^\top\dot{\boldsymbol{\mathcal{B}}}(t)\boldsymbol{y} - \delta\boldsymbol{x}^\top\boldsymbol{\mathcal{B}}(t)(\boldsymbol{\Gamma}\boldsymbol{\mathcal{B}}_p(t,\boldsymbol{x})^\top - \boldsymbol{g}(t,\boldsymbol{y}))\end{aligned} \tag{3.61}$$

which we can restructure into

$$\begin{aligned}\dot{V}_2(t,\boldsymbol{x},\boldsymbol{y}) &= \boldsymbol{x}^\top\boldsymbol{\mathcal{A}}(t)\boldsymbol{x} + \boldsymbol{x}^\top\boldsymbol{\mathcal{B}}(t)\boldsymbol{y} \\ &\quad - \boldsymbol{y}^\top\boldsymbol{\mathcal{B}}_p(t,\boldsymbol{x})^\top + \boldsymbol{y}^\top\boldsymbol{\Gamma}^{-1}\boldsymbol{g}(t,\boldsymbol{y}) \\ &\quad - \delta\boldsymbol{x}^\top\boldsymbol{\mathcal{A}}(t)^\top\boldsymbol{\mathcal{B}}(t)\boldsymbol{y} - \delta\boldsymbol{y}^\top\boldsymbol{\mathcal{B}}(t)^\top\boldsymbol{\mathcal{B}}(t)\boldsymbol{y} \\ &\quad - \delta\boldsymbol{x}^\top\dot{\boldsymbol{\mathcal{B}}}(t)\boldsymbol{y} - \delta\boldsymbol{x}^\top\boldsymbol{\mathcal{B}}(t)(\boldsymbol{\Gamma}\boldsymbol{\mathcal{B}}_p(t,\boldsymbol{x})^\top - \boldsymbol{g}(t,\boldsymbol{y}))\end{aligned} \tag{3.62}$$

To deal with the projection we will both use the inequalities related to them which are

$$\begin{aligned}-\boldsymbol{y}^\top\boldsymbol{\Gamma}^{-1}\text{Proj}_y(\boldsymbol{\tau}) &\leq -\boldsymbol{y}^\top\boldsymbol{\Gamma}^{-1}(\boldsymbol{\tau}) \\ \|\text{Proj}_y(\boldsymbol{\tau})\| &\leq \|\boldsymbol{\tau}\|\end{aligned} \tag{3.63}$$

from [68, E.1]. We make the set $\mathcal{P}$ containing all the indices of all the inverse range estimates where the projection is activated, and $\mathcal{P}^c$ is the complementary set with all the projections not activated. The terms related to $\boldsymbol{g}(t,\boldsymbol{y})$ can then be written

$$\boldsymbol{g}_i(t,\boldsymbol{y}) = \begin{cases}\tilde{d}_i(d_i + \hat{d}_i)(\boldsymbol{u}_{\delta i}^b)^\top\boldsymbol{v}^b & i \in \mathcal{P}^c \\ d_i^2(\boldsymbol{u}_{\delta i}^b)^\top\boldsymbol{v}^b & i \in \mathcal{P} \\ 0 & i > m\end{cases} \tag{3.64}$$

resulting also in

$$\begin{aligned}\boldsymbol{y}^\top\boldsymbol{\Gamma}^{-1}\boldsymbol{g}(t,\boldsymbol{y}) &= \sum_{i\in\mathcal{P}^c}\frac{1}{\gamma_i}\tilde{d}_i{}^2(d_i + \hat{d}_i)(\boldsymbol{u}_{\delta i}^b)^\top\boldsymbol{v}^b \\ &\quad + \sum_{i\in\mathcal{P}} -\frac{1}{\gamma_i}|\tilde{d}_i d_i^2(\boldsymbol{u}_{\delta i}^b)^\top\boldsymbol{v}^b|\end{aligned} \tag{3.65}$$

where γ_i can be derived from the entries of $\boldsymbol{\Gamma}$. The other terms with projection however can be handled quite straigth forward by (3.63), resulting in

$$-\boldsymbol{y}^\top\boldsymbol{\mathcal{B}}_p(t,\boldsymbol{x})^\top \leq -\boldsymbol{y}^\top\boldsymbol{\mathcal{B}}(t)^\top\boldsymbol{x} \tag{3.66}$$

$$\|\delta\boldsymbol{x}^\top\boldsymbol{\mathcal{B}}(t)\|\|\boldsymbol{\Gamma}\boldsymbol{\mathcal{B}}_p(t,\boldsymbol{x})^\top\| \leq \|\delta\boldsymbol{x}^\top\boldsymbol{\mathcal{B}}(t)\|\|\boldsymbol{\Gamma}\boldsymbol{\mathcal{B}}(t)^\top\boldsymbol{x}\| \tag{3.67}$$

The inequality from the derivative of the Lyapunov function is then

$$\begin{aligned}\dot{V}_2(t,\boldsymbol{x},\boldsymbol{y}) \leq\ & \boldsymbol{x}^\top \boldsymbol{\mathcal{A}}(t)\boldsymbol{x} + \|\delta \boldsymbol{x}^\top \boldsymbol{\mathcal{B}}(t)\|\|\boldsymbol{\Gamma}\boldsymbol{\mathcal{B}}(t)^\top \boldsymbol{x}\| \\ & - \delta \boldsymbol{y}^\top \boldsymbol{\mathcal{B}}(t)^\top \boldsymbol{\mathcal{B}}(t)\boldsymbol{y} + \boldsymbol{y}^\top \boldsymbol{\Gamma}^{-1}\boldsymbol{g}(t,\boldsymbol{y})| \\ & - \delta \boldsymbol{x}^\top (\boldsymbol{\mathcal{A}}(t)^\top \boldsymbol{\mathcal{B}}(t) + \dot{\boldsymbol{\mathcal{B}}}(t))\boldsymbol{y} - \delta \boldsymbol{x}^\top \boldsymbol{\mathcal{B}}(t)\boldsymbol{g}(t,\boldsymbol{y}) \end{aligned} \tag{3.68}$$

To show that this expression is in fact negative definite, we will expand the matrix expressions, term by term, and derive a bound for each term. We start with the term $\boldsymbol{x}^\top \boldsymbol{\mathcal{A}}(t)\boldsymbol{x}$ where we recall that the matrix $\boldsymbol{\mathcal{A}}(t)$ is block diagonal matrix with a skew-symmetric term. The skew-symmetric term becomes zero when multiplied with $\boldsymbol{x}$ from both sides, which means

$$\begin{aligned}\boldsymbol{x}^\top \boldsymbol{\mathcal{A}}(t)\boldsymbol{x} &= \sum_{i=1}^{m} k_i \tilde{\boldsymbol{u}}_{\delta i}^b \boldsymbol{S}(\boldsymbol{u}_{\delta i}^b)\boldsymbol{S}(\hat{\boldsymbol{u}}_{\delta i}^b)\tilde{\boldsymbol{u}}_{\delta i}^b \\ &= \sum_{i=1}^{m} -k_i (\boldsymbol{u}_{\delta i}^b)^\top \hat{\boldsymbol{u}}_{\delta i}^b \|\tilde{\boldsymbol{u}}_{\delta i}^b\|^2 \\ &\leq -k_\epsilon \cos(\epsilon) \sum_{i=1}^{m} \|\tilde{\boldsymbol{u}}_{\delta i}^b\|^2 = -k_\epsilon c_\epsilon \|\boldsymbol{x}\|^2 \end{aligned} \tag{3.69}$$

where we have used $\boldsymbol{S}(\boldsymbol{u}_{\delta i}^b)\boldsymbol{S}(\hat{\boldsymbol{u}}_{\delta i}^b)\tilde{\boldsymbol{u}}_{\delta i}^b = -((\boldsymbol{u}_{\delta i}^b)^\top \hat{\boldsymbol{u}}_{\delta i}^b)\tilde{\boldsymbol{u}}_{\delta i}^b$, which can be verified using the triple product, and $c_\epsilon = \cos(\epsilon)$. The term $\|\boldsymbol{x}^\top \boldsymbol{\mathcal{B}}(t)\|\|\boldsymbol{\Gamma}\boldsymbol{\mathcal{B}}(t)\boldsymbol{x}\|$ can be expanded to

$$\begin{aligned}&\|\delta \boldsymbol{x}^\top \boldsymbol{\mathcal{B}}(t)\|\|\boldsymbol{\Gamma}\boldsymbol{\mathcal{B}}(t)^\top \boldsymbol{x}\| \leq \delta\bar{\gamma}\|\boldsymbol{x}^\top \boldsymbol{\mathcal{B}}(t)\|\|\boldsymbol{\mathcal{B}}(t)^\top \boldsymbol{x}\| \\ &= \delta\bar{\gamma}\|\boldsymbol{\mathcal{B}}(t)^\top \boldsymbol{x}\|^2 = \\ &\delta\bar{\gamma}\sum_{i=1}^{m} -(\tilde{\boldsymbol{u}}_{\delta i}^b)^\top \boldsymbol{S}(\hat{\boldsymbol{u}}_{\delta i}^b)\boldsymbol{S}(\boldsymbol{u}_{\delta i}^b)^2 \boldsymbol{v}^b (\boldsymbol{v}^b)^\top \boldsymbol{S}(\boldsymbol{u}_{\delta i}^b)^2 \boldsymbol{S}(\hat{\boldsymbol{u}}_{\delta i}^b)\tilde{\boldsymbol{u}}_{\delta i}^b \\ &+ \delta\bar{\gamma}(\sum_{i=1}^{m} \boldsymbol{S}(\hat{\boldsymbol{u}}_{\delta i}^b)\boldsymbol{S}(\boldsymbol{u}_{\delta i}^b)\tilde{\boldsymbol{u}}_{\delta i}^b)^\top (\sum_{i=1}^{m} \boldsymbol{S}(\hat{\boldsymbol{u}}_{\delta i}^b)\boldsymbol{S}(\boldsymbol{u}_{\delta i}^b)\tilde{\boldsymbol{u}}_{\delta i}^b) \\ &\leq \delta\bar{\gamma}\|\boldsymbol{v}^b\|^2 \sum_{i=1}^{m} \|\tilde{\boldsymbol{u}}_{\delta i}^b\|^2 + \delta\bar{\gamma} m \sum_{i=1}^{m} \|\tilde{\boldsymbol{u}}_{\delta i}^b\|^2 \leq \delta\bar{\gamma}(\bar{v}^2 + m)\|\boldsymbol{x}\|^2 \end{aligned} \tag{3.70}$$

where we used the Cauchy-Schwarz inequalety. We can also use these results to

find a bound for

$$
\begin{aligned}
&- \delta \boldsymbol{x}^\top (\boldsymbol{\mathcal{A}}(t)^\top \boldsymbol{\mathcal{B}}(t) + \dot{\boldsymbol{\mathcal{B}}}(t)) \boldsymbol{y} \\
&\leq \delta \|\boldsymbol{x}\| ((\bar{d}\bar{v} + \bar{\omega})(\bar{v} + m) + \boldsymbol{\rho}_b) \|\boldsymbol{y}\| && (3.71) \\
&- \delta \boldsymbol{x}^\top \operatorname{diag}(\{k_i \boldsymbol{S}(\boldsymbol{u}_{\delta i}^b) \boldsymbol{S}(\hat{\boldsymbol{u}}_{\delta i}^b)\}_i^m) \boldsymbol{\mathcal{B}}(t) \boldsymbol{y} && (3.72) \\
&\leq \delta \|\boldsymbol{x}\| ((\bar{d}\bar{v} + \bar{\omega})(\bar{v} + m) + \boldsymbol{\rho}_b) \|\boldsymbol{y}\| && (3.73) \\
&- \delta k \boldsymbol{x}^\top [\operatorname{diag}(\{k_i \boldsymbol{S}(\boldsymbol{u}_{\delta i}^b) \boldsymbol{S}(\hat{\boldsymbol{u}}_{\delta i}^b)\}_i^m) && (3.74) \\
&+ (1-1)\frac{1}{2} \min(k_\epsilon c_\epsilon, \delta \underline{\gamma} \mu) \boldsymbol{I}] \boldsymbol{\mathcal{B}}(t) \boldsymbol{y} && (3.75) \\
&\leq \delta \|\boldsymbol{x}\| ((\bar{d}\bar{v} + \bar{\omega})(\bar{v} + m) + \boldsymbol{\rho}_b + k(\bar{v} + m)) \|\boldsymbol{y}\| && (3.76) \\
&+ \delta \frac{1}{2} \boldsymbol{x}^\top \min(k_\epsilon c_\epsilon, \delta \underline{\gamma} \mu) \boldsymbol{\mathcal{B}}(t) \boldsymbol{y} && (3.77)
\end{aligned}
$$

where $k > k_i > k_\epsilon$, $\boldsymbol{\rho}_b > \|\dot{\boldsymbol{\mathcal{B}}}(t)\|$, and from Lemma 1 we have

$$
-\delta \boldsymbol{y}^\top \boldsymbol{\mathcal{B}}(t)^\top \boldsymbol{\mathcal{B}}(t) \boldsymbol{y} \leq -\delta \mu \|\boldsymbol{y}\|^2 \tag{3.78}
$$

C) Handle the projected perturbation Finally, we have to deal with the $\boldsymbol{g}(t, \boldsymbol{y})$, where we see that

$$
\begin{aligned}
&\boldsymbol{y}^\top \boldsymbol{\Gamma}^{-1} \boldsymbol{g}(t, \boldsymbol{y}) - \delta \boldsymbol{x}^\top \boldsymbol{\mathcal{B}}(t) \boldsymbol{g}(t, \boldsymbol{y}) \\
&= \sum_{i \in \boldsymbol{\mathcal{P}}} -\frac{1}{\gamma_i} |\tilde{d}_i d_i^2 (\boldsymbol{u}_{\delta i}^b)^\top \boldsymbol{v}^b| + \sum_{i \in \boldsymbol{\mathcal{P}}^c} \frac{1}{\gamma_i} \tilde{d}_i^2 (d_i + \hat{d}_i) (\boldsymbol{u}_{\delta i}^b)^\top \boldsymbol{v}^b \\
&+ \delta \sum_{i \in \boldsymbol{\mathcal{P}}} (\tilde{\boldsymbol{u}}_{\delta i}^b)^\top \boldsymbol{S}(\hat{\boldsymbol{u}}_{\delta i}^b) \boldsymbol{S}(\boldsymbol{u}_{\delta i}^b)^2 \boldsymbol{v}^b d_i^2 (\boldsymbol{u}_{\delta i}^b)^\top \boldsymbol{v}^b \\
&+ \delta \sum_{i \in \boldsymbol{\mathcal{P}}^c} (\tilde{\boldsymbol{u}}_{\delta i}^b)^\top \boldsymbol{S}(\hat{\boldsymbol{u}}_{\delta i}^b) \boldsymbol{S}(\boldsymbol{u}_{\delta i}^b)^2 \boldsymbol{v}^b \tilde{d}_i (d_i + \hat{d}_i) (\boldsymbol{u}_{\delta i}^b)^\top \boldsymbol{v}^b \\
&\leq + \frac{1}{\underline{\gamma}} 2 \bar{d} \bar{v} \sum_{i \in \boldsymbol{\mathcal{P}}^c} \tilde{d}_i^2 + \delta \bar{v}^2 2 \bar{d} \sum_{i \in \boldsymbol{\mathcal{P}}^c} \|\tilde{\boldsymbol{u}}_{\delta i}^b\| |\tilde{d}_i| \\
&+ \sum_{i \in \boldsymbol{\mathcal{P}}} -\frac{1}{\bar{\gamma}} |\tilde{d}_i d_i^2 (\boldsymbol{u}_{\delta i}^b)^\top \boldsymbol{v}^b| + \delta \bar{v} \sin(\epsilon) d_i^2 (\boldsymbol{u}_{\delta i}^b)^\top \boldsymbol{v}^b \\
&\leq \frac{1}{\underline{\gamma}} 2 \bar{d} \bar{v} \|\boldsymbol{y}\|^2 + \delta 2 \bar{v}^2 \bar{d} \|\boldsymbol{x}\| \|\boldsymbol{y}\| && (3.79)
\end{aligned}
$$

as long as we can guarantee that

$$
\begin{aligned}
&\frac{1}{\bar{\gamma}} |\tilde{d}_i| |d_i^2 (\boldsymbol{u}_{\delta i}^b)^\top \boldsymbol{v}^b| > \delta \bar{v} \sin(\epsilon) |d_i^2 (\boldsymbol{u}_{\delta i}^b)^\top \boldsymbol{v}^b|, \ \forall i \in \boldsymbol{\mathcal{P}} \\
&\qquad \Updownarrow \\
&\frac{1}{\bar{\gamma}} |\tilde{d}_i| > \delta \bar{v} \sin(\epsilon), \ \forall i \in \boldsymbol{\mathcal{P}} && (3.80)
\end{aligned}
$$

where $\underline{\gamma}$ is the smallest singular value of $\mathbf{\Gamma}$, and we recall from (3.57) that $\sin(\epsilon) > \frac{\bar{v}+\bar{b}_\omega}{k_\epsilon}$. Hence, we can substitute the inequality into (3.80) and get

$$k_\epsilon > \bar{\gamma}\delta\frac{\bar{v}(\bar{v}\bar{d}+\bar{b})}{\check{d}} \tag{3.81}$$

where $\check{d}$ is the minimum value that $\tilde{d}_i$ can have when the projection is activated.
D) Gains exisit that yield explonential stabillity in the large From these bounds we see that the derivative of the Lyapunov function satisfies

$$\begin{aligned}\dot{V}_2(t,\boldsymbol{x},\boldsymbol{y}) \leq & -k_\epsilon c_\epsilon\|\boldsymbol{x}\|^2 + \delta\bar{\gamma}(\bar{v}^2+m)\|\boldsymbol{x}\|^2 \\ & - \delta\mu\|\boldsymbol{y}\|^2 + \frac{1}{\underline{\gamma}}2\bar{d}\bar{v}\|\boldsymbol{y}\|^2 \\ & + \delta\|\boldsymbol{x}\|\|\boldsymbol{y}\|(k(\bar{v}+m)+((\bar{d}\bar{v}+\bar{\omega})(\bar{v}^2+m)+\boldsymbol{\rho}_b)) \\ & + \delta 2\bar{v}^2\bar{d}\|\boldsymbol{x}\|\|\boldsymbol{y}\| + \frac{1}{2}\delta\min(k_\epsilon c_\epsilon, \delta\underline{\gamma}\mu)\boldsymbol{x}^\top\boldsymbol{\mathcal{B}}(t)\boldsymbol{y},\end{aligned} \tag{3.82}$$

which we then can restructure to

$$\begin{aligned}\dot{V}_2(t,\boldsymbol{x},\boldsymbol{y}) \leq & -\frac{1}{4}k_\epsilon c_\epsilon\|\boldsymbol{x}\|^2 - \frac{\delta\mu}{4}\|\boldsymbol{y}\|^2 \\ & + \frac{1}{2}\delta\min(k_\epsilon c_\epsilon, \delta\underline{\gamma}\mu)\boldsymbol{x}^\top\boldsymbol{\mathcal{B}}(t)\boldsymbol{y} \\ & - \|\boldsymbol{x}\|^2(\frac{k_\epsilon c_\epsilon}{2} - \delta\bar{\gamma}(\bar{v}^2+m)) - \|\boldsymbol{y}\|^2(\frac{\delta\mu}{2} - \frac{1}{\underline{\gamma}}2\bar{d}\bar{v}) \\ & - \frac{1}{2}\begin{bmatrix}\|\boldsymbol{x}\| \\ \|\boldsymbol{y}\|\end{bmatrix}^\top\begin{bmatrix}\frac{k_\epsilon c_\epsilon}{2} & -\delta(k\bar{\rho}_2+\bar{\rho}_d) \\ -\delta(k\bar{\rho}_2+\bar{\rho}_d) & \frac{\delta\mu}{2}\end{bmatrix}\begin{bmatrix}\|\boldsymbol{x}\| \\ \|\boldsymbol{y}\|\end{bmatrix}\end{aligned} \tag{3.83}$$

where $\bar{\rho}_2 = \bar{v}+m$ and $\bar{\rho}_d = ((\bar{d}\bar{v}+\bar{\omega})(\bar{v}^2+m)+\boldsymbol{\rho}_b) + \bar{v}^2\bar{d}$. We see that if the inequaleties

$$\frac{k_\epsilon c_\epsilon}{2} > \delta\bar{\gamma}(\bar{v}^2+m) \tag{3.84}$$

$$\frac{\delta\mu}{2} > \frac{1}{\underline{\gamma}}2\bar{d}\bar{v} \tag{3.85}$$

$$\frac{k_\epsilon c_\epsilon\delta\mu}{4} > \delta^2(k\bar{\rho}_2+\bar{\rho}_d)^2 \tag{3.86}$$

hold, the Lyapunov derivative is negative definite. We combine these with all the previous inequalities, (3.57),(3.59) and (3.81) to see that gains can be chosen to comply with all the inequalities. First we combine (3.59) and (3.85) and get

$$\delta < \frac{\mu}{4\bar{d}\bar{v}(\bar{v}+m)^2} \tag{3.87}$$

$$\frac{4\bar{d}\bar{v}}{\mu\delta} < \gamma < \frac{1}{(v+m)^2\delta^2} \tag{3.88}$$

and also introducing the inequalities (3.81), (3.84) and (3.86) we get

$$\delta < \min\left(\frac{k_\epsilon c_\epsilon \mu}{4(k\bar{\rho}_2 + \bar{\rho}_d)^2}, \frac{\mu}{4\bar{d}\bar{v}(\bar{v}+m)^2}\right) \tag{3.89}$$

$$\frac{4\bar{d}\bar{v}}{\mu\delta} < \gamma < \min\left(\frac{1}{(v+m)^2\delta^2}, \frac{k_\epsilon c_\epsilon}{2\delta(\bar{v}^2+m)}, \frac{k_\epsilon \check{d}}{\delta\bar{v}(\bar{v}\bar{d}+\bar{b})}\right). \tag{3.90}$$

What is left to find is a lower bound on k_ϵ which ensures that solution a to the system of inequalities exist. Then also introducing (3.57), and bounds on k_ϵ, ensuring that the upper bounds of the γ are larger than the lower bound in (3.90), gives the total system of inequalities

$$k > k_\epsilon > \max\left(\frac{\bar{v}\bar{d}+\bar{b}}{\sin(\epsilon)}, \frac{8\bar{v}\bar{d}(\bar{v}^2+m)}{\mu c_\epsilon}, \frac{4\bar{d}\bar{v}(\bar{v}\bar{d}+\bar{b})}{\check{d}\mu\delta}\right) \tag{3.91}$$

$$\delta < \min\left(\frac{k_\epsilon c_\epsilon \mu}{4(k\bar{\rho}_2 + \bar{\rho}_d)^2}, \frac{\mu}{4\bar{d}\bar{v}(\bar{v}+m)^2}\right) \tag{3.92}$$

$$\frac{4\bar{d}\bar{v}}{\mu\delta} < \gamma < \min\left(\frac{1}{(v+m)^2\delta^2}, \frac{k_\epsilon c_\epsilon}{2\delta(\bar{v}^2+m)}, \frac{k_\epsilon \check{d}}{\delta\bar{v}(\bar{v}\bar{d}+\bar{b})}\right). \tag{3.93}$$

Thus we see that if the gain $k_\epsilon < k_i < k$ is chosen large enough, the k_{di} and K_b can be chosen according to the bounds in (3.93).

We recall the bounds $\bar{v}, \bar{d}, \bar{b}_\omega, \bar{\omega}$ are the bounds on the velocity, inverse range, gyro-bias gyro rate consecutively. Other bounds are $\bar{\rho}_d = ((\bar{d}\bar{v}+\bar{\omega})(\bar{v}^2+m)+\boldsymbol{\rho}_b)+\bar{v}^2\bar{d}$ and $\bar{\rho}_2 = \bar{v}+m$, where $\boldsymbol{\rho}_b > \|\dot{\boldsymbol{\mathcal{B}}}\|$. In addition, the fact that the inequalities hold result in that the following inequality also holds

$$\dot{V}_2(t, \boldsymbol{x}, \boldsymbol{y}) \leq -\frac{1}{2}\min(k_\epsilon c_\epsilon, \delta\underline{\gamma}\mu)V_2(t, \boldsymbol{x}, \boldsymbol{y})$$

from which we can conclude that the error will converge exponentially fast to zero at this rate, when all the unit vector estimate errors are within the set $(\hat{\boldsymbol{u}}^b_{\delta i})^\top \boldsymbol{u}^b_{\delta i} > \cos(\epsilon)$. textbfE) Conclusion, USGAS and UES We have already proven that the estimates will converge and be bounded within this set in finite time. In addition, since they will converge from arbitrarily close to the unstable equilibrium if a high enough gains are chosen, we can conclude that the error dynamics of the observer are semi-globally asymptotically stable, and exponentially stable in the large.

□

3.6.1 Decoupling of gyro bias estimation

Remark 2. *It should be noted that inertial/body reference vectors, such as magnetometer and gravity, can also be used in the gyro bias observer, where the vectors can be included by using $\boldsymbol{u}^b_{\delta i} = \boldsymbol{r}^b_i$ and by setting $d_i = \hat{d}_i = 0$, and thus annihilate its effect.*

As will be seen later in the article, the rate of convergence of the gyro bias estimation error can be quite different in different axes. This affects how big gain one might desire to have for the gyro bias estimation in different directions. An example of this is when a reference vector $\boldsymbol{r}^b$ is available. Since this reference vector makes the gyro bias with axis orthogonal to this vector more available, it can be desirable to divide the gyro bias estimation into the space orthogonal $\boldsymbol{r}^{b\perp}$ and parallel $\boldsymbol{r}^{b\parallel}$ to this vector. We recall the projection transformations

$$\boldsymbol{U}_r^{\perp} = -\boldsymbol{S}(\boldsymbol{r}^b)^2 \ , \ \boldsymbol{U}_r^{\parallel} = \boldsymbol{r}^b(\boldsymbol{r}^b)^\top \tag{3.94}$$

This can then be used to provide one gain for the gyro bias estimation parallel to, and another one for the bias estimation orthogonal to, the reference vector

$$\dot{\hat{\boldsymbol{u}}}_{\delta i}^b = -\boldsymbol{S}(\boldsymbol{\omega}_m - \hat{\boldsymbol{b}}_\omega + k_i\boldsymbol{\sigma}_i)\hat{\boldsymbol{u}}_{\delta i}^b + \hat{d}_i\boldsymbol{S}(\hat{\boldsymbol{u}}_{\delta i}^b)\boldsymbol{S}(\boldsymbol{u}_{\delta i}^b)\boldsymbol{v}^b \tag{3.95}$$

$$\dot{\hat{\boldsymbol{r}}}^b = -\boldsymbol{S}(\boldsymbol{\omega}_m - \hat{\boldsymbol{b}}_\omega + k_i\boldsymbol{\sigma}_r)\hat{\boldsymbol{r}}^b \tag{3.96}$$

$$\begin{aligned}\dot{\hat{d}}_i = &\ \mathrm{Proj}_{di}(\hat{d}_i^2(\boldsymbol{u}_{\delta i}^b)^\top\boldsymbol{v}^b) \\ &+ k_{di}\mathrm{Proj}_{di}((\boldsymbol{v}^b)^\top\boldsymbol{S}(\boldsymbol{u}_{\delta i}^b)^2\boldsymbol{S}(\hat{\boldsymbol{u}}_{\delta i}^b)\boldsymbol{\sigma}_i)\end{aligned} \tag{3.97}$$

$$\begin{aligned}\dot{\hat{\boldsymbol{b}}}_\omega = &\ (k_{1b}\boldsymbol{U}_r^{\parallel} + k_{2b}\boldsymbol{U}_r^{\perp})\mathrm{Proj}_b(\sum_{i=1}^{m} -(\boldsymbol{S}(\hat{\boldsymbol{u}}_{\delta i}^b)\boldsymbol{S}(\boldsymbol{u}_{\delta i}^b)\boldsymbol{\sigma}_i) \\ &- \boldsymbol{S}(\hat{\boldsymbol{r}}^b)\boldsymbol{S}(\boldsymbol{r}^b\boldsymbol{\sigma}_r)\end{aligned} \tag{3.98}$$

$$\boldsymbol{\sigma}_i = \boldsymbol{S}(\boldsymbol{u}_{\delta i}^b)\hat{\boldsymbol{u}}_{\delta i}^b \tag{3.99}$$

$$\boldsymbol{\sigma}_r = \boldsymbol{S}(\boldsymbol{r}^b)\hat{\boldsymbol{r}}^b \tag{3.100}$$

The crucial part is that the gyro bias estimation can be tuned to balance the difference in the convergence rate. We believe that the reason for this difference in convergence rate along the different axis can be related to the distinct eigenvalues of the matrix (3.30) which will be shown for different scenarios later in the article.

3.6.2 Attitude estimate

As was shown in [16], as the gyro-bias is estimated by the bearing nonlinear observer, it can be fed to an attitude observer in cascade. The benefits of this setup is that the gyro bias estimate is independent of the attitude estimates. We can then use the bias estimated in cascade with the attitude observer from [48] (see also [43])

$$\dot{\hat{\boldsymbol{\mathcal{R}}}}_{nb} = \hat{\boldsymbol{\mathcal{R}}}_{nb}\boldsymbol{S}(\boldsymbol{\omega_m} - \hat{\boldsymbol{b}}_\omega + \boldsymbol{\sigma}_{\mathcal{R}}) \tag{3.101}$$

$$\boldsymbol{\sigma}_{\mathcal{R}} = \sum_{i=1}^{n} c_i\boldsymbol{S}(\boldsymbol{r}_i^b)\hat{\boldsymbol{\mathcal{R}}}_{nb}^\top\boldsymbol{r}_i^n \tag{3.102}$$

where semi-globally stability can be achieved. However we need an assumption about the set of reference vectors.

Theorem 4. *Assume there are n unit vectors $\boldsymbol{r}_j$ that are known or measurable in both body- and inertial-frame, $\boldsymbol{r}_j^n = \boldsymbol{\mathcal{R}}_{nb}\boldsymbol{r}_j^b,\ j \in 1,..,n$. In addition, there exists a constant $c_{obs} > 0$ so as, for each $t \geq 0$, the inequality $\|\boldsymbol{S}(\boldsymbol{r}_j^b)\boldsymbol{r}_k^b\| > c_{obs}$ holds for at least two of the indices $j,k \in \{1,...,n\}$*

Consider the kinematics of a vehicle with bearing measurements from landmarks, in addition to velocity measurement, and gyro measurements with a bias (2.9)*. Under the conditions of Theorem 3, a large enough gain c_i exist so that the observer* (3.14)-(3.16) *in cascade with* (3.101)-(3.102)*, will be semi-globally asymptotically stable for time varying reference vectors.*

Proof. The proof is shown in [16] □

The total observer is summarized in Table 3.2.

Table 3.2: Summary of the cascade range and attitude observer

CASCADE RANGE AND ATTITUDE OBSERVER	
Measurements: $\boldsymbol{\omega}_m, \boldsymbol{v}^b, \boldsymbol{u}_{\delta i}^b, \boldsymbol{r}_i^b, \boldsymbol{r}_i^n$	
$\dot{\hat{\boldsymbol{u}}}_{\delta i}^b = -\boldsymbol{S}(\boldsymbol{\omega}_m - \hat{\boldsymbol{b}}_\omega + k_i\boldsymbol{\sigma}_i + \hat{d}_i\boldsymbol{S}(\boldsymbol{u}_{\delta i}^b)\boldsymbol{v}^b)\hat{\boldsymbol{u}}_{\delta i}^b$	(3.14)
$\boldsymbol{\sigma}_i = \boldsymbol{S}(\boldsymbol{u}_{\delta i}^b)\hat{\boldsymbol{u}}_{\delta i}^b$	(3.15)
$\dot{\hat{d}}_i = \mathrm{Proj}_{di}(\hat{d}_i^2(\boldsymbol{u}_{\delta i}^b)^\top\boldsymbol{v}^b) + k_{di}\mathrm{Proj}_{di}((\boldsymbol{v}^b)^\top\boldsymbol{S}(\boldsymbol{u}_{\delta i}^b)^2\boldsymbol{S}(\hat{\boldsymbol{u}}_{\delta i}^b)\boldsymbol{\sigma}_i))$	(3.16)
$\dot{\hat{\boldsymbol{b}}}_\omega = \mathrm{Proj}_b(-\sum_{i=1}^{m} k_{bi}\boldsymbol{S}(\hat{\boldsymbol{u}}_{\delta i}^b)\boldsymbol{S}(\boldsymbol{u}_{\delta i}^b)\boldsymbol{\sigma}_i)$	(3.17)
$\dot{\hat{\boldsymbol{\mathcal{R}}}}_{nb} = \hat{\boldsymbol{\mathcal{R}}}_{nb}\boldsymbol{S}(\boldsymbol{\omega_m} - \hat{\boldsymbol{b}}_\omega + \boldsymbol{\sigma}_\mathcal{R})$	(3.101)
$\boldsymbol{\sigma}_\mathcal{R} = \sum_{i=1}^{n} c_i\boldsymbol{S}(\boldsymbol{r}_i^b)\hat{\boldsymbol{\mathcal{R}}}_{nb}^\top\boldsymbol{r}_i^n$	(3.102)

3.7 Simulation Results and Performance Evaluation

One interesting thing to investigate is how the landmark distribution will affect the convergence of the observer. By examining Lemma 1, we see that the convergence of the inverted distance estimate to the landmark is dependent on that the velocity is not parallel to the landmark bearing, which is intuitive as the distance to the landmark is unobservable if the bearing measurement is stationary. This is

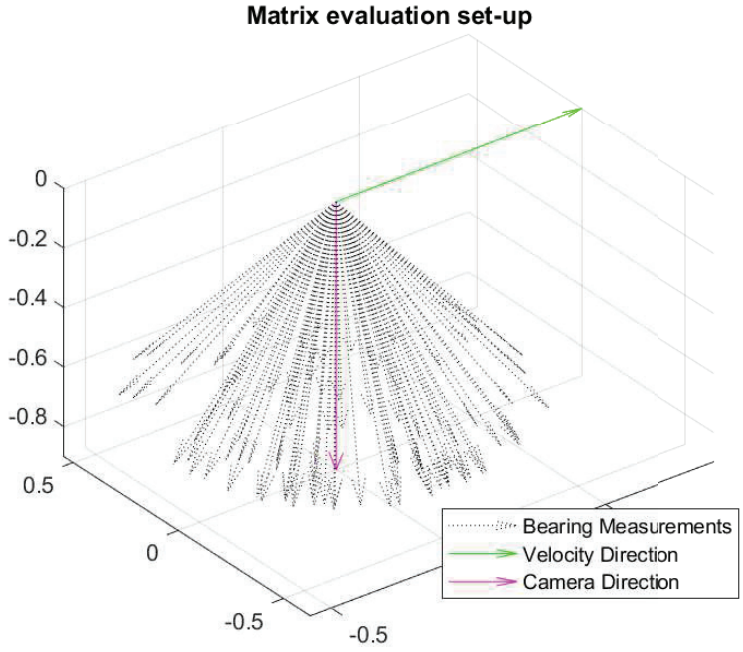

Figure 3.9: Simulation setup for evaluating the matrix (3.104)

consistent with the observability results and PE conditions found in [19, 17, 77, 49]. For the convergence of the bias estimate, we see that it is related to the inequality

$$-\sum_{i=1}^{m} \frac{1}{\xi^\top \xi} S(\hat{u}_{\delta i}^b) S(u_{\delta i}^b) S(\xi) S(\xi) S(u_{\delta i}^b) S(\hat{u}_{\delta i}^b) > \mathbf{0} \tag{3.103}$$

where we recall that $\xi = -S(\hat{u}_{\delta i}^b) S(u_{\delta i}^b)^2 v^b$. To better understand this inequality, and how its positive definiteness depend on landmark positions, the related matrix

$$\sum_{i=1}^{m} \frac{1}{\hat{\xi}^\top \hat{\xi}} S(u_{\delta i}^b)^2 S(\hat{\xi}) S(\hat{\xi}) S(u_{\delta i}^b)^2 \tag{3.104}$$

$$\hat{\xi} = -S(u_{\delta i}^b)^3 v^b \tag{3.105}$$

was calculated and the eigenvalues were compared in the different setups. We note that the matrix is independent of the range estimates, the gyro, as well as the attitude and the magnitude of the velocity as long as it is non-zero. A scenario can be seen in Figure 3.9.

The matrix eqreftestMatrix and its eigenvalues were calculated for several consecutive scenarios where the virtual camera setup was varied to have different

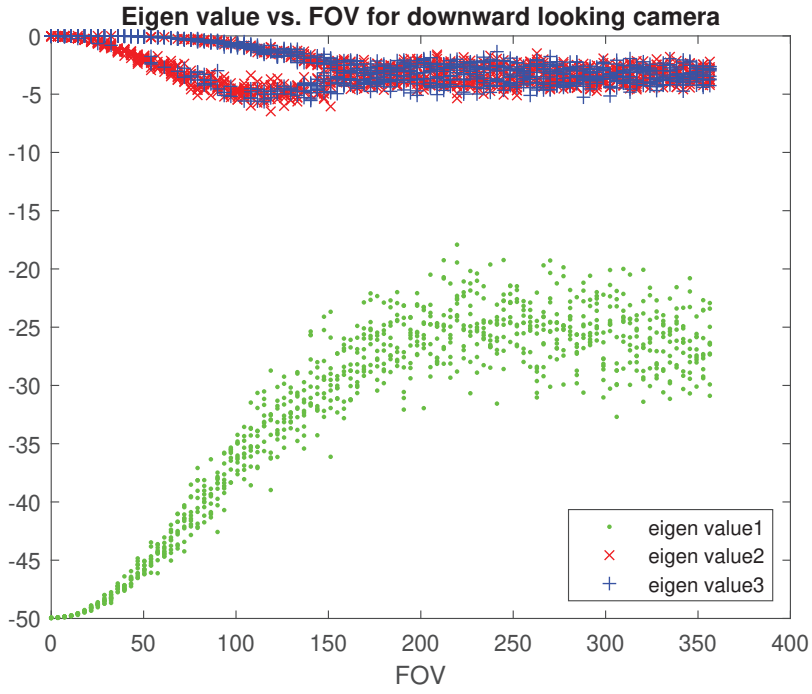

Figure 3.10: The eigenvalues of matrix (3.104) plotted against the FOV in the downward looking camera, with 50 bearing measurements

number of bearing measurements, different angle between the velocity and the camera axis, and different FOV of the camera. Each parameter setup had its matrix calculated 10 times with the bearing vectors chosen randomly within the constraints of the parameters. The eigenvalues of these matrices can be seen in Figures 3.10-3.13.

From these plots, one can see how the camera position relative to the velocity would affect the gyro bias convergence. This example however does not take into account the difference in noise that the bearing measurements experience because of changing FOV. Not surprisingly, having too narrow FOV will make gyro bias estimation difficult. From figure 3.10 one can see that after having an FOV of 150^o, an increase of FOV will not make the eigenvalues more negative. For the case when the camera is looking in the same direction as the velocity, as typical for an automotive application, the matrix has an optimal FOV close to 90^o. We see from Figure 3.12 that for a camera with 90^o FOV, the optimal angle between the camera and the velocity is 0^o, 60^o, 120^o and 180^o. These results somewhat agrees with what was found in [114], where the Perspective-n-Point (PnP) problem was solved, estimating the pose from observing n points with known position, through an optimization with different FOV. In the mentioned article, the noise as a result

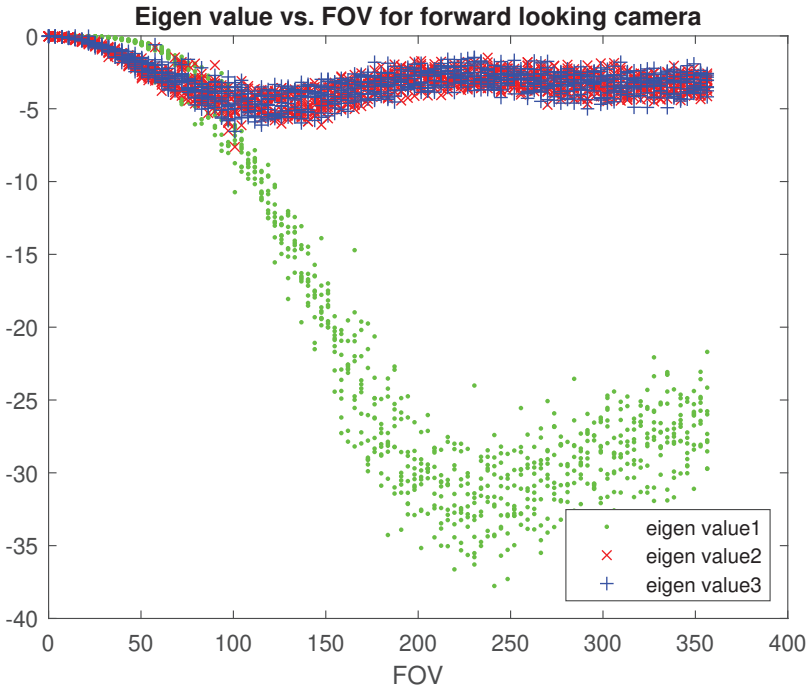

Figure 3.11: The eigenvalues of matrix (3.104) plotted against the FOV in the forward looking camera, with 50 bearing measurements

of different FOV was also included, and the results showed that in a confined space, the rotation error of the pose estimate decrease with increasing FOV until $120^o - 150^o$ where it is the lowest. For the scenario where the camera has infinite range, the increased noise because of higher FOV then makes the rotation error increase with the larger FOV. As described in [114]; it can be interpreted as the result of two competing effects. On the one hand a larger FOV provides a better conditioning for the PnP problem, and increases the pose estimation accuracy. On the other hand, as the FOV grows, the angular resolution decreases leading to increased bearing measurement noise.

Next a simulation of the observer was run, with randomly placed landmarks, and white noise on the bearing, velocity and gyro measurements with a bias $\boldsymbol{\omega}_m$. The standard deviation of the white noise was $\sigma_\omega = 0.001 \cdot \boldsymbol{I}, \sigma_v = 0.01 \cdot \boldsymbol{I}$ and $\sigma_u = 0.00314 \cdot \boldsymbol{I}$. An example simulation is seen in Figures 3.14-3.17. The gyro bias estimate converges, and the ranges are estimated with variable accuracy depending on the magnitude of the range. By plotting this error divided by the range of different order, it became clear that the error grows approximately quadratic to the range, as can be seen if Figure 3.18. The estimates does not seen to be too much biased. This is confirmed in Figure 3.19 where the averaged estimation

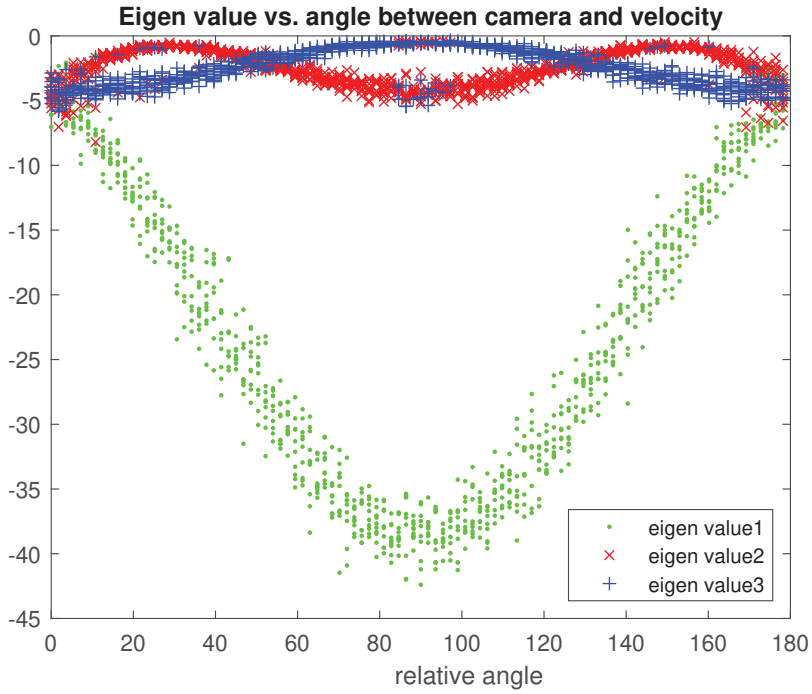

Figure 3.12: The eigenvalues of matrix (3.104) from ploted against the angle between the camera and the velocity with FOV 90^o with 50 bearing measurements

error at every time step of 200 Monte Carlo (MC) simulation was plotted, for the distance vector $\boldsymbol{\delta}_i^b = \frac{\boldsymbol{u}_{\delta i}^b}{\hat{d}_i}$.

3.7.1 Downward looking camera

For the next simulation we have investigated a common setup for UAV camera navigation, where a UAV has a downward looking camera. From the plot in Figure 3.10, we see that for the camera we are simulating, a 90^o FOV can be troublesome, as the movement of the UAV is often perpendicular to the camera direction. Never the less, we will show that the sensor setup presented in (3.95)-(3.100), will still give satisfactory results. The camera will work both as a gyro bias estimator, especially in yaw, as well as a depth or range to landmarks which are seen. The setup was tested in simulations. A vehicle is moving in a circle with radius of 10 m, looking downward at a plane from a height of 13 m. The simulation setup can be seen in Figure 3.20

For this setup, one can see that the landmarks dies and are born. When the system had converged and all innovations were kept under a threshold, a timer was introduced for new states so that they could converge before they affected

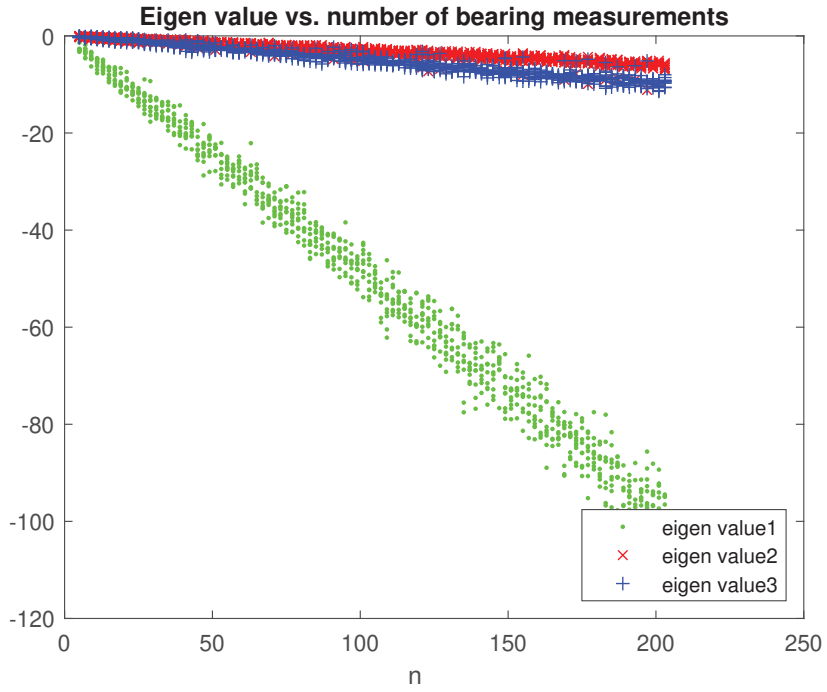

Figure 3.13: The eigenvalues of matrix (3.104) plottet against the number n of bearing measurements. The camera was pointed at 45^o forwards with regards to the velocity, and with a FOV of 90^o

the gyro bias estimate. This let the inverse range estimates converge before they affected the gyro bias estimate. An expansion of this could be to estimate whether a bearing measurement was PE, and let this influence the gains of the observer. However, for the scenarios encountered both in simulations and experiments, such a setup was not deemed necessary to achieve good results.

The simulator was discretized with the Euler method with step length $\Delta t = 0.067$, and white measurement and process noise were also added. In addition a gyro measurement $\boldsymbol{\omega}_m$ had a bias that was initialized as $\boldsymbol{b}_\omega = [0.05,\ 0.4,\ -0.25]^\top$ and driven by a white noise with standard deviation $\sigma_{bw} = 0.001$ according to

$$\boldsymbol{b}_\omega(t + \Delta t) = \boldsymbol{b}_\omega(t) + \mathcal{N}(0, \sigma_{bw}) \tag{3.106}$$

In addition, the gyro measurement was corrupted with a white noise with standard deviation $\sigma_\omega = 0.001 \cdot \boldsymbol{I}$. The noise of the bearing measurements were $\sigma_u = 0.00314 \cdot \boldsymbol{I}$. The bearing noise was orthogonal to the bearing measurement $\boldsymbol{u}^b_{\delta i} = \boldsymbol{S}(\boldsymbol{u}^b_{\delta i})\boldsymbol{w}_u$, where the noise $\boldsymbol{w}_u$ was a white noise vector $\boldsymbol{w}_u = \mathcal{N}(0, \sigma_u)$, as the bearing also is normalized the noise becomes nonlinear.

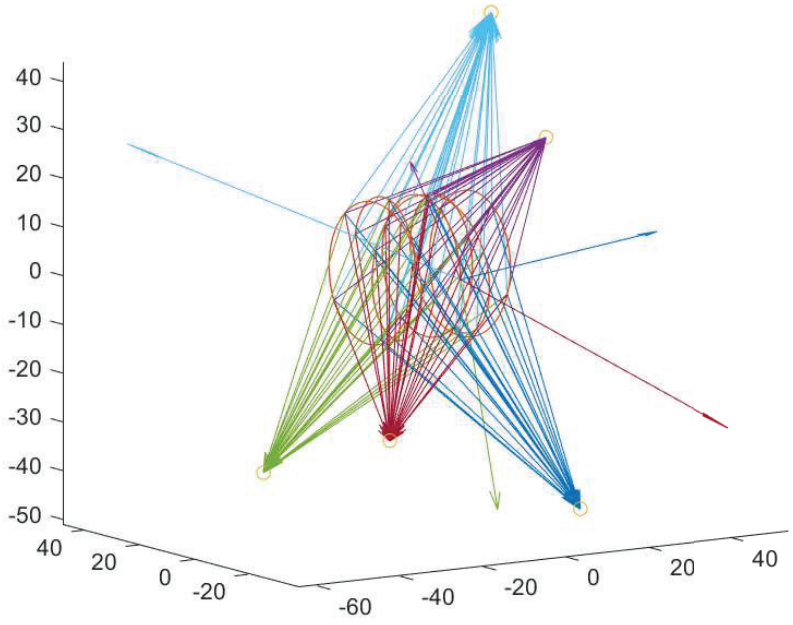

Figure 3.14: The trajectory for the Monte Carlo simulations, were the landmarks were chosen randomly within a box of 50 m^3

The gravity was utilized as a reference vector in the gyro bias range observer

$$\boldsymbol{r}_1^n = [0,\ 0,\ -1]^\top \tag{3.107}$$

$$\boldsymbol{r}_1^b = \boldsymbol{\mathcal{R}}_{nb}^\top (\boldsymbol{a}^n - \boldsymbol{g}^n + \boldsymbol{w}_f)/\|\boldsymbol{a}^n - \boldsymbol{g}^n + \boldsymbol{w}_f\| \tag{3.108}$$

$$= \boldsymbol{f}_{imu}/\|\boldsymbol{f}_{imu}\| \tag{3.109}$$

where $\boldsymbol{w}_f = \mathcal{N}(0, \boldsymbol{I}\sigma_f)$ and $\sigma_f = 0.002$. For the attitude estimate the GNSS and camera velocity were also used as a reference vector.

$$\boldsymbol{r}_2^n = (\boldsymbol{v}^n + \boldsymbol{w}_v)/\|\boldsymbol{v}^n + \boldsymbol{w}_v\| \tag{3.110}$$

$$\boldsymbol{r}_2^b = (\boldsymbol{v}_{cam}^b + \boldsymbol{w}_{vc})/\|\boldsymbol{v}_{cam}^b + \boldsymbol{w}_{vc}\| \tag{3.111}$$

with $\sigma_v = 0.05$ and $\sigma_{vc} = 0.05$, as a reference attitude observer we used the complimentary filter [43], with the same reference vectors.

The velocity was set to zero four times at $t = 33.3$, 80.0, 126.7 and 173.3 for 13.2 seconds. From Figure 3.21, it can be seen that the observers are able to estimate the gyro bias quite accurately. In addition, it can be seen how the novel observer is able handle the hovering compared to the velocity based observer. Another benefit is also seen for the loosely coupled system, since the bias estimation is

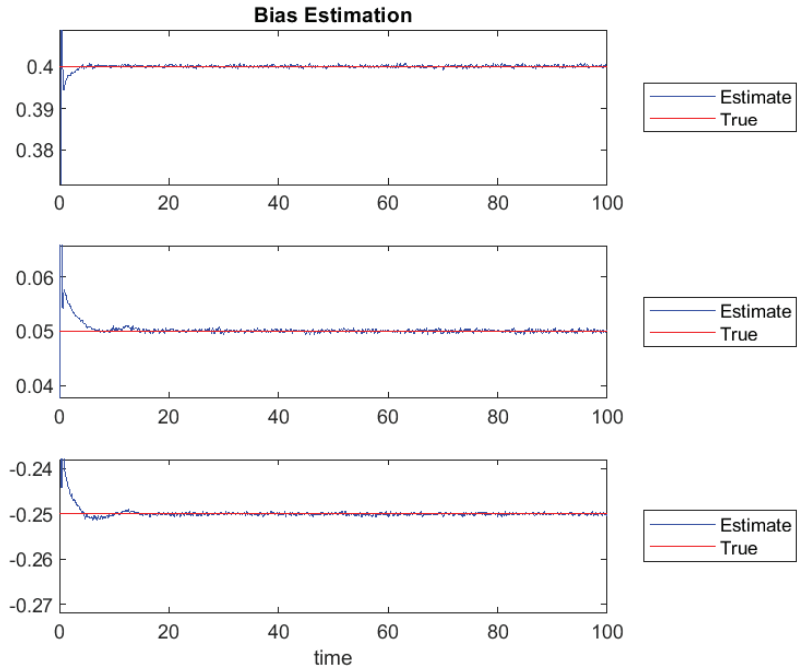

Figure 3.15: The bias estimate of one of the generic simulation runs equalt to Figure 3.14

independent of the attitude estimate, and the error in the attitude does not affect the gyro bias estimation and vice versa. It can also be seen how this affects the yaw estimates in Figure 3.23. In Figure 3.22, the height estimate acquired from the observer inverse range estimates are shown. For this setup, the height estimate is found by averaging the projected length estimates onto the gravity vector

$$\hat{h} = \frac{1}{n(C)} \sum_{i \in C} \frac{1}{\hat{d}} (\boldsymbol{r}^b)^\top \hat{\boldsymbol{l}}_i^b \tag{3.112}$$

where the set C contains the indices of the estimates that are regarded as converged, meaning that the bearing error σ_{ui} has become sufficiently small. This is also a reason why there are no height estimate at the beginning, as it takes some time for the bearing estimates to converge. The $n(C)$ is the cardinality of the set C. The estimate can hence be used to have a more accurate height estimate, without having to use pressure or laser altimeter together with the GNSS. From the simulations we see that the camera can both replace a pressure sensor and a magnetometer, assuming a sufficient number of landmarks are detected.

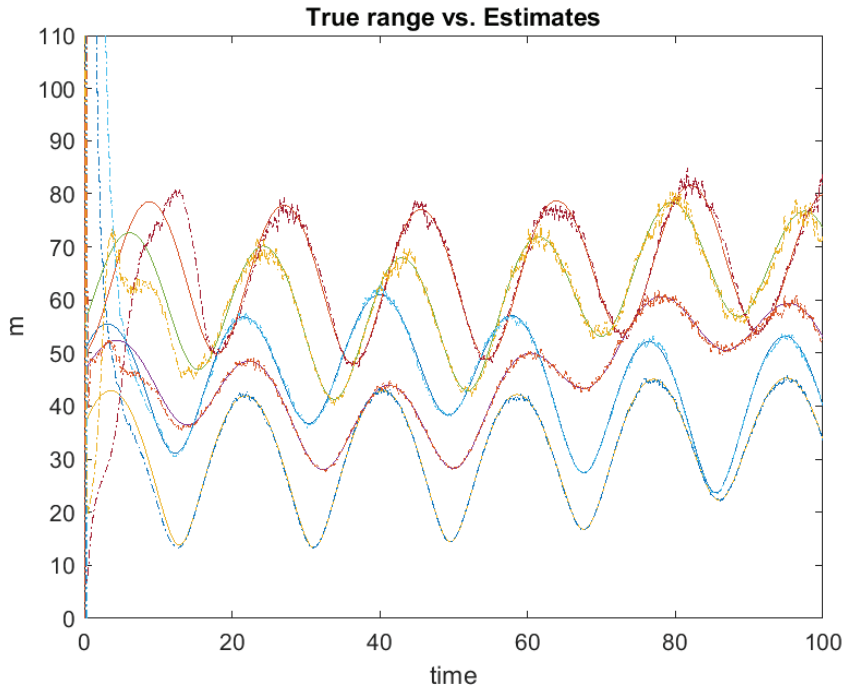

Figure 3.16: The range estimates acquired from the inverse range estimates vs. the true ranges.

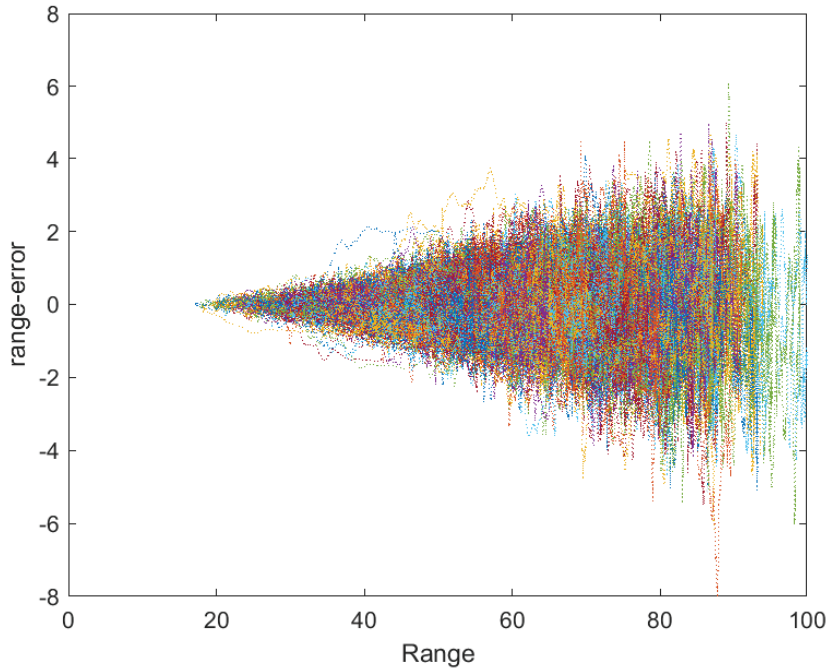

Figure 3.17: The range estimate error plotted against the true ranges for 200 MC simulations

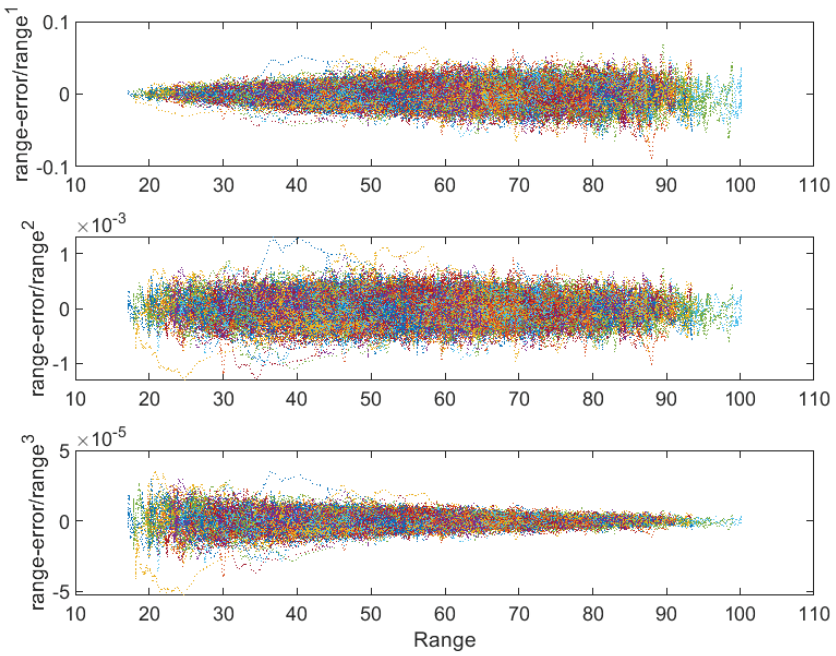

Figure 3.18: The range estimate error divided by the range to the 1st 2nd and 3rd order plotted against the true ranges for 200 MC simulations

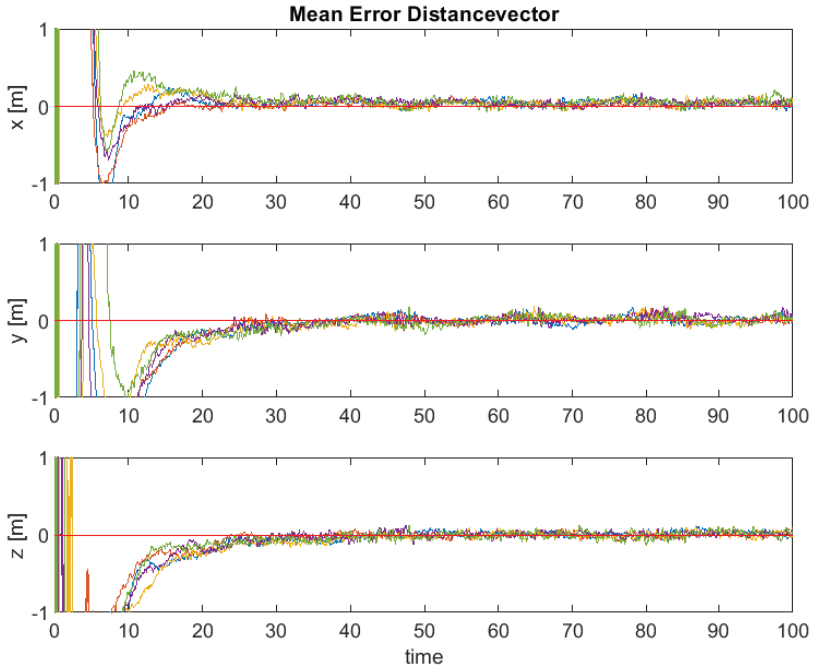

Figure 3.19: The averaged estimate error $\tilde{\delta}_i^b = \delta_i^b - \frac{\hat{u}_{\delta i}^b}{\hat{d}_i}$ of the 5 distance-vectors, for 200 MC simultaneous

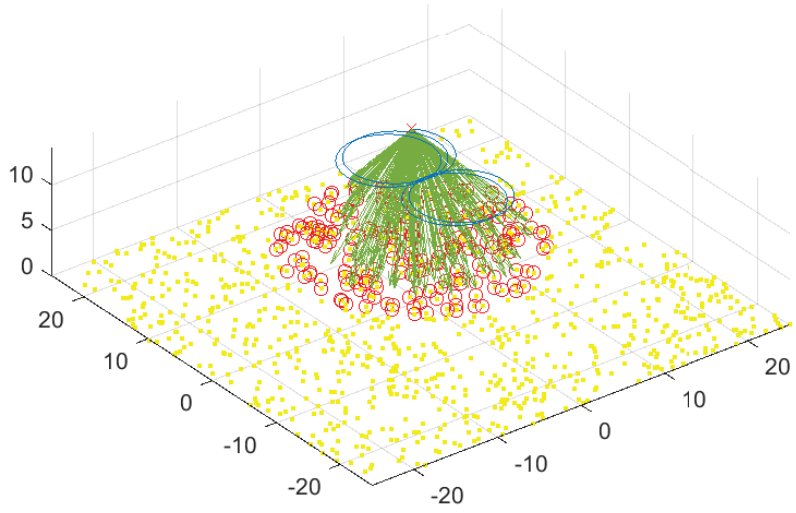

Figure 3.20: The trajectory of the UAV with a downward looking camera. The red points are the landmarks that are observed by the camera, and the green arrows are the bearing measurements scaled according to the inverse range estimates.

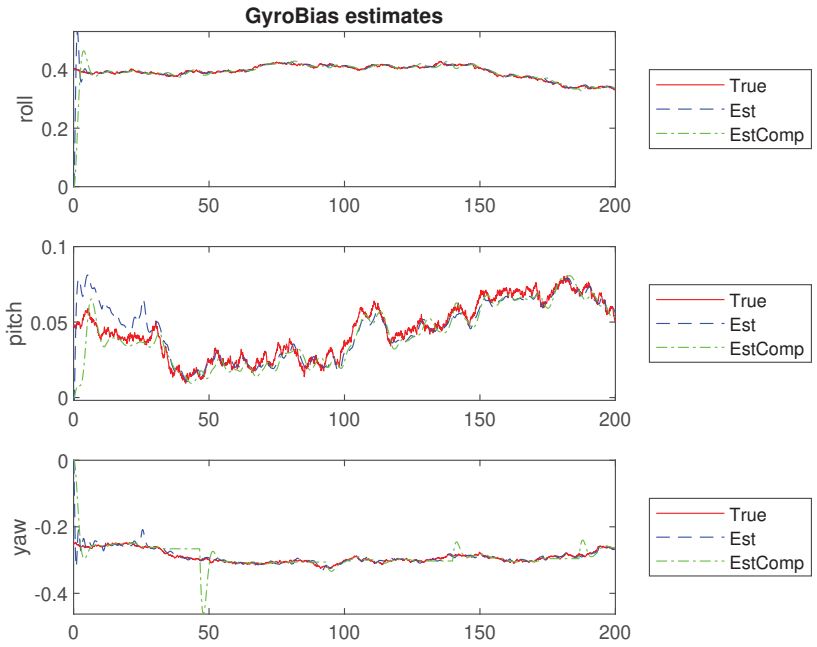

Figure 3.21: The gyro bias estimation, where the true bias is propagated acording to (3.106). The blue estimate is from the novel observer, while the green estimate is from the complimentary filter [43]

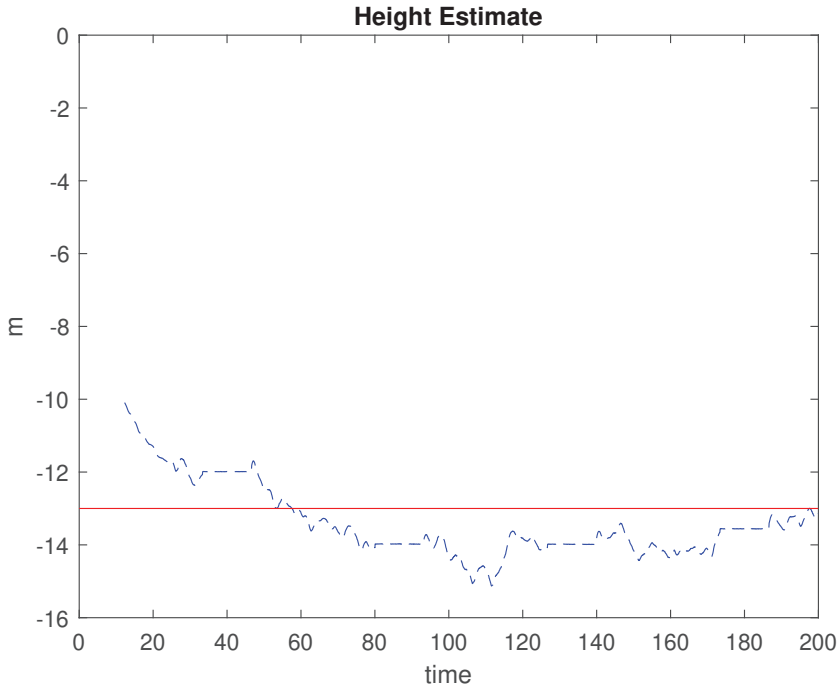

Figure 3.22: The height estimate derived from the inverse range estimates compared to the truth.

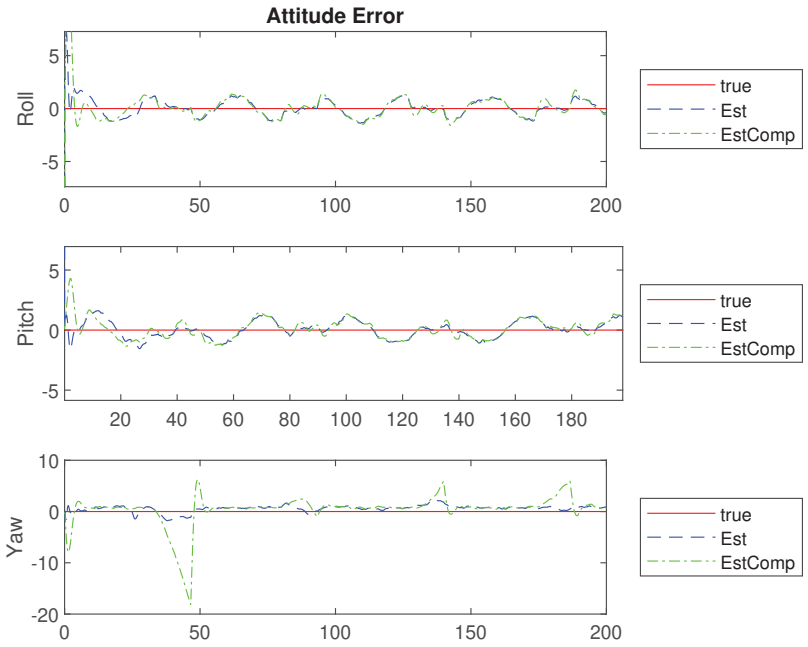

Figure 3.23: The attitude estimates with the estimates from the complimentary filter from the simulations

3.8 Experimental Verification

The experimental verification was carried out by using an octocopter flying in a circle with an autopilot for 150 seconds. The data set was recorded from a payload consisting of SenTiStack, which is built up of a SenTiBoard, a uBlox GNSS receiver and a STIM300 tactical grade IMU [2]. The SenTiBoard was also connected to the flash signal of a uEye UI-3140CP camera, time stamping the flash signal from the camera so that accurate timing of the images were available. The sensor data and images were stored using an Odroid UX4. Before the flight, a IMU, camera and temporal calibration was performed using the Kalibr toolbox [37, 36], finding IMU biases, as well as the time delay and coordinate transformation between the camera and the IMU. In the data set used in this article, the image capture time delay estimated was less than 3 ms, and as the timing of the image was related to the flash signal it was independent of the kernel load and thus assumed to be constant. As the IMU was tactical grade, the accelerometer and gyro biases were assumed constant for the duration of the experiment and respectively $\boldsymbol{b}_a = [0.03,\ 0.005,\ 0.085]^\top$ [m/s^2] and $\boldsymbol{b}_\omega = [0.007,\ -0.0002,\ 0.0017]^\top$ [rad/s]. As the object of the experiment was to verify that the observer could estimate a gyro bias, we added a synthetic gyro-bias following (3.106) and initialized with values $\check{\boldsymbol{b}}_\omega = [0.1,\ 0.4,\ -0.25]^\top$. Thus we could verify that the gyro bias estimated by the observer was equal to the synthetic one.

As the experiments were performed while flying over flat fields, homography transformation between two images were used to acquire the camera velocity needed. For more detail on how this is done see [41]. For feature extraction we used Harris Min Eigen features [98] which then were tracked with Kanade-Lucas-Tomasi feature tracker [106]. The homography matrix was found with a 4-point direct linear transformation (DLT) [1] and outlier rejection was done using RANSAC. The velocity was extracted from the homography using techniques based on [84], this provided the camera velocity $\boldsymbol{v}^c_{hom} = \frac{v^c}{h}$, which is divided by the height over the plane. The GNSS velocity was then used to scale the velocity so that the body velocity used in the observer was

$$\hat{\boldsymbol{v}}^b = \boldsymbol{\mathcal{R}}_{bc} \frac{\boldsymbol{v}^c_{hom}}{\|\boldsymbol{v}^c_{hom}\|} \|\boldsymbol{v}^n_{gnss}\| \tag{3.113}$$

where the lever arm effects were neglected. The trajectory of the filter can be seen in Figure 3.24. From the plots, it is evident that the observer is also able to converge with experimental data. The gyro bias estimate seems to work with acceptable accuracy, and the height estimate is also able to give a reasonable estimate for the octo-copter over the ground. As in the simulations there seems to be some bias in the estimates. Never the less, this shows that applying the novel observer presented together with a camera can give robust gyro bias estimation as well as a height estimate.

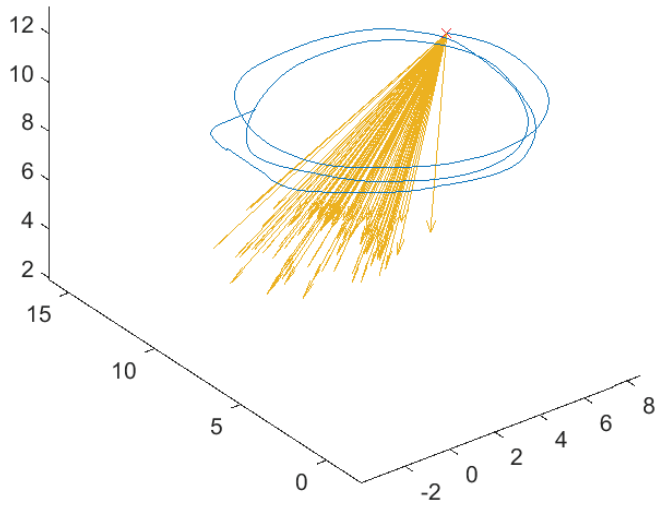

Figure 3.24: The trajectory of the UAV with a downward looking camera. The yellow arrows are the bearing measurements scaled according to the inverse range estimates.

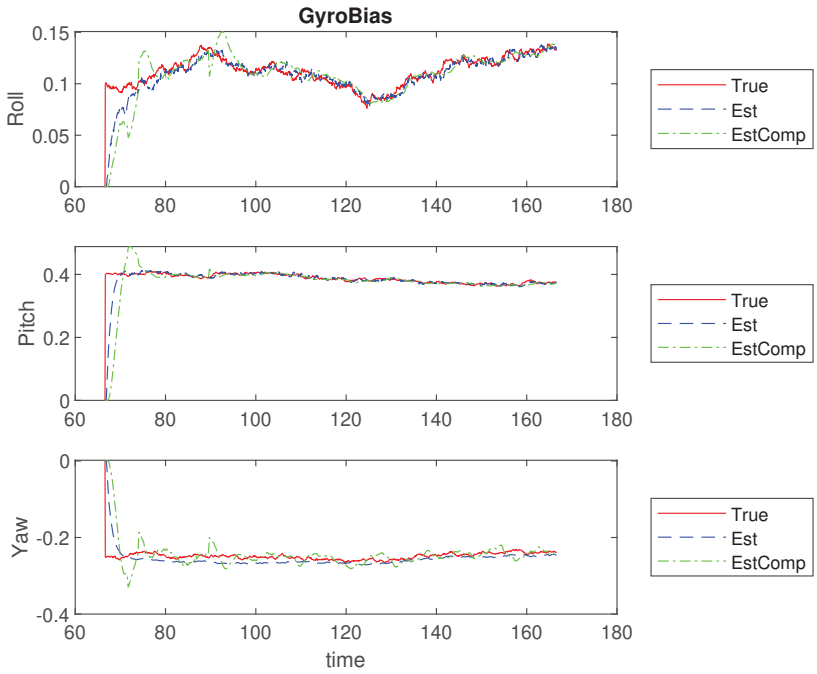

Figure 3.25: The gyro bias estimation preformed by the novel observer and complimentary filter on experimental data

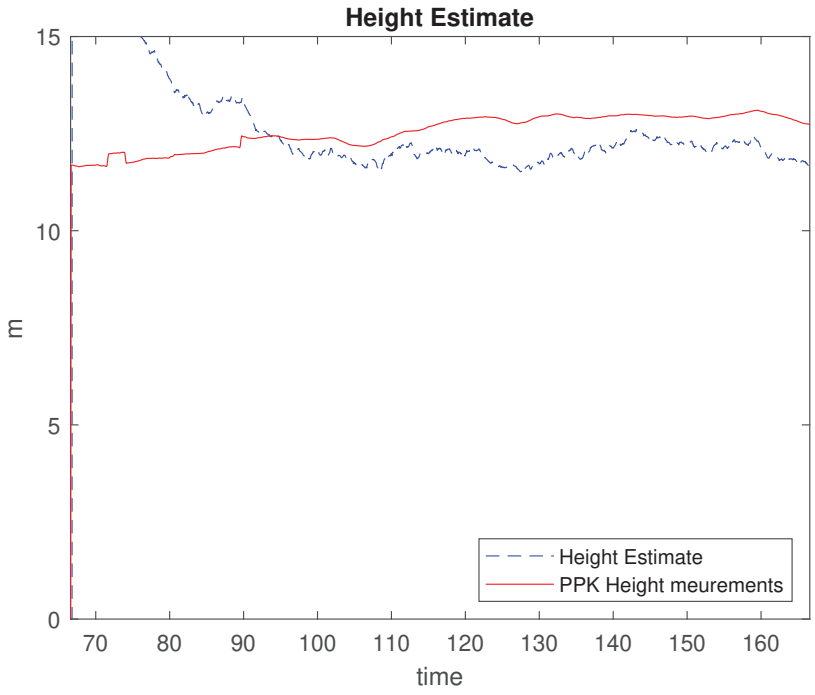

Figure 3.26: The height estimate derived from the inverted range estimates compared with the post process kinematic (PPK) height estimate

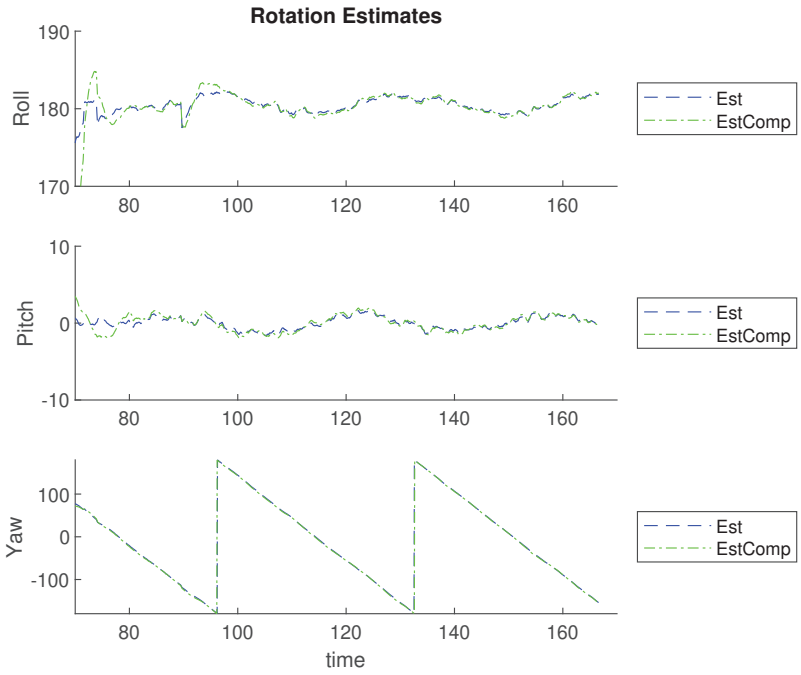

Figure 3.27: The attitude estimate of the complimentary filter vs the cascade attitude setup.

3.9 Conclusion

The article introduces a nonlinear observer that combines velocity, gyro and bearing measurements from landmarks to estimate the distance to the landmarks as well as the gyro-bias and attitude. It was proven to be semi-globally asymptotically stable and exponentially stable in the large if a persistence of excitation condition holds. The observer was demonstrated in simulations and on experimental data, where it was shown how a camera could replace a magnetometer and altimeter.

It should also be noted that if GNSS is unavailable, the body velocity could also be acquired with an altimeter or laser scanner as this could be used for scaling the camera velocity, and thus the observer could be used for more accurate and drift free position estimates, similar to what was shown in [19]. If in addition it is combined with optimization as in [79] and a loop closing system as in [90] the bearing only SLAM with semi global asymptotic stability is possible.

4 Vector Magnitude Observer

4.1 Introduction

In some estimation problems, the measurements available can be of a vector with unknown magnitude, which we then want to estimate. This is especially relevant for bearing-only localization or tracking, in which the scale from a monocular camera is ambigous without any further knowledge or sensors [51]. In other words, the direction of the velocity can be measured [93], but not the magnitude. In the simultaneous localization and mapping (SLAM) literature, there are many solutions to fusing bearing mesurments with different sensors and assumptions to find the scale, howerver, there is a lack of theoretical stability proof on many of the most popular solutions, which either use a version of extended Kalman filter (EKF)[112, 88], probability graphs [45] or particle filters [15]. These are optimization based solutions often resulting in accurate estimates, however, they are computationally demanding, and guaranteed stability can often be difficult if not impossible to acquire. This has given some motivation to attack the SLAM filter problem with nonlinear observers (NLO), as they usually have complimentary characteristics to the mentioned methods: defined stability traits with defined region of attraction, low computational cost, although lacking optimality when they handle noisy measurements[17, 79]. Other NLO approaches for the SLAM problem are presented in [41, 57, 71], where [57] and [71] assume velocity measurement or biased velocity measurement, while in [41] the authors present a NLO for fusing measurements from the homography with IMU data.

In this article we present a novel observer for estimating the magnitude of a time varying vector. We prove that if we assume a lower bound on the magnitude of the vector, and a persistently exciting vector measurement, the vector magnitude observer is uniformly semi-globally asymptotically stable (USGAS) and uniformly locally exponentially stable (ULES) and will hence estimate the magnitude of the vector. We employ the vector magnitude observer to the bearing-only SLAM problem with AHRS measurements, and this also demonstrates two instances of the vector magnitude observer working in cascade; once for velocity and once for range to landmark estimation.

The rest of the chapter is structured as follows: Section 4.2 presents the stability analysis of the observer. Section 4.3 presents how the the novel observer can be applied to the bearing-only SLAM filter problem. In Section 4.4 simulations of the presented setup is shown, and Section 4.4 concludes the work.

4.2 Vector Magnitude Observer

The main goal of the observer is to estimate the magnitude of a vector, given that its unit vector (direction) is measured together with the time derivative of the vector.

The observer using measurements in the inertial frame is

$$\dot{\hat{\boldsymbol{u}}}^n_{\delta i} = -\boldsymbol{S}(k\boldsymbol{\sigma})\hat{\boldsymbol{u}}^n_{\delta i} - \hat{d}\boldsymbol{S}(\hat{\boldsymbol{u}}^n_{\delta i})\boldsymbol{S}(\boldsymbol{u}^n_{\delta i})\boldsymbol{w}^n_x \tag{4.1}$$

$$\begin{aligned}\dot{\hat{d}} &= \mathrm{Proj}_d(-\gamma(\boldsymbol{w}^n_x)^\top \boldsymbol{S}(\boldsymbol{u}^n_{\delta i})^2\boldsymbol{S}(\hat{\boldsymbol{u}}^n_{\delta i})\boldsymbol{\sigma}) \\ &\quad + \mathrm{Proj}_d(\hat{d}^2(\boldsymbol{u}^n_{\delta i})^\top \boldsymbol{w}^n_x))\end{aligned}$$

$$\boldsymbol{\sigma} = \boldsymbol{S}(\boldsymbol{u}^n_{\delta i})\hat{\boldsymbol{u}}^n_{\delta i} \tag{4.2}$$

where $\boldsymbol{u}^n_{\delta i}$ is the unit vector measurement with corresponding estimate $\hat{\boldsymbol{u}}^n_{\delta i}$; the input $\boldsymbol{w}^n_x$ is the vector derivative; the estimate $\hat{d}$ is the estimate of the *unknown* inverted magnitude d; k and γ are positive tuning parameters. $\mathrm{Proj}_d(\bullet)$ is the projection operator from [68, Lemma E.1] working as a continuous saturation ensuring $\underline{d} < \hat{d} < \bar{d}$. All the functions and inputs are continuous in all parameters and locally Lipschitz so that a unique solution is guaranteed. We note that the estimate $\hat{\boldsymbol{u}}^n_{\delta i}$ will be maintained on the unit sphere if it starts on the unit sphere, since $(\hat{\boldsymbol{u}}^n_{\delta i})^\top \dot{\hat{\boldsymbol{u}}}^n_{\delta i} = 0$. We continue by investigating the error dynamics of the observer, defined by the error variables $\tilde{\boldsymbol{u}}^n_{\delta i} = \boldsymbol{S}(\boldsymbol{u}^n_{\delta i})\hat{\boldsymbol{u}}^n_{\delta i}$, $\tilde{d} = d - \hat{d}$

$$\dot{\tilde{\boldsymbol{u}}}^n_{\delta i} = \boldsymbol{S}(\boldsymbol{u}^n_{\delta i})\dot{\hat{\boldsymbol{u}}}^n_{\delta i} - \boldsymbol{S}(\hat{\boldsymbol{u}}^n_{\delta i})\dot{\boldsymbol{u}}^n_{\delta i} \tag{4.3}$$

$$\begin{aligned}&= \boldsymbol{S}(\boldsymbol{u}^n_{\delta i})(-\boldsymbol{S}(k\boldsymbol{\sigma})\hat{\boldsymbol{u}}^n_{\delta i} - \hat{d}\boldsymbol{S}(\hat{\boldsymbol{u}}^n_{\delta i})\boldsymbol{S}(\boldsymbol{u}^n_{\delta i})\boldsymbol{w}^n_x) \\ &\quad + d\boldsymbol{S}(\hat{\boldsymbol{u}}^n_{\delta i})\boldsymbol{S}(\boldsymbol{u}^n_{\delta i})^2\boldsymbol{w}^n_x\end{aligned} \tag{4.4}$$

$$\begin{aligned}&= k\boldsymbol{S}(\boldsymbol{u}^n_{\delta i})\boldsymbol{S}(\hat{\boldsymbol{u}}^n_{\delta i})\tilde{\boldsymbol{u}}^n_{\delta i} - \hat{d}\boldsymbol{S}(\boldsymbol{u}^n_{\delta i})\boldsymbol{S}(\hat{\boldsymbol{u}}^n_{\delta i})\boldsymbol{S}(\boldsymbol{u}^n_{\delta i})\boldsymbol{w}^n_x \\ &\quad + (\tilde{d} + \hat{d})\boldsymbol{S}(\hat{\boldsymbol{u}}^n_{\delta i})\boldsymbol{S}(\boldsymbol{u}^n_{\delta i})\boldsymbol{S}(\boldsymbol{u}^n_{\delta i})\boldsymbol{w}^n_x\end{aligned} \tag{4.5}$$

$$\begin{aligned}&= k\boldsymbol{S}(\boldsymbol{u}^n_{\delta i})\boldsymbol{S}(\hat{\boldsymbol{u}}^n_{\delta i})\tilde{\boldsymbol{u}}^n_{\delta i} + \tilde{d}\boldsymbol{S}(\hat{\boldsymbol{u}}^n_{\delta i})\boldsymbol{S}(\boldsymbol{u}^n_{\delta i})\boldsymbol{S}(\boldsymbol{u}^n_{\delta i})\boldsymbol{w}^n_x \\ &\quad + \hat{d}\boldsymbol{S}(\boldsymbol{S}(\boldsymbol{u}^n_{\delta i})\boldsymbol{w}^n_x)\tilde{\boldsymbol{u}}^n_{\delta i}\end{aligned} \tag{4.6}$$

where we note that $\boldsymbol{S}(\boldsymbol{u}^n_{\delta i})\boldsymbol{S}(\hat{\boldsymbol{u}}^n_{\delta i}) - \boldsymbol{S}(\hat{\boldsymbol{u}}^n_{\delta i})\boldsymbol{S}(\boldsymbol{u}^n_{\delta i}) = \boldsymbol{S}(\tilde{\boldsymbol{u}}^n_{\delta i})$ is utilized. We then get the following expression for the error dynamics

$$\begin{aligned}\dot{\tilde{\boldsymbol{u}}}^n_{\delta i} &= k\boldsymbol{S}(\boldsymbol{u}^n_{\delta i})\boldsymbol{S}(\hat{\boldsymbol{u}}^n_{\delta i})\tilde{\boldsymbol{u}}^n_{\delta i} + \hat{d}\boldsymbol{S}(\boldsymbol{S}(\boldsymbol{u}^n_{\delta i})\boldsymbol{w}^n_x)\tilde{\boldsymbol{u}}^n_{\delta i} \\ &\quad + \boldsymbol{S}(\hat{\boldsymbol{u}}^n_{\delta i})\boldsymbol{S}(\boldsymbol{u}^n_{\delta i})\boldsymbol{S}(\boldsymbol{u}^n_{\delta i})\boldsymbol{w}^n_x\tilde{d}\end{aligned} \tag{4.7}$$

$$\begin{aligned}\dot{\tilde{d}} &= d^2(\boldsymbol{u}^n_{\delta i})^\top \boldsymbol{w}^n_x \\ &\quad - \mathrm{Proj}_d(-\gamma(\boldsymbol{w}^n_x)^\top \boldsymbol{S}(\boldsymbol{u}^n_{\delta i})\boldsymbol{S}(\boldsymbol{u}^n_{\delta i})\boldsymbol{S}(\hat{\boldsymbol{u}}^n_{\delta i})\tilde{\boldsymbol{u}}^n_{\delta i}) \\ &\quad - \mathrm{Proj}_d(\hat{d}^2(\boldsymbol{u}^n_{\delta i})^\top \boldsymbol{w}^n_x)\end{aligned} \tag{4.8}$$

We will also use the the angle error $\tilde{\theta}$ between $\boldsymbol{u}^n_{\delta i}$ and $\hat{\boldsymbol{u}}^n_{\delta i}$, with $\|\tilde{\boldsymbol{u}}^n_{\delta i}\| = \sin(\tilde{\theta})$ and $(\boldsymbol{u}^n_{\delta i})^\top \hat{\boldsymbol{u}}^n_{\delta i} = \cos(\tilde{\theta})$.

For the guaranteed stability of the observers error dynamic, we need the unit vector derivative and the vector magnitude to be non zero, this will ensure that the system is persistently excited

Lemma 1. *Consider the function*

$$\mathcal{B}_u(t) = \mathcal{B}(t, \boldsymbol{u}_{\delta i}^n, \hat{\boldsymbol{u}}_{\delta i}^n, \boldsymbol{w}_x^n) = \boldsymbol{S}(\hat{\boldsymbol{u}}_{\delta i}^n)\boldsymbol{S}(\boldsymbol{u}_{\delta i}^n)\boldsymbol{S}(\boldsymbol{u}_{\delta i}^n)\boldsymbol{w}_x^n \tag{4.9}$$

representing the skew-symmetric part of the error dynamics (4.7)-(4.8)*. If there exist a constant* $\underline{u}$ *such that* $\|\dot{\boldsymbol{u}}_{\delta i}^n\| \geq \underline{u} > 0$ *and the magnitude of the vector satisfies* $z > \underline{z} > 0$ *and there is a small positive number* $\epsilon > 0$ *so that* $(\hat{\boldsymbol{u}}_{\delta i}^n)^\top \boldsymbol{u}_{\delta i}^n > \cos(\epsilon)$*, then there exists a* $\mu > 0$ *so that*

$$\mathcal{B}_u(t)^\top \mathcal{B}_u(t) > \mu \tag{4.10}$$

Proof. If we substitute (2.27) into (4.9), we get

$$\mathcal{B}_u(t) = z\boldsymbol{S}(\hat{\boldsymbol{u}}_{\delta i}^n)\dot{\boldsymbol{u}}_{\delta i}^n \tag{4.11}$$

We know that $\dot{\boldsymbol{u}}_{\delta i}^n$ is orthogonal to $\boldsymbol{u}_{\delta i}^n$ and will therefore not be parallel to $\hat{\boldsymbol{u}}_{\delta i}^n$. Using (2.3) we see that the norm $\|\mathcal{B}_u(t)\|$ will be bounded from below as long as $\|\dot{\boldsymbol{u}}_{\delta i}^n\|$ and z are bounded from below

$$\mathcal{B}_u(t)^\top \mathcal{B}_u(t) \geq \cos\epsilon^2 \underline{z}^2 \underline{u}^2 > \mu \tag{4.12}$$

□

More specific assumptions on the system are

A1 The vector measurement is so that the constants from Lemma 1 $\|\dot{\boldsymbol{u}}_{\delta i}^n\| \geq \underline{u}$, $z > \underline{z}(d < \bar{d})$ exists. The input derivative is also bounded from above $\|\boldsymbol{w}_x^n\| < \bar{w}$.

A2 There exist an arbitrary small angle $0 < \epsilon < \pi$, and the tuning parameters γ and k are chosen to satisfy

$$k > \max\left(\frac{\bar{d}\bar{w}}{\sin(\epsilon)}, \frac{4\bar{w}^3\bar{d}}{\cos(\epsilon)}, \frac{\bar{w}^2\bar{d}}{\mu} - \frac{\bar{\rho}_\delta}{\bar{w}}, \frac{2\bar{w}^3\bar{d}^2}{\check{d}\mu}\right) \tag{4.13}$$

$$\frac{\bar{w}^3\bar{d}}{(k\bar{w} + \bar{\rho}_\delta)^2} < \delta < \min\left(\frac{\mu}{4\bar{w}^3\bar{d}}, \frac{k\cos(\epsilon)\mu}{4(k\bar{w} + \bar{\rho}_\delta)^2}\right) \tag{4.14}$$

$$\frac{2\bar{d}\bar{w}}{\mu\delta} < \gamma < \min\left(\frac{1}{\bar{w}^2\delta^2}, \frac{2(k\bar{w} + \bar{\rho}_\delta)^2}{\bar{w}^2\mu}\right) \tag{4.15}$$

where the details of the constants δ, ϵ, $\check{d}$ and $\bar{\rho}_\delta$ are seen in the proof of Theorem 1.

Theorem 5. *Consider the vector* $\boldsymbol{x}^n$ *with the* unknown *time varying magnitude* $z = \frac{1}{d}$*. Assume its unit vector* $\boldsymbol{u}_{\delta i}^n = \frac{\boldsymbol{x}^n}{\|\boldsymbol{x}^n\|}$ *is measured together with its derivative vector* $\dot{\boldsymbol{x}}^n = \boldsymbol{w}_x^n$*, and the assumptions A1-A2 holds. Then the error dynamics of the observer* (4.1)-(4.2) *will be UAS for every initial condition satisfying* $(\hat{\boldsymbol{u}}_{\delta i}^n)^\top \boldsymbol{u}_{\delta i}^n > -\cos(\epsilon)$*,* $\hat{d} \leq \bar{d}$ *and UES for* $\underline{d} \leq \hat{d} \leq \bar{d}$ *and* $(\hat{\boldsymbol{u}}_{\delta i}^n)^\top \boldsymbol{u}_{\delta i}^n > \cos(\epsilon)$*, so that the errors* $(\hat{\boldsymbol{u}}_{\delta i}^n)^\top \boldsymbol{u}_{\delta i}^n \to 1$*,* $\tilde{\boldsymbol{u}}_{\delta i}^n = \boldsymbol{S}(\boldsymbol{u}_{\delta i}^n)\hat{\boldsymbol{u}}_{\delta i}^n \to \boldsymbol{0}$ *and* $\tilde{d} = d - \hat{d} \to 0$ *as* $t \to \infty$

The proof will be structured in the following way:

Outline of the proof

A) First prove that the the errors of the observer (4.1)-(4.2) is bounded so the angular error $\tilde{\theta}$ between $\boldsymbol{u}_{\delta i}^n$ and $\hat{\boldsymbol{u}}_{\delta i}^n$ is bounded away from $|\tilde{\theta}| < \pi - \epsilon$ and converges in finite time to the set $|\tilde{\theta}| \leq \epsilon$.

B) Define a Lyapunov function candidate and its derivative

C) Utilise the conditions and bounds from the assumptions, and prove that the Lyapunov function candidate derivative is negative definite in the set $|\tilde{\theta}| \leq \epsilon$ found in A)

D) Verify that it is maintained negative definite when projection is activated.

Proof. **A)** We know that the estimate $\hat{d}$ is bounded by the projection, and we have assumed that $d < \bar{d}$ since $z > \underline{z}$, which means the $\tilde{d}$ is also bounded. To obtain the boundedness of the error $\tilde{\theta}$ we use the Lyapunov-like function

$$V_1 = 1 - (\boldsymbol{u}_{\delta i}^n)^\top \hat{\boldsymbol{u}}_{\delta i}^n = 1 - cos(\tilde{\theta}) \tag{4.16}$$

which is positive definite for $0 < |\tilde{\theta}| < \pi$. Its derivative is

$$\begin{aligned}
\dot{V}_1 &= -(\dot{\boldsymbol{u}}_{\delta i}^n)^\top \hat{\boldsymbol{u}}_{\delta i}^n - (\boldsymbol{u}_{\delta i}^n)^\top \dot{\hat{\boldsymbol{u}}}_{\delta i}^n && (4.17)\\
&= -(d\boldsymbol{S}(\boldsymbol{u}_{\delta i}^n)^2 \boldsymbol{w}_x^n)^\top \hat{\boldsymbol{u}}_{\delta i}^n \cdots \\
&\quad - (\boldsymbol{u}_{\delta i}^n)^\top (-\boldsymbol{S}(k\boldsymbol{\sigma})\hat{\boldsymbol{u}}_{\delta i}^n + \hat{d}\boldsymbol{S}(\hat{\boldsymbol{u}}_{\delta i}^n)\boldsymbol{S}(\boldsymbol{u}_{\delta i}^n)\boldsymbol{w}_x^n) && (4.18)\\
&= (\boldsymbol{u}_{\delta i}^n)^\top \boldsymbol{S}(k\boldsymbol{\sigma})\hat{\boldsymbol{u}}_{\delta i}^n + \tilde{d}(\boldsymbol{u}_{\delta i}^n)^\top (\boldsymbol{S}(\hat{\boldsymbol{u}}_{\delta i}^n)\boldsymbol{S}(\boldsymbol{u}_{\delta i}^n)\boldsymbol{w}_x^n) && (4.19)\\
&= -k\|\tilde{\boldsymbol{u}}_{\delta i}^n\|^2 + \tilde{d}(\tilde{\boldsymbol{u}}_{\delta i}^n)^\top \boldsymbol{S}(\boldsymbol{u}_{\delta i}^n)\boldsymbol{w}_x^n && (4.20)\\
&\leq -\|\tilde{\boldsymbol{u}}_{\delta i}^n\|(k\|\tilde{\boldsymbol{u}}_{\delta i}^n\| - \bar{d}\bar{w}) && (4.21)
\end{aligned}$$

We know that $\tilde{\theta} = \pi - \epsilon$ corresponds to an error $\|\tilde{\boldsymbol{u}}_{\delta i}^n\| = \sin(\epsilon)$. So for any arbitary small $\epsilon > 0$ there exists $\underline{k} > \frac{\bar{d}\bar{w}}{\sin(\epsilon)}$ so that any $k \geq \underline{k}$ will ensure that $\dot{V}_1 < 0$; hence we can conclude that the error is bounded away from $\tilde{\theta} = \pm\pi$ and that the unit vector estimate will converge to the set $|\tilde{\theta}| \leq \epsilon$ in finite time [64, Theorem 3.18]. From here we will use that this bound holds, which implies that $\|\tilde{\boldsymbol{u}}_{\delta i}^n\| < 1 \Leftrightarrow |\tilde{\theta}| < \frac{\pi}{2}$, and $\|\tilde{\boldsymbol{u}}_{\delta i}^n\| = 0 \Leftrightarrow |\tilde{\theta}| = 0$. We will then show that the system is UES when $|\tilde{\theta}| \leq \epsilon$.
B) We choose the Lyapunov function candidate

$$V_2(t, \tilde{\boldsymbol{u}}_{\delta i}^n, \tilde{d}) = \frac{1}{2}(\tilde{\boldsymbol{u}}_{\delta i}^n)^\top (\tilde{\boldsymbol{u}}_{\delta i}^n) + \frac{1}{2\gamma}\tilde{d}^2 - \delta(\tilde{\boldsymbol{u}}_{\delta i}^n)^\top \mathcal{B}_u(t)\tilde{d} \tag{4.22}$$

with $\delta > 0$. To ensure that the Lyapunov function candidate is positive definite, we impose the constraint $\delta^2 < \frac{1}{\gamma\bar{w}^2}$ since we know that $\bar{w} \geq \|\mathcal{B}_u(t)\|$ by Assumption

A1. If we then take the time-derivative along the trajectory of the error dynamics (4.7)-(4.8) we get

$$\begin{aligned}\dot{V}_2 = \; & (\tilde{\boldsymbol{u}}^n_{\delta i})^\top (k\boldsymbol{S}(\boldsymbol{u}^n_{\delta i})\boldsymbol{S}(\hat{\boldsymbol{u}}^n_{\delta i})\tilde{\boldsymbol{u}}^n_{\delta i} + \hat{d}\boldsymbol{S}(\boldsymbol{S}(\boldsymbol{u}^n_{\delta i})\boldsymbol{w}^n_x)\tilde{\boldsymbol{u}}^n_{\delta i}) \\ & + (\tilde{\boldsymbol{u}}^n_{\delta i})^\top \mathcal{B}_u(t)\tilde{d} + \frac{1}{\gamma}\tilde{d}d^2(\boldsymbol{u}^n_{\delta i})^\top \boldsymbol{w}^n_x \\ & - \frac{1}{\gamma}\tilde{d}\text{Proj}_d(\hat{d}^2(\boldsymbol{u}^n_{\delta i})^\top \boldsymbol{w}^n_x) - \frac{1}{\gamma}\tilde{d}\text{Proj}_d(\gamma\mathcal{B}_u(t)^\top \tilde{\boldsymbol{u}}^n_{\delta i})) \\ & - \delta\tilde{\boldsymbol{u}}^n_{\delta i}\dot{\mathcal{B}}_u(t)\tilde{d} - \delta\tilde{d}\mathcal{B}_u(t)^\top\mathcal{B}_u(t)\tilde{d} \\ & + \delta\hat{d}(\tilde{\boldsymbol{u}}^n_{\delta i})^\top \boldsymbol{S}(\boldsymbol{S}(\boldsymbol{u}^n_{\delta i})\boldsymbol{w}^n_x)\mathcal{B}_u(t)\tilde{d} \\ & + \delta k((\boldsymbol{u}^n_{\delta i})^\top \hat{\boldsymbol{u}}^n_{\delta i})(\tilde{\boldsymbol{u}}^n_{\delta i})^\top \mathcal{B}_u(t)\tilde{d} \\ & - \delta(\tilde{\boldsymbol{u}}^n_{\delta i})^\top \mathcal{B}_u(t)d^2(\boldsymbol{u}^n_{\delta i})^\top \boldsymbol{w}^n_x \\ & + \delta(\tilde{\boldsymbol{u}}^n_{\delta i})^\top \mathcal{B}_u(t)(\text{Proj}_d(\hat{d}^2(\boldsymbol{u}^n_{\delta i})^\top \boldsymbol{w}^n_x) + \text{Proj}_d(\gamma\mathcal{B}_u(t)^\top \tilde{\boldsymbol{u}}^n_{\delta i}))\end{aligned} \tag{4.23}$$

where we use the vector product to get $\boldsymbol{S}(\boldsymbol{u}^n_{\delta i})\boldsymbol{S}(\hat{\boldsymbol{u}}^n_{\delta i})\tilde{\boldsymbol{u}}^n_{\delta i} = -((\boldsymbol{u}^n_{\delta i})^\top \hat{\boldsymbol{u}}^n_{\delta i})\tilde{\boldsymbol{u}}^n_{\delta i}$, **C)**

First we assume that projection is not being activated. We use the bounds in the assumption A1, where there exists positive constants $\bar{\rho}_2 = \bar{w}$, $\bar{\rho}_4 = 2\bar{d}\bar{w}$ and $\bar{\rho}_5 = \bar{d}\bar{w}$. From the Lipschitz property a constant $\bar{b}_d > \|\dot{\mathcal{B}}_u(t)\|$ exist, and from the boundedness from paragraph A) there is a maximum angle ϵ between $\boldsymbol{u}^n_{\delta i}$ and $\hat{\boldsymbol{u}}^n_{\delta i}$ so that $k_\epsilon = k\cos(\epsilon) < k(\hat{\boldsymbol{u}}^n_{\delta i})^\top \boldsymbol{u}^n_{\delta i}$. In addition, the ϵ combined with the assumptions in A1 guarantee that Lemma 1 will hold, hence we can use (4.10). With these bounds we can rearrange $\dot{V}_2$ to the inequality

$$\begin{aligned}\dot{V}_2 \leq \; & -k_\epsilon\|\tilde{\boldsymbol{u}}^n_{\delta i}\|^2 + \delta\gamma\bar{\rho}_2^2\|\tilde{\boldsymbol{u}}^n_{\delta i}\|^2 - \delta\mu\tilde{d}^2 + \frac{1}{\gamma}\tilde{d}^2\bar{\rho}_4 \\ & + \delta\bar{b}_d\|\tilde{\boldsymbol{u}}^n_{\delta i}\|\tilde{d} + \delta\|\tilde{\boldsymbol{u}}^n_{\delta i}\|\tilde{d}\bar{\rho}_2(\bar{\rho}_4 + \bar{\rho}_5) \\ & (-k(\boldsymbol{u}^n_{\delta i})^\top \hat{\boldsymbol{u}}^n_{\delta i} + (\frac{1}{2} - \frac{1}{2})(\min(k_\epsilon, \delta\mu\gamma))\delta(\tilde{\boldsymbol{u}}^n_{\delta i})^\top \mathcal{B}_u(t)\tilde{d}\end{aligned}$$

where the last zero term is added to easier see the exponential result, and by using $k > k(\boldsymbol{u}^n_{\delta i})^\top \hat{\boldsymbol{u}}^n_{\delta i} - \frac{1}{2}\min(k_\epsilon, \delta\mu\gamma)$, the inequality can be reorganized to

$$\begin{aligned}\dot{V}_2 < & -\|\tilde{\boldsymbol{u}}^n_{\delta i}\|^2\frac{k_\epsilon}{4} - \tilde{d}^2\frac{\delta\mu}{4} \\ & + \frac{1}{2}\min(k_\epsilon, \delta\mu\gamma)\delta(\tilde{\boldsymbol{u}}^n_{\delta i})^\top \mathcal{B}_u(t)\tilde{d} \\ & - \|\tilde{\boldsymbol{u}}^n_{\delta i}\|^2(\frac{k_\epsilon}{2} - \delta\gamma\bar{\rho}_2^2) - \tilde{d}^2(\frac{\delta\mu}{2} - \frac{\bar{\rho}_4}{\gamma})\end{aligned} \tag{4.24}$$

$$-\frac{1}{2}\begin{bmatrix}\|\tilde{\boldsymbol{u}}^n_{\delta i}\| \\ \tilde{d}\end{bmatrix}^\top \begin{bmatrix}\frac{k_\epsilon}{2} & -\delta(k\bar{\rho}_2 + \bar{\rho}_\delta) \\ -\delta(k\bar{\rho}_2 + \bar{\rho}_\delta) & \frac{\delta\mu}{2}\end{bmatrix}\begin{bmatrix}\|\tilde{\boldsymbol{u}}^n_{\delta i}\| \\ \tilde{d}\end{bmatrix} \tag{4.25}$$

where $\bar{\rho}_\delta = \bar{b}_d + \bar{\rho}_2(\bar{\rho}_4 + \bar{\rho}_5)$. We see that we need the variables and tuning parameters to satisfy the following inequalities,

$$k > \max(\frac{\bar{d}\bar{w}}{\sin(\epsilon)}, \frac{2\delta\gamma\bar{\rho}_2^2}{\cos(\epsilon)}) \tag{4.26}$$

$$\delta^2 < \frac{1}{\gamma\bar{\rho}_2^2}, \frac{2\bar{\rho}_4}{\gamma\mu} < \delta < \frac{k\cos(\epsilon)\mu}{4(k\bar{\rho}_2 + \bar{\rho}_\delta)^2} \tag{4.27}$$

to ensure that $\dot{V}_2 \leq -\frac{1}{2}\min(k_\epsilon, \delta\mu\gamma)V_2$. We can reorganize the inequaleties

$$k > \max(\frac{\bar{d}\bar{w}}{\sin(\epsilon)}, \frac{2\bar{\rho}_2^2\bar{\rho}_4}{\mu\cos(\epsilon)}, \frac{\bar{\rho}_2\bar{\rho}_4}{\mu} - \frac{\bar{\rho}_\delta}{\bar{\rho}_2}) \tag{4.28}$$

$$\frac{2\bar{\rho}_2^2\bar{\rho}_4}{4(k\bar{\rho}_2 + \bar{\rho}_\delta)^2} < \delta < \min(\frac{k\cos(\epsilon)\mu}{4(k\bar{\rho}_2 + \bar{\rho}_\delta)^2}, \frac{\mu}{2\bar{\rho}_2^2\bar{\rho}_4}) \tag{4.29}$$

$$\frac{2\bar{\rho}_4}{\mu\delta} < \gamma < \min(\frac{1}{\delta^2\bar{\rho}_2^2}, \frac{2(k\bar{\rho}_2 + \bar{\rho}_\delta)^2}{\mu\bar{\rho}_2^2}) \tag{4.30}$$

by substituting the $\bar{\rho}_\bullet$ with their corresponding bounds, we see that this will hold by assumption A2. Hence, we can conclude that δ and γ can be choosen if k is high enough so that the system is uniformly exponentially stable when the projection is not activated, and it will have converges rate of $\frac{1}{2}\min(k_\epsilon, \delta\mu\gamma)$. **D)** There are four projections in (4.23). By using

$$-\boldsymbol{y}^\top\boldsymbol{\Gamma}^{-1}\text{Proj}_y(\tau) \leq -\boldsymbol{y}^\top\boldsymbol{\Gamma}^{-1}(\tau)$$
$$\|\text{Proj}_y(\tau)\| < \|\tau\|$$

from [68, E.1], three of the terms can be handled trivially.

$$-\frac{1}{\gamma}\tilde{d}\text{Proj}_d(\hat{d}^2(\boldsymbol{u}_{\delta i}^n)^\top\boldsymbol{w}_x^n) < -\frac{1}{\gamma}\tilde{d}\hat{d}^2(\boldsymbol{u}_{\delta i}^n)^\top\boldsymbol{w}_x^n \tag{4.31}$$

$$-\frac{1}{\gamma}\tilde{d}\text{Proj}_d(\gamma\mathcal{B}_u(t)^\top\tilde{\boldsymbol{u}}_{\delta i}^n)) < -\frac{1}{\gamma}\tilde{d}\gamma\mathcal{B}_u(t)^\top\tilde{\boldsymbol{u}}_{\delta i}^n \tag{4.32}$$

$$\|\delta(\tilde{\boldsymbol{u}}_{\delta i}^n)^\top\mathcal{B}_u(t)\text{Proj}_d(\gamma\mathcal{B}_u(t)^\top\tilde{\boldsymbol{u}}_{\delta i}^n)\| < \tag{4.33}$$

$$\|\delta(\tilde{\boldsymbol{u}}_{\delta i}^n)^\top\mathcal{B}_u(t)\gamma\mathcal{B}_u(t)^\top\tilde{\boldsymbol{u}}_{\delta i}^n\| \tag{4.34}$$

Which gives the same inequality terms as in (4.25). The fourth projection term is

$$\delta(\tilde{\boldsymbol{u}}_{\delta i}^n)^\top\mathcal{B}_u(t)\text{Proj}_d(\hat{d}^2(\boldsymbol{u}_{\delta i}^n)^\top\boldsymbol{w}_x^n) \tag{4.35}$$

which cancels out term

$$-\delta(\tilde{\boldsymbol{u}}_{\delta i}^n)^\top\mathcal{B}_u(t)d^2(\boldsymbol{u}_{\delta i}^n)^\top\boldsymbol{w}_x^n \tag{4.36}$$

when the projection is not activated; utilizing $(d^2 - \hat{d}^2) < 2\tilde{d}\bar{d}$. When the projection (4.35) is activated, the projection term becomes zero, meaning that another term is needed to handle (4.36). However, since the projection (4.35) is activated, it implies that $\tilde{d}\hat{d}^2(\boldsymbol{u}_{\delta i}^n)^\top \boldsymbol{w}_x^n < 0 \Leftrightarrow \frac{1}{\gamma}\tilde{d}d^2(\boldsymbol{u}_{\delta i}^n)^\top \boldsymbol{w}_x^n < 0$, which is available as the projection counter part (4.31) is zero, since it is also activated. This term can therefore be used against (4.36), meaning that if the inequality

$$\|\frac{1}{\gamma}\tilde{d}\hat{d}^2(\boldsymbol{u}_{\delta i}^n)^\top \boldsymbol{w}_x^n\| > \|\delta(\tilde{\boldsymbol{u}}_{\delta i}^n)^\top \mathcal{B}_u(t)d^2(\boldsymbol{u}_{\delta i}^n)^\top \boldsymbol{w}_x^n\| \tag{4.37}$$

holds, inequality (4.25) will also hold when the projection is activated. By utilizing that the $\tilde{d}$ is non zero as the projection is activated, and the bound $\tilde{\boldsymbol{u}}_{\delta i}^n < \sin(\epsilon)$ we see that this inequality is equivalent to

$$\sin(\epsilon) < \frac{|\tilde{d}|}{\gamma\delta\bar{\rho}_2} \Rightarrow k > \frac{2\bar{w}^3\bar{d}^2}{\check{d}\mu} \tag{4.38}$$

where $\check{d}$ is the minimum error $|\tilde{d}|$ can be while the projection is activated. Thus we see that the derivative of the Lyapunov function candidate is maintained negative definite while the projection is activated. Proving that the observer converges to zero exponentially fast when $|\tilde{\theta}| \leq \epsilon$. In addition, we proved in A) that the error will converge to this set $|\tilde{\theta}| \leq \epsilon$ in finite time, so combining these results the observer is UAS for the error dynamics for all initial conditions according to Theorem 1, and and UES when $|\tilde{\theta}| \leq \epsilon$. □

From the proof we see that the region of attraction for the observer is determined by a parameter ϵ, which can be arbitrary small while increasing k, so the stability is in practice semi-global on the sphere. From the proof we also see that the exponential convergence rate is $\frac{1}{2}\min(k_\epsilon, \delta\mu\gamma)$, although as can be seen in the proof it is a conservative estimate. We also note that the larger the k is, the smaller δ will be, so k should be set large enough, however, if the k is too large, this can limit the convergence of the $\tilde{d}$. The observer is also be presented in body coordinates, where the difference is the added rotation of the vehicle

$$\dot{\hat{\boldsymbol{u}}}_{\delta i}^b = -\boldsymbol{S}(\boldsymbol{\omega} + k\boldsymbol{\sigma})\hat{\boldsymbol{u}}_{\delta i}^b - \hat{d}\boldsymbol{S}(\hat{\boldsymbol{u}}_{\delta i}^b)\boldsymbol{S}(\boldsymbol{u}_{\delta i}^b)\boldsymbol{w}_x^b \tag{4.39}$$

$$\begin{aligned}\dot{\hat{d}} &= \text{Proj}_d(-\gamma(\boldsymbol{w}_x^b)^\top \boldsymbol{S}(\boldsymbol{u}_{\delta i}^b)^2\boldsymbol{S}(\hat{\boldsymbol{u}}_{\delta i}^b)\boldsymbol{\sigma}) \\ &\quad + \text{Proj}_d(\hat{d}^2(\boldsymbol{u}_{\delta i}^b)^\top \boldsymbol{w}_x^b)\end{aligned}$$

$$\boldsymbol{\sigma} = \boldsymbol{S}(\boldsymbol{u}_{\delta i}^b)\hat{\boldsymbol{u}}_{\delta i}^b \tag{4.40}$$

Theorem 6. *Consider the vector $\boldsymbol{x}^b$ with the* unknown *time varying magnitude $z = \frac{1}{d}$. If the assumptions A1-A2 holds in addition to the angular rate being bounded $\|\boldsymbol{\omega}\| < \bar{\omega}$. Then given the unit vector $\boldsymbol{u}_{\delta i}^b$ and the derivative $\boldsymbol{w}_x^b = \boldsymbol{\mathcal{R}}_{nb}\boldsymbol{w}_x^n = \boldsymbol{\mathcal{R}}_{nb}\dot{\boldsymbol{x}}^n$, the error dynamics of the observer* (4.39)-(4.40) *will be UAS for every initial condition satisfying $(\hat{\boldsymbol{u}}_{\delta i}^b)^\top \boldsymbol{u}_{\delta i}^b > -\cos(\epsilon)$, $\hat{d} \leq \bar{d}$ and UES for $\underline{d} < \hat{d} < \bar{d}$ and $(\hat{\boldsymbol{u}}_{\delta i}^b)^\top \boldsymbol{u}_{\delta i}^b > \cos(\epsilon)$, so that the errors $(\hat{\boldsymbol{u}}_{\delta i}^b)^\top \boldsymbol{u}_{\delta i}^b \to 1$, $\tilde{\boldsymbol{u}}_{\delta i}^b = \boldsymbol{S}(\boldsymbol{u}_{\delta i}^b)\hat{\boldsymbol{u}}_{\delta i}^b \to \boldsymbol{0}$ and $\tilde{d} = d - \hat{d} \to 0$ as $t \to \infty$*

Proof. Bounded error dynamics follows from

$$\dot{V}_1^b =\leq \|\tilde{\boldsymbol{u}}_{\delta i}^b\|(k\|\tilde{\boldsymbol{u}}_{\delta i}^b\| - \bar{d}\boldsymbol{w} + \bar{\omega}) \tag{4.41}$$

The error dynamics are now

$$\begin{aligned}\dot{\tilde{\boldsymbol{u}}}_{\delta i}^b &= k\boldsymbol{S}(\boldsymbol{u}_{\delta i}^b)\boldsymbol{S}(\hat{\boldsymbol{u}}_{\delta i}^b)\tilde{\boldsymbol{u}}_{\delta i}^b - \hat{d}\boldsymbol{S}(\boldsymbol{S}(\boldsymbol{u}_{\delta i}^b)\boldsymbol{w}_x^b)\tilde{\boldsymbol{u}}_{\delta i}^b \\ &\quad - \boldsymbol{S}(\hat{\boldsymbol{u}}_{\delta i}^b)\boldsymbol{S}(\boldsymbol{u}_{\delta i}^b)\boldsymbol{S}(\boldsymbol{u}_{\delta i}^b)\boldsymbol{w}_x^b\tilde{d} + \boldsymbol{S}(\boldsymbol{\omega})\tilde{\boldsymbol{u}}_{\delta i}^b \end{aligned} \tag{4.42}$$

$$\dot{\tilde{d}} = d^2(\boldsymbol{u}_{\delta i}^b)^\top \boldsymbol{w}_x^b \tag{4.43}$$

$$- \text{Proj}_d(-\gamma(\boldsymbol{w}_x^b)^\top \boldsymbol{S}(\boldsymbol{u}_{\delta i}^b)\boldsymbol{S}(\boldsymbol{u}_{\delta i}^b)\boldsymbol{S}(\hat{\boldsymbol{u}}_{\delta i}^b)\tilde{\boldsymbol{u}}_{\delta i}^b) \tag{4.44}$$

$$- \text{Proj}_d(\hat{d}^2(\boldsymbol{u}_{\delta i}^b)^\top \boldsymbol{w}_x^b)$$

where we see that the difference in error dynamic is the additional skew-symmetric term $\boldsymbol{S}(\boldsymbol{\omega})\tilde{\boldsymbol{u}}_{\delta i}^b$. We also note that the skew-symmetric part between $\tilde{\boldsymbol{u}}_{\delta i}^b$ and $\tilde{d}$ is equal to the one from Lemma 1, only that it is in body coordinates, and we know that the norm is preserved by coordinate change, implying that Lemma 1 also applies for the magnitude observer in body coordinates. The only difference of the derivative of V_2^b along this trajectory will be the constant $\bar{\rho}_5 > \boldsymbol{w}\bar{d} + \bar{\omega}$. So similar stability as in Theorem 1 can be concluded for the system (4.39)-(4.40), with straight forward change to the proof. □

Cascade

The next result shows that two instances of the observer can be used in cascade, this means that the output of one observer can be the input of the next observer. One motivation for this can be seen in bearing only SLAM. The first observer is then used to estimate the velocity vector; this vector can then be considered the input of a second observer used for estimating the distance to a landmark.

Theorem 7. *Consider two vectors $\boldsymbol{x}_1$ and $\boldsymbol{x}_2$, with corresponding derivatives $\boldsymbol{w}_{x1}$ and $\boldsymbol{w}_{x2}$. Assume directional vectors $\boldsymbol{u}_{x1}$, $\boldsymbol{u}_{x2}$ and the derivative $\boldsymbol{w}_{x1}$ are measured, and the first directional vector $\boldsymbol{u}_{x1} = \frac{\boldsymbol{w}_{x2}}{\|\boldsymbol{w}_{x2}\|}$. Let two observers either according to Theorem 1 or Theorem 2 be in cascade, where the second observer has the input $\hat{\boldsymbol{w}}_{x2} = \frac{\hat{\boldsymbol{u}}_{x1}}{\hat{d}_1}$. We assume assumptions A1-A2 to be true for both observer, in addition, the gain k in the second observer is chosen large enough, and $\hat{d}_1 > \underline{d}_1$ is bounded from below by the projection in the first observer. Then the error dynamics of the whole system will be UAS for every initial condition satisfying $(\hat{\boldsymbol{u}}_{xi})^\top \boldsymbol{u}_{xi} > -\cos(\epsilon)$ and $\hat{d}_i < \bar{d}_i$ for both observers $i \in \{1, 2\}$.*

Proof. From cascade theory [76, 23] we know that two sub-systems in cascade being USGAS combined with whole system being bounded implies the whole system being USGAS. What is crucial is to show that regardless of the error from the first observer in cascade, the error in the second observer has the states bounded in the

region of attraction, and will not be destabilized. From Theorem 1 or 2 we know that the first observer in the cascade will output an estimate with bounded errors

$$\tilde{\boldsymbol{w}}_{x2} = \boldsymbol{w}_{x2} - \hat{\boldsymbol{w}}_{x2} \tag{4.45}$$

with the bound $|\tilde{\boldsymbol{w}}_{x2}| \leq \bar{w} \leq \frac{1}{\underline{d}_1}$. We continue by investigating if the second observer in the cascade is still bounded when exposed to this error. For this proof we investigate the boundedness of the observer in Theorem 1, although similar procedure can be done for an observer in Theorem 2, with similar results. We already know that the inverse magnitude estimate $\hat{d}_2 < \bar{d}_2$ and its error $\tilde{d}_2 < \bar{d}_2$ is bounded by the projection operator. We re-examine the Lyapunov-like function $V_1 = 1 - (\boldsymbol{u}^n_{\delta i})^\top \hat{\boldsymbol{u}}^n_{\delta i}$ which will have the derivative

$$\begin{aligned}
\dot{V}_1 &= -(\dot{\boldsymbol{u}}^n_{\delta i})^\top \hat{\boldsymbol{u}}^n_{\delta i} - (\boldsymbol{u}^n_{\delta i})^\top \dot{\hat{\boldsymbol{u}}}^n_{\delta i} \\
&= -(d\boldsymbol{S}(\boldsymbol{u}^n_{\delta i})^2 \boldsymbol{w}^n_x)^\top \hat{\boldsymbol{u}}^n_{\delta i} \cdots \\
&\quad -(\boldsymbol{u}^n_{\delta i})^\top(-\boldsymbol{S}(k\boldsymbol{\sigma})\hat{\boldsymbol{u}}^n_{\delta i} + \hat{d}\boldsymbol{S}(\hat{\boldsymbol{u}}^n_{\delta i})\boldsymbol{S}(\boldsymbol{u}^n_{\delta i})\hat{\boldsymbol{w}}^n_x)
\end{aligned}$$

$$\begin{aligned}
&= (\boldsymbol{u}^n_{\delta i})^\top \boldsymbol{S}(k\boldsymbol{\sigma})\hat{\boldsymbol{u}}^n_{\delta i} + (\boldsymbol{u}^n_{\delta i})^\top \boldsymbol{S}(\hat{\boldsymbol{u}}^n_{\delta i})\boldsymbol{S}(\boldsymbol{u}^n_{\delta i})(d\boldsymbol{w}^n_x - \hat{d}\hat{\boldsymbol{w}}^n_x) \\
&= -k\|\tilde{\boldsymbol{u}}^n_{\delta i}\|^2 + (\tilde{\boldsymbol{u}}^n_{\delta i})^\top \boldsymbol{S}(\boldsymbol{u}^n_{\delta i})(\tilde{\boldsymbol{w}}^n_x \tilde{d} + \tilde{\boldsymbol{w}}^n_x \hat{d} + \hat{\boldsymbol{w}}^n_x \hat{d}) \\
&\leq -\|\tilde{\boldsymbol{u}}^n_{\delta i}\|(k\|\tilde{\boldsymbol{u}}^n_{\delta i}\| - 3\bar{d}\bar{w})
\end{aligned}$$

and with the same argument as from Theorem 1 we can choose a k so that the unit vector estimates are bounded away from $|\tilde{\theta}| < \pi - \epsilon$, and the ϵ can be chosen arbitrary small by increasing k. The estimates are maintained in the region of attraction of the observer, resulting in the observer error $\tilde{\boldsymbol{u}}^n_2 \to \boldsymbol{0}$ and $\tilde{d}_2 \to 0$ as the error $\tilde{\boldsymbol{w}}_{x2} \to \boldsymbol{0}$ converges to zero. □

Usually in cascade stabillity, a growth condition [76, 23] is introduced to show that the error from a previous system in a cascade will not push the following system out of its region of attraction. For our system this growth condition is not satisfied for the $\tilde{d}$, but due to the projection on this parameter, the observer will not be destabalized. As for the previous results, since ϵ can be chosen arbitrary small we call this USGAS. However, the *peaking phenomenon* should be in mind [105] [76] when tuning the observer in cascade, meaning the second part should be tuned modestly to avoid unnecessary transient error for the second observer.

4.3 Example: bearing-only SLAM

To illustrate how the vector magnitude observer may be used, we apply it to the bearing-only SLAM problem. For an overview of the SLAM problem, the readers are refered to [28, 6] and references therein. For our SLAM problem, we

want to estimate the ranges $\varrho_i = \|\boldsymbol{\delta}_i\|$ from the vehicle to different landmarks, where $\boldsymbol{\delta}_i$ are the relative position vectors from the vehicle pose to the different landmarks. We assume that we have line of sight (LOS) measurements $\boldsymbol{u}^b_{i\delta} = \frac{\boldsymbol{\delta}^b_i}{\|\boldsymbol{\delta}^b_i\|}$ from these landmarks, in addition, we assume that measurements from an IMU and an attitude heading reference system (AHRS)[43] is available. The AHRS can potentially also estimate the gyro bias, and be viewed as a cascade into the vector magnitude observer, although the setup we present for velocity estimation will be sensitive to attitude error, hence the attitude error should be small. We see that if the LOS measurements are rotated in the earth-fixed frame

$$\boldsymbol{u}^n_{i\delta} = \boldsymbol{\mathcal{R}}_{nb}\boldsymbol{u}^b_{i\delta} \tag{4.46}$$

the derivative of the corresponding relative position vectors is the velocity in the inertial-frame

$$\dot{\boldsymbol{\delta}}^n = -\boldsymbol{v}^n \tag{4.47}$$

which raises the need of a velocity estimate to use the vector magnitude observer to estimate the different ranges.

We assume that we can measure the normalized velocity $\boldsymbol{u}^b_v = \frac{\boldsymbol{v}^b}{\|\boldsymbol{v}^b\|}$; this being for instance available from a camera using methods from optical flow or using homography [41], essential matrix [93] or visual odometry [33]. To estimate the magnitude $\|\boldsymbol{v}^n\|$, we noticing that we can rotate the vector into the inertial-frame $\boldsymbol{u}^n_v = \boldsymbol{\mathcal{R}}_{nb}\boldsymbol{u}^b_v$. In addition, the derivative of the velocity in the inertial-frame is available through the IMU and AHRS

$$\dot{\boldsymbol{v}}^n = \boldsymbol{\mathcal{R}}_{nb}\boldsymbol{f}^b_{IMU} - \boldsymbol{g}^n \tag{4.48}$$

where $\boldsymbol{f}^b_{IMU}$ is the specific force measurements from the IMU, and $\boldsymbol{g}^n$ is the known gravity vector in inertia frame. Meaning the observer can estimate the velocity. The observer is summarized in the following equations

$$\begin{aligned}
&\boldsymbol{u}^n_v = \boldsymbol{\mathcal{R}}_{nb}\frac{\boldsymbol{v}^b}{\|\boldsymbol{v}^b\|}, \quad \boldsymbol{w}^n_v = \boldsymbol{\mathcal{R}}_{nb}\boldsymbol{f}^b_{IMU} - \boldsymbol{g}^n, \quad d_v = \frac{1}{\boldsymbol{v}^n} \\
&\dot{\hat{\boldsymbol{u}}}^n_v = -S(k_v\boldsymbol{\sigma}_v)\hat{\boldsymbol{u}}^n_v + \hat{d}_v\boldsymbol{S}(\hat{\boldsymbol{u}}^n_v)\boldsymbol{S}(\boldsymbol{u}^n_v)\boldsymbol{w}^n_v \\
&\dot{\hat{d}}_v = \gamma(\boldsymbol{w}^n_v)^\top\boldsymbol{S}(\boldsymbol{u}^n_v)^2\boldsymbol{S}(\hat{\boldsymbol{u}}^n_v)\boldsymbol{\sigma}_v + \hat{d}^2_v(\boldsymbol{u}^n_v)^\top\boldsymbol{w}^n_v \\
&\boldsymbol{\sigma}_v = \boldsymbol{S}(\boldsymbol{u}^n_v)\hat{\boldsymbol{u}}^n_v, \quad \hat{\boldsymbol{v}}^n = \frac{\hat{\boldsymbol{u}}^n_v}{\hat{d}_v}
\end{aligned} \tag{4.49}$$

where we for each landmark with index i have

$$\begin{aligned}
\boldsymbol{u}_{\delta i}^n &= \boldsymbol{\mathcal{R}}_{nb}\boldsymbol{u}_{i\delta}^b, \quad \hat{\boldsymbol{w}}_\delta^n = -\frac{\hat{\boldsymbol{u}}_v^n}{\hat{d}_v}, \quad d_{\delta i} = \frac{1}{\varrho_i} \\
\dot{\hat{\boldsymbol{u}}}_{\delta i}^n &= -S(k_{\delta i}\boldsymbol{\sigma}_{\delta i})\hat{\boldsymbol{u}}_{\delta i}^n + \hat{d}_{\delta i}\boldsymbol{S}(\hat{\boldsymbol{u}}_{\delta i}^n)\boldsymbol{S}(\boldsymbol{u}_{\delta i}^n)\hat{\boldsymbol{w}}_\delta^n \\
\dot{\hat{d}}_{\delta i} &= \gamma(\hat{\boldsymbol{w}}_\delta^n)^\top \boldsymbol{S}(\boldsymbol{u}_{\delta i}^n)^2\boldsymbol{S}(\hat{\boldsymbol{u}}_{\delta i}^n)\boldsymbol{\sigma}_{\delta i} + \hat{d}_{\delta i}^2(\boldsymbol{u}_{\delta i}^n)^\top\hat{\boldsymbol{w}}_\delta^n \\
\boldsymbol{\sigma}_{\delta i} &= \boldsymbol{S}(\boldsymbol{u}_{\delta i}^n)\hat{\boldsymbol{u}}_{\delta i}^n, \quad \dot{\hat{\boldsymbol{\delta}}}_i^n = \frac{\hat{\boldsymbol{u}}_{\delta i}^n}{\hat{d}_{\delta i}}
\end{aligned} \tag{4.50}$$

The cascade structure of this bearing only SLAM with 4 landmarks can be seen in Figure 4.1. By the theorems in the previous chapters the error dynamics of this system is USGAS under certain assumptions. One of these assumptions is that the velocity vector is bounded from below, meaning that the USGAS of the velocity magnitude observer is lost when the velocity goes to zero.

Remark 3. *For this setup we have assumed available AHRS measurements. Although, an equivilant setup is possible in the body-frame with observers from Theorem 2, if a gravity vector estimate is available in body-frame as in [41].*

4.3.1 Position estimate

As we have no knowledge of absolute position, we will only care about relative position change. The position estimate is derived from the estimated relative position vectors

$$\hat{\boldsymbol{p}}^n(t) = \sum_{i=1}^m w_i(t)(\hat{\boldsymbol{\delta}}_i^n(0) - \hat{\boldsymbol{\delta}}_i^n(t)) \tag{4.51}$$

where w_i are gains that sum up to one $\sum_{i=1}^m w_i = 1$. The estimate of the pose will converge as the relative position vector estimates converge, although there will be a constant offset due to the initial position estimate error

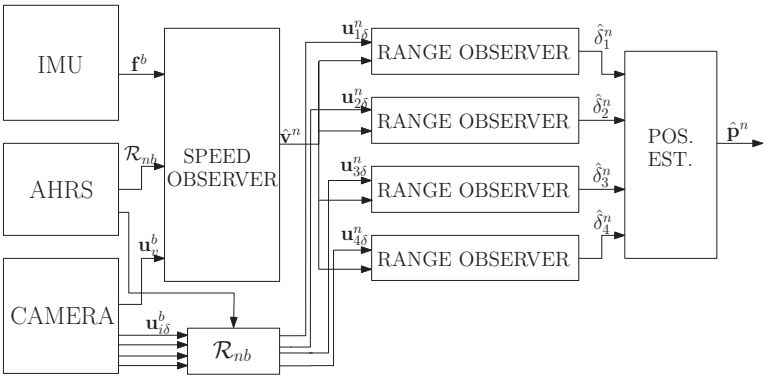

Figure 4.1: Block diagram of the cascade structure of the speed observer (4.49) and range observer (4.50), for Bearing Only SLAM with 4 landmarks

4.4 Results

The observer was tested in simulations. The scenario presented in this section is a vehicle travelling in a circle in 3D-space at constant velocity $\boldsymbol{v}^b = [0.5,\ 0,\ 0][m/s]$. The trajectory of the vessel, with the landmarks positions, can be seen in Figure 5.9. The simulator is implemented using Euler integration, having step length $h = 0.025[s]$ and lasts for $40[s]$. Four landmarks were placed in the corners of a

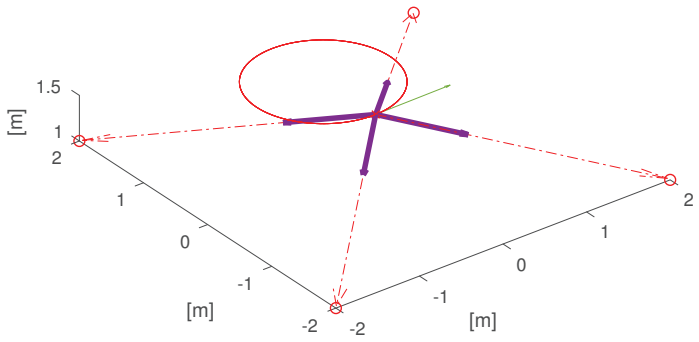

Figure 4.2: The figure shows the trajectory of the vehicle, and the landmarks. The green arrow represent the normalized velocity measurement; the blue arrows represent the LOS measurements; the red dashed arrows represent the estimated distance vectors using $\frac{1}{\hat{d}_{xi}}\hat{\boldsymbol{u}}^n_{xi}$ at the end of the simulation.

box with sides of $4[m]$. The IMU measurements were corrupted by white noise with standard deviation $\boldsymbol{\sigma}_\omega = \boldsymbol{I}0.02[rad/s]$ and $\boldsymbol{\sigma}_f = \boldsymbol{I}0.02[m/s^2]$, which is meant to resemble a low cost MEMS IMU. The noise in the bearing measurements was $\boldsymbol{\sigma}_u = \boldsymbol{I}0.00314[rad]$, resembeling a pixel error for a camera with 90^o field of view and 500 pixels image height/width; the AHRS noise was $\boldsymbol{\sigma}_{\mathcal{R}} = \boldsymbol{I}0.0116[rad]$ giving a 3σ value of 2^o; the velocity direction had a white noise of $\boldsymbol{\sigma}_v = \boldsymbol{I}0.1060[rad]$, which is what you can expect from a Homography with the above image [41]. The bearing noise is orthogonal to the bearing $\boldsymbol{u}_n = \boldsymbol{S}(\boldsymbol{u}_{\delta i}^n)\boldsymbol{w}_u$, in which the noise $\boldsymbol{w}_u$ is a white noise vector $\boldsymbol{w}_u = \mathcal{N}(0, \boldsymbol{\sigma}_u)$, the same is applied to the noise of the normalized velocity.

The speed observer was tuned with $k_v = 2\sqrt{\alpha}$ and $\gamma_v = \alpha/\|\mathcal{B}_u(t)\|$, with $\alpha = 0.5$. The range observers were tuned with $k_{\delta i} = 2\sqrt{2}$ and $\gamma_{\delta i} = 2$. The tuning is based on [101]. The observers were also implemented using the Euler method with $h = 0.025[s]$; the unit vector estimates should be normalized for every iteration to compensate for numerical errors. In Figure 4.3, we note that since the acceleration input is found by subtracting the gravity from the rotated specific force, most of the noise comes from the noisy attitude measurements. In Figure 5.11 we see how the velocity direction estimates are smooth compared to the measurents. Further, in Figure 5.10 we see how the velocity magnitude estimate converges, and in Figures 4.6 and 4.7 we see how the range and position estimates converge; this confirms that the observers can be used in cascade.

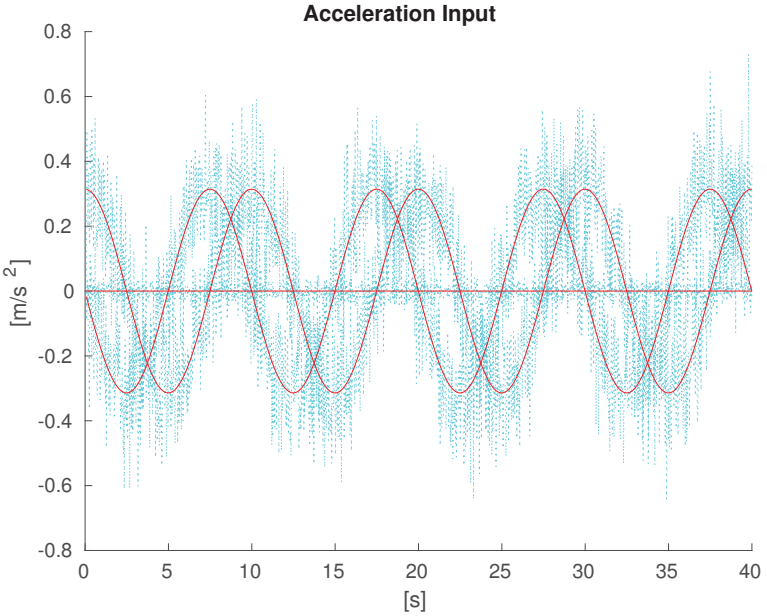

Figure 4.3: The figure shows the acceleration input to the velocity magnitude observer. The red is the true acceleration, and the blue is the input for the velocity observer.

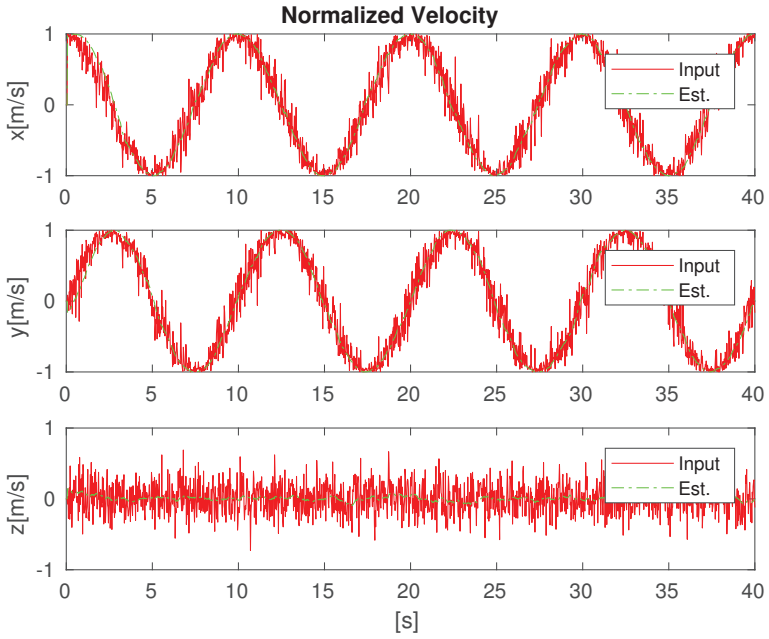

Figure 4.4: The figure show the normalized velocity, in combination with the velocity direction estimate.

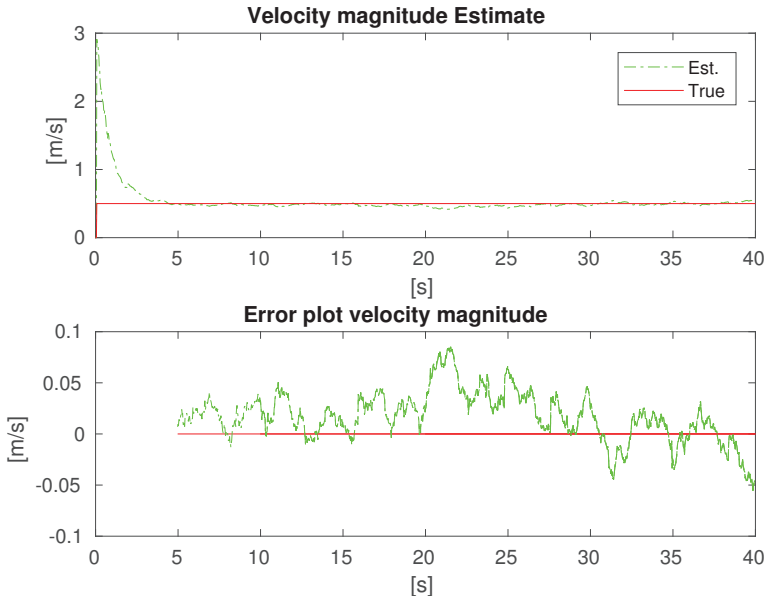

Figure 4.5: The upper plot shows the velocity magnitude estimate combined with the true norm of the velocity, while the bottom plot shows the velocity error

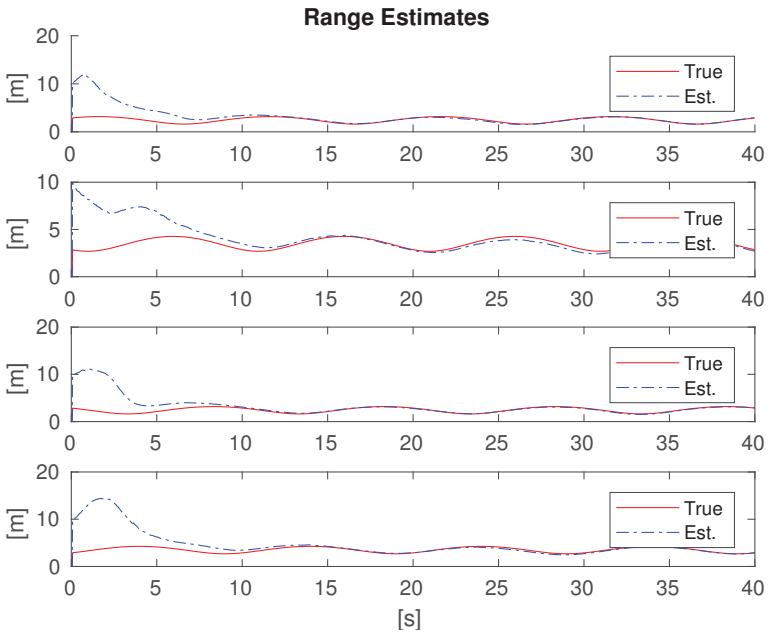

Figure 4.6: The figure shows the range estimates and true ranges for the 4 landmarks.

The authors still want to emphasise that there are assumptions for this scenario which are often broken when bearing only SLAM is used. The landmarks are assumed to be observed for the entire period; the attitude is only corrupted by white noise, so gravity is removed from the specific force. However, the setup is able to estimate the position of the vessel, and the distance to the landmarks by only having IMU, AHRS, bearing and optical flow measurements, and without dead reckoning. This also shows the duality between the range estimation problem, and speed estimation problem; implying that other globally stable observers can be used for velocity estimation fusing camera with IMU and AHRS data [17, 71, 79], making velocity measurements redundant.

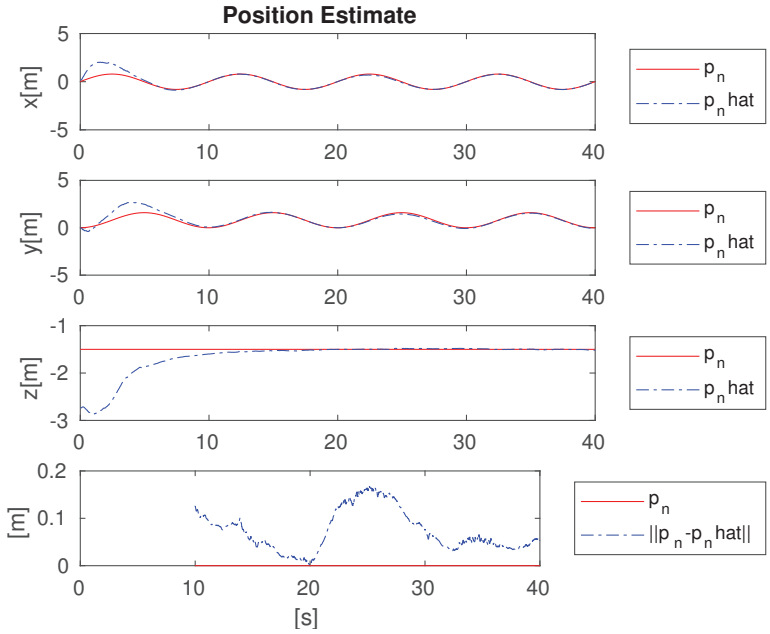

Figure 4.7: The figure shows the position estimates for x, y and z direction, and the lowermost plot shows the norm of the position error. To make comparison between the position estimate and the true position easier, the position estimate is shifted so that there is zero position error at time $t = 20[s]$

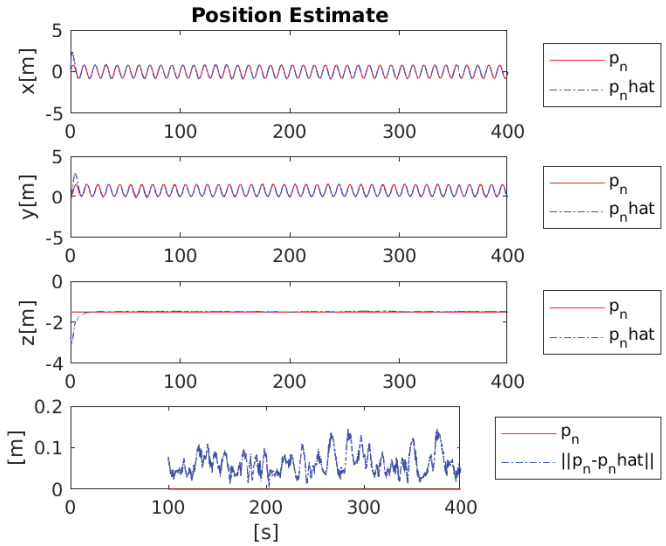

Figure 4.8: The figure shows the position estimate. The dot dasshed blue based on the estimated distance vector estimates. The estimates are plotet so that there are no error at $1 = 20[s]$, to see how its bounded when it has converged. The three upper plots are position in x- y- and z-direction, and the bottom shows the norm of the position error.

4.5 Conclusion

We presented a novel vector magnitude observer, which uses unit vector measurement and derivative. The observer was proven to be uniformly semi-globally stable (USGAS) and UES in a defined region, moreover, the stability was of multiple instances, and in cascade. The vector magnitude framework was then applied to a bearing-only SLAM filter problem with AHRS, which demonstrated the filtering properties and convergence of the observer. This also demonstrated how a velocity estimation could be performed with camera, IMU and AHRS, making velocity measurement possibly redundant when these sensors are available

5 Ego Motion Estimation

5.1 Introduction

Vision-based navigation is an important topic in robotics. With the reduced size, weight, power and financial cost of modern digital cameras, they are a key navigation component in many robotics systems. In the literature, the techniques are often referred to as real-time structure from motion (SFM), visual odometry (VO) or visual/bearing only simultaneous localization and mapping (SLAM). Several methods have been developed over the years, where the methods are often divided into graph SLAM and SLAM filters. The graph SLAM methods are based on non-linear optimization ([33, 89, 66]) also called bundle adjustment (BA). The most efficient approaches store key-frames, making the optimization problem sparse, and hence they are solvable in real time. The SLAM filters are often based on EKF [26], where the estimates are stored in the states and the co-variance, making the computational load grow quadratic with regards to the number of features. A further discussion of the pros and cons between the methods can be seen in [104].

An inherit problem when using a monocular camera is that the metric scale of the world is not observable. The scale is either given during the initialization through stereo vision, laser scanner, IMU information or by having known features or tags at the initialization, or it is just neglected. For some applications, especially long duration navigation, scale drift can be a limiting factor. There are also several Visual-Inertial Odometry (VIO) methods able to estimate the scale with the IMU information([88, 20]). Methods for estimating scale from a camera world to the real world have also been presented in [112] and [80], where an EKF setup estimates the scale by comparing the pose measurements from a camera system to IMU data. These methods then need the scale estimate to be close to the real scale at the initialization to guarantee convergence.

Initialization procedures have also been presented, with different kind of assumptions, such as in [111, 31, 91] and [61]. In [111] a throw and go procedure is demonstrated, however as the scale is estimated through an EKF scheme there is no guarantee of convergence, and the scale is therefore initialized close to the true scale. In [31] a similar procedure is demonstrated for SVO+MSF, where the scale is acquired from an altimeter. In [91] and [61], closed form and optimization schemes are developed, that can initialize the scale and gravity from IMU and bearing measurements. This however relies on features being detected for several time steps, or in the case of [91] that the monocular SLAM is initialized. They also lack conditions that could guarantee good initialization.

In [41] an ego-motion estimation using a continuous homography scheme is presented, where estimation of metric velocity is performed with a calibrated IMU and pitch and roll estimates. This work differentiates itself from the most common implementations of visual navigation in two ways. First, as it relies on

the homography transform, it only requires matching of features between pairs of images. Thus the requirement of observing features for consecutive images is no longer necessary. The other benefit of the system ([41]) is inherited from its application of nonlinear observer techniques presented in [101] and [102]. In addition to acquire global convergence under a defined persistent of excitation (PE) condition, the system can be tuned close to a second order differential equation under certain conditions so that convergence rate and frequency response can be defined for the observer. The main drawback for the setup presented in [41] is the necessity of observing a flat surface in order to utilize the homography transformation, which is an assumption that is violated for many applications.

This has given the motivation for developing an observer which only relies on normalized velocity. Thus, it would no longer be necessary to observe a flat surface. In fact, this enables the ego motion estimation to be applicable to any VO, Visual SLAM or SFM method able to provide a normalized camera velocity. Methods include two view methods such as, essential matrix ([93]), two point ([66]), three point ([110]) or homography ([41]), or a combination of these as shown in [89], where homography and the 5 point algorithm are used in parallel. It also includes VO methods such as SVO ([33]) and SLAM ([89]). Such a method could either be used to initialize the scale of these methods, work in parallel as scale estimator to ensure drift free scale or it could work as a velocity measurement in itself.

5.1.1 Contribution

An observer able to estimate velocity with a similar sensor setup as in [41], is presented in [19]. The main difference is that a normalized velocity is assumed to come from the camera instead of a homography transform. Thus, globally stable velocity estimation with a defined PE condition, and without the need of observing features for several images is possible without the need of observing a flat surface. The chapter builds on the idea presented in the previous chapter 4, where we compare the observer presented to other similar observers, and how they perform when used for the ego-motion estimation.

There are several observers able to perform this estimation, since the ego-motion estimation with normalized velocity measurement is mathematically identical to the problem of estimating the distance to a landmark assuming velocity and bearing measurements are available. This implies that the ego motion estimation assuming normalized velocity measurements can be performed by several observers, that originally were designed for the latter problem ([77, 19, 71, 49]). In addition, the observers will have the same stability results. In fact all the nonlinear observers have the same PE condition; that the velocity and acceleration of the vehicle is not co-linear. Thus, the design of globally stable velocity observers with defined PE conditions guaranteeing convergence is possible without any initialized VO method, observable plane or the need of observing features for several

images.

The different observers are compared qualitatively, in simulations and with experimental data. It is also shown how the novel observer presented in [19], can tune its convergence rate. They are also compared to an EKF and the homography based observer [41]. The observers are able to estimate the velocity accurately, where the observer presented in [19] has the best performance in simulations and on experiments. It is also shown how the nonlinear observers have more robust behavior than the EKF.

The rest of the chapter is structured as follows: Section 5.3 the kinematics of bearing and normalized velocity are presented, and their similarities are investigated. In section 5.4 the observer that will be compared on the ego-motion estimation are presented. In Section 5.5 simulations of the presented setup is shown, and experiments are shown in 5.6. Finally section 5.7 concludes the chapter.

5.2 Equivalence Between bearing only position estimation and Velocity estimation using normalized velocity

We first represent the ego-motion estimation similar to what is presented in [41], where the goal is to estimate the velocity of a vehicle provided that a camera and a tactical grade IMU with roll and pitch estimates were available. We will show that this mathematical system is identical to the problem of filtering velocity and bearing measurements to estimate the distance to a landmark, and thus we can conclude that observers designed for one of the problems are applicable to the other.

To build an observer based on normalized velocity measurements, we need to examine the unit vector kinematics of the normalized velocity. A vehicle has a position $\boldsymbol{p}^n$ in the inertial frame, and moves with a velocity

$$\dot{\boldsymbol{p}}^n = \boldsymbol{v}^n \tag{5.1}$$

and it has an acceleration

$$\ddot{\boldsymbol{p}}^n = \dot{\boldsymbol{v}}^n = \boldsymbol{a}^n.$$

We assume that the IMU measurements are transformed to the camera frame, thus the acceleration can be measured by an IMU in camera frame, provided that it has an internal gravity estimate $\boldsymbol{g}^c$ from filtering

$$\boldsymbol{a}^c = \boldsymbol{\mathcal{R}}_{nc}^\top \boldsymbol{a}^n = \boldsymbol{f}^c - \boldsymbol{g}^c.$$

Here $\boldsymbol{f}^c$ is the specific force experienced by the camera, which can be measured by an IMU. In addition, we assume that the camera provides normalized velocity measurements in the camera coordinates

$$\boldsymbol{u}_v^c = \boldsymbol{\mathcal{R}}_{nc}^\top \boldsymbol{u}_v^n = \boldsymbol{\mathcal{R}}_{nc}^\top \frac{\boldsymbol{v}^n}{\|\boldsymbol{v}^n\|} = \boldsymbol{\mathcal{R}}_{nc}^\top \boldsymbol{v}^n d_v$$

where the inverted velocity magnitude $d_v = \frac{1}{\|v^n\|}$ has the time derivative

$$\dot{d}_v = -d_v^2 (\boldsymbol{u}_v^n)^\top \boldsymbol{a}^n = -d_v^2 (\boldsymbol{u}_v^c)^\top \boldsymbol{a}^c.$$

The time derivative of $\boldsymbol{u}_v^c$ is then

$$\begin{aligned}
\dot{\boldsymbol{u}}_v^c &= \dot{\boldsymbol{\mathcal{R}}}_{nb}^\top \boldsymbol{v}^n d_v + \boldsymbol{\mathcal{R}}_{nc}^\top \dot{\boldsymbol{v}}^n d_v + \boldsymbol{\mathcal{R}}_{nc}^\top \boldsymbol{v}^n \dot{d}_v \\
&= -S(\boldsymbol{\omega}^c) \boldsymbol{\mathcal{R}}_{nb}^\top \boldsymbol{v}^n d_v + \boldsymbol{\mathcal{R}}_{nc}^\top \boldsymbol{a}^n d_v - \boldsymbol{\mathcal{R}}_{nc}^\top \boldsymbol{v}^n d_v^2 (\boldsymbol{u}_v^c)^\top \boldsymbol{a}^c \\
&= -S(\boldsymbol{\omega}^c) \boldsymbol{u}_v^c + \boldsymbol{a}^c d_v - \boldsymbol{v}^c d_v^2 (\boldsymbol{u}_v^c)^\top \boldsymbol{a}^c \\
&= -S(\boldsymbol{\omega}^c) \boldsymbol{u}_v^c + d_v (\boldsymbol{I} - \boldsymbol{u}_v^c (\boldsymbol{u}_v^c)^\top) \boldsymbol{a}^c \\
&= -S(\boldsymbol{\omega}^c) \boldsymbol{u}_v^c - d_v \boldsymbol{S}(\boldsymbol{u}_v^c)^2 \boldsymbol{a}^c,
\end{aligned}$$

which means that we end up with the system

$$\dot{\boldsymbol{u}}_v^c = -S(\boldsymbol{\omega}^c) \boldsymbol{u}_v^c - d_v \boldsymbol{S}(\boldsymbol{u}_v^c)^2 \boldsymbol{a}^c \tag{5.2}$$

$$\dot{d}_v = -d_v^2 (\boldsymbol{u}_v^c)^\top \boldsymbol{a}^c, \tag{5.3}$$

where we assume that we can measure $\boldsymbol{u}_v^c$, $\boldsymbol{a}^c$, and $\boldsymbol{\omega}^c$, and we want to estimate the velocity magnitude $\|\boldsymbol{v}^c\| = \frac{1}{d_v}$.

We then want to compare this system to the bearing and velocity measurement system, and verify their equivalence. The relative distance vector $\boldsymbol{\delta}^n = \boldsymbol{p}_i^n - \boldsymbol{p}^n$, is the vector from the vehicle to the landmark. Its direction can be measured by a camera, which provides bearing measurements

$$\boldsymbol{u}_\delta^c = \boldsymbol{\mathcal{R}}_{nc}^\top \frac{\boldsymbol{\delta}_i^n}{\|\boldsymbol{\delta}_i^n\|} = \boldsymbol{\mathcal{R}}_{nc}^\top \frac{\boldsymbol{p}_i^n - \boldsymbol{p}^n}{\|\boldsymbol{p}_i^n - \boldsymbol{p}^n\|}.$$

Since the landmark is stationary $\dot{\boldsymbol{p}}_i^n = \boldsymbol{0}$,

$$\dot{\boldsymbol{\delta}}^n = \dot{\boldsymbol{p}}_i^n - \dot{\boldsymbol{p}}^n = -\boldsymbol{v}^n,$$

where we have used (5.1). The time derivatives of $\boldsymbol{u}_\delta^c$ and $d_\delta = \frac{1}{\|\boldsymbol{\delta}_i^n\|}$ can then be found following the same steps as was done for the normalized velocities, which gives

$$\dot{\boldsymbol{u}}_\delta^c = -\boldsymbol{S}(\boldsymbol{\omega}^c) \boldsymbol{u}_\delta^c + d_\delta \boldsymbol{S}(\boldsymbol{u}_\delta^c)^2 \boldsymbol{v}^c \tag{5.4}$$

$$\dot{d}_\delta = d_\delta^2 (\boldsymbol{u}_\delta^c)^\top \boldsymbol{v}^c, \tag{5.5}$$

where we have the measurements $\boldsymbol{u}_\delta^c$, $\boldsymbol{\omega}^c$ and $\boldsymbol{v}^c$, and we want to estimate the distance to the landmark $\|\boldsymbol{\delta}_i^n\| = \frac{1}{d_\delta}$. We see that the systems (5.2)-(5.3) and (5.4)-(5.5) are mathematically identical except a sign difference, since $\dot{\boldsymbol{v}}^n = \boldsymbol{a}^n$ and $\dot{\boldsymbol{\delta}}^n = -\boldsymbol{v}^n$.

If we then want to design an observer for the ego motion estimation (5.2)-(5.3) we can use observers that were originally designed for system (5.4)-(5.5), where range to a landmark is estimated. This is an extensively studied system in the literature, and several observers have been designed. In the next section we will review the observers that have global stability proven, and apply them on ego motion estimation.

5.3 Velocity estimation

There exist several observers that estimate the distance to a landmark provided bearing, angular and linear velocity measurements. In this section, however, we apply the same formulas to the camera velocity estimation, where the velocity can be estimated provided normalized velocity, acceleration and angular rate measurement.

What the reviewed nonlinear observers have in common is that they use similar measurements and have proof of global or semi-global stability. Even though the observers are structured differently, with PE condition differently defined, they all have in common that they rely on the unit vector measurement to be non stationary in the inertial frame. In practice this means that the observers are PE when the vehicle velocity has a change of direction. For the ego motion estimation, this means that the PE conditions are fulfilled when the acceleration and velocity are not co-linear. In addition we compare the observers to an EKF inspired by the states used in robust visual inertial odometery ([20]). A qualitative comparison between the observers is presented in Table 5.1. In the rest of this section we present the sensor setup for the ego motion estimation, and the observers that will be compared.

5.3.1 Sensor setup

The IMU is assumed to be of high quality with an internal filter available to calculate gravity estimates and biases. In addition a camera is available, providing information about the velocity direction (course). The camera is calibrated and the transformation between the camera and the IMU is known through calibration. The following measurements and known values are then:

- Constant transformations $\boldsymbol{p}_{cb}^{c}$ and $\mathcal{R}_{cb}$ between the IMU and and the camera.
- $\boldsymbol{\omega}^{c} = \mathcal{R}_{cb}\boldsymbol{\omega}^{b}$, The gyro rate from the IMU in camera frame
- $\boldsymbol{u}_{v}^{c}$, normalized camera velocity in the camera frame
- $\hat{\boldsymbol{a}}^{c} = \mathcal{R}_{cb}(\boldsymbol{f}^{b} + \boldsymbol{g}^{b}) + \boldsymbol{S}(\boldsymbol{\omega}^{c})^{2}\boldsymbol{p}_{cb}^{c}$, perceived acceleration provided by the IMU from the specific force and gravity estimates together with the lever arm compensation.

The term related to the angular acceleration $\dot{\boldsymbol{\omega}}$ is neglected and assumed to be zero for this setup, as done for the sensor setup in [41].

As the observers will be able to estimate velocity from only normalized velocity, they can be used for initializing visual SLAM or VO methods, with the setup shown in Figure 5.1. The normalized velocity can then come from a scheme as described in [89], where a normalized velocity can be acquired from two-view algorithms such as homography or the 5 point algorithm ([93]), not requiring any initialization. An

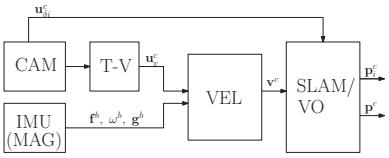

Figure 5.1: Block diagram of a possible initialization setup, where a two-view algorithms as explained in [89] can provide a normalized velocity without any initialization. The velocity observer can thus combine the normalized velocity with IMU data and initialize the scale of a visual SLAM/VO method, or provide velocity measurements.

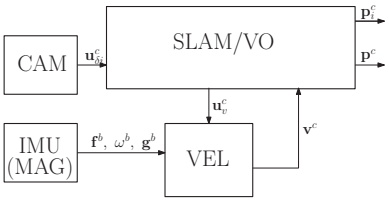

Figure 5.2: Block diagram of a possible setup between the velocity estimation and a SLAM/VO, where the VEL observer gets normalized velocity from the SLAM/VO method, and fuses it with the IMU information which then can be used to maintain a drift free scale for the visual SLAM/VO.

alternative approach is shown in Figure 5.2, where the observer works in parallel with a visual SLAM or VO. Acquiring the normalized velocity and fusing it with the IMU data to return the metric velocity, a drift free scale estimate can therefore be acquired.

5.3.2 Robust Extended Kalman Filter

Inspired by the work in [20], we use the robust EKF for comparison, where the range and bearing states are separated, and the range estimate is inverted. As we assume there are no biases in the IMU, and that a gravity estimate is available, the states for the ego motion estimation are $\boldsymbol{x}_{EKF} = [(\boldsymbol{u}_v^c)^\top,\ d_v]^\top$. The $d_v = \frac{1}{\|\boldsymbol{v}^c\|}$ is the inverse metric speed, and the time derivative of the states are (5.2)-(5.3). We show the discrete time implementation for the EKF, and we use the Euler method to discretize the system. We apply the Rodriguez formula (2.35)-(2.36) for propagating the unit vector

$$
\begin{aligned}
\boldsymbol{\omega}_u^c[k] &= \boldsymbol{\omega}^c[k] + d_v[k|k]\boldsymbol{S}(\hat{\boldsymbol{a}}^c[k])\boldsymbol{u}_v^c[k|k] \\
\boldsymbol{u}_v^c[k+1|k] &= \boldsymbol{\mathcal{R}}(\Delta t\, \boldsymbol{\omega}_u^c[k])^\top \boldsymbol{u}_v^c[k|k] \\
&\approx \boldsymbol{I} - \Delta t(\boldsymbol{S}(\boldsymbol{\omega}^c[k])\boldsymbol{u}_v^c[k|k] - d_v[k|k]\boldsymbol{S}(\boldsymbol{u}_v^c[k|k])^2\hat{\boldsymbol{a}}^c[k]) \\
d_v[k+1|k] &= d_v[k|k] - \Delta t\, d_v^2[k|k](\boldsymbol{u}_v^c[k|k])^\top \hat{\boldsymbol{a}}^c[k],
\end{aligned}
\tag{5.6}
$$

where $k \in \mathbb{N}$ denotes the kth iteration step, and $\bullet[k|l]$ is the estimate of the state at time-step kth given the lth measurement. In addition, $\boldsymbol{\omega}^c[k]$ and $\hat{\boldsymbol{a}}^c[k]$

are the averaged sensor measurements between time instants t_k and t_{k+1}. When calculating the Jacobi matrices we utilize (5.6)

$$\boldsymbol{F}_{ekf} = \begin{bmatrix} \frac{\partial \boldsymbol{u}_v^c[k+1|k]}{\partial \boldsymbol{u}_v^c[k|k]} & \frac{\partial \boldsymbol{u}_v^c[k+1|k]}{\partial d_v[k|k]} \\ \frac{\partial d_v[k+1|k]}{\partial \boldsymbol{u}_v^c[k|k]} & \frac{\partial d_v[k+1|k]}{\partial d_v[k|k]} \end{bmatrix} \tag{5.7}$$

$$\begin{aligned} \frac{\partial \boldsymbol{u}_v^c[k+1]}{\partial \boldsymbol{u}_v^c[k]} &= \boldsymbol{I} - \Delta t(\boldsymbol{S}(\boldsymbol{\omega}^c[k] + d_v[k]\boldsymbol{S}(\hat{\boldsymbol{a}}^c[k])\boldsymbol{u}_v^c[k]) \\ &\quad - d[k]\boldsymbol{S}(\boldsymbol{u}_v^c[k])\boldsymbol{S}(\hat{\boldsymbol{a}}^c[k])) \\ \frac{\partial \boldsymbol{u}_v^c[k+1]}{\partial d_v[k]} &= -\Delta t \boldsymbol{S}(\boldsymbol{u}_v^c[k])^2 \hat{\boldsymbol{a}}^c[k] \\ \frac{\partial d_v[k+1]}{\partial \boldsymbol{u}_v^c[k]} &= -\Delta t d_v^2[k](\hat{\boldsymbol{a}}^c[k])^\top \\ \frac{\partial d_v[k+1]}{\partial d_v[k]} &= \boldsymbol{I} - \Delta t 2 d_v[k](\hat{\boldsymbol{a}}^c[k])^\top \boldsymbol{u}_v^c[k]. \end{aligned}$$

The covariance matrix is then propagated according to

$$\boldsymbol{P}[k+1|k] = \boldsymbol{F}_{ekf}\boldsymbol{P}[k|k]\boldsymbol{F}_{ekf}^\top + \boldsymbol{R}_{ekf},$$

where $\boldsymbol{R}_{ekf}$ are approximated through linearization

$$\boldsymbol{R}_{ekf} = \boldsymbol{V}\begin{bmatrix} \text{cov}(\boldsymbol{\omega}^c[k]) & 0 \\ 0 & \text{cov}(\hat{\boldsymbol{a}}^c[k]) \end{bmatrix}\boldsymbol{V}^\top + \boldsymbol{R}_{reg}, \tag{5.8}$$

where $\boldsymbol{R}_{reg}$ is a regularization matrix and

$$\boldsymbol{V} = \begin{bmatrix} \frac{\partial \boldsymbol{u}_v^c[k+1|k]}{\partial \boldsymbol{\omega}^c[k]} & \frac{\partial \boldsymbol{u}_v^c[k+1|k]}{\partial \hat{\boldsymbol{a}}^c[k]} \\ \frac{\partial d_v[k+1|k]}{\partial \boldsymbol{\omega}^c[k]} & \frac{\partial \hat{\boldsymbol{a}}^c[k]}{\partial d_v[k|k]} \end{bmatrix}$$

$$\begin{aligned} \frac{\partial \boldsymbol{u}_v^c[k+1|k]}{\partial \boldsymbol{\omega}^c[k]} &= \Delta t \boldsymbol{S}(\boldsymbol{u}_v^c[k|k]) \\ \frac{\partial \boldsymbol{u}_v^c[k+1|k]}{\partial \hat{\boldsymbol{a}}^c[k]} &= -d_v[k|k]\boldsymbol{S}(\boldsymbol{u}_v^c[k|k])^2 \\ \frac{\partial d_v[k+1|k]}{\partial \boldsymbol{\omega}^c[k]} &= \boldsymbol{0} \\ \frac{\partial \hat{\boldsymbol{a}}^c[k]}{\partial d_v[k|k]} &= \Delta t d_v^2[k|k](\boldsymbol{u}_v^c[k|k])^\top. \end{aligned}$$

The $\text{cov}(\boldsymbol{\omega}^c[k])$ and $\text{cov}(\hat{\boldsymbol{a}}^c[k])$ can be calculated from the data sheet from the IMU, or found empirically. The most challenging task is to find $\text{cov}(\hat{\boldsymbol{a}}^c[k])$, as it is both the combination of the gravity estimate and the specific force measurement. The unit velocity vector $\boldsymbol{z}_{ekf} = \boldsymbol{u}_v^c(t_{k+1})$ is measured at time t_{k+1}, and the Jacobian of the measurement is thus trivial

$$\boldsymbol{J}_{ekf} = \begin{bmatrix} \boldsymbol{I} & \boldsymbol{0}_{3\times 1} \end{bmatrix}.$$

The Kalman gain is then calculated using

$$\boldsymbol{K}_{ekf} = \boldsymbol{P}[k|k]\boldsymbol{J}_{ekf}^\top(\boldsymbol{J}_{ekf}\boldsymbol{P}[k|k]\boldsymbol{J}_{ekf}^\top + \text{cov}(\boldsymbol{z}_{ekf}))^{-1}. \tag{5.9}$$

The the estimate update is as follows

$$\boldsymbol{x}_{EKF}[k+1|k+1] = \begin{bmatrix} \boldsymbol{u}_v^c[k+1|k+1] \\ d_v[k+1|k+1] \end{bmatrix} \tag{5.10}$$

$$= \begin{bmatrix} \boldsymbol{u}_v^c[k+1|k] \\ d_v[k+1|k] \end{bmatrix} + \boldsymbol{K}_{ekf}(\boldsymbol{z}_{ekf} - \boldsymbol{u}_v^c[k+1|k]) \tag{5.11}$$

$$\boldsymbol{P}[k+1|k+1] = (\boldsymbol{I} - \boldsymbol{K}_{ekf}\boldsymbol{J}_{ekf})\boldsymbol{P}[k+1|k]. \tag{5.12}$$

As the magnitude parameter d_v is inverted, the filter can be initialized without any special procedure [20]. However as the filter is based on the EKF, there are no guarantees of convergence, and the requirements for having the filter converge are not clear

5.3.3 Sensor-centric observer - KF

The sensor-centric bearing-only SLAM is presented in [77]. By augmenting the states and transforming the outputs, they are able to formulate the bearing only SLAM problem as a linear system. This means that the filter can be implemented with a Kalman filter, therefore, we give it the abbreviation *KF*. For a single bearing measurement the states to be estimated are $\boldsymbol{x}_{KF} = [\boldsymbol{v}^c,\ s]^\top$ and the input is $\boldsymbol{w}_{KF} = \hat{\boldsymbol{a}}^c$. Where $\boldsymbol{v}^c$ is the metric velocity of the camera, and s is its speed; the resulting system dynamics are

$$\dot{\boldsymbol{x}}_{KF} = \boldsymbol{\mathcal{A}}_{KF}(t)\boldsymbol{x}_{KF} + \boldsymbol{\mathcal{B}}_{KF}(t)\boldsymbol{w}_{KF} \tag{5.13}$$

$$\boldsymbol{y}_{KF} = \boldsymbol{C}_{KF}(t)\boldsymbol{x}_{KF}, \tag{5.14}$$

where the time varying system matrices are partially built up by sensor data. The matrices are then

$$\mathcal{A}_{KF}(t) = \begin{bmatrix} -S(\omega^c(t)) & \mathbf{0} \\ \mathbf{0} & 0 \end{bmatrix} \quad \mathcal{B}_{KF}(t) = \begin{bmatrix} I \\ u_v^c(t)^\top \end{bmatrix} \tag{5.15}$$

$$C_{KF}(t) = \begin{bmatrix} I & -u_v^c(t) \end{bmatrix}, \tag{5.16}$$

where the virtual measurement $y_{KF} = \mathbf{0}$ works as a constraint on the system. The system is proved to be Uniformly Completely Observable (UCO) if there exist a time when $\|\dot{u}_v^n\| > 0$, implying that the KF can be designed to be globally exponentially stable (GES) [3]. However, as the set-up provides noise that is not Gaussian, introduced by the unit vector parametrization which gives a banana shaped distribution, the optimality of the KF can not be expected. In addition the system state space model is not minimal, and the noise is state dependent. This may compromise the performance of this observer for noisy measurements.

5.3.4 Position Observer - PO

The position observers presented in [49] and [71] have measurements rotated in the inertial frame. However since the comparison between the observers is made in the body-frame, we transform the observers to work with measurements in the body-frame. As the transformation from inertial to body-frame can be regarded as a similarity transformation and hence preserves the observability properties of the system, the observer in body-frame will have the same properties as the observer in the inertial frame, which for both observers are GES.

In [49] a similar framework as described in section 5.3.3 is presented. The system is augmented to a linear time-varying system, and an observer can be created by applying the Riccati equations. However, the range is not explicitly estimated, but implicitly estimated in the relative position estimate from the vehicle to the landmark. In our case we estimate the velocity $x_{PO} = v^c$ instead. It is also shown how input bias estimation is possible with an expansion of the observer. The system for one unit vector measurement in camera-frame, the normalized camera velocity u_v^c, and no bias estimation is

$$\mathcal{A}_{PO}(t) = -S(\omega^c), \ \mathcal{B}_{PO} = I \tag{5.17}$$

$$C_{PO}(t) = S(u_v^c(t))^2 \tag{5.18}$$

with the input $w_{PO} = \hat{a}^c$, and a similar virtual measurements $y_{PO} = \mathbf{0}$ as seen previously, is used. The observer will have the same pros and cons as the observer presented above, although it can be argued that the number of states of the system is minimal. A similar fixed gain version was presented in [71], which is also able

to estimate velocity bias. The simple observer for the system (5.17)-(5.18) is

$$\dot{\hat{\boldsymbol{v}}}^c_{PO} = -\boldsymbol{S}(\boldsymbol{\omega}^c)\hat{\boldsymbol{v}}^c_{PO} + \hat{\boldsymbol{a}}^c - k_{PO}\boldsymbol{S}(\boldsymbol{u}^c_v)^2\hat{\boldsymbol{v}}^c_{PO} \tag{5.19}$$

In addition, as it is argued in [29], that the difference between finding gains through the Riccatti solution compared to using fixed gains is a matter of tuning. As it is noted in [49], by designing the Kalman filter with certain covariance matrices, the observer (5.19) is recovered. Hence we will use the fixed gain observer when we compare this setup to the other observers. The observer is also proven to be GES, assuming that a PE condition is satisfied. For a system with one bearing measurement the PE condition is similar to the KF above; i.e. there exist a time between t and $t + \Delta T$ when $\|\dot{\boldsymbol{u}}^n_v\| > 0$, assuming $\dot{\boldsymbol{u}}^n_v$ is uniformly continuous.

5.3.5 Magnitude Observer - MO

The last observer was originally presented in [19], with proof of semi-global asymptotic stability and locally exponential stability. The observer utilizes the time derivative of the normalized vector and how it relates to the magnitude of the vector corresponding to the unit vector measurement. From this, the inverse magnitude of the vector is estimated, leading to $\boldsymbol{v}^c_{MO} = \frac{\boldsymbol{u}^c_x}{\hat{d}_v}$. Thus, the state representation is identical to the robust EKF in section 5.3.2. The nonlinear observer is driven by the input $\hat{\boldsymbol{a}}^c$ and $\boldsymbol{\omega}^c$, and is as follows

$$\dot{\hat{\boldsymbol{u}}}^b_{\delta i} = -\boldsymbol{S}(\boldsymbol{\omega}^c - k_{MO}\tilde{\boldsymbol{u}}^c)\hat{\boldsymbol{u}}^c_v + \hat{d}_v\boldsymbol{S}(\hat{\boldsymbol{u}}^c_v)\boldsymbol{S}(\boldsymbol{u}^c_v)\hat{\boldsymbol{a}}^c \tag{5.20}$$

$$\dot{\hat{d}}_v = \text{proj}_d(\hat{d}^2_v(\boldsymbol{u}^c_v)^\top\hat{\boldsymbol{a}}^c - \gamma_{MO}(\hat{\boldsymbol{a}}^c)^\top\boldsymbol{S}(\boldsymbol{u}^c_v)^2\boldsymbol{S}(\hat{\boldsymbol{u}}^c_v)\tilde{\boldsymbol{u}}^b_{\delta i}) \tag{5.21}$$

$$\tilde{\boldsymbol{u}}^c = \boldsymbol{S}(\boldsymbol{u}^c_v)\hat{\boldsymbol{u}}^c_v \tag{5.22}$$

For this observer, the cross product between the unit vector estimate and measurement is used as the error term. The system is proven to have semi-global stability when a projection operator is applied in the estimation and $\|\dot{\boldsymbol{u}}^n_{\delta i}\| > 0$. This means that there also is an upper limit on the estimate $\hat{d}_v$ to guarantee convergence for the system. It is then natural to think that a similar bound should be set on the EKF as well to increase the robustness. Another aspect with the MO observer is that it has the skew-symetric structure similar to what is discussed in [101]. This means that the observer can be tuned similarly to a second order system by using the gains $k_{MO} = 2\sqrt{\alpha}\lambda$ and $\gamma_{MO} = \frac{\alpha}{\|\mathcal{B}_u\|}$, where $\mathcal{B}_u = (\hat{\boldsymbol{a}}^c)^\top\boldsymbol{S}(\boldsymbol{u}^b_{\delta i})^2 S(\hat{\boldsymbol{u}}^b_{\delta i})$. The convergence rate will increase linearly with α, and λ is the damping ratio of the observer.

Remark 4. *The various PE conditions discussed in this section are a bit different, however they all depend on some excitation of the normalized velocity in the inertia frame $\|\boldsymbol{u}^n_v\| > 0$ at some time. However when uncertainty and noise is added to the system, the requirement for the PE becomes stronger resulting in that the normalized velocity measurement $\|\boldsymbol{u}^n_v\| > 0$ should be exited regularly to get acceptable convergence.*

Table 5.1: Qualitative comparisons of the observers presented

Observers	States	Observer Innovation	Tuning parameters	Stability	PE condition
EKF	$[\boldsymbol{u}_v^c, d_v]$	$\tilde{\boldsymbol{y}} = \boldsymbol{u}_v^c - \hat{\boldsymbol{u}}_v^c$	$\boldsymbol{Q}_{EKF}$, $\boldsymbol{R}_{EKF}$	Unknown	Unknown
KF	$[\boldsymbol{v}^c, \varrho]$	$\tilde{\boldsymbol{y}} = \boldsymbol{0} - \hat{\boldsymbol{v}}^c - \hat{s}\boldsymbol{u}^c$	$\boldsymbol{Q}_{KF}$, $\boldsymbol{R}_{KF}$	GES	$\|\dot{\boldsymbol{u}}_v^n\| > 0$
PO	$\boldsymbol{v}^c$	$\tilde{\boldsymbol{y}} = \boldsymbol{0} + \boldsymbol{S}(\boldsymbol{u}^c)^2\hat{\boldsymbol{v}}^c$	k_{PO}	GES	$\int_t^{t+T} \boldsymbol{S}(\boldsymbol{u}^n(\tau))^2 d\tau > \mu I, \|\boldsymbol{v}^c\| > 0$
MO	$[\boldsymbol{u}_v^c, d_v]$	$\tilde{\boldsymbol{y}} = \boldsymbol{S}(\boldsymbol{u}^c)\hat{\boldsymbol{u}}^c$	k_{MO}, γ_{MO}	USGAS LES	$\|\dot{\boldsymbol{u}}_v^n\| > \mu,\ \|\boldsymbol{v}^c\| > c_\delta$

5.4 Ego-Motion Estimation

5.5 Simulation Results

The scenario presented in this section is of a vehicle traveling in a circle in 3D-space at constant velocity $\boldsymbol{v}^b = [0.5,\ 0,\ 0][m/s]$. The trajectory of the vehicle can be seen in Figure 5.3, which was the same trajectory used in the experiment. The simulator was implemented using Euler integration, having step length $h = 0.025[s]$.

The choice of circular trajectory was made so that the system matrices would be close to constant and PE, making it easier to find what we call the optimal tuning, and thus the comparison was made simpler.

When comparing different observers, how they perform is related to the tuning of the observers. We found the tuning parameters that gave the lowest root mean square error (RMSE) for the selected trajectory and noise parameters presented. We regarded these tunings as optimal, and the mean and variance of the RMSE of consecutive Monte Carlo (MC) simulations was used a metric of how well the observers performed.

In addition to the observers presented in section 5.3, we introduced a velocity observer, where the direction measurements were first filtered in the MO observer and later used as measurements for the sensor-centric KF. The MO and KF were thus in cascade and we named the filter XKF as it was inspired by [59]. The motivation for this was to reduce the apparent noise sensitivity of the sensor-centric KF which was seen in the results presented in [18], where also the semi-global stability of this setup was proven.

5.5.1 Simulation without noise

To verify that the nonlinear observers presented in Section 5.3 had the exponential stability claimed by the authors, prior simulations were performed without noise. In addition, it was investigated how the convergence rate could be tuned for the different observers. For the MO observer we was able to change the convergence rate of the observer by utilizing the tuning presented in section 5.3.5, which were confirmed through simulations. For the PO observer the convergence rate was related to the gain k_{PO}, however, there seemed to be a maximum acceptable con-

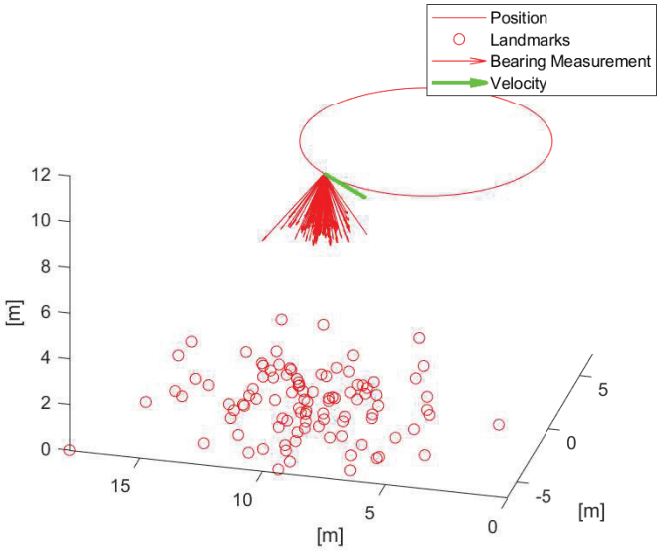

Figure 5.3: The figure shows the trajectory of the vehicle flying in a circle over a plane with a camera pointing downwards. The green arrow represents the normalized velocity measurement; red arrows represent the bearing measurements,(100 of in this plot). The circles are the corresponding landmarks.

vergence rate, and choosing a gain for faster convergence resulted in oscillations without faster convergence. It was tested if the numerical implementation played a role in the oscillations, where reducing the step length of the discretization did not affect the oscillations. As for the sensor-centric KF, the KF was tuned by changing the diagonal entries for the measurement and process noise covariance matrices. And changing these did not affect the rate of convergence of the observer, it was also tried to change the matrix $\boldsymbol{P}(0)$, which also resulted in similar convergence rate. The EKF was tuned with a combination of diagonal matrices and changing the values of $\text{cov}(\boldsymbol{\omega}^c)$ and $\text{cov}(\hat{\boldsymbol{a}}^c)$ in (5.8). The results can be seen in Figure 5.4, where the MO observer could be tuned to have arbitrary fast convergence. The PO observer had approximately similar convergence rate as the KF and XKF, when not oscillating. The KF and XKF did not change convergence rate by changing the diagonal entries of the covariance matrix. In [5], the notion of tuneability and how it is connected to observability was presented. Whether an observability analysis can explain the lack of tunable convergence rate for the sensor-centric KF, XKF and PO observers needs to be investigated further, as the circle maneuver ensures that the system is PE for all the observers. The notion of tunable convergence rate becomes increasingly important when the observer is working with a controller, as it allows the control designer to decide the convergence rate of the observer to meet the design criteria of the the state feedback controller transient response specification and/or constraint.

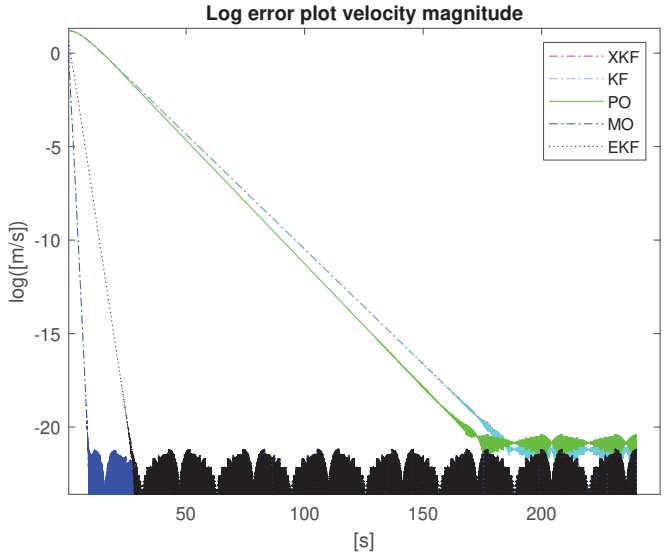

Figure 5.4: Logplot of the velocity magnitude estimation error without noise. The observers except of the MO were tuned to be as fast as possible. The XKF can not be seen as it lies behind the KF line.

5.5.2 Noisy simulation and tuning

For the noisy simulations, realistic values of the sensor noise were chosen. The IMU measurements were corrupted by white noise with standard deviation $\sigma_\omega = 0.02\boldsymbol{I}$ [rad/s] and $\sigma_f = 0.02\boldsymbol{I}$ [m/s^2], which was meant to resemble a low cost MEMS IMU. The white noise in the bearing measurements was $\sigma_u = 0.00314\boldsymbol{I}$ [rad], resembling a pixel error for a camera with 90^o field of view and 500 pixels image height/width; the attitude heading reference system (AHRS) white noise was $\sigma_{\mathcal{R}} = 0.0116\boldsymbol{I}$ [rad] giving a 3σ value of 2^o for the gravity; the velocity direction had a white noise of $\sigma_v = 0.1060\boldsymbol{I}$ [rad], which was the mean error from a homography with the setup in [41]. The bearing vector noise was orthogonal to the bearing $\boldsymbol{u}_n = \boldsymbol{S}(\boldsymbol{u}^n_{\delta i})\boldsymbol{w}_u$, in which the noise $\boldsymbol{w}_u$ was a white noise vector $\boldsymbol{w}_u = \mathcal{N}(0, \sigma_u)$. This noise was then added, and the bearing was normalized, thus the noise became nonlinear. As the camera velocity also was normalized after the noise was added, this noise was also nonlinear. The unmeasured state for the observers is the magnitude of the velocity, hence we utilized the velocity magnitude estimation RMSE as a performance metric when we compared the observers.

The four observers and the EKF that we compared have different tuning parameters. The MO observer has two parameters k_{MO} and γ_{MO}; the PO has one k_{PO}, this can also be expanded to a matrix $\boldsymbol{K}_{PO} \in \mathbb{R}^{3\times3}$ although this expansion did not lead to significantly improved performance. The sensor-centric KF has two matrices, corresponding to the process and measurement noise covariance noise matrices, $\boldsymbol{Q}_{KF} \in \mathbb{R}^{4\times4}$ and $\boldsymbol{R}_{KF} \in \mathbb{R}^{3\times3}$. As the XKF is a cascade of the MO

filter and the KF, its tuning parameters are inherited from the MO observer and the KF observer. The EKF has the tuning covariance matrices $\boldsymbol{Q}_{EKF}$ and $\boldsymbol{R}_{EKF}$. A summary of the observers is found in Table 5.1.

The observers were tuned using Monte Carlo (MC) simulations, where the tuning parameter candidates were chosen randomly from various pools. For the candidate MO and PO observers, as there were few parameters to choose from, selecting the pool of possible tuning parameters was straightforward. The results from these MC simulations can be seen in Figure 5.5 and 5.6. From these simulations, it was evident that the MO observer was able to estimate the velocity using a large set of tuning parameters (yellow area), and the PO observer also seemed to have an optimal tuning.

To investigate how the sensor-centric KF and XKF observer could be tuned properly, the covariance matrix of the process noise and innovation was found empirically. This was done by simulating the system in parallel with and without noise, and the covariances were estimated from the difference between these two simulations. As the observer was implemented by Euler discretization, the covariance estimate was of the discrete system, where $\Delta \boldsymbol{x} = h\boldsymbol{f}(\boldsymbol{x}, \boldsymbol{u})$

$$\begin{aligned}\hat{\boldsymbol{Q}} &= cov(\Delta \boldsymbol{x} - \Delta \boldsymbol{x}_m) \\ &= h^2 cov((\boldsymbol{\mathcal{A}}_{KF}(t_k) - \boldsymbol{\mathcal{A}}_{KF}(t_k)_m)\boldsymbol{x} \\ &+ \boldsymbol{\mathcal{B}}_{KF}(t_k)\boldsymbol{u}(t_k) - \boldsymbol{\mathcal{B}}_{KF}(t_k)_m \boldsymbol{u}(t_k)_m),\end{aligned}$$

where h is the discretization interval, and the t_k is the discrete time and $\boldsymbol{\mathcal{A}}_{KF}(t_k)$ is the system matrix from (5.16) with noise-free sensor input, while $\boldsymbol{\mathcal{A}}_{KF}(t_k)_m$ has noisy sensor input. The same applies to $\boldsymbol{\mathcal{B}}_{KF}(t_k)$ and $\boldsymbol{u}(t_k)$ and their corresponding noisy version. The measurement noise covariance matrix

$$\begin{aligned}\hat{\boldsymbol{R}} &= cov(\boldsymbol{y} - \boldsymbol{y}_m) \\ &= cov(\boldsymbol{0} - \boldsymbol{C}_{KF}(t_k)_m \boldsymbol{x})\end{aligned}$$

was estimated by running 10000 simulations and averaging the covariance estimates from these runs. The matrices were then tested by calculating the normalized error (NE)

$$\begin{aligned}&\mathrm{NE}_Q(t_k) = \\ &\frac{1}{N}\sum [\Delta \boldsymbol{x}(t_k) - \Delta \boldsymbol{x}(t_k)_m]_i^\top \hat{\boldsymbol{Q}}^{-1} [\Delta \boldsymbol{x}(t_k) - \Delta \boldsymbol{x}(t_k)_m]_i,\end{aligned}$$

where $[\Delta \boldsymbol{x}(t_k) - \Delta \boldsymbol{x}(t_k)_m]_i$ is the discrete process noise of the ith MC simulation at time t_k. From this test we could verify that the covariance found was consistent by verifying that $E[\mathrm{NE}_Q(t)] \approx 4$, as $\dim(\hat{\boldsymbol{Q}}) = 4$.

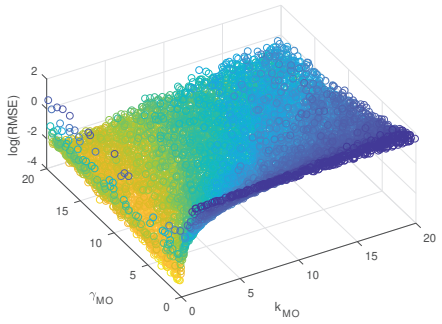

Figure 5.5: Plot of the velocity log(RMSE) error of the MO from 10000 MC simulations with varying tuning parameter

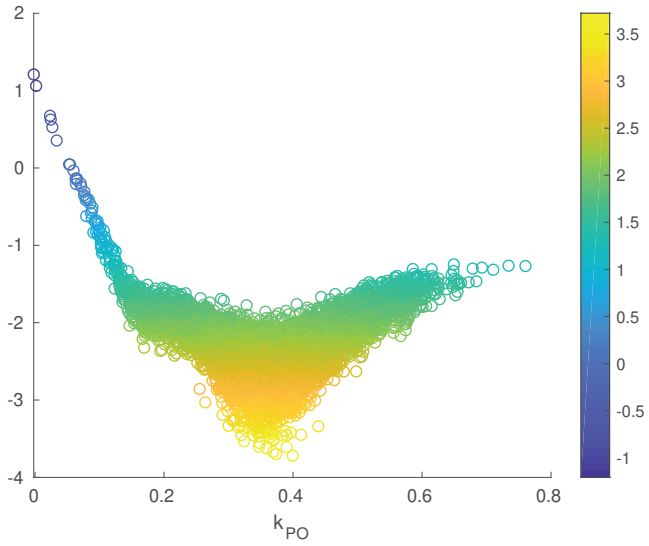

Figure 5.6: Plot of log(RMSE) of the PO from 10000 MC simulations with varying tuning parameters

These covariance matrices were then used as starting point for the tuning of the KF and XKF. It was tried to add a diagonal regularization matrix to these, which improved the performance for the sensor-centric XKF. For the KF the tuning variant giving the best results was multiplying the covariance matrices by gains $\boldsymbol{Q}_{KF} = q_g \hat{\boldsymbol{Q}}_{KF}$ and $\boldsymbol{R}_{KF} = r_g \hat{\boldsymbol{R}}_{KF}$. The results of the KF simulations can be seen in Figure 5.7. The initial covariance $\boldsymbol{P}(0)$ was initialized according to the initial estimate error.

From the result of the MC simulations for the sensor-centric KF, it was evident that the best result with lowest RMSE was $q_g = 0.22$ and $r_g = 4$, as seen in Figure

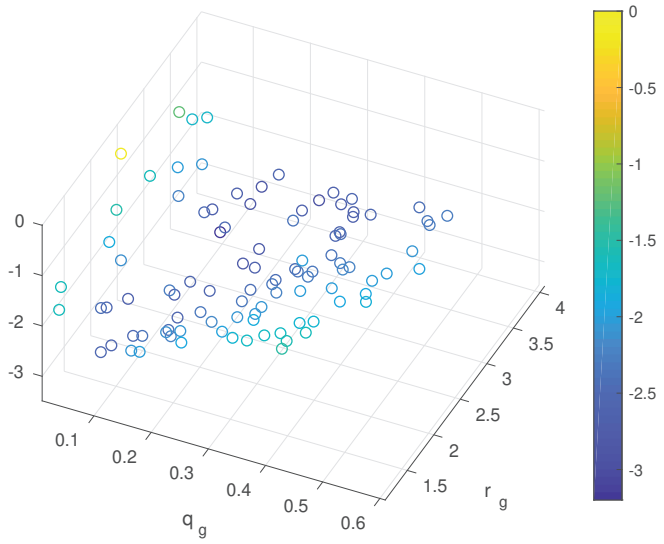

Figure 5.7: Scatter plot of the log(RMSE) error of the KF for different gains multiplied to the covariance matrices. The simulations were run 30 000 times, and tuning parameters were repeated over 300 times. The log(RMSE) shown is the average of 300 runs.

5.7. Why the empirical covariance did not perform best, was probably because the noise is state dependent and the empirical noise was found for actual state estimates. The EKF was similarly tuned, where the covariance of both $\hat{\boldsymbol{a}}^c$ and $\boldsymbol{u}_v^c$ were found through 10000 MC simulations, and later tuning parameters r_{EKF} and q_{EKF} were used so that

$$\begin{aligned}\boldsymbol{Q}_{EKF} &= \boldsymbol{V}\text{cov}([\boldsymbol{\omega}^c; \hat{\boldsymbol{a}}^c])\boldsymbol{V}^\top + \boldsymbol{I}q_{EKF} \\ \boldsymbol{R}_{EKF} &= \text{cov}(\boldsymbol{u}_v^c)r_{EKF}.\end{aligned}$$

where the best values were found to be $q_{EKF} = 2.6 \cdot 10^{-3}$ and $r_{EKF} = 3.6$, and the Jacobian matrix $\boldsymbol{V}$ is defined in the Appendix.

From the MC simulations, we found what we regarded as the best tuning. The observers with the optimal tuning were tested in MC simulations, where the mean and variance of the RMSE can be seen in Table 5.2 columns Mean RMSE B and VAR RMSE B. It can be concluded that the observers performing the best are the MO observer followed by the XKF, as these observers have the combination of low mean and variance of their RMSE. We see that the variance of the sensor-centric KF is significantly larger than the other observers, and by examining the histogram of the RMSE values from the MC simulation we saw that for about 0.61% of the runs the KF failed to converge properly. The relationship between the noise and

In Figure 5.8 we see how the tuning parameters of the MO part of the XKF affected the observer. Both tuning parameters of the MO and KF were varied, however, the most significant parameter for the performance of the XKF seemed to be the k_{MO}. The authors believe the result in Figure 5.8 can be explained by the noise sensitivity of the KF in the cascade. The gain k_{MO} had a large effect on the noise level of the bearing measurements provided to the KF system matrices. And for the gain $k_{MO} = 0.5$, the MO observer worked as a smoothing filter for the bearing measurements. It was also seen how the XKF seemed to have a much larger set of tunings parameters that gave good results compared to the KF.

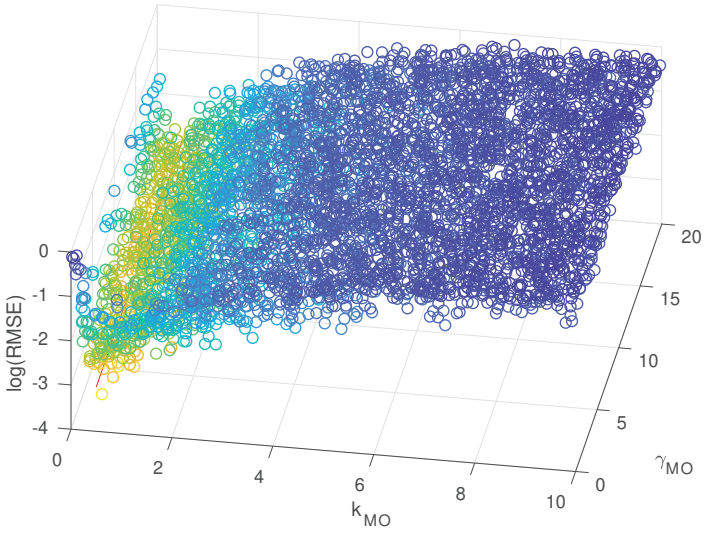

Figure 5.8: Scatter plot of the log(RMSE) of the XKF observer versus the tuning parameters of the MO observer. The results are from 10000 MC simulations, where the diagonal entries of the parameters of the KF are varied from $[0.2,\ 1.5]10^{-3}$ for the process noise covariance matrix $\boldsymbol{Q}$, for the measurement matrix $\boldsymbol{R}$ the parameters varied from $\text{diag}([0.0015,\ 0.01,\ 0.01])$ to $\text{diag}([0.01,\ 0.02,\ 0.02])$

the estimate can also explain why this filter failed to converge for certain runs. For the XKF this problem was not seen, possibly because the noise was significantly reduced by the MO filter.

5.5.3 High Noise simulation

To investigate the noise level robustness of the methods, an MC simulation was run where the variance of all the noise parameters were increased by three times. The same tuning as from the previous simulation was used to see how the observers would react to the change. The results are displayed in Table 5.2 in columns Mean RMSE C and VAR RMSE C. It was seen that the PO and XKF suffered from a substantial bias, and the noisy measurements drove all the KF velocity estimates close to zero, which explained its low variance in the RMSE. The MO

Table 5.2: Table of the resulted mean and variance of the RMSE for 10000 MC simulations for the optimal tuning of the observers. The columns with B ending are for normal noise described in section 5.5.2, while the columns with C ending are from the high noise scenario described in section 5.5.3

Observer	Mean RMSE B	VAR RMSE B	Mean RMSE C	VAR RMSE C
(MO)	0.046	$1.47 \cdot 10^{-4}$	0.192	$5.7 \cdot 10^{-3}$
(PO)	0.076	$4.49 \cdot 10^{-4}$	0.324	$1.8 \cdot 10^{-3}$
(KF)	0.061	0.030	0.638	$6.6 \cdot 10^{-4}$
(XKF)	0.051	$1.349 \cdot 10^{-4}$	0.414	0.015
(EKF)	0.067	$2.473 \cdot 10^{-4}$	2.592*	4.74*

* 45% of the EKF runs had problems converging and ended up with an RMSE that was saturated to 5. None of the other observers had similar problems.

also showed substantially worse results, however, it had the best performance for this simulation. The EKF failed in almost half of the simulations which is reflected in the results. Note the degeneration of the XKF, as this has previously been shown to be resilience toward noise in [18]. However, a re-tuning of the observer would make it perform better, which would be expected to be true for all the observers, especially the EKF.

5.6 Experimental Verification

5.6.1 Experimental setup

The experimental verification was carried out by using an Octocopter flying in a circle with an autopilot for 150 seconds. The data set was recorded from a payload consisting of SenTiStack, which was built up of a SenTiBoard, an uBlox GNSS receiver and a STIM300 tactical grade IMU ([2]). The SenTiBoard was also connected to the flash signal of an uEye UI-3140CP camera, time stamping the flash from the camera so that accurate timing from the images were available. The sensor data and images were stored using an Odroid UX4. Before the flight IMU, camera and temporal calibration was performed using the Kalibr toolbox ([37, 36]), finding IMU biases, as well as the time delay and coordinate transformation between the camera and the IMU. In the data set presented in this article, the image time delay estimated was less than 3 ms, and as the timing of the image was related to the flash signal, it was independent of the kernel load and thus assumed to be constant. As the IMU was tactical grade, the acceleromter and gyro biases were assumed constant for the duration of the experiment and respectively $\boldsymbol{b}_a = [0.03,\ 0.005,\ 0.085]^\top$ [m/s^2] and $\boldsymbol{b}_\omega = [0.007,\ -0.0002,\ 0.0017]^\top$ [rad/s]. The gravity vector was also estimated using this scheme and was propagated using

the gyro for the rest of the flight and used as a gravity measurement, which was possible as the gyro-bias was stable for the time frame recorded. The data set used consists of synchronized and calibrated IMU and camera measurements, in addition, gravity direction estimate in body was initialized according to the calibration, and GNSS was also available as navigation reference.

We also wanted to compare the velocity observers to the homography observer presented in [41]. The nonlinear homography observer is denoted HOM. The UAV flew over a flat field, so that we could use homography transformation between two images to obtain the camera velocity we needed. For more details on how this is done see [41], although we emphasize that for the observers using normalized velocity, the camera velocity can come from many other computer vision algorithms. For feature extraction we used the Kanade-Lucas-Tomasi feature tracker ([106]). The homography matrix was found with a 4-point direct linear transformation (DLT) ([1]). Outlier rejection was done using RANSAC ([32]). The velocity was extracted from the homography using techniques based on [84]. As discussed in [41], the homography can be a limitation for several scenarios. Nevertheless, our experience is that the method is superior to other methods based on epipolar geometry when the features are observed on a close to planar surface ([97]). We therefore chose to use the homography to acquire the camera velocity, and this velocity was then normalized to fit into the unit vector framework. Alternatively we could have applied the two-view framework in [89], where homography and the 5 point algorithm is used in parallel, and the velocity is chosen through a weighting scheme, which would choose the homography as the superior method in this setting. This also shows the flexibility of the unit velocity framework, by how easily the unit velocity measurement is acquired from either the homography or essential matrix.

The velocity reference magnitude in Figure 5.10 was the ublox GNSS velocity. For the reference velocity in Figure 5.11, an RTK and camera aided inertial navigation system (INS) was utilized; based on the unit quaternion and a multiplicative extended Kalman filter (MEKF) ([85]).

5.6.2 Experimental Results

The scenario presented in this section was a vehicle travelling in a circular pattern in 3D-space, with a camera pointing downwards. The trajectory of the vehicle can be seen in Figure 5.9, where the GNSS measurements, velocity and bearing measurements at the last frame are shown. The number of bearing measurements were between 317 and 400.

For the experimental data set, the MO and PO observers were tuned similarly to the simulations. The XKF, KF and EKF had to be re-tuned as they had poor performance with the tuning found in the simulations. The tuning for the experimental data was done with MC simulations.

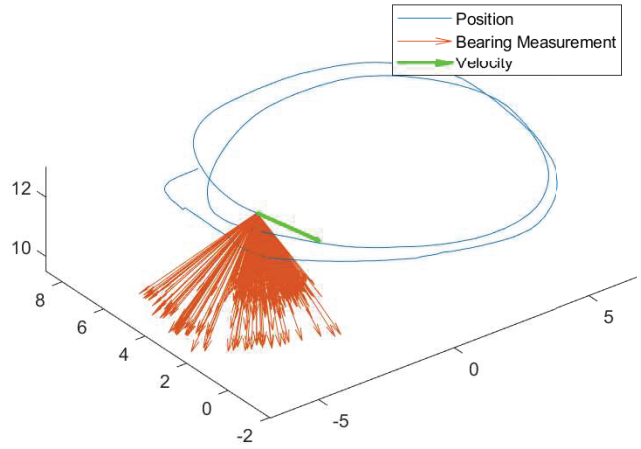

Figure 5.9: The figure shows the trajectory of the vehicle for the experimental verification. The green arrow represents the normalized velocity measurement; the red arrows represent the bearing measurements from the camera, which there are 365 of in this plot.

The continues-time observers were discretized using forward Euler at every image time stamp, where the measurements from the IMU were integrated between the images. The observers were tested on the data with two different initial conditions, and the results can be seen in Table 5.3. From Figure 5.10, we see how the different observers performed on the recorded data set when the velocity was initialized with magnitude $\|\hat{v}^c\| = 3m/s$. The MO observer had comparable results to the HOM observer, and performed superior to the other unit vector observers, with fast convergence and low RMSE error. The EKF started out with a poor transient, that was not seen when the observer was initialized closer to the true value. However the EKF was able to show satisfactory results with a small increase in the error compared to the MO and HOM. The PO, KF and XKF were able to stabilize their estimates, although with varying error. The PO had slow convergence, though, it acquired good accuracy after convergence. The XKF and KF had quite poor estimation, in the steady state condition at the end of the sequence. In the simulation these methods also struggled for small excitation to noise ratios especially KF, which the authors believe is because nonlinear noise is introduced to the system matrices. In Figure 5.11, we see the estimated velocities compared to the estimated velocity from the GNSS and camera aided INS, and especially MO, HOM and eventually PO were able to provide accurate velocity estimates for the experimental setup.

As some of the observers used inverted velocity magnitude as state, it was

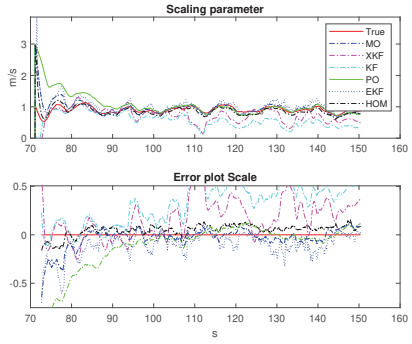

Figure 5.10: The upper plot shows the velocity magnitude estimate combined with the norm of the GNSS velocity, while the bottom plot shows the velocity error

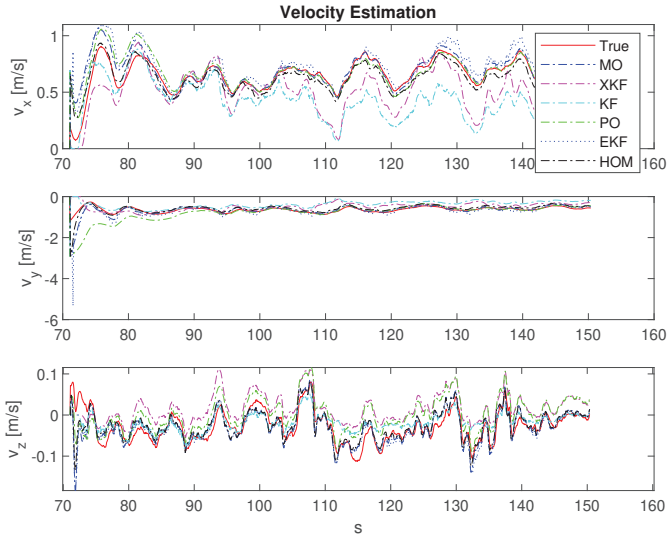

Figure 5.11: The figure shows the estimates of the velocity of the camera compared to the reference velocity.

natural to examine what happened when the inverted estimate increased. The observers were therefore initialized with low velocity. For a velocity lower than $\|\hat{v}^c\| \leq 0.11 m/s$ the EKF had problems converging. A test was therefore performed just above this limit with initial value $\|\hat{v}^c\| = 0.115 m/s$ where the result can be seen in Figure 5.12. Initially, we saw that all the nonlinear observers were able to converge without any issues. Even the MO, which relies on the inverted magnitude estimate, converged. The EKF however struggled when the inverted estimate became small enough, and it overshot the estimates and used tens of seconds to converge. Once they all converged, they had similar accuracy as the previous run,

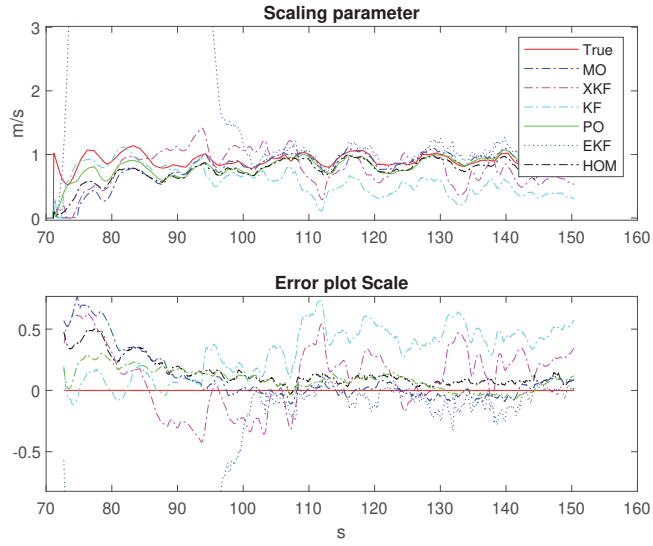

Figure 5.12: The upper plot shows the velocity magnitude estimate combined with the norm of the GNSS velocity, while the bottom plot shows the velocity error.

Table 5.3: RMS error from the experimental results in Figure 5.10. 1: velocity estimate is initialized as $\|\hat{v}^c\| = 3$. 2: velocity estimate is initialized as $\|\hat{v}^c\| = 0.0115$.

	time	MO	PO	XKF	KF	EKF	HOM
1:	$70 \leq t \leq 110$	0.308	0.585	0.270	0.294	0.381	0.215
	$110 \leq t \leq 150$	0.0542	0.0599	0.307	0.477	0.107	0.0820
2:	$70 \leq t \leq 110$	0.346	0.205	0.336	0.260	47.7	0.281
	$110 \leq t \leq 150$	0.0543	0.0762	0.282	0.244	0.107	0.0855

as expected.

5.6.3 Error in Gravity

A possibly optimistic assumption for the presented setup was that an accurate gravity estimate was available through rotation of the gravity vector in NED/ENU coordinates using tactical grade IMU or AHRS measurements. However, there exist several industrial IMU with sub degree error in pitch and roll. To evaluate how an error in gravity could affect the observers, the data set was ran with a time-varying error of the gravity direction oscillating between 0.2^o-0.4^o. The resulting performance can be seen in Figure 5.13, with the corresponding RMSE

presented in Table 5.4. The velocity estimates were initialized similarly as for the previous run with $\|\hat{v}^c\| = 0.115 m/s$. We see that the nonlinear observers

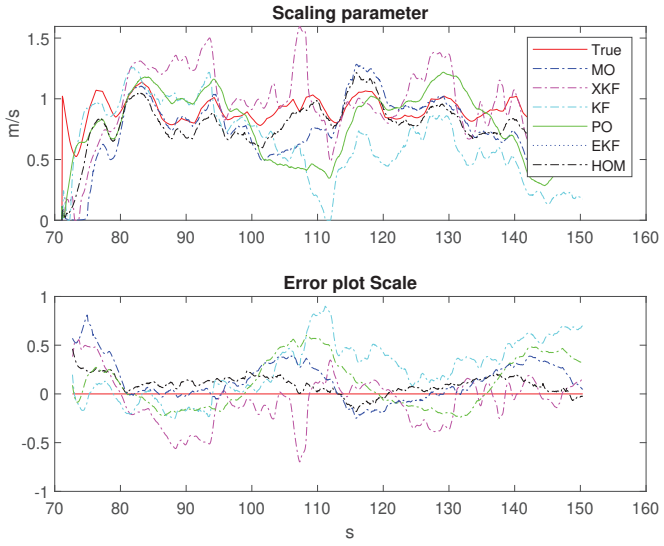

Figure 5.13: The upper plot shows the velocity magnitude estimates combined with the norm of the GNSS velocity, while the bottom plot shows the velocity error, for the data set run with an error in gravity oscillating from $0.2^o - 0.4^o$

Table 5.4: RMSE error from the experimental results in Figure 5.13 with the error in gravity oscilationg from $0.2^o - 0.4^o$

	MO	PO	XKF	KF	EKF	HOM
$70 \leq t \leq 110$	0.324	0.297	0.348	0.300	NaN	0.212
$110 \leq t \leq 150$	0.192	0.277	0.173	0.463	NaN	0.101

were not destabilized, but affected by the error introduced. The EKF diverged in this scenario as the initial estimate $\hat{d}_v$ was too large with gravity error. Among the nonlinear observers, the most affected was the PO observer, which had large oscillations, while the least affected was the HOM observer that had almost the same RMSE, but in this scenario the error was oscillating. The MO observer was also affected by the error, but less than the PO, which can be due to the slow convergence of the PO observer. A surprising result was that the XKF in this scenario had actually better results than without the error. Why this was the case is uncertain, but it could be because the velocity estimates of the XKF were shifted

upwards as a result of the added gravity error, which can be seen by comparing Figures 5.10 and 5.13.

From the experimental results, we thus saw that the nonlinear observers were able to estimate the velocity of the vehicle, with global convergence of the velocity estimate, by only having calibrated IMU/AHRS and camera measurements. This also showed that the ego-motion estimation can be performed by the observers presented. It was also shown that the nonlinear observers had more robust behavior than the robust EKF implementation. It was also seen that the fixed gain observers were easier to tune, and could reuse their tuning on the experimental data set. The proposed setup can either be used for initializing a VO or VIO algorithms if a calibrated IMU/AHRS is available or it can provide globally stable velocity estimates for globally stable bearing-only navigation methods such as in [17, 71, 77], paving the way for a globally stable SLAM solution using self calibrating IMU and camera.

5.7 Conclusion

We presented a comparative study of globally stable observers applied to the ego motion estimation. The solutions give globally stable velocity estimates provided that a camera and an IMU with pitch and roll estimates are available. The comparison was shown both in simulations and using experimental data. The tuning of the different observers was discussed and performed using Monte Carlo simulations and by estimating the measurement and process noise of some of the observers. In simulations the MO observer performed the best, followed by the XKF observer, where it was also shown how the MO observer could filter the unit vector measurements. Also on experimental data, the MO observer was shown to have the best overall performance of the velocity direction observers, with fast convergence and small RMSE in steady state. The nonlinear observers were also compared to an EKF, and the observers were shown to have a more robust performance than the EKF.

The results of this article confirms that ego-motion estimation with camera is possible with global convergence of the velocity estimate, provided that an IMU, with pitch/roll estimates and camera is available, which becomes a more favorable setup as IMU sensors improve their performance in the future.

6 *Globally stable inertia bearing only SLAM Part 1: Redesign*

6.1 Introduction

Robust navigation and positioning of unmanned aerial vehicles (UAVs) are fundamental for any autonomous mission, particularly in challenging environments where absolute positioning systems are absent or unreliable. A scenario were the UAV's and other autonomous vehicles are used for inspection missions, demonstrates the need of high accuracy and consistency in position and attitude estimates. In this scenario the vehicles will have to work as closely as possible to the inspection target, which increases the need for stable, consistent and accurate estimates. Missions can be the inspection of structures such as bridges, power lines, windmills etc. In this case, the electromagnetic interference and the existence of ferromagnetic materials from the environment may degrade any magnetometer to the point of becoming unusable [47]. To tackle these situations, aided navigation techniques such as simultaneous localization and mapping algorithm (SLAM) can be used. SLAM fuses the data from the surroundings with the data from the inertal measurements unit (IMU) to increase accuracy in the navigation. By assuming stationary landmarks, the change in the landmarks relative positions (LRP) can give information about the motion of the vessel, and hence can be fused with the IMU to increas navigation estimates. These sensors are typically provided in ranges and/or bearing angles between the vehicle and each landmark, and with these SLAM also builds a map of the surroundings of the vehicle. Over the past decades, the research community has devoted tremendous effort in the field of probabilistic SLAM. For a detailed review on SLAM see [28] and [6], and the references within, which includes several successful implementations of SLAM algorithms in experiments. A common approach is to use the extended Kalman filter (EKF) SLAM, however, there are some challenges related to consistency and stability, especially in regards of the error in the linearization due to wrong attitude estimates [22]. For bearing only SLAM, there are a variety of methods; filter banks [70], Rao-Blackwellized particle filters (RBPF)[15], linear mono SLAM [115] and multi-state constraint Kalman filter (MSCKF) [88]. In [73], a hybridized SLAM decides if a feature is processed using MSCKF or EKF, depending on the feature's track length; this in order to decrease computation time.

A proposed structure for global exponentially stable (GES) estimation was presented by Johansen and Brekke [58], for range and bearing, bearing only and range only SLAM. Nonlinearities from the attitude are handled by a nonlinear observer [42], so that the the nonlinear system can be represented as a linear time

varying (LTV) system. This gives the LTV system

$$\dot{x}(t) = A(z(t), t)x(t) + B(z(t), t)u(t) \tag{6.1}$$
$$y(t) = C(z(t), t)x(t) \tag{6.2}$$

where x is a vector with the states of the vehicle and landmark positions, y is the vector output with a linear time varying dependency to the states. The vector z contains auxilliary, possible nonlinear, measurements, such as attitude and bearing angles represented as a linear time varying rotation matrix and line of sight (LOS) vectors; The u are the inputs to the system such as acceleration. This representation makes the SLAM problem solvable with the Kalman filter (KF), and global stabillety can be proven by observability analysis [3]. Further, necessary and sufficient conditions on the observability of the nonlinear system are derived in [12]. Similar work, is done by Lourenco and Guerreiro [79][47], in which a globally asymptotically stable (GAS) sensor-based SLAM estimation is presented, for range and bearing, bearing only and range only measurements. In addition, they are able to estimate the gyro bias with range and bearing measurements. They also present the SLAM problem as a LTV system and uses KF for estimation, however, they present the system in the coordinate system of the sensors, called robosentric coordinate system.

6.1.1 Contribution

The contribution of this paper is two-folded. The main contribution is the redesign of the bearing only SLAM presented in [58]. The new design requires less sensors as it uses neither gyro nor bearing derivative. In addition, an intuitive assumption for achieving observability is found, and is less restrictive compared to the one from [58], explained in Section 6.8. In addition, a novel design of the output covariance matrices through linearisation are proposed and analysed. Simulations are done in 2D, and Monte Carlo (MC) simulations were used to investigate the consistency of the SLAM estimator.

The structure of this paper is as follows: Section 6.2 contains the previous work of the presented SLAM estimation; Section 6.3 presents the new bearing only SLAM estimation, with observability analysis of the system. Section 6.4 presents the the design of the covariance matrix, while Section 6.5 shows the simulation results. Section 6.6 concludes the paper and suggests future work.

6.2 Previous Work

As mentioned, a GES SLAM estimation was presented by [58]. Both range and bearing, bearing only and range only SLAM were presented as a LTV system, and solved with Kalman filter. The nonlinearities from the attitude are estimated with the comlimentary filter [42], with semi-globally exponetially stability. The stability

of the system is then proved by observability for the LTV system. Similar work has been done by Lourence and Guerreiro [79] [47], where a range and bearing, and bearing only, SLAM filter is presented in body-frame coordinate system. The global stability is proven with an observability analysis, thus guaranteeing GES of estimator using the Kalman filter. When using the Kalman filter, an assumption is that the process and measurement noise is Gaussian and white, and can therefore be represented by the covariance matrices $\boldsymbol{Q}$ and $\boldsymbol{R}$ although this is not the case for the nonlinear measurements coming out of the LOS vector and rotation matrix. This means the LTV solution is not necessary optimal but the strong convergence provided by the KF, combined with approximation of the noise characteristics; results in a stable and useful estimation.

For the observability analysis of [58], an assumption was made in which

$$\|\boldsymbol{S}(\omega)\boldsymbol{l}_i^b + \dot{\boldsymbol{l}}_i^b\| \geq \epsilon \tag{6.3}$$

for some $\epsilon > 0$. By examining the dynamics of the bearing measurements (2.32), we see that this assumption is violated every time the velocity $\boldsymbol{v}^b$ is parallel to the bearing measurement $\boldsymbol{l}_i^b$, which gives a restriction on the suitable paths. To address this, a new bearings only SLAM estimation is presented with a new observability analysis.

In addition, an algorithm for estimating the vehicles position was presented in [58]; where the vehicle estimate is set to zero at the start $\boldsymbol{p}^n(0) = \boldsymbol{0}$, which gives

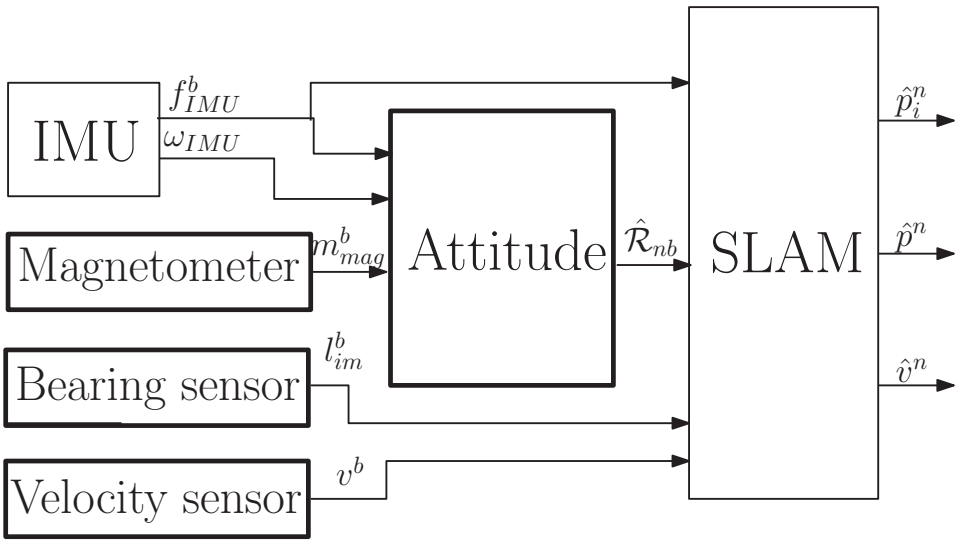

Figure 6.1: Block Diagram of the structure of the SLAM attitude observer in cascade with the SLAM filter

$\boldsymbol{p}_i^n = \boldsymbol{\delta}_i^n(0)$. The position can then be estimated as

$$\hat{\boldsymbol{p}}^n(t) = \sum_{i=1}^{m} w_i(t)(\dot{\hat{\boldsymbol{\delta}}}_i^n(0) - \dot{\hat{\boldsymbol{\delta}}}_i^n(t)) \tag{6.4}$$

$$\hat{\boldsymbol{p}}_i^n(t) = \hat{\boldsymbol{p}}^n(t) + \dot{\hat{\boldsymbol{\delta}}}_i^n(t), \quad i = \{1, m\} \tag{6.5}$$

where it should be noted that the estimate will converge with a constant deviation so that $\hat{\boldsymbol{p}}^n(t) = \boldsymbol{p}^n(t) + \boldsymbol{d}$, in which $\boldsymbol{d} = \sum_{i=1}^{m} w_i(t)\tilde{\boldsymbol{\delta}}_i^n(0)$.

Table 6.1: Overview of the Bearing only SLAM, for the corresponding matrices see [58]

Bearing Only SLAM, [58]	
States	Input
$x = [v^n,\ \delta_1^n,\ \cdots,\ \delta_m^n,\ \varrho_1,\ \cdots,\ \varrho_m]^\top$	$u = \boldsymbol{\mathcal{R}}_{nb} f_{IMU}^b + g^n$
Measurement model	
$y^v = v^b = (\boldsymbol{\mathcal{R}}_{nb})^\top v^n\ ,\ y = [y^v,\ y_1^V,\ \cdots,\ y_m^V,\ y_1^E,\ \cdots,\ y_m^E]^\top$ $y_i^V = 0 = \delta_i^n - \boldsymbol{\mathcal{R}}_{nb}\varrho_i l_i^b$ $y_i^E = 0 = w_i v^n - q_i \varrho_i l_i^b$ $w_i = S(l_i^b)^2(\boldsymbol{\mathcal{R}}_{nb})^\top,\ q_i = S(\omega) l_i^b + \dot{l}_i^b$	
Dynamics model	
$\dot{v}^n = u$ $\dot{\delta}_i^n = -v^n$ $\dot{\varrho}_i = -(l_i^b)^\top(\boldsymbol{\mathcal{R}}_{nb})^\top v^n$	

Table 6.2: Overview of proposed the Bearing only SLAM

New Bearing Only SLAM	
States	Input
$x = [v^n,\ \delta_1^n,\ \cdots,\ \delta_m^n \varrho_1,\ \cdots,\ \varrho_m]^\top$	$u = \boldsymbol{\mathcal{R}}_{nb} f_{IMU}^b + g^n$
Measurement model	
$y^v = v^b = (\boldsymbol{\mathcal{R}}_{nb})^\top v^n \ ,\ y = [y^v,\ y_1^V,\ \cdots,\ y_m^V]^\top$ $y_i^V = 0 = \delta_i^n - \boldsymbol{\mathcal{R}}_{nb} \varrho_i l_i^b$	
Dynamics model	
$\dot{v}^n = u$ $\dot{\delta}_i^n = -v^n$ $\dot{\varrho}_i = -(l_i^b)^\top (\boldsymbol{\mathcal{R}}_{nb})^\top v^n$	

6.3 Observability analysis

The proposed bearing only SLAM model is presented in Table 6.2. For the states $\boldsymbol{x} = [\boldsymbol{v}^n,\ \boldsymbol{\delta}_1^n,\ \cdots,\ \boldsymbol{\delta}_m^n \varrho_1,\ \cdots,\ \varrho_m]^\top$, the corresponding system matrices will be

$$\boldsymbol{A}^B = \begin{bmatrix} \boldsymbol{0} & \boldsymbol{0} \cdots & \boldsymbol{0} \\ -\boldsymbol{I}_3 & \boldsymbol{0} \cdots & \boldsymbol{0} \\ \vdots & \ddots & \vdots \\ -\boldsymbol{I}_3 & \boldsymbol{0} \cdots & \boldsymbol{0} \\ -(\boldsymbol{\mathcal{R}}_{nb}\boldsymbol{u}_1^b)^\top & \boldsymbol{0} \cdots & \boldsymbol{0} \\ \vdots & \ddots & \vdots \\ -(\boldsymbol{\mathcal{R}}_{nb}\boldsymbol{u}_m^b)^\top & \boldsymbol{0} \cdots & \boldsymbol{0} \end{bmatrix} \boldsymbol{B}^B = \begin{bmatrix} \boldsymbol{I}_3 \\ \boldsymbol{0} \\ \vdots \\ \boldsymbol{0} \\ \boldsymbol{0} \\ \vdots \\ \boldsymbol{0} \end{bmatrix}$$

$$\boldsymbol{C}^B = \begin{bmatrix} \boldsymbol{\mathcal{R}}_{nb}^\top & \boldsymbol{0} & \cdots & \boldsymbol{0} & \boldsymbol{0} & \cdots & \boldsymbol{0} \\ \boldsymbol{0} & \boldsymbol{I}_3 & \cdots & \boldsymbol{0} & -\boldsymbol{\mathcal{R}}_{nb}\boldsymbol{u}_1^b & \cdots & \boldsymbol{0} \\ \vdots & \vdots & \ddots & \vdots & \vdots & \ddots & \vdots \\ \boldsymbol{0} & \boldsymbol{0} & \cdots & \boldsymbol{I}_3 & \boldsymbol{0} & \cdots & -\boldsymbol{\mathcal{R}}_{nb}\boldsymbol{u}_m^b \end{bmatrix}$$

We make an assumption on the trajectory of the vessel, to ensure observability of the bearing only SLAM:

Assumption 2. *There exist a $T > 0$, so that for every landmark a $\tau_i > 0$ exists, so that for all $t > 0$ we have $t < \tau_i < t + T$, and that $\dot{\boldsymbol{u}}_i^n(\tau_i) \neq 0$. In addition, $\dot{\boldsymbol{u}}_v^n$ is uniformly continuous.*

This assumption ensures that the vehicle does not moves on a fixed line from a landmark (see Figure 6.2), ensuring that $\dot{\boldsymbol{u}}_i^n(\tau_i) \neq 0$ for any landmarks for the entire observation period.

Theorem 8. *The model presented in Table 6.2, is UCO if and only if assumption 2 holds.*

Proof. We will use the same techniques as in [78]. In the proof we will show that the subsystems $x_i^B = [\boldsymbol{v}^n,\ \boldsymbol{\delta}_i^n,\ \varrho_i]^\top$ for each landmark is observable. Because of the independence of the landmarks, the entire system is completely characterized by the subsystem in terms of observability. This gives the system

$$\boldsymbol{\mathcal{A}}^B(t) = \begin{bmatrix} \boldsymbol{0} & \boldsymbol{0} & \boldsymbol{0} \\ -\boldsymbol{I}_3 & \boldsymbol{0} & \boldsymbol{0} \\ -(\boldsymbol{\mathcal{R}}_{nb}(t)\boldsymbol{u}_i^b(t))^\top & \boldsymbol{0} & \boldsymbol{0} \end{bmatrix}$$

$$\boldsymbol{C}^B = \begin{bmatrix} \boldsymbol{\mathcal{R}}_{nb}^\top(t) & \boldsymbol{0} & \boldsymbol{0} \\ \boldsymbol{0} & \boldsymbol{I}_3 & -\boldsymbol{\mathcal{R}}_{nb}(t)\boldsymbol{u}_i^b(t) \end{bmatrix}$$

which is UCO as proven by calculating the transition matrix for the subsystem, and then calculateing the observability Gramian. The state transition matrix is found by the Peano-Baker series [25]

$$\boldsymbol{\Phi}(t,t_0) = \boldsymbol{I}_3 + \int_{t_0}^{t} \boldsymbol{\mathcal{A}}^B(\sigma_1)d\sigma_1 + \int_{t_0}^{t} \boldsymbol{\mathcal{A}}^B(\sigma_1)\int_{t_0}^{\sigma_1} \boldsymbol{\mathcal{A}}^B(\sigma_2)d\sigma_2 d\sigma_1 \cdots \tag{6.6}$$

where we see by the structure of $\boldsymbol{\mathcal{A}}^B(\sigma_2)$ that $\boldsymbol{\mathcal{A}}^B(\sigma_2)^2 = \boldsymbol{0}$, which also is the case for $\boldsymbol{\mathcal{A}}^B(\sigma_1)\int_{t_0}^{\sigma_1} \boldsymbol{\mathcal{A}}^B(\sigma_2)d\sigma_2 = \boldsymbol{0}$, because the integral preserves the zero elements of the matrix. This eliminates all the higher terms of the Peano-Baker serie, so we are left with

$$\boldsymbol{\Phi}(t,t_0) = \boldsymbol{I}_3 + \int_{t_0}^{t} \boldsymbol{\mathcal{A}}^B(\sigma_1)d\sigma_1 = \begin{bmatrix} \boldsymbol{I}_3 & \boldsymbol{0} & \boldsymbol{0} \\ (t-t_0)\boldsymbol{I}_3 & \boldsymbol{I}_3 & \boldsymbol{0} \\ -\boldsymbol{RL}_*(t,t_0)^\top & \boldsymbol{0} & \boldsymbol{I}_3 \end{bmatrix}$$

where $\boldsymbol{RL}_*(t,t_0) = \int_{t_0}^{t} \boldsymbol{\mathcal{R}}_{nb}(\tau)\boldsymbol{u}_i^b(\tau)d\tau$. This can be inserted to (2.52) for confirmation. We can then calculate the observability Gramian

$$\boldsymbol{\mathcal{W}}(t+T,t) = \int_{t}^{t+T} (\boldsymbol{C}^B\boldsymbol{\Phi}(\tau,t))^\top(\boldsymbol{C}^B\boldsymbol{\Phi}(\tau,))d\tau \tag{6.7}$$

(6.8)

where

$$\boldsymbol{C}^B\boldsymbol{\Phi}(\tau,t) = \begin{bmatrix} \boldsymbol{\mathcal{R}}_{nb}^\top & 0 & 0 \\ \boldsymbol{c}_{[1]}(\tau,t) & I & \boldsymbol{\mathcal{R}}_{nb}\boldsymbol{u}_{\delta i}^b \end{bmatrix} \tag{6.9}$$

and $\boldsymbol{c}_{[1]}(t,t_0) = \boldsymbol{I}(t-t_0)+\boldsymbol{\mathcal{R}}_{nb}\boldsymbol{u}_{\delta i}^b\boldsymbol{RL}_*(t,t_0)^\top$ If the observability Gramian is full rank, the system is UCO. If $\boldsymbol{\mathcal{W}}(t,t_0)$ is not full rank, there exist a vector $\boldsymbol{c} = [\boldsymbol{c}_v^\top,\ \boldsymbol{c}_\delta^\top,\ c_\varrho^\top]^\top$ with magnitude $\|\boldsymbol{c}\| = 1$ such that

$$\boldsymbol{c}^\top\boldsymbol{\mathcal{W}}(t,t_0)\boldsymbol{c} = 0 \tag{6.10}$$

which corresponds to

$$\boldsymbol{c}^\top\boldsymbol{\mathcal{W}}(t+T,t)\boldsymbol{c} = \int_{t}^{t+T} \|\boldsymbol{C}^B\boldsymbol{\Phi}(\tau,t)\boldsymbol{c}\|d\tau = \int_{t}^{t+T} \|\boldsymbol{f}(\tau,t)\|d\tau$$

We then need to find a $\boldsymbol{c}$ so that $\boldsymbol{f}(\tau, t) = \boldsymbol{C}^B \boldsymbol{\Phi}(\tau, t)\boldsymbol{c}$ and its derivative is zero for all $\tau > 0$. Which gives the equations

$$\boldsymbol{f}(\tau, t) = \begin{bmatrix} \boldsymbol{\mathcal{R}}_{nb}^\top(\tau)\boldsymbol{c}_v \\ \boldsymbol{c}_v \boldsymbol{c}_{[1]}(\tau, t) + \boldsymbol{c}_\delta + \boldsymbol{u}_i^n(\tau) c_\varrho \end{bmatrix} = \boldsymbol{0} \tag{6.11}$$

$$\dot{\boldsymbol{f}}(\tau, t_0) = \begin{bmatrix} -\boldsymbol{S}(\omega(\tau))\boldsymbol{\mathcal{R}}_{nb}^\top(\tau)c_v \\ \boldsymbol{c}_v \dot{\boldsymbol{c}}_{[1]}(\tau, t) + \dot{\boldsymbol{u}}_i^n(\tau) c_\varrho \end{bmatrix} = \boldsymbol{0} \tag{6.12}$$

Immediately we see from (6.11) that it is necessary with $\boldsymbol{c}_v = \boldsymbol{0}$, which leads to the equality $\boldsymbol{c}_\delta = \boldsymbol{u}_i^n \boldsymbol{c}_\varrho$. We also see from (6.12) that we need to have $\dot{\boldsymbol{u}}_i^n c_\varrho = \boldsymbol{0}$. By Assumption 2, there exist a τ_i such that $\dot{\boldsymbol{u}}_i^n(\tau_i) \neq \boldsymbol{0}$, which implies that we need $c_\varrho = 0$, which again imply that $\boldsymbol{c}_\delta = \boldsymbol{0}$, following from (6.11). This contradicts that $\|\boldsymbol{c}\| = 1$. We have proven that the the Gramian $\boldsymbol{\mathcal{W}}(t + T, t)$ is full rank, and the system is UCO, if and only if Assumption 2 holds. □

In the proof we showed that the bearing only SLAM is UCO, if and only if, there exist a τ_i such that $\dot{\boldsymbol{u}}_i^n(\tau_i) \neq \boldsymbol{0}$, which implies that the inertia-frame bearing measurement $\boldsymbol{\mathcal{R}}_{nb}\boldsymbol{u}_{\delta i}^b$ can't be constant. This is shown by assuming that the bearing measurement is indeed constant, and showing that it makes the system unobservable. For the assumption $\dot{\boldsymbol{u}}_i^n \neq \boldsymbol{0}$ not to hold, we can see from (2.27), that the velocity vector of the vehicle has to be zero or parallel to the bearing such that $\boldsymbol{S}(\boldsymbol{u}_i^n)\boldsymbol{v}^n = 0$ for all time. By definition of observability [99], an observable system must be able to distinguish two different initial states, by the knowledge of the input and output only. Then consider the two cases, scenario a and b, where two vehicles start at different distance from a landmark, but along the same angle and moving parallel to the bearing measurements $\boldsymbol{u}_i^n$ at the same velocity and orientation, and has the same acceleration (see Figure 6.2). This would result in them having the same matrices $\boldsymbol{\mathcal{A}}^B$ and $\boldsymbol{C}^B$. If then, they in addition start with the same estimates $[\hat{\boldsymbol{v}}_a^n(0),\ \hat{\boldsymbol{\delta}}_a^n(0),\ \hat{\boldsymbol{\varrho}}_a(0)] = [\hat{\boldsymbol{v}}_b^n(0),\ \hat{\boldsymbol{\delta}}_b^n(0),\ \hat{\boldsymbol{\varrho}}_b(0)]$, it would lead to the same state estimate evolution and output $\boldsymbol{y}_a(t) = \boldsymbol{y}_b(t)$, thus the different initial conditions are not indistinguishable from each other which makes the system unobservable. Since we have shown that the system $(\boldsymbol{\mathcal{A}}^B, \boldsymbol{C}^B)$ is UCO if the Assumption 2 holds, we know that globally exponentially stability can be achieved for the KF in the nominal case.

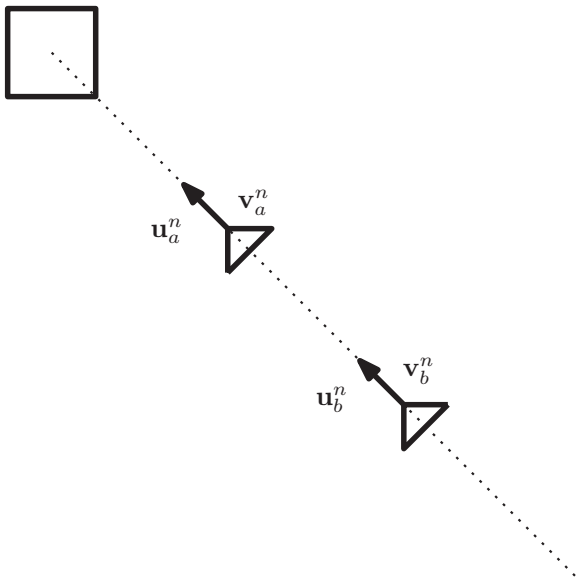

Figure 6.2: Two scenarios where the vehicle starts at the same angle from a landmark, with the same velocity along parallel trajectory to its global bearing measurement.

6.4 Covariance matrix design

In this section we will estimate the covariance matrices $\boldsymbol{Q}_B$ and $\boldsymbol{R}_B$ for the plant noise $\boldsymbol{w}_x$ and output noise $\boldsymbol{w}_y$, respectivly, when the bearings only SLAM is implemented. As mentioned, the dependency of $\boldsymbol{A}^B$ and $\boldsymbol{C}^B$ on bearing measurements and the rotation matrix, gives the need of approximating the noise characteristics. If the noises are small perturbations, linearisation can give good approximation of the noise characteristics. It should be noted that suboptimal covariance matrices $\boldsymbol{Q}_B$ and $\boldsymbol{R}_B$ will not damage the global stability, which can be seen in [3]. It is shown in the proof that symmetry and positive definiteness are sufficient conditions on $\boldsymbol{Q}_B$ and $\boldsymbol{R}_B$ for the nominal system to be GAS. The sensor models in Section 2.5 for the 2-D scenario will be used.

6.4.1 Introduction of virtual noise

When approximating $\boldsymbol{w}_x$ and $\boldsymbol{w}_y$ through linearisation, a problem is that the dimension of the output vector $\boldsymbol{y}$ from the bearing only SLAM in 2-D have dimension $2m + 2$, while the number of sensor measurements used in the output are $m + 3$. The rank of the covariance matrix of the sensor matrix $\boldsymbol{S}_B$ is therefore less than the dimension of the covariance of the output matrix $\boldsymbol{R}_B$, which can result in a singular output covariance matrix approximation

$$\hat{\boldsymbol{R}}_B = \boldsymbol{Y}_w \boldsymbol{S}_B \boldsymbol{Y}_w^\top. \tag{6.13}$$

The vector $\boldsymbol{w}$ contains all the noise variable from the measurements, which for our case could be $\boldsymbol{w} = [w_{v1},\ w_{v2},\ w_{\psi},\ w_{\beta 1}, \cdots,\ w_{\beta m}]^{\top}$. The matrix $\boldsymbol{Y}_w$ is then the Jacobian $\boldsymbol{Y}_w = \frac{\partial \boldsymbol{y}}{\partial \boldsymbol{w}}$. With this in mind, and the fact that the distributions from the bearing vectors is nonlinear and has a covariance with dimensions two, while the bearing angle has dimension one; it is natural to introduce a virtual noise parallel to the bearing measurement

$$\boldsymbol{u}^b_{\delta i m} = \begin{bmatrix} \cos(\beta_i + w_{\beta i}) \\ \sin((\beta_i + w_{\beta i}) \end{bmatrix} (1 + w_{li}) \tag{6.14}$$

By introducing the virtual noise, the dimension of the sensor matrix increases to $2m+3$, which ensures a full rank output covariance matrix when using (6.13). This also improved the performance of the filter substantially, compared to just using regularization.

6.4.2 Noise model Linearization

As mentioned, linearisation was used for approximating the nonlinear stochastic models. Hence we need the partial derivatives with regard to the noise inputs for the rotation matrix

$$\frac{\partial \boldsymbol{\mathcal{R}}_{nb}}{\partial w_{\psi}} = \boldsymbol{\mathcal{R}}_{nb} \boldsymbol{S}(1) \tag{6.15}$$

where $S(1)$ is the matrix

$$\boldsymbol{S}(1) = \begin{bmatrix} 0 & -1 \\ 1 & 0 \end{bmatrix} \tag{6.16}$$

The LOS partial derivatives with regard to the noise inputs is then

$$\frac{\partial \boldsymbol{u}^b_{\delta i m}}{\partial w_{\beta j}} = \begin{cases} S(1)\boldsymbol{u}^b_{\delta i} & i = j \\ \boldsymbol{0} & i \neq j \end{cases} \tag{6.17}$$

$$\frac{\partial \boldsymbol{u}^b_{\delta i m}}{\partial w_{l j}} = \begin{cases} \boldsymbol{u}^b_{\delta i} & i = j \\ \boldsymbol{0} & i \neq j \end{cases} \tag{6.18}$$

Where i and j are different indices for LOS measurements. For the process model, the main noise will come from the accelerometer, as an input to the velocity estimate $\hat{\boldsymbol{v}}^n$ thus propagating to the rest of the estimates by the Kalman filter. In addition, the range estimates have noise coming from the auxiliary measurement vectors $\boldsymbol{u}^b_{\delta i}$ and matrix $\boldsymbol{\mathcal{R}}_{nb}$. Since these occur in both $\boldsymbol{A}^B$ and $\boldsymbol{C}^B$, there will be correlations between the plant noise and the measurement noise. Simulations where done, where the noise in $\boldsymbol{A}^B$ was turned of, without any notable difference, so in this

paper the noise from $\boldsymbol{A}^B$ and $\boldsymbol{C}^B$ are assumed uncorrelated, and implemented that way. Recall that the landmark distances are given by the differential equations

$$\begin{aligned}\dot{\varrho}_i = f_i(\boldsymbol{x}, t) &= (\boldsymbol{\mathcal{R}}_{nb}(\psi_m)\boldsymbol{u}^b_{\delta i}(\beta_m))^\top \boldsymbol{v}^n \\ &= (\boldsymbol{\mathcal{R}}_{nb}(\psi)\boldsymbol{u}^b_{\delta i}(\beta))^\top \boldsymbol{v}^n + w_{xi}\end{aligned}$$

where w_{xi} is the plant noise. From Table 2.1, we see that the measurements related to $\boldsymbol{u}^b_{\delta i}$ and $\boldsymbol{\mathcal{R}}_{nb}$ are the attitude ψ, and bearing angles β_i. In addition, the virtual noise w_l was introduced, as explained in Section 2.5. We therefore introduce the noise vector $\boldsymbol{w}_i = [w_\psi,\ w_{\beta i},\ w_{li}]$, with covariance $\boldsymbol{S}_{Bi} = \text{diag}(\sigma^2_\psi,\ \sigma^2_{\beta i},\ \sigma^2_{li})$. To estimate the plant noise w_{xi} linearisation is used

$$\hat{w}_{xi} = \frac{\partial f_i}{\partial \boldsymbol{w}_i}\boldsymbol{w}_i = \boldsymbol{f}_{wi}\boldsymbol{w}_i. \tag{6.19}$$

With partial derivatives from above we find

$$\begin{aligned}\boldsymbol{f}_{wi} &= \begin{bmatrix}\frac{\partial f_i}{\partial w_\psi} & \frac{\partial f_i}{\partial w_{\beta i}} & \frac{\partial f_i}{\partial w_{li}}\end{bmatrix} \\ \boldsymbol{f}_{wi} &= \begin{bmatrix}-(\boldsymbol{\mathcal{R}}_{nb}\boldsymbol{S}(1)\boldsymbol{u}^b_{\delta i})^\top \boldsymbol{v}^n & -(\boldsymbol{\mathcal{R}}_{nb}\boldsymbol{S}(1)\boldsymbol{u}^b_{\delta i})^\top \boldsymbol{v}^n & -(\boldsymbol{\mathcal{R}}_{nb}\boldsymbol{u}^b_{\delta i})^\top \boldsymbol{v}^n\end{bmatrix}\end{aligned}$$

Giving the covariance of the ϱ_i dynamic to be estimated as

$$\hat{q}_{B\varrho i} = \boldsymbol{f}_{wi}\boldsymbol{S}_{Bi}\boldsymbol{f}^\top_{wi} \tag{6.20}$$

the plant noise covariance matrix of the whole system will then become

$$\hat{\boldsymbol{Q}}_B = \boldsymbol{Q}_B + \boldsymbol{Q}_{Bf} + \boldsymbol{F}_w\boldsymbol{S}_B\boldsymbol{F}^\top_w. \tag{6.21}$$

The covariance matrix $\boldsymbol{Q}_{Bf} = \text{diag}(\sigma^2_f,\ \sigma^2_f,\ 0, \cdots, 0)$ is from the accelerometer; The matrix $\boldsymbol{Q}_B$ is included to allow some tuning, although it was left zero in the implementation. The matrix $\boldsymbol{S}_B$ is the covariance matrix of the vector $\boldsymbol{w} = [w_\psi,\ w_{\beta 1},\ w_{l1},\ \cdots,\ w_{\beta m},\ w_{lm}]^\top$, which is the noise vector for the whole system, dependent on how many landmarks there are. The matrix $\boldsymbol{F}_w$ is the Jacobian matrix with respect to the $\boldsymbol{w}$ of $\dot{\boldsymbol{x}} = \boldsymbol{f}(t, x) = \boldsymbol{A}^B\boldsymbol{x}$ for the whole system

$$\boldsymbol{F}_w = \begin{bmatrix}\boldsymbol{0} & \boldsymbol{0} & \dots & \boldsymbol{0} & \boldsymbol{f}^{1\top}_w & \dots & \boldsymbol{f}^{m\top}_w\end{bmatrix}^\top \tag{6.22}$$

where the row vector $\boldsymbol{f}^i_w$ is the partial derivative of row number i of $\boldsymbol{f}(t, x)$ with respect of the the vector $\boldsymbol{w}$, i.e. $\boldsymbol{f}^i_w = [\frac{\partial f_i}{\partial w_\psi}, \cdots \frac{\partial f_i}{\partial w_{\beta i}}, \frac{\partial f_i}{\partial w_{li}}, \cdots]$

The same method is employed for the output model. The outputs are

$$\boldsymbol{y}^B_v = \boldsymbol{g}_v(t, x) = \boldsymbol{\mathcal{R}}^\top_{nb}\boldsymbol{v}^n \tag{6.23}$$

$$\boldsymbol{y}^B_i = \boldsymbol{g}_i(t, x) = \boldsymbol{\delta}^b_i - \boldsymbol{\mathcal{R}}_{nb}\boldsymbol{u}^b_{\delta i}\varrho_i \tag{6.24}$$

where i is the index of the landmark. To approximate the noise of the output, linearisation can also be used here

$$\hat{\boldsymbol{w}}_{yv} = \frac{\partial \boldsymbol{g}_v}{\partial \boldsymbol{w}_i} \boldsymbol{w}_i = \boldsymbol{G}_{wv} \boldsymbol{w}_i \tag{6.25}$$

$$\hat{\boldsymbol{w}}_{yi} = \frac{\partial \boldsymbol{g}_i}{\partial \boldsymbol{w}_i} \boldsymbol{w}_i = \boldsymbol{G}_{wi} \boldsymbol{w}_i \tag{6.26}$$

With partial derivatives from section 2.5 we find

$$\boldsymbol{G}_{wv} = \begin{bmatrix} \frac{\partial \boldsymbol{g}_v}{\partial w_\psi} & \frac{\partial \boldsymbol{g}_v}{\partial w_{\beta i}} & \frac{\partial \boldsymbol{g}_v}{\partial w_{li}} \end{bmatrix}, \; \boldsymbol{G}_{wi} = \begin{bmatrix} \frac{\partial \boldsymbol{g}_i}{\partial w_\psi} & \frac{\partial \boldsymbol{g}_i}{\partial w_{\beta i}} & \frac{\partial \boldsymbol{g}_i}{\partial w_{li}} \end{bmatrix}$$

leading to

$$\boldsymbol{G}_{wv} = \begin{bmatrix} -\boldsymbol{S}(1) \boldsymbol{\mathcal{R}}_{nb}^\top \boldsymbol{v}^n & \boldsymbol{0} & \boldsymbol{0} \end{bmatrix}$$

$$\boldsymbol{G}_{wi} = \begin{bmatrix} -\varrho_i \boldsymbol{\mathcal{R}}_{nb} \boldsymbol{S}(1) \boldsymbol{u}_{\delta i}^b & -\varrho_i \boldsymbol{\mathcal{R}}_{nb} \boldsymbol{S}(1) \boldsymbol{u}_{\delta i}^b & -\varrho_i \boldsymbol{\mathcal{R}}_{nb} (\boldsymbol{u}_{\delta i}^b) \end{bmatrix}$$

We can then use the same elements for the whole system, where we linearise the entire output $\boldsymbol{y} = \boldsymbol{C}^B \boldsymbol{x} = g(t, x) = [\boldsymbol{g}_v{}^\top, \; \boldsymbol{g}_1{}^\top, \; \cdots, \; \boldsymbol{g}_m{}^\top]^\top$ with respect of the whole noise vector $\boldsymbol{w}$. The linearisation becomes

$$\boldsymbol{G}_w = \begin{bmatrix} \frac{\partial \boldsymbol{g}_v}{\partial w_\psi} & \boldsymbol{0} & \boldsymbol{0} & \cdots & \boldsymbol{0} & \boldsymbol{0} \\ \frac{\partial \boldsymbol{g}_1}{\partial w_\psi} & \frac{\partial \boldsymbol{g}_1}{\partial w_{\beta 1}} & \frac{\partial \boldsymbol{g}_1}{\partial w_{l1}} & \cdots & \boldsymbol{0} & \boldsymbol{0} \\ \vdots & \vdots & \vdots & \ddots & \vdots & \vdots \\ \frac{\partial \boldsymbol{g}_m}{\partial w_\psi} & \boldsymbol{0} & \boldsymbol{0} & \cdots & \frac{\partial \boldsymbol{g}_m}{\partial w_{\beta m}} & \frac{\partial \boldsymbol{g}_m}{\partial w_{lm}} \end{bmatrix}$$

We get the approximate output covariance matrix the same way we obtained the process noise covariance matrix

$$\hat{\boldsymbol{R}}_B = \boldsymbol{R}_B + \boldsymbol{G}_w \boldsymbol{S}_B \boldsymbol{G}_w^\top \tag{6.27}$$

Here, matrix $\boldsymbol{G}_w$ is the Jacobian of the function $\boldsymbol{g}(t, x)$, and $\boldsymbol{S}_B$ is a positive definite tuning matrix, where in addition, the covariance of the velocity are maintained in the matrix elements $\boldsymbol{R}_{B(1:2,1:2)} = \boldsymbol{I} {\sigma_v}^2$. The matrix $\boldsymbol{R}_B$ is also for tuning/regularization, ensuring that the covariance matrix is always full rank, regardless if $\hat{\varrho}_i = 0$. This was tuned so that the the covariance estimates where consistent with the estimate errors.

6.5 Simulation Results and Performance Evaluation

The bearings only SLAM estimator was simulated in Matlab, where the model was discretized with a time-step $\Delta t = 1[s]$ using Euler. It was implemented using the discrete-time Kalman filter, with estimates starting at the origin. The simulations are in 2D environment, and for simplicity all the landmarks are observed at all

time steps. The sensors are implemented as presented in section 2.5 with white noise having standard deviation as follows: accelerometer $\sigma_f = 0.1[m/s^2]$, AHRS $\sigma_\psi = 0.8^o$, bearing angle $\sigma_\beta = 0.4^o$, velocity $\sigma_v = 1[m/s]$ and the virtual noise $\sigma_l = 4.5 \cdot 10^{-4}$. These were also used in the design of the covariance matrices $\hat{\boldsymbol{R}}_B$ and $\hat{\boldsymbol{Q}}_B$. The tuning/regularization matrix $\boldsymbol{S}_B$ had diagonal entries $\boldsymbol{S}_B = \text{diag}(\sigma_v^2,\ 50^2, \cdots, 50^2)$. The standard deviation σ_v combined with the expected initial distance to the landmarks, helped determine $\boldsymbol{P}(0)$. The vehicle travelled in a spiral for 1350 seconds. The results can be seen in Figure 6.3. The estimated vehicle trajectory and landmark estimates are in blue, while the true vehicle trajectory is in red, and the landmarks are marked with 1,2,3,4. The position estimates have also been translated, making comparison easier. The estimates converge fast, and the estimate error of landmark 1 can be seen in Figure 6.4. The error characteristics were the same for all the landmarks. From the error plots, it is apparent that there is a bias in the estimate error, which is oscillating. MC simmulations were made for 2500 seconds, where the results of Landmark 1 are shown in Figures 6.5-6.24. In Figure 6.5, the average error of all the simulations is plotted for every time step. This bias vanishes if the the bearing and attitude noise is turned off in the matrix $\boldsymbol{C}_B$ in both filter model and simulation model. Bias compensation from Bar-Shalom [7] has been explored, without success. Nevertheless, it is apparent that the bias is predictable; and with an 1-2% error it is regarded as aceptable; which is suported by examining Figure 6.3. To examine the concistency of the SLAM solution, a normalized error squeared (NES) test [7][p.234-236] was also preformed, resulting in Figure 6.24. The authors acknowledge that the NES test fails in the strictest sense, especially because of the bias. However, the result of the NES test also demonstrated stability of the solutions and the covariance estimates. So it is hardly critical, but future research should address this with more detail.

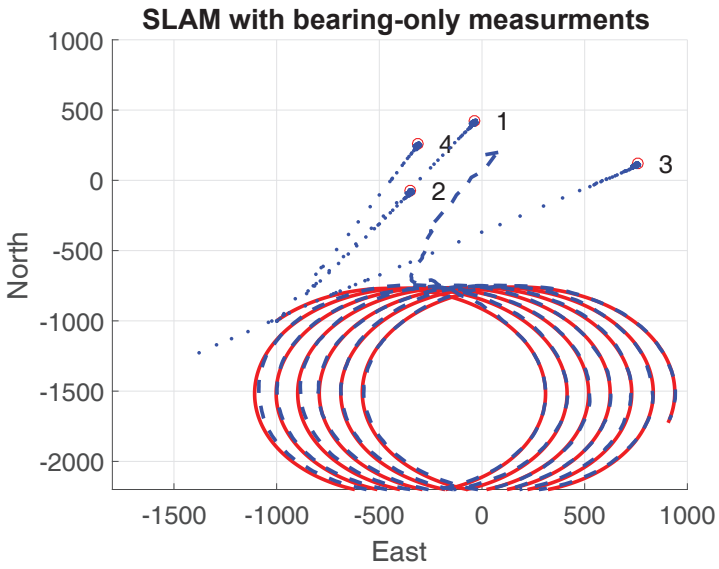

Figure 6.3: The landmark and vehicle position estimates of the bearing only SLAM. For this figure, the end position estimate is set equal to the true end position for easier comparison in the figure, and one can see that the evolution of the position estimates converge to the same trajectory as the true vessel.

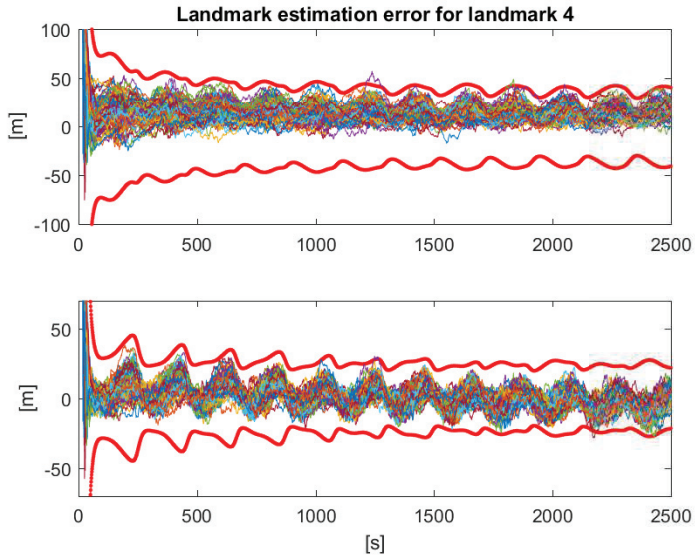

Figure 6.4: The error of 150 trajectories of the Landmark 3 estimates, with 3σ plotted red. Here the covariance matrix is the covariance from linearization added with a diagonal matrix. It is apparent that the biassed estimates offsets the error.

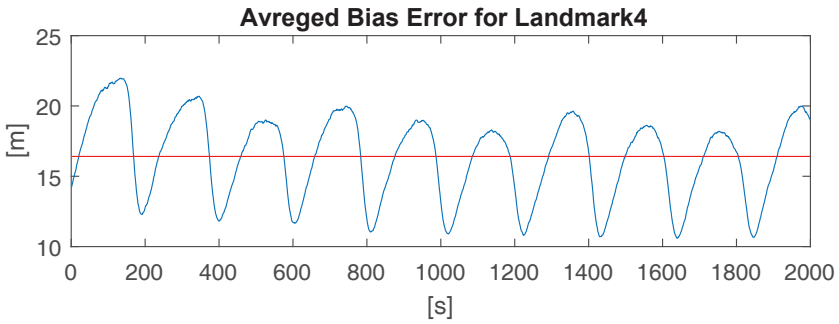

Figure 6.5: The mean error in range estimates of landmark 4 from 3000 MC simulations, from $500 < t < 2500$.

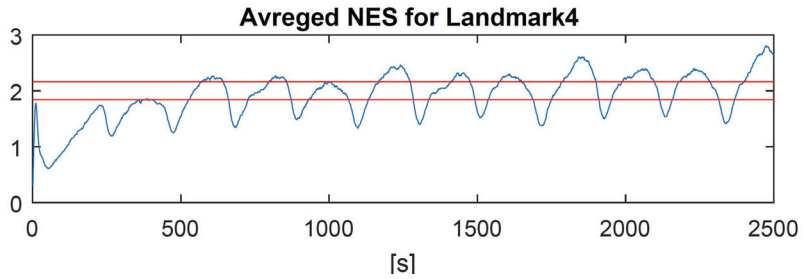

Figure 6.6: NES test of Bearing only SLAM with 1000 MC simmulations and 1% confidence interval for landmark 4, with only linearised covariance matrix. It is apparent that the NES estimates are optimistic, due to the bias estimates.

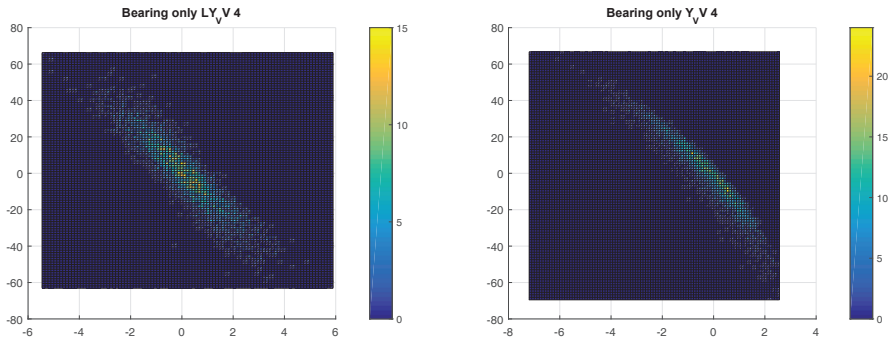

(a) . **(b)** .

Figure 6.7: The histogram of the bearings only output (b) along with the approximated noise through linearisation (a). The histogram is created from the output at t=1000, from 3000 MC simulations.

6.6 Conclusion

In this article we have presented a globally asymptotically stable bearing only SLAM estimation, that is able to estimate landmarks and its relative position with bearing only measurements in addition to IMU, velocity and attitude measurements. The system was represented as an LTV system, where an observability analysis was performed; in which conditions on the trajectory was found so that with KF, global convergence could be achieved in the nominal case. A new design of the input covariances was proposed, using the Jacobian of the system.

6.6.1 Future work

Future work include further analysis of the noise characteristics of the bearing only SLAM solution and exploration of the noise correlation structure in detail. In addition, the goal is to develop an attitude observer for bearing only measurements, which is not dependent on magnetometer to estimate gyro bias, and experimental validation of the SLAM solution together with solutions presented in [58].

While working with the KF in this chapter, it was evident that the introduction of nonlinear noise degenerated the KF, especially for high noise values. In order to mitigate this sensitivity, a cascaded observer setup between the KF in this chaper and the nonlinear observer from Chapter 4 was tested. The hypothesis was that the nonlinear observer would filter the bearing measurements for the KF, thus reducing the noise exposure of the KF.

Globally stable inertia bearing only SLAM Part 2: eXogenus Kalman Filter

6.7 Introduction

Robust navigation and positioning of unmanned aerial vehicles (UAVs) are fundamental for any autonomous mission, with particular challenges in environments where absolute positioning systems are absent or unreliable. To tackle these situations, aided inertial navigation techniques such as simultaneous localization and mapping algorithm (SLAM) or visual odometry (VO) can be used. What all these methods have in common is that they rely solely on on-board sensors to preform the navigation. A common setup is fusing camera measurements with inertia measurements unit (IMU) and/or velocity measurements. VO and SLAM are differentiated on whether they preform loop closure or not, where SLAM is the category preforming loop closure [21]. This means that a consistent filter [7] is especially important for a SLAM algorithm, as a consistency property would help make the search for possible loop closure faster and more robust. Over the past decades, the research community has devoted tremendous effort in the field of probabilistic SLAM. For a detailed review on SLAM see [28] and [6], and the references therein, which include several successful implementations of SLAM algorithms in experiments. However, a remaining open problem within SLAM is robustness, especially for initialization and recovery [21]. This motivated research on bearing only SLAM and VO solutions with global stability [77, 71, 58, 17, 19, 50]

Some of these filters [77, 58, 17, 50] get their result of global stability by setting up the SLAM problem as an LTV system, where they introduce measurements into the system matrices.

$$\dot{\boldsymbol{x}}(t) = \boldsymbol{A}(\boldsymbol{z}(t), t)\boldsymbol{x}(t) + \boldsymbol{B}(\boldsymbol{z}(t), t)\boldsymbol{u}(t) \tag{6.28}$$

$$\boldsymbol{y}(t) = \boldsymbol{C}(\boldsymbol{z}(t), t)\boldsymbol{x}(t) \tag{6.29}$$

where $\boldsymbol{x}$ is a vector with the states of the vehicle and landmark positions, $\boldsymbol{y}$ is the vector output with a linear time varying dependency to the states. The vector $\boldsymbol{z}$ contains auxilliary measurements, such as attitude and bearing angles represented as a linear time varying rotation matrix and bearing vectors; The vector $\boldsymbol{u}$ contains the inputs to the system such as acceleration and velocity. This representation makes the SLAM problem solvable with the Kalman filter (KF), and global stability follows from observability analysis [3].

Using measurements to compute the system matrices, violates the assumption of the processes noise and measurement noise being uncorrelated. Furthermore, the treatment of the noises is no longer straightforward as the noise is neither additive nor Gaussian, so the optimallity of the KF is lost. Nevertheless, in [17], it was

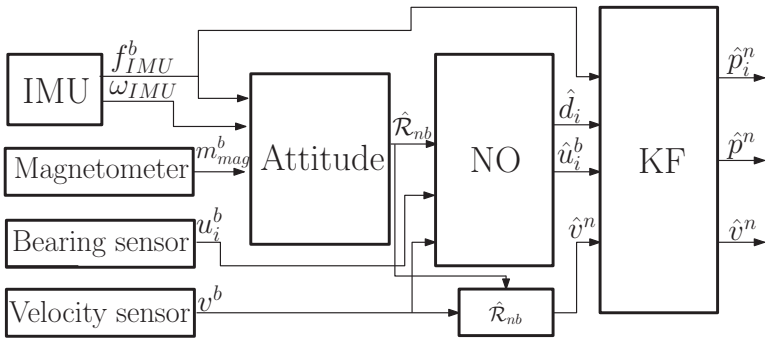

Figure 6.8: Block Diagram of the XKF cascade, of the nonlinear observer (NO) and KF

demonstrated that the setup, if the covariance matrices are approximated through linearization, can give estimates with approximate consistency and acceptable bias. However, for larger noise levels, especially in the bearing measurements, the noise matches the linearization inaccurate and the LTV setup has problems giving satisfactory results.

6.7.1 Contribution

In this article we take inspiration from the XKF filter setup, introduced in [59]. We will use the nonlinear filter [19] as a first-stage filter of the bearing measurements and feed these to system matrices in the time varying KF presented in [17]. The cascade structure can be seen in Figure 6.8. We prove that this setup is USGAS, and simulations demonstrate that the cascade setup is more robust against large measurement noise, than the filters individually. In addition we investigate how the novel nonlinear observer [19] preforms against the KF [17].

The structure of this paper is as follows: Section 6.8 presents the KF and nonlinear observer, and in Section 6.9 we prove USGAS for the error dynamics of the cascade setup; 6.10 shows the comparative analysis between the new cascade setup and the individual filters. Section 6.11 concludes the paper.

6.8 Bearing only filters

The cascade setup for bearing only SLAM, is of a nonlinear observer [19] in a cascade with a time varying KF [17]. In this section we give a quick summary of both filters.

6.8.1 Kalman filter

The Kalman filter presented here was first presented in [17], with including design of the covariance matrices as well as consistency analysis; and the readers are re-

ferred to this article for further details. It was a redesign of the bearing only filter in [58], where the filter assumes that in addition to bearing and velocity measurements, an AHRS is available. Thus the bearing only SLAM filtering problem can be reformulated as an LTV system. The measurement model and dynamic model are summarized in Table 6.3. For the states $\boldsymbol{x}_{KF} = [\boldsymbol{v}^n,\ \boldsymbol{\delta}_1^n,\ \cdots,\ \boldsymbol{\delta}_m^n \varrho_1,\ \cdots,\ \varrho_m]^\top$, the corresponding system matrices are

$$\boldsymbol{u}_{\delta i}^n = \boldsymbol{\mathcal{R}}_{nb}\boldsymbol{u}_{\delta i}^b$$

$$\boldsymbol{A}^B(\boldsymbol{u}_{\delta i}^n) = \begin{bmatrix} \boldsymbol{0} & \boldsymbol{0}\cdots & \boldsymbol{0} \\ -\boldsymbol{I}_3 & \boldsymbol{0}\cdots & \boldsymbol{0} \\ \vdots & \ddots & \vdots \\ -\boldsymbol{I}_3 & \boldsymbol{0}\cdots & \boldsymbol{0} \\ -(\boldsymbol{u}_{\delta 1}^n)^\top & \boldsymbol{0}\cdots & \boldsymbol{0} \\ \vdots & \ddots & \vdots \\ -(\boldsymbol{u}_{\delta m}^n)^\top & \boldsymbol{0}\cdots & \boldsymbol{0} \end{bmatrix}, \boldsymbol{B}^B = \begin{bmatrix} \boldsymbol{I}_3 \\ \boldsymbol{0} \\ \vdots \\ \boldsymbol{0} \\ \boldsymbol{0} \\ \vdots \\ \boldsymbol{0} \end{bmatrix}$$

$$\boldsymbol{C}^B(t, \boldsymbol{u}_{\delta i}^n) = \begin{bmatrix} \boldsymbol{\mathcal{R}}_{nb}^\top & \boldsymbol{0} & \cdots & \boldsymbol{0} & \boldsymbol{0} & \cdots & \boldsymbol{0} \\ \boldsymbol{0} & \boldsymbol{I}_3 & \cdots & \boldsymbol{0} & -\boldsymbol{u}_{\delta 1}^n & \cdots & \boldsymbol{0} \\ \vdots & \vdots & \ddots & \vdots & \vdots & \ddots & \vdots \\ \boldsymbol{0} & \boldsymbol{0} & \cdots & \boldsymbol{I}_3 & \boldsymbol{0} & \cdots & -\boldsymbol{u}_{\delta m}^n \end{bmatrix}$$

The system was proven to be observable if the bearing vectors $\boldsymbol{u}_{\delta i}^b$ were guaranteed to be non-stationary. Thus, as the system is LTV, the Kalman filter can yield a UGES filter [3] as discussed.

In addition, an algorithm for estimating the vehicle's position was presented in [58]; where the vehicle position estimate is set to zero at the start $\boldsymbol{p}^n(0) = \boldsymbol{0}$, which gives $\boldsymbol{p}_i^n = \boldsymbol{\delta}_i^n(0)$. The position can then be estimated as

$$\hat{\boldsymbol{p}}^n(t) = \sum_{i=1}^{m} w_i(t)(\hat{\dot{\boldsymbol{\delta}}}_i^n(0) - \hat{\dot{\boldsymbol{\delta}}}_i^n(t)) \tag{6.30}$$

$$\hat{\boldsymbol{p}}_i^n(t) = \hat{\boldsymbol{p}}^n(t) + \hat{\dot{\boldsymbol{\delta}}}_i^n(t), \quad i = \{1, m\} \tag{6.31}$$

where w_i are weights that sums up to 1. It should be noted that the estimate will converge with a constant bias so that $\hat{\boldsymbol{p}}^n(t) = \boldsymbol{p}^n(t) + \boldsymbol{d}$, in which $\boldsymbol{d} = \sum_{i=1}^{m} w_i(t)\tilde{\boldsymbol{\delta}}_i^n(0)$. The relative position estimate will converge as $\tilde{\delta}_i^n(t)$ converges to zero. To improve the position estimate, the initial state can be estimated. Because of the observability of the system, by definition it can be estimated using [53]

$$\hat{\boldsymbol{x}}(t_0) = \boldsymbol{W}_O(t, t_0)^{-1} \int_{t_0}^{t_1} \boldsymbol{\Phi}(\tau, t_0)^\top \boldsymbol{C}(\tau)^\top (\boldsymbol{y}(t) - \boldsymbol{C}(\tau)\boldsymbol{x}) \tag{6.32}$$

So that better estimates of $\dot{\hat{\boldsymbol{\delta}}}_i^n(0)$ can be found.

6.8.2 Nonlinear observer Bearing Only SLAM

The nonlinear observer, in Table 6.4, was first presented in [17], and the readers are referred to this article for further details. The observer filters unit vector measurements and uses techniques from high gain observers and skew-symmetric systems to estimate the range from the bearing and velocity measurements. The observer was proven to be USGAS, with exponential stability for the bearing estimate error being less than $\frac{\pi}{2}$.

The states of the observer can also be stacked in a vector $\boldsymbol{x}_{NO} = [\boldsymbol{u}_1^n, \cdots, \boldsymbol{u}_m^n, d_1, \cdots, d_m]^\top$, where $\boldsymbol{u}_{\delta i}^n$ is the unit vector and d_i is the inverted range, so that the LRP is found using $\boldsymbol{\delta}_i^n = \frac{\boldsymbol{u}_{\delta i}^n}{d_i}$.

6.8.3 Computational aspects of the nonlinear observer

Using inverted range estimates results in the substantial small estimates if the range is large. If it is desirable to keep the inverted parameter larger, bearing vector estimate can be implemented with an arbitrary magnitude, so that $\|{}^M\hat{\boldsymbol{u}}_{\delta i}^b\| = M$ and $\dot{\hat{\boldsymbol{\delta}}}_i^n = \frac{{}^M\hat{\boldsymbol{u}}_{\delta i}^b}{{}^M\hat{d}_i}$ resulting in that the inverted range estimate is ${}^M\hat{d}_i = \frac{M}{\|\dot{\hat{\boldsymbol{\delta}}}_i^n\|}$. The

Table 6.3: KF Bearing only SLAM

Bearing Only SLAM [17]	
States	Input
$\boldsymbol{x} = [\boldsymbol{v}^n, \boldsymbol{\delta}_1^n, , \cdots, \boldsymbol{\delta}_m^n, \varrho_1, \cdots, \varrho_m]^\top$	$\boldsymbol{u} = \boldsymbol{\mathcal{R}}_{nb}\boldsymbol{f}^{bm} + \boldsymbol{g}^n$
Measurement model	
$\boldsymbol{y} = [\boldsymbol{y}^v, \boldsymbol{y}_1^V, \cdots, \boldsymbol{y}_m^V]^\top, \quad \boldsymbol{u}_{\delta i}^{nm} = \boldsymbol{\mathcal{R}}_{nb}^m \boldsymbol{u}_{\delta i}^{bm}$ $\boldsymbol{y}_i^V = 0 = \boldsymbol{\delta}_i^n - \boldsymbol{u}_{\delta i}^{nm}\varrho_i, \quad \boldsymbol{y}^v = \boldsymbol{v}^b = (\boldsymbol{\mathcal{R}}_{nb}^m)^\top \boldsymbol{v}^{bm}$	
Dynamics model	
$\dot{\boldsymbol{v}}^n = \boldsymbol{u}$ $\dot{\boldsymbol{\delta}}_i^n = -\boldsymbol{v}^n$ $\dot{\varrho}_i = -(\boldsymbol{u}_{\delta i}^b)^\top (\boldsymbol{\mathcal{R}}_{nb})^\top \boldsymbol{v}^n$	

observer dynamic will be the same as before, only multiplied by M

$$ {}^{M}\dot{\hat{\boldsymbol{u}}}^{n}_{\delta i} = M\dot{\hat{\boldsymbol{u}}}^{n}_{\delta i},\ {}^{M}\dot{\hat{d}} = M\dot{\hat{d}} \tag{6.33} $$

Another aspect of the implementation of the observer is that it is originally designed for 3-D especially as a result of the cross product. However, if it is desirable not to use the skew symmetric matrix and keep the vectors in two dimensions, the following identities can be used

$$ -\boldsymbol{S}(\boldsymbol{S}(\boldsymbol{u}^{n}_{\delta i})\hat{\boldsymbol{u}}^{n}_{\delta i}) = (\boldsymbol{u}^{n}_{\delta i}(\hat{\boldsymbol{u}}^{n}_{\delta i})^{\top} - \hat{\boldsymbol{u}}^{n}_{\delta i}(\boldsymbol{u}^{n}_{\delta i})^{\top}) \tag{6.34} $$

$$ -\boldsymbol{S}(\boldsymbol{u}^{b}_{\delta i})^{2} = \boldsymbol{I} - \boldsymbol{u}^{b}_{\delta i}(\boldsymbol{u}^{b}_{\delta i})^{\top} \tag{6.35} $$

$$ \boldsymbol{S}(\boldsymbol{u}^{b}_{\delta i})\boldsymbol{S}(\hat{\boldsymbol{u}}^{b}_{\delta i}) = (\boldsymbol{u}^{n}_{\delta i})^{\top}\hat{\boldsymbol{u}}^{n}_{\delta i}\boldsymbol{I} - \boldsymbol{u}^{n}_{\delta i}(\hat{\boldsymbol{u}}^{n}_{\delta i})^{\top} \tag{6.36} $$

In addition, due to the non-linearity of the propagation of the $\hat{d}$ estimate, the Euler method can become an insufficient implementation of the adaptation law for larger time steps. For this reason the 4th order Runge Kutta was implemented for the observer.

Table 6.4: Nonlinear Bearing only SLAM observer presented in [19]

Nonlinear Bearing Only SLAM, [19]	
States	Input
$\boldsymbol{x} = [\boldsymbol{u}^{n}_{\delta 1}, \cdots, \boldsymbol{u}^{n}_{\delta m}, d_1, \cdots, d_m]^{\top}$	$\boldsymbol{u} = \boldsymbol{\mathcal{R}}^{m}_{nb}\boldsymbol{v}^{bm}$
Measurement model	
$y_i = \boldsymbol{u}^{nm}_{\delta i} = \boldsymbol{\mathcal{R}}^{m}_{nb}\boldsymbol{u}^{bm}_{\delta i} \qquad \tilde{\boldsymbol{y}}_i = \boldsymbol{S}(\boldsymbol{u}^{nm}_{\delta i})\hat{\boldsymbol{u}}^{n}_{\delta i}$	
Dynamics model and observer	
$\dot{\boldsymbol{u}}^{n}_{\delta i} = -\boldsymbol{S}(\boldsymbol{u}^{n}_{\delta i})^{2}\boldsymbol{v}^{n} \qquad \dot{d}_i = d^{2}(\boldsymbol{v}^{n})^{\top}\boldsymbol{u}^{n}_{\delta i}$	
$\dot{\hat{\boldsymbol{u}}}^{n}_{\delta i} = -\boldsymbol{S}(k\tilde{\boldsymbol{y}}_i + \hat{d}\boldsymbol{S}(\boldsymbol{u}^{nm}_{\delta i})\boldsymbol{v}^{nm})\hat{\boldsymbol{u}}^{b}_{\delta i}$ $\dot{\hat{d}}_i = \hat{d}^{2}(\boldsymbol{v}^{nm})^{\top}\boldsymbol{u}^{nm}_{\delta i} + \gamma(\boldsymbol{v}^{nm})^{\top}\boldsymbol{S}(\boldsymbol{u}^{nm}_{\delta i})^{2}\boldsymbol{S}(\hat{\boldsymbol{u}}^{n}_{\delta i})\tilde{\boldsymbol{y}}_i$	

$$k_{1u} = \dot{\hat{\boldsymbol{u}}}^n_{\delta i}(\hat{\boldsymbol{u}}^n_{\delta i}, \hat{d}, \tilde{\boldsymbol{u}}^n_{\delta i}(t_k), t_k) \tag{6.37}$$

$$k_{1d} = \dot{\hat{d}}(\hat{d}, \tilde{\boldsymbol{u}}^n_{\delta i}(t_k), t_k) \tag{6.38}$$

$$k_{2u} = \dot{\hat{\boldsymbol{u}}}^n_{\delta i}(\hat{\boldsymbol{u}}^n_{\delta i} + k_{1u}\frac{dt}{2}, \hat{d} + k_{1d}\frac{dt}{2}, \tilde{\boldsymbol{u}}^n_{\delta i}(t_k), t_k) \tag{6.39}$$

$$k_{2d} = \dot{\hat{d}}(\hat{d} + k_{1d}\frac{dt}{2}, \tilde{\boldsymbol{u}}^n_{\delta i}(t_k), t_k) \tag{6.40}$$

$$k_{3u} = \dot{\hat{\boldsymbol{u}}}^n_{\delta i}(\hat{\boldsymbol{u}}^n_{\delta i} + k_{2u}\frac{dt}{2}, \hat{d} + k_{2d}\frac{dt}{2}, \tilde{\boldsymbol{u}}^n_{\delta i}(t_k), t_k) \tag{6.41}$$

$$k_{3d} = \dot{\hat{d}}(\hat{d} + k_{3d}\frac{dt}{2}, \tilde{\boldsymbol{u}}^n_{\delta i}(t_k), t_k) \tag{6.42}$$

$$k_{4u} = \dot{\hat{\boldsymbol{u}}}^n_{\delta i}(\hat{\boldsymbol{u}}^n_{\delta i} + k_{3u}dt, \hat{d} + k_{3d}dt, \tilde{\boldsymbol{u}}^n_{\delta i}(t_k), t_k) \tag{6.43}$$

$$k_{4d} = \dot{\hat{d}}(\hat{d} + k_{3d}dt, \tilde{\boldsymbol{u}}^n_{\delta i}(t_k), t_k) \tag{6.44}$$

$$\{\hat{\boldsymbol{u}}^n_{\delta i}\}^{t_k+dt} = \hat{\boldsymbol{u}}^n_{\delta i} + dt\frac{k_{1u} + 2k_{2u} + 2k_{3u} + k_{4u}}{6} \tag{6.45}$$

$$\{\hat{d}_i\}^{t_k+dt} = \hat{d}_i + dt\frac{k_{1u} + 2k_{2u} + 2k_{3u} + k_{4u}}{6} \tag{6.46}$$

6.9 Cascade bearing only SLAM

In this section we will discuss the cascade setup of the KF and nonlinear observer presented in the previous section. The cascade structure can be seen in the block-diagram in Figure 6.8. The KF uses the bearing estimates from the nonlinear observer, instead of the bearing measurements directly, when building the system matrices. The covariance are build up using (2.43)-(2.44), however, the estimates from the nonlinear observer are also used here. The setup is thus, the special case of the XKF when the system can be linearly represented. The nonlinear observer and KF in cascade is thus

$$\Sigma_1 \begin{cases} \dot{\hat{\boldsymbol{x}}}^B & = \boldsymbol{A}^B(\hat{\boldsymbol{u}}^n_{\delta i})\hat{\boldsymbol{x}}^B + \boldsymbol{B}u + \boldsymbol{K}(\boldsymbol{y} - \boldsymbol{C}^B(t, \hat{\boldsymbol{u}}^n_{\delta i})\hat{\boldsymbol{x}}^B) \\ \dot{\boldsymbol{P}} & = \boldsymbol{A}^B(\hat{\boldsymbol{u}}^n_{\delta i})\boldsymbol{P} + \boldsymbol{P}(\boldsymbol{A}^B(\hat{\boldsymbol{u}}^n_{\delta i}))^\top \\ & \quad -\boldsymbol{K}\boldsymbol{C}^B(t, \hat{\boldsymbol{u}}^n_{\delta i})\boldsymbol{P} + \hat{\boldsymbol{Q}}(\hat{\boldsymbol{u}}^n_{\delta i}, \hat{d}_i) \\ \boldsymbol{K} & = \boldsymbol{P}\boldsymbol{C}^B(t, \hat{\boldsymbol{u}}^n_{\delta i})(\hat{\boldsymbol{R}}(\hat{\boldsymbol{u}}^n_{\delta i}, \hat{d}_i))^{-1} \end{cases} \tag{6.47}$$

$$\Sigma_2 \begin{cases} \dot{\hat{\boldsymbol{u}}}^n_{\delta i} & = -\boldsymbol{S}(k_u\tilde{\boldsymbol{y}}_i + \hat{d}\boldsymbol{S}(\boldsymbol{u}^n_{\delta i})\boldsymbol{v}^n)\hat{\boldsymbol{u}}^n_{\delta i} \\ \dot{\hat{d}}_i & = \hat{d}^2(\boldsymbol{v}^n)^\top\boldsymbol{u}^n_{\delta i} + k_d(\boldsymbol{v}^n)^\top\boldsymbol{S}(\boldsymbol{u}^b_{\delta i})^2\boldsymbol{S}(\hat{\boldsymbol{u}}^n_{\delta i})\tilde{\boldsymbol{y}}_i \end{cases} \tag{6.48}$$

As mentioned, the KF is UGES [17], and the nonlinear observer is USGAS. However, for the XKF setup, the assumption is that the nonlinear observer is either

UGAS, UGES or USGES, which means we can not use the Theorem from [59] directly. Regardless, we are still able to show that the system is USGAS by showing that the system Σ_1 is input to state stable (ISS) with respect to the error from Σ_2.

Theorem 9. *Consider the observer* (6.47)-(6.48)*, for a system where velocity, attitude and bearing measurements from landmarks are available, and are continuous and Lipschitz. Further assume that the trajectory of the vehicle is so that the bearing measurements satisfies* $\|\dot{\boldsymbol{u}}^n_{\delta i}\| > 0$ *and estimates satisfies* $\|\dot{\hat{\boldsymbol{u}}}^n_{\delta i}\| > 0$*, and that the states* $\boldsymbol{x}^B$ *are bounded. Then there exist gains* k_u *and* k_d *for* (6.48)*, such that the estimate error* (6.48) *will converge to zero. In addition, assume that, the bearing estimates* $\hat{\boldsymbol{u}}^n_{\delta i}$ *from* (6.48) *are used in building the system matrices* $\boldsymbol{A}^B(\hat{\boldsymbol{u}}^n_{\delta i})$ *and* $\boldsymbol{C}^B(\hat{\boldsymbol{u}}^n_{\delta i})$ *, and* $\hat{\boldsymbol{Q}}(\hat{\boldsymbol{u}}^n_{\delta i}, \hat{d}_i)$ *and* $\hat{\boldsymbol{R}}^{-1}(\hat{\boldsymbol{u}}^n_{\delta i}, \hat{d}_i)$ *are built from the estimates* $\hat{\boldsymbol{u}}^n_{\delta i}$ *and* $\hat{d}_i$ *so that they are bounded and positive definite and* $(\boldsymbol{A}^B(\hat{\boldsymbol{u}}^n_{\delta i}), \hat{\boldsymbol{Q}}(\hat{\boldsymbol{u}}^n_{\delta i}, \hat{d}_i))$ *is controllable, then the origin of the error dynamics of the cascade is USGAS.*

Proof. As said, we will show that the KF Σ_1 is ISS with respect to the error from the nonlinear observer. For convenience we organize the system into the cascaded

$$\Sigma_1 \begin{cases} \dot{\boldsymbol{\eta}}_1 = \boldsymbol{f}_1(t, \boldsymbol{\eta}_1) + \boldsymbol{g}(t, \boldsymbol{\eta}) \end{cases} \tag{6.49}$$

$$\Sigma_2 \begin{cases} \dot{\boldsymbol{\eta}}_2 = \boldsymbol{f}_2(t, \boldsymbol{\eta}_2) \end{cases} \tag{6.50}$$

with $\boldsymbol{\eta} = [\boldsymbol{\eta}_1^\top, \boldsymbol{\eta}_2^\top]^\top$. Where we will use the stability property of the KF without error

$$\dot{\boldsymbol{\eta}}_1 = \boldsymbol{f}_1(t, \boldsymbol{\eta}_1) \tag{6.51}$$

called the unforced system, to show that Σ_1 is ISS. We introduce the additive bearing error

$${}^e\boldsymbol{u}^n_{\delta i} = \boldsymbol{u}^n_{\delta i} - \hat{\boldsymbol{u}}^n_{\delta i} \tag{6.52}$$

We note that $\hat{\boldsymbol{u}}^n_{\delta i}$ is maintained on the unit ball, which means both $\boldsymbol{u}^n_{\delta i}$ and $\hat{\boldsymbol{u}}^n_{\delta i}$ are unit vectors. Through trigonometric relations we find the relationship between the errors

$$\|{}^e\boldsymbol{u}^n_{\delta i}\| = 2\sin(\frac{\tilde{\theta}_{ui}}{2}) \leq 2 \tag{6.53}$$

where $\tilde{\theta}_{ui}$ is the bearing angle estimate error from Σ_2 and is both bounded and will go to zero, as the error dynamics of Σ_2 is USGAS. We see that the additive bearing error is both bounded by 2, and by $\tilde{\theta}_{ui}$ which means it will also converge to zero as $\tilde{\theta}_{ui} \to 0$. Which means that eventually all $\|{}^e\boldsymbol{u}^n_{\delta i}\|$ will go to zero when $\|\boldsymbol{\eta}_2\| \to 0$.

What we notice next, is that the system matrices $\boldsymbol{A}^B(\boldsymbol{u}^n_{\delta i})$ and $\boldsymbol{C}^B(\boldsymbol{u}^n_{\delta i})$ are linear with respect to the bearing, which means that we can define the error matrices

$$\tilde{\boldsymbol{A}}^B({}^e\boldsymbol{u}^n_{\delta i}) = \boldsymbol{A}^B(\boldsymbol{u}^n_{\delta i}) - \boldsymbol{A}^B(\hat{\boldsymbol{u}}^n_{\delta i}) \tag{6.54}$$

$$\tilde{\boldsymbol{C}}^B({}^e\boldsymbol{u}^n_{\delta i}) = \boldsymbol{C}^B(\boldsymbol{u}^n_{\delta i}) - \boldsymbol{C}^B(\hat{\boldsymbol{u}}^n_{\delta i}) \tag{6.55}$$

where it is evident that these matrices are bounded as $\|{}^e\boldsymbol{u}^n_{\delta i}\| \leq 2$, moreover $\|\tilde{\boldsymbol{A}}^B({}^e\boldsymbol{u}^n_{\delta i})\| \to 0$ and $\|\tilde{\boldsymbol{C}}^B({}^e\boldsymbol{u}^n_{\delta i})\| \to 0$ as $\|\boldsymbol{\eta}_2\| \to 0$, as it would mean $\hat{\boldsymbol{u}}^n_{\delta i} = \boldsymbol{u}^n_{\delta i}, \forall i$.

If we then look at the error dynamics for (6.47) $\tilde{\boldsymbol{x}}^B = \boldsymbol{x}^B - \hat{\boldsymbol{x}}^B$ of the KF

$$\dot{\tilde{\boldsymbol{x}}}^B = \dot{\boldsymbol{x}}^B - \dot{\hat{\boldsymbol{x}}}^B \tag{6.56}$$

$$= \boldsymbol{A}^B(\boldsymbol{u}^n_{\delta i})\boldsymbol{x}^B - \boldsymbol{A}^B(\hat{\boldsymbol{u}}^n_{\delta i})\hat{\boldsymbol{x}}^B \tag{6.57}$$

$$+ \boldsymbol{K}(t)(\boldsymbol{C}^B(\boldsymbol{u}^n_{\delta i})\boldsymbol{x}^B - \boldsymbol{C}^B(\hat{\boldsymbol{u}}^n_{\delta i})\hat{\boldsymbol{x}}^B) \tag{6.58}$$

which we can reorganize to

$$\begin{aligned}\dot{\tilde{\boldsymbol{x}}}^B =& (\tilde{\boldsymbol{A}}^B({}^e\boldsymbol{u}^n_{\delta i}) + \boldsymbol{A}^B(\hat{\boldsymbol{u}}^n_{\delta i}))\boldsymbol{x}^B - \boldsymbol{A}^B(\hat{\boldsymbol{u}}^n_{\delta i})\hat{\boldsymbol{x}}^B \\ &+ \boldsymbol{K}(t)((\tilde{\boldsymbol{C}}^B({}^e\boldsymbol{u}^n_{\delta i}) + \boldsymbol{C}^B(\hat{\boldsymbol{u}}^n_{\delta i}))\boldsymbol{x}^B - \boldsymbol{C}^B(\hat{\boldsymbol{u}}^n_{\delta i})\hat{\boldsymbol{x}}^B) \\ =& \boldsymbol{A}^B(\hat{\boldsymbol{u}}^n_{\delta i})\tilde{\boldsymbol{x}}^B + \boldsymbol{K}(t)\boldsymbol{C}^B(\hat{\boldsymbol{u}}^n_{\delta i})\tilde{\boldsymbol{x}}^B \qquad (6.59)\\ &+ \tilde{\boldsymbol{A}}^B({}^e\boldsymbol{u}^n_{\delta i})\boldsymbol{x}^B + \boldsymbol{K}(t)\tilde{\boldsymbol{C}}^B({}^e\boldsymbol{u}^n_{\delta i})\boldsymbol{x}^B \qquad (6.60)\end{aligned}$$

We see that the error dynamics can be divided into two parts, one which resembles the error dynamics of a KF, and one part which is with the induced error from the nonlinear filter. The terms related to the error dynamics of the KF combined with $\dot{\boldsymbol{P}}$ and $\boldsymbol{K}$ in (6.47) is then

$$\dot{\tilde{\boldsymbol{x}}}^B = \boldsymbol{A}^B(\hat{\boldsymbol{u}}^n_{\delta i})\tilde{\boldsymbol{x}}^B + \boldsymbol{K}(t)\boldsymbol{C}^B(\hat{\boldsymbol{u}}^n_{\delta i})\tilde{\boldsymbol{x}}^B \tag{6.61}$$

$$\begin{aligned}\dot{\boldsymbol{P}} =& \boldsymbol{A}^B_{\hat{\boldsymbol{u}}}(\hat{\boldsymbol{u}}^n_{\delta i})\boldsymbol{P} + \boldsymbol{P}(\boldsymbol{A}^B_{\hat{\boldsymbol{u}}}(\hat{\boldsymbol{u}}^n_{\delta i}))^\top \\ &- \boldsymbol{K}\boldsymbol{C}^B_{\hat{\boldsymbol{u}}}(t, \hat{\boldsymbol{u}}^n_{\delta i})\boldsymbol{P} + \hat{\boldsymbol{Q}}(\hat{\boldsymbol{u}}^n_{\delta i}, \hat{d}_i) \qquad (6.62)\end{aligned}$$

$$\boldsymbol{K} = \boldsymbol{P}\boldsymbol{C}^B_{\hat{\boldsymbol{u}}}(t, \hat{\boldsymbol{u}}^n_{\delta i})(\hat{\boldsymbol{R}}(\hat{\boldsymbol{u}}^n_{\delta i}, \hat{d}_i))^{-1} \tag{6.63}$$

which resembles the error dynamics of a continues-time KF with system matrices $\boldsymbol{A}^B(\hat{\boldsymbol{u}}^n_{\delta i})$ and $\boldsymbol{C}^B(\hat{\boldsymbol{u}}^n_{\delta i})$. $(\boldsymbol{A}^B(\hat{\boldsymbol{u}}^n_{\delta i}), \boldsymbol{C}^B(\hat{\boldsymbol{u}}^n_{\delta i}))$ is observable as $\|\dot{\hat{\boldsymbol{u}}}^n_{\delta i}\| > 0$, and we have assumed that $\hat{\boldsymbol{Q}}(\hat{\boldsymbol{u}}^n_{\delta i}, \hat{d}_i)$ and $\hat{\boldsymbol{R}}^{-1}(\hat{\boldsymbol{u}}^n_{\delta i}, \hat{d}_i)$ are bounded and $(\boldsymbol{A}^B(\hat{\boldsymbol{u}}^n_{\delta i}), \hat{\boldsymbol{Q}}(\hat{\boldsymbol{u}}^n_{\delta i}, \hat{d}_i))$ is controllable, meaning that the error dynamic (6.61)-(6.63) UGES [3, 17]. Thus the unforced system of Σ_1 (6.51) is UGES, implying that Σ_1 is input to state stable with respect to the input $\boldsymbol{\eta}_2$ [65, Lemma 4.6]. What is then left, is to identify perturbation $\boldsymbol{g}(t, \boldsymbol{\eta})$ which is the remaining part of the dynamic (6.60)

$$\boldsymbol{g}(t, \boldsymbol{\eta}) = (\tilde{\boldsymbol{A}}^B({}^e\boldsymbol{u}^n_{\delta i}) + \boldsymbol{K}(t)\tilde{\boldsymbol{C}}^B({}^e\boldsymbol{u}^n_{\delta i}))\boldsymbol{x}^B \tag{6.64}$$

which we know is bounded, since the matrices $\boldsymbol{P}$ and $\boldsymbol{C}^B_{\hat{\boldsymbol{u}}}(t, \hat{\boldsymbol{u}}^n_{\delta i})$ and $\hat{\boldsymbol{R}}(\hat{\boldsymbol{u}}^n_{\delta i}, \hat{d}_i)^{-1}$ are bounded, implying that $\boldsymbol{K}(t)$ is also bounded. In addition, we have that the

true states $\boldsymbol{x}^b$ are also bounded. We thus see that the perturbation term is indeed bounded, and will go to zero as $\|\boldsymbol{\eta}_2\| \to 0$.

Then proving the that the entire system (6.49)-(6.50) will converge to zero can either be done using the converse Lyapunov theorem for UGES systems [65, Theorem 14.4], or follow the steps preformed in [65, Lemma 4.7] where UGAS together with ISS in cascade is proven to give a UGAS system. □

6.10 Simulation Results and Performance Evaluation

The filters and observers were tested in simulations, where a vehicle moves in circles in 2-D, while observing four landmarks positioned randomly in a box 1500m away. The simulations were discretized with the method having step-length $\Delta t = 0.25[s]$. The system matrices used in the KF and XKF where the discretized similarly and implemented as discrete time KF. The nonlinear observer was implemented with 4th order Runge Kutta discretization due to its nonlinearities, and with a magnitude $\|^M \hat{\boldsymbol{u}}^b_{\delta i}\| = 3000$. The sensors were implemented as presented in section 2.5 with white noise having standard deviation as follows: accelerometer $\sigma_f = 0.25[m/s^2]$, heading $\sigma_\psi = 0.46^o$, bearing angle $\sigma_\beta = 0.26^o$, velocity $\sigma_v = 1[m/s]$. These were also used in the design of the covariance matrices $\hat{\boldsymbol{R}}_B$ and $\hat{\boldsymbol{Q}}_B$, as done in [17] with virtual noise $\sigma_l = 1.2 \cdot 10^{-3}$. The tuning/regularization matrices had diagonal entries $\boldsymbol{G}_Q = 0.01\boldsymbol{I}$ and $\boldsymbol{H}_R = \text{diag}(\sigma_v^2, 50^2, \cdots, 50^2)$, which was used in both the KF and XKF. The tuning of the nonlinear filter was based on the tuning in [101]. Through quasi pole placement, where the parameter α (frequency) and λ (damping-ratio), the gains where chosen respectively $k_u = 2\sqrt{\alpha}\lambda$, and $k_d = \frac{\alpha}{\|\boldsymbol{v}^n\|}$, and through Monte Carlo (MC) simmulations the tuning parameters $\alpha = 2 \cdot 10^{-4}$ and $\lambda = 1.75$ equivalent to an over damped system, were found to give the lest amount of error. To tune the nonlinear observer in the XKF, a similar MC simmulation was preformed. Where the tuning giving the least amount or error for the XKF was chosen, and resulted in $\alpha = 4 \cdot 10^{-3}$ and $\lambda = 0.9$, which is equivalent to slightly under damped system.

To test the KF, XKF and the nonlinear observer against each-other, 1000 MC simulations were run. Example run for each observers can be seen in Figures 6.9-6.11, where we see that all the methods are able to localize and estimate the landmark position with varying accuracy. The error trajectories were also plotted, with the KF and XKF having their 3σ boundaries plotted, which can be seen in figures 6.12-6.14. Also the bias and normalized estimation error squared (NEES) [7][p.234-236] was calculated with results seen in Table 6.5. From these figures it is evident that the even though the KF has the most precise estimates, in the sense of having least amount of variance, there is a bias which becomes evident by examining Figure 6.15 and Table 6.5. The nonlinear observer has the largest error, never the less it is still able to preform localization with some accuracy, and its bias is not much larger than for the KF. For the XKF, the estimates are a bit more spread

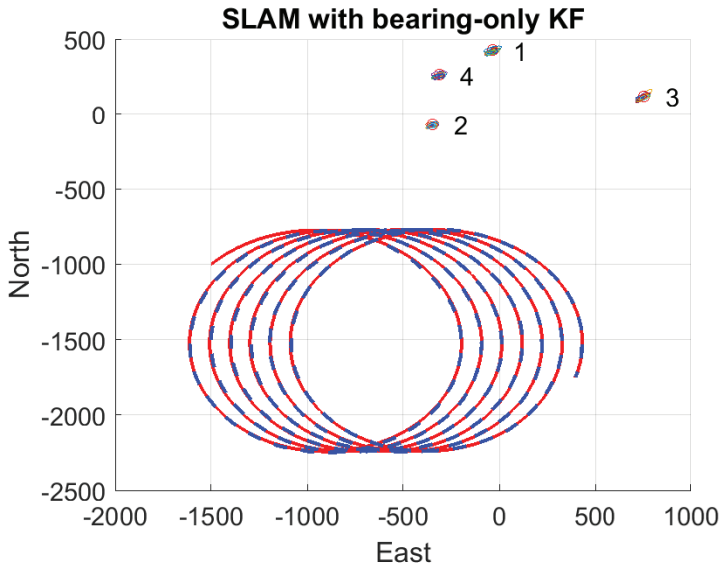

Figure 6.9: The landmark and vehicle position estimates of the KF bearing only SLAM. For this figure, the end position estimate is set equal to the true end position for easier comparison in the figure, and one can see that the evolution of the position estimates converge to the same trajectory as the true vessel.

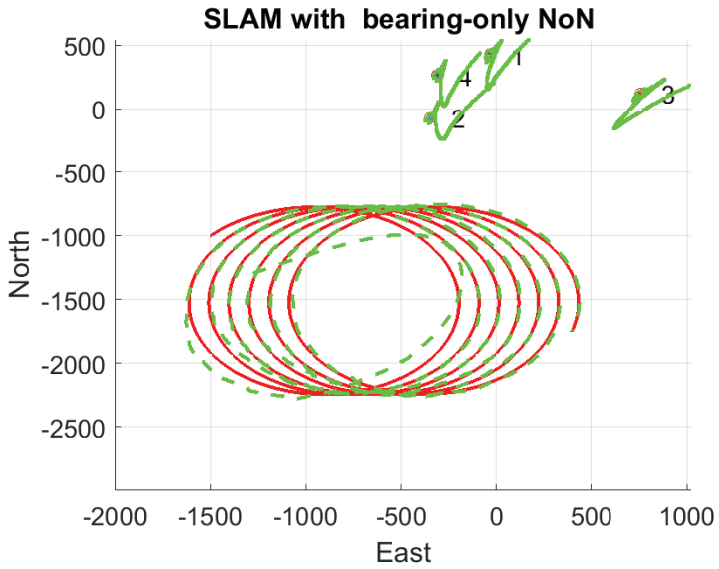

Figure 6.10: The landmark and vehicle position estimates of the nonlinear observer bearing only SLAM. Simmilar setup as Figure 6.9

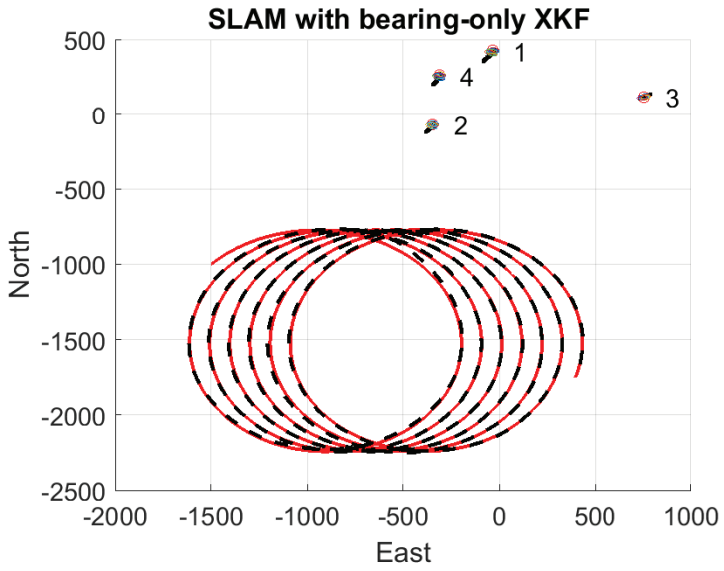

Figure 6.11: The landmark and vehicle position estimates of the XKF bearing only SLAM. Simmilar setup as Figure 6.9

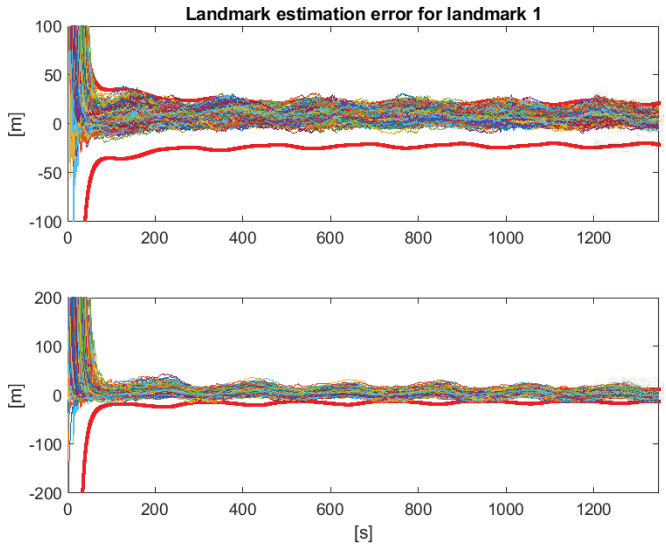

Figure 6.12: The error of 1000 trajectories from the KF of the Landmark 1 estimates, with 3σ plotted red.

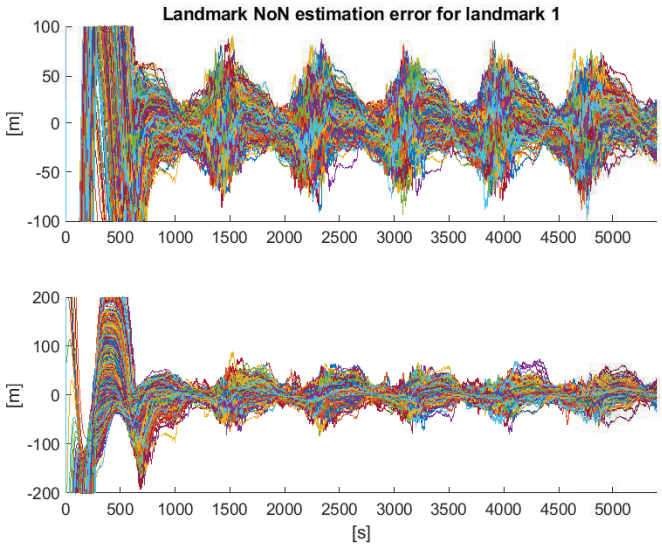

Figure 6.13: The error of 1000 trajectories from the Nonlinear Observer of the Landmark 1 estimates, with 3σ plotted red.

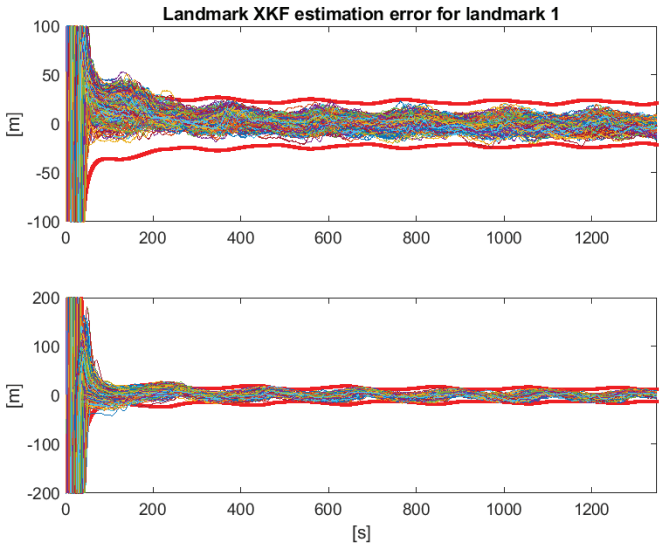

Figure 6.14: The error of 1000 trajectories from the XKF of the Landmark 1 estimates, with 3σ plotted red.

and consistent than the KF, but with less bias as can be seen in Table 6.5. This is because the nonlinear filter reduces the bearing noise significantly, as can be seen in Figure 6.18, which leads to a less banana shaped noise experienced by the filter in the XKF.

To test the methods when subjected to an increase in nonlinear noise, new simulation were preformed where the variance of the measurement noise related to the nonlinearities; bearing and attitude measurements were quadrupled. The results is seen in the Figures 6.19-6.21 where the new error plots with co-variance estimates are shown. In Figures 6.22 and 6.23 the new bias for the KF and XKF can be seen. We see that the KF starts to have problems, which results in a significant bias. The nonlinear observer also seems to have an increased variance as a result. Conversly, the XKF is the setup least affected by the increase in nonlinear noise, and is able to keep its consistency properties and accuracy when it is allowed to

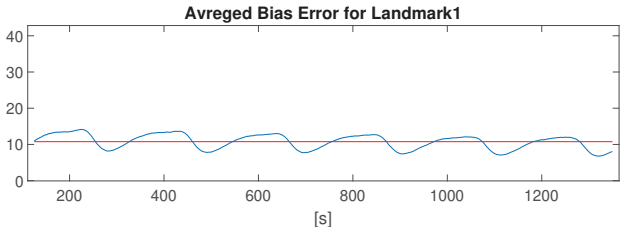

Figure 6.15: The mean error in range estimates from the KF of landmark 1 from 1000 MC simulations, from $500 < t < 2500$.

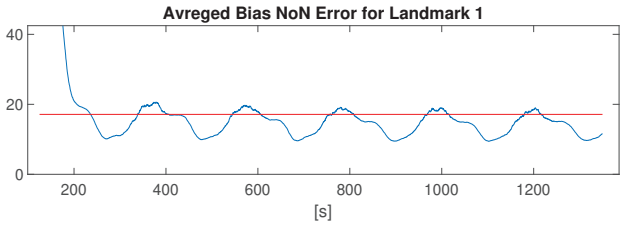

Figure 6.16: The mean error in range estimates from the nonlinear observer of landmark 1 from 1000 MC simulations, from $500 < t < 2500$.

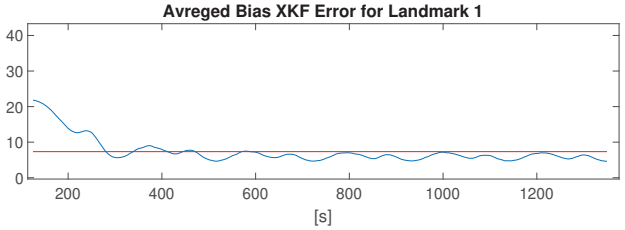

Figure 6.17: The mean error in range estimates from theXKF of landmark 3 from 1000 MC simulations, from $500 < t < 2500$.

converge. Also, we see that even though the nonlinear observer has a greater variance that the KF, it seems less biased, which is seen in Table 6.5. Regardless, the XKF was shown to be the most robust setup against a high noise levels.

Table 6.5: The results of 1000 MC simmulations, for both a normal and high noise scenario.

Noise level	Average	KF	NON	XKF
Low	Bias	10.5	18	7.5
	NEES	2.3	N/A	2.1
High	Bias	38	26	9
	NEES	20	N/A	3

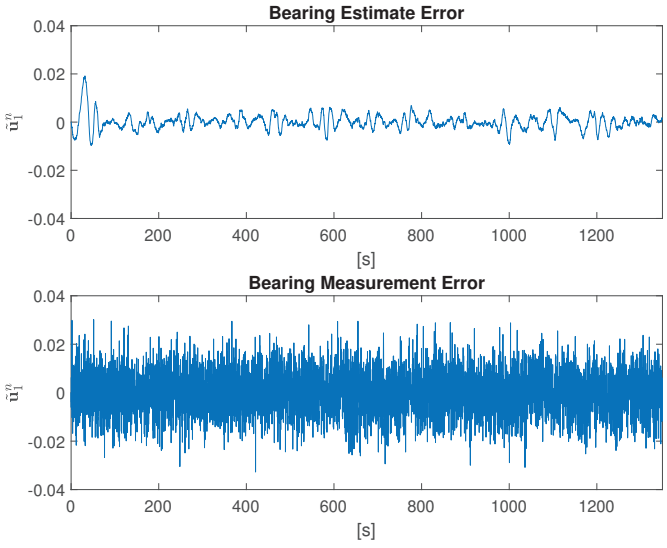

Figure 6.18: The bearing measurement error vs. the bearing estimate error from the nonlinear observer

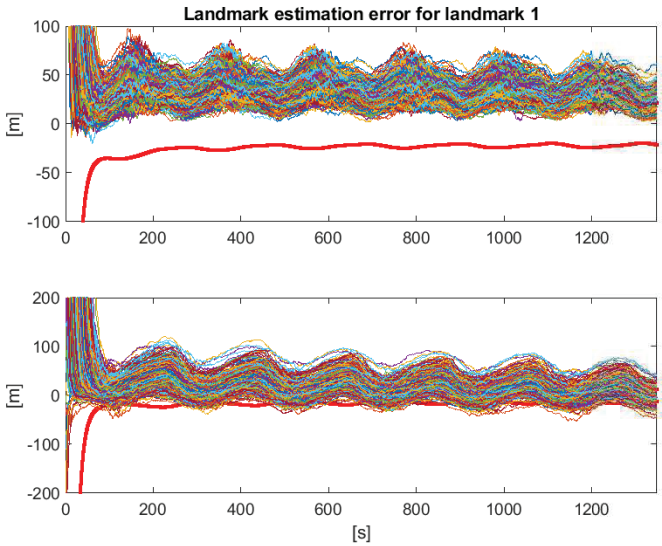

Figure 6.19: The error of 1000 trajectories when the noise is quadrupled from the KF of the Landmark 1 estimates, with 3σ plotted red.

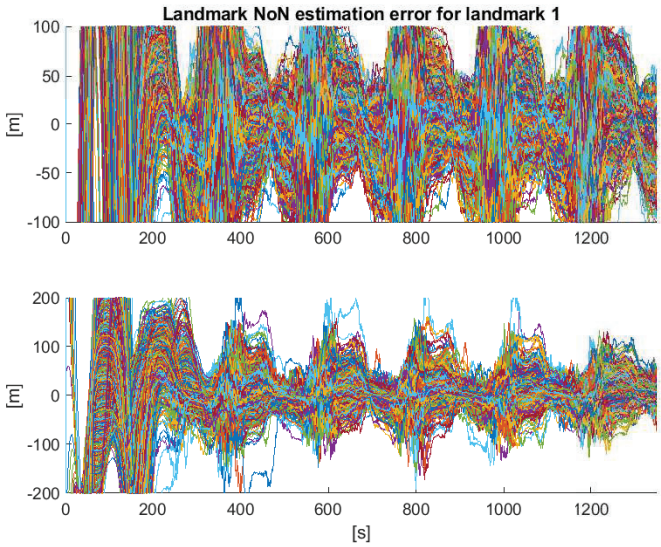

Figure 6.20: The error of 1000 trajectories from the Nonlinear Observer when the noise is quadrupled of the Landmark 1 estimates, with 3σ plotted red.

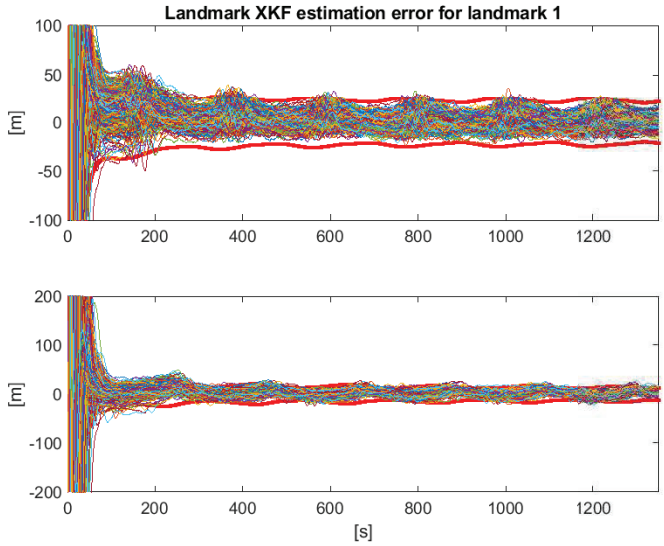

Figure 6.21: The error of 1000 trajectories from the XKF when the noise is quadrupled of the Landmark 1 estimates, with 3σ plotted red.

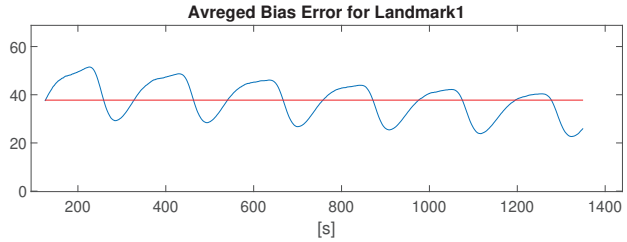

Figure 6.22: The mean error in range estimates when the noise is quadrupled from the KF of landmark 1 from 1000 MC simulations, from $500 < t < 2500$.

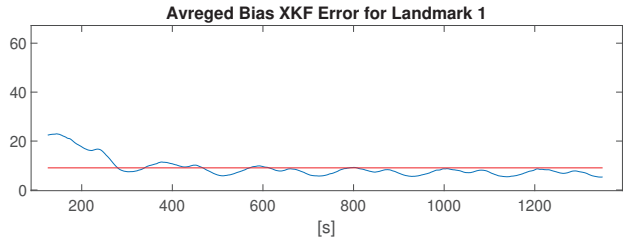

Figure 6.23: Test The mean error in range estimates when the noise is quadrupled from the XKF of landmark 3 from 1000 MC simulations, from $500 < t < 2500$.

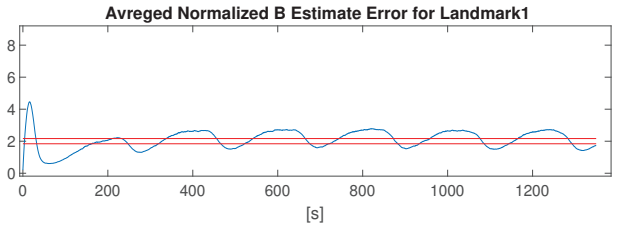

Figure 6.24: NES test of Bearing only KF SLAM with 1000 MC simmulations and 1% confidence interval for landmark 1, with only linearised covariance matrix.

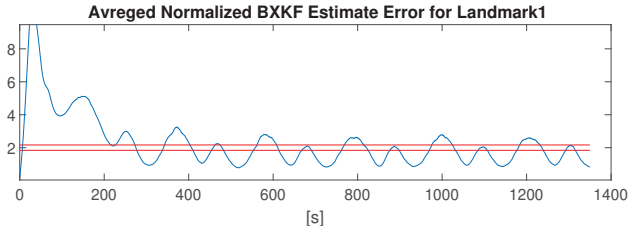

Figure 6.25: NES test of Bearing only XKF SLAM with 1000 MC simmulations and 1% confidence interval for landmark 1, with only linearised covariance matrix.

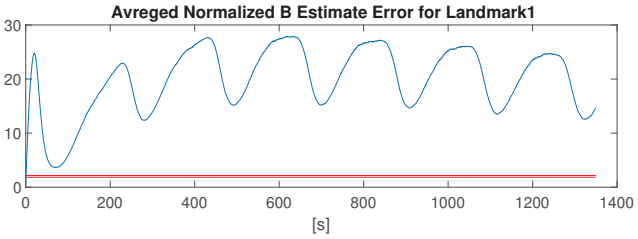

Figure 6.26: NES test of Bearing only KF SLAM with 1000 MC simmulations and 1% confidence interval when the nonlinear noise is quadrupled for landmark 1, with only linearised covariance matrix.

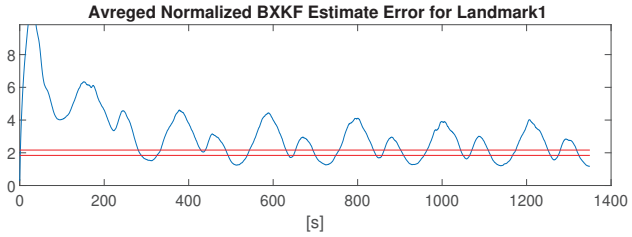

Figure 6.27: NES test of Bearing only XKF SLAM with 1000 MC simmulations and 1% confidence interval when the nonlinear noise is quadrupled for landmark 1, with only linearised covariance matrix.

6.11 Conclusion

In this article we have compared three bearing only SLAM observers, one based on KF, a nonlinear observer and a cascade combination of these which was based on the XKF framework. The cascade was proved to be USGAS, and all the observers were able to preform satisfactorily. However for high noise level the benefits of the XKF bacame apparent, as the nonlinear observer suppressed the nonlinear noise exposing the KF, and thus was able to have a significantly less increase in bias due to the increased noise as well as it was able to maintain its consistency property.

7 *Concluding Remarks*

This thesis presented new theoretical results relevant to simultaneous localization and mapping, with corresponding simulations and field experiments. A common thread in the thesis was developing robust observers, with defined condition for convergence, and large region of attraction.

In Chapter 3, it was shown how decoupling the gyro bias and attitude estimate could lead to a more robust setup. It was also shown how landmark measurements could be used in gyro bias estimation. In tightly coupled observers, a large error in the attitude could compromise the gyro bias estimation, especially if the gyro bias is large. Conversely as seen in the second part of Chapter 3; if the attitude suddenly recovers measurements and is corrected after some drift, an unnecessary error will be induced in the gyro bias estimation. Thus having the attitude and gyro bias estimation decoupled, makes the gyro bias estimation more robust, which in turn will make the attitude estimate more robust. For the presented setups, velocity measurement was required. However, classical reference vectors can also be used by setting distance to the landmark to infinity.

The gyro bias estimator in the second part of Chapter 3, can estimate both gyro bias and distance to the landmarks. This makes the observer useful with a monocular camera. In fact, as the observer is USGAS and exponentially stable, it is the first observer the author is aware of that can preform bearing only measurements from *unknown* landmarks with semi-global stability when gyro bias is estimated. Also a condition for the convergence is derived, and is related to the dispersal of the bearing measurements and where they point relative to the velocity. This condition was calculated for several setups, which gave an insight on when the effects of gyro bias and velocity can be distinguished by observing the landmark kinematics. In addition it is has been verified experimentally on a UAV, thus demonstrating the robust behavior.

In chapter 4, the vector magnitude estimator was first introduced. The notion of using inverse depth estimates to achieve robust estimation has been used before. The contribution here was to formalize the semi global stabillity for the inverse depth observer, and thus also verify that the system is PE as long as the normalized vector is non stationary in the inertial frame. The fact that the observer was designed with bearing measurements represented as unit vector, and not a pixel in the pin-hole model also made the observer applicable a larger set of systems, including large field of view cameras as well as normalized velocity. It was also shown how the observer was able to estimate velocity, provided that a high grade IMU with pitch and roll estimates is available, and how it could be applied in cascade to preform bearing only SLAM with a self calibrating IMU.

This opened up the possibility of estimating velocity by fusing normalized velocity measurements with a high grade IMU. This fusion for estimating velocity was called ego-motion estimation and, and the idea was thoroughly investigated

in Chapter 5. The way the ego-motion estimation was framed, allowed other observers from the literature to be applied to the problem. In addition an EKF implementation was tested. In the comparative study, it was evident that the observers based on nonlinear observer theory had an increased robustness compared to the EKF implementation, and that the inverse depth nonlinear observer had higher accuracy, robustness and was easier to tune among the nonlinear observers.

In Chapter 6, the scenario where an AHRS was available for bearing only SLAM was investigated. How the rotation information could be applied to transform SLAM into a linear system was shown. In addition, a proof of observability of the system when the bearing measurements were non stationary in the inertia frame was proved. Since the system requires sensor values in the system matrices. A design of the tuning covariance matrices was proposed, with simulations showing the consistency of the KF.

In the last part of chapter 6, the KF was combined with the nonlinear observer in a cascade structure. Such a framework was inspired by the recently developed XKF. Normally such a setup is desirable in order to stabilize an EKF. In the presented case, the KF was UGES, however, since the KF had sensor values in the system matrices, it was experienced that it was sensitive to high noise, especially as it was nonlinear from the bearing measurements. The nonlinear observer was therefore used as a filter for the bearing measurements, and the filtered states were provided to the KF. The result was more accurate estimation than the two observers separately in the simulations, and it was shown how it was more robust against high noise levels compared to the KF.

The course of the work, has shown that positioning with the help of landmarks with semi-global stability is possible. For vehicles where velocity measurement is present, a low cost gyro and bearing measurements are enough to estimate the distance to landmarks. When a AHRS is available, or a self calibrating IMU with gravity estimates, only a camera is sufficient to get global stability.

7.1 Future Work

Incorporating the observers and filters developed in the thesis in a full SLAM system and preforming a thorough experimental verification would be a first task. It would be especially interesting to see how the observer would react in a loop closure. The hypothesis would be that the UGES property of the KF SLAM would be especially beneficial and help the states to avoid converging into local minimums; thus making the loop closure robust. What is still not fixed with the proposed setup is the scaling problem, as the computational load increases cubic with the number of landmarks. Assuming sparse structure in the co-variance matrix and investigating how the co-variance update could be preformed more efficiently is another interesting task.

Need less to say, visual SLAM is still a difficult problem, especially for application requiring a real-time robust solution. Never the less, as computationally power increase, sensors improve their performance and drops their price. Simultaneous localization and mapping will be the backbone of many autonomous systems in the future. Already vacuuming your home and moving the lawn, and in the future driving us to work and delivering pizza to our home.

References

[1] Anubhav Agarwal, CV Jawahar, and PJ Narayanan. A survey of planar homography estimation techniques. *Centre for Visual Information Technology, Tech. Rep. IIIT/TR/2005/12*, 2005.

[2] SM Albrektsen and TA Johansen. User-configurable timing and navigation for uavs. *Sensors*, 18(8), 2018.

[3] B D O Anderson. Stability properties of Kalman-Bucy filters. *Journal of the Franklin Institute*, 291(2):137–144, 1971.

[4] Brian Anderson. Exponential stability of linear equations arising in adaptive identification. *IEEE Transactions on Automatic Control*, 22(1):83–88, 1977.

[5] Vincent Andrieu, Gildas Besancon, Ulysse Serres, and Gildas Besançon. Observability necessary conditions for the existence of observers (long version). Technical report, 2013.

[6] Tim Bailey and Hugh Durrant-Whyte. Simultaneous localization and mapping(SLAM): Part ii. *IEEE Robotics & Automation Magazine*, 13(3):108–117, 2006.

[7] Yaakov Bar-Shalom, X Rong Li, and Thiagalingam Kirubarajan. *Estimation with applications to tracking and navigation: theory algorithms and software*. John Wiley & Sons, 2004.

[8] Axel Barrau and Silvere Bonnabel. An ekf-slam algorithm with consistency properties. *arXiv preprint arXiv:1510.06263*, 2015.

[9] Axel Barrau and Silvère Bonnabel. An EKF-SLAM algorithm with consistency properties. Technical report, 2016.

[10] Pedro Batista, Carlos Silvestre, and Paulo Oliveira. Optimal position and velocity navigation filters for autonomous vehicles. *Automatica*, 46(4):767–774, 2010.

[11] Pedro Batista, Carlos Silvestre, and Paulo Oliveira. Single range aided navigation and source localization: Observability and filter design. *Systems & Control Letters*, 60(8):665–673, 2011.

[12] Pedro Batista, Carlos Silvestre, and Paulo Oliveira. Single range aided navigation and source localization: Observability and filter design. *Systems & Control Letters*, 60(8):665–673, 2011.

[13] Pedro Batista, Carlos Silvestre, and Paulo Oliveira. Globally exponentially stable cascade observers for attitude estimation. *Control Engineering Practice*, 20(2):148–155, 2012.

[14] Pedro Batista, Carlos Silvestre, and Paulo Oliveira. Sensor-based globally asymptotically stable filters for attitude estimation: Analysis, design, and performance evaluation. *IEEE Transactions on Automatic Control*, 57(8):2095–2100, 2012.

[15] Kostas E Bekris, Max Glick, and Lydia E Kavraki. Evaluation of algorithms for bearing-only slam. In *Robotics and Automation, 2006. ICRA 2006. Proceedings 2006 IEEE International Conference on*, pages 1937–1943. IEEE, 2006.

[16] Elias Bjørne, Edmund Førland Brekke, Tor Arne Johansen, et al. Cascade attitude observer for the SLAM filtering problem. In *Control Technology and Applications (CCTA), 2017 IEEE Conference on*, pages 945–952. IEEE, 2017.

[17] Elias Bjørne, Tor Arne Johansen, and Edmund Førland Brekke. Redesign and analysis of globally asymptotically stable bearing only SLAM. In *Information Fusion (Fusion), 2017 20th International Conference on*, pages 1–8. IEEE, 2017.

[18] Elias Bjørne, Tor Arne Johansen, and Edmund Førland Brekke. Cascaded bearing only SLAM with uniform Semi-Global asymptotic stability. In *2019 22nd International Conference on Information Fusion (FUSION) (FUSION 2019)*, Ottawa, Canada, July 2019.

[19] Elias Bjørne, Tor Arne Johansen, and Jeff Delaune. Estimating vector magnitude from its direction and derivative, with application to bearing-only SLAM filter problem. In *2018 IEEE Conference on Decision and Control (CDC)*, pages 1353–1360. IEEE, 2018.

[20] Michael Bloesch, Sammy Omari, Marco Hutter, and Roland Siegwart. Robust visual inertial odometry using a direct ekf-based approach. In *Intelligent Robots and Systems (IROS), 2015 IEEE/RSJ International Conference on*, pages 298–304. IEEE, 2015.

[21] C Cadena, L Carlone, H Carrillo, Y Latif, D Scaramuzza, J Neira, I Reid, and J Leonard. Past, Present, and Future of Simultaneous Localization And Mapping: Towards the Robust-Perception Age. *IEEE Transactions on Robotics*, 32(6):1309–1332, 2016.

[22] José A Castellanos, José Neira, and Juan D Tardós. Limits to the consistency of EKF-based SLAM 1. 2004.

[23] Antoine Chaillet and Antonio Loría. Uniform semiglobal practical asymptotic stability for non-autonomous cascaded systems and applications. *Automatica*, 44(2):337–347, 2008.

[24] Mark Cummins and Paul Newman. Appearance-only SLAM at large scale with FAB-MAP 2.0. *The International Journal of Robotics Research*, 30(9):1100–1123, 2011.

[25] Jeffrey J Dacunha. Transition matrix and generalized matrix exponential via the peano-baker series. *Journal of Difference Equations and Applications*, 11(15):1245–1264, 2005.

[26] Andrew J Davison, Ian D Reid, Nicholas D Molton, and Olivier Stasse. MonoSLAM: Real-time single camera SLAM. *IEEE Transactions on Pattern Analysis & Machine Intelligence*, (6):1052–1067, 2007.

[27] Alessandro De Luca, Giuseppe Oriolo, and Paolo Robuffo Giordano. Feature Depth Observation for Image-based Visual Servoing: Theory and Experiments. *The International Journal of Robotics Research*, 27(10):1093–1116, 2008.

[28] Hugh Durrant-Whyte and Tim Bailey. Simultaneous localization and mapping(SLAM): part i. *IEEE robotics & automation magazine*, 13(2):99–110, 2006.

[29] Bertil Ekstrand. Some aspects on filter design for target tracking. *Journal of Control Science and Engineering*, 2012:10, 2012.

[30] Jakob Engel, Thomas Schöps, and Daniel Cremers. Lsd-slam: Large-scale direct monocular slam. In *European conference on computer vision*, pages 834–849. Springer, 2014.

[31] Matthias Faessler, Flavio Fontana, Christian Forster, and Davide Scaramuzza. Automatic re-initialization and failure recovery for aggressive flight with a monocular vision-based quadrotor. In *2015 IEEE International Conference on Robotics and Automation (ICRA)*, pages 1722–1729. IEEE, 2015.

[32] Martin A Fischler and Robert C Bolles. Random sample consensus: a paradigm for model fitting with applications to image analysis and automated cartography. *Communications of the ACM*, 24(6):381–395, 1981.

[33] Christian Forster, Matia Pizzoli, and Davide Scaramuzza. Svo: Fast semi-direct monocular visual odometry. In *IEEE International Conference on Robotics and Automation (ICRA)*, pages 15–22. IEEE, 2014.

[34] T. I. Fossen. *Handbook of Marine Craft Hydrodynamics and Motion Control*. Wiley, 2011.

[35] Thor Fossen, Antonio Loría, Andrew Teel, et al. A theorem for ugas and ules of (passive) nonautonomous systems: Robust control of mechanical systems and ships. *International Journal of Robust and Nonlinear Control*, 11(2):95–108, 2001.

[36] Paul Furgale, Timothy D Barfoot, and Gabe Sibley. Continuous-time batch estimation using temporal basis functions. In *IEEE International Conference on Robotics and Automation (ICRA)*, pages 2088–2095. IEEE, 2012.

[37] Paul Furgale, Joern Rehder, and Roland Siegwart. Unified temporal and spatial calibration for multi-sensor systems. In *Intelligent Robots and Systems (IROS), 2013 IEEE/RSJ International Conference on*, pages 1280–1286. IEEE, 2013.

[38] Lorenzo Fusini, Thor I Fossen, and Tor Arne Johansen. Nonlinear observers for gnss-and camera-aided inertial navigation of a fixed-wing uav. *IEEE Transactions on Control Systems Technology*, 26(5):1884–1891, 2018.

[39] Dorian Gálvez-López and Juan D Tardos. Bags of binary words for fast place recognition in image sequences. *IEEE Transactions on Robotics*, 28(5):1188–1197, 2012.

[40] Paolo Robuffo Giordano, Alessandro De Luca, and Giuseppe Oriolo. 3d structure identification from image moments. In *2008 IEEE International Conference on Robotics and Automation*, pages 93–100. IEEE, 2008.

[41] Volker Grabe, Heinrich H. Bülthoff, Davide Scaramuzza, and Paolo Robuffo Giordano. Nonlinear ego-motion estimation from optical flow for online control of a quadrotor UAV. *The International Journal of Robotics Research*, 34(8):1114–1135, 2015.

[42] Håvard Fjær Grip, Thor I Fossen, Tor A Johansen, and Ali Saberi. Attitude estimation based on time-varying reference vectors with biased gyro and vector measurements. *IFAC World Congress*, 44(1):8497–8502, 2011.

[43] Håvard Fjær Grip, Thor I Fossen, Tor A Johansen, and Ali Saberi. Attitude estimation using biased gyro and vector measurements with time-varying reference vectors. *IEEE Transactions on Automatic Control*, 57(5):1332–1338, 2012.

[44] Håvard Fjær Grip, Thor I Fossen, Tor A Johansen, and Ali Saberi. Globally exponentially stable attitude and gyro bias estimation with application to gnss/ins integration. *Automatica*, 51:158–166, 2015.

[45] Giorgio Grisetti, Rainer Kummerle, Cyrill Stachniss, and Wolfram Burgard. A tutorial on graph-based SLAM. *IEEE Intelligent Transportation Systems Magazine*, 2(4):31–43, 2010.

[46] Paul D Groves. *Principles of GNSS, inertial, and multisensor integrated navigation systems*. Artech house, 2013.

[47] Bruno JN Guerreiro, Pedro Batista, Carlos Silvestre, and Paulo Oliveira. Globally asymptotically stable sensor-based simultaneous localization and mapping. *IEEE Transactions on Robotics*, 29(6):1380–1395, 2013.

[48] Tarek Hamel and Robert Mahony. Attitude estimation on so [3] based on direct inertial measurements. In *Proceedings 2006 IEEE International Conference on Robotics and Automation, 2006. ICRA 2006.*, pages 2170–2175. IEEE, 2006.

[49] Tarek Hamel and Claude Samson. Position estimation from direction or range measurements. *Automatica*, 82:137–144, aug 2017.

[50] Tarek Hamel and Claude Samson. Riccati observers for the nonstationary pnp problem. *IEEE Transactions on Automatic Control*, 63(3):726–741, 2017.

[51] Richard Hartley and Andrew Zisserman. *Multiple view geometry in computer vision*. Cambridge university press, 2003.

[52] Sejong Heo and Chan Gook Park. Consistent ekf-based visual-inertial odometry on matrix lie group. *IEEE Sensors Journal*, 18(9):3780–3788, 2018.

[53] Joao P Hespanha. *Linear systems theory*. Princeton university press, 2009.

[54] Minh-Duc Hua. Attitude estimation for accelerated vehicles using gps/ins measurements. *Control Engineering Practice*, 18(7):723–732, 2010.

[55] Minh-Duc Hua, Mohammad Zamani, Jochen Trumpf, Robert Mahony, and Tarek Hamel. Observer design on the special euclidean group SE(3). In *2011 50th IEEE Conference on Decision and Control and European Control Conference*, pages 8169–8175. IEEE, 2011.

[56] Guoquan P Huang, Anastasios I Mourikis, and Stergios I Roumeliotis. Observability-based rules for designing consistent EKF SLAM estimators. *The International Journal of Robotics Research*, 29(5):502–528, 2010.

[57] Mrdjan Jankovic and Bijoy K Ghosh. Visually guided ranging from observations of points, lines and curves via an identifier based nonlinear observer. *Systems & Control Letters*, 25(1):63–73, 1995.

[58] Tor A Johansen and Edmund Brekke. Globally exponentially stable kalman filtering for SLAM with AHRS. In *Information Fusion (FUSION), 2016 19th International Conference on*, pages 909–916. IEEE, 2016.

[59] Tor A Johansen and Thor I Fossen. The exogenous kalman filter (XKF). *International Journal of Control*, 90(2):161–167, 2017.

[60] Thomas Kailath. *Linear systems*, volume 156. Prentice-Hall Englewood Cliffs, NJ, 1980.

[61] Jacques Kaiser, Agostino Martinelli, Flavio Fontana, and Davide Scaramuzza. Simultaneous state initialization and gyroscope bias calibration in visual inertial aided navigation. *IEEE Robotics and Automation Letters*, 2(1):18–25, 2017.

[62] Rudolf Emil Kalman. Mathematical description of linear dynamical systems. *Journal of the Society for Industrial and Applied Mathematics, Series A: Control*, 1(2):152–192, 1963.

[63] Rudolph E Kalman and Richard S Bucy. New results in linear filtering and prediction theory. *Journal of basic engineering*, 83(3):95–108, 1961.

[64] Hassan K. Khalil. *Nonlinear Systems*. Prentice Hall, 2002.

[65] Hassan K Khalil and JW Grizzle. *Nonlinear systems*, volume 3. Prentice hall New Jersey, 1996.

[66] Laurent Kneip, Margarita Chli, and Roland Y Siegwart. Robust real-time visual odometry with a single camera and an imu. In *Proceedings of the British Machine Vision Conference 2011*. British Machine Vision Association, 2011.

[67] Dimitrios G Kottas, Kejian J Wu, and Stergios I Roumeliotis. Detecting and dealing with hovering maneuvers in vision-aided inertial navigation systems. In *2013 IEEE/RSJ International Conference on Intelligent Robots and Systems*, pages 3172–3179. IEEE, 2013.

[68] M. Krstic, I. Kanellakopoulos, and P. V. Kokotovic. *Nonlinear and Adaptive Control Design*. Wiley, 1995.

[69] Rainer Kümmerle, Giorgio Grisetti, Hauke Strasdat, Kurt Konolige, and Wolfram Burgard. g 2 o: A general framework for graph optimization. In *2011 IEEE International Conference on Robotics and Automation*, pages 3607–3613. IEEE, 2011.

[70] Ngai Ming Kwok, Gamini Dissanayake, and Quang Phuc Ha. Bearing-only SLAM using a SPRT based gaussian sum filter. In *Proceedings of ICRA 2005*, pages 1109–1114. IEEE, 2005.

[71] Florent Le Bras, Tarek Hamel, Robert Mahony, and Claude Samson. Observers for position estimation using bearing and biased velocity information. In *Sensing and Control for Autonomous Vehicles*, pages 3–23. Springer, 2017.

[72] Vincent Lepetit, Francesc Moreno-Noguer, and Pascal Fua. Epnp: An accurate o (n) solution to the pnp problem. *International journal of computer vision*, 81(2):155, 2009.

[73] Mingyang Li and Anastasios I Mourikis. Optimization-based estimator design for vision-aided inertial navigation: Supplemental materials. 2012.

[74] Mingyang Li and Anastasios I Mourikis. High-precision, consistent ekf-based visual-inertial odometry. *The International Journal of Robotics Research*, 32(6):690–711, 2013.

[75] Antonio Lorıa and Elena Panteley. Uniform exponential stability of linear time-varying systems: revisited. *Systems & Control Letters*, 47(1):13–24, 2002.

[76] Antonio Loría and Elena Panteley. cascaded nonlinear time-varying systems: Analysis and design. In *Advanced topics in control systems theory*, pages 23–64. Springer, 2005.

[77] Pedro Lourenço, Pedro Batista, Paulo Oliveira, and Carlos Silvestre. A globally exponentially stable filter for bearing-only simultaneous localization and mapping with monocular vision. *Robotics and Autonomous Systems*, 100:61–77, feb 2018.

[78] Pedro Lourenço, Pedro Batista, Paulo Oliveira, Carlos Silvestre, and CL Philip Chen. Sensor-based globally exponentially stable range-only simultaneous localization and mapping. *Robotics and Autonomous Systems*, 68:72–85, 2015.

[79] Pedro Lourenço, Bruno J Guerreiro, Pedro Batista, Paulo Oliveira, and Carlos Silvestre. 3-d inertial trajectory and map online estimation: Building on a GAS sensor-based SLAM filter. In *Control Conference (ECC), 2013 European*, pages 4214–4219. IEEE, 2013.

[80] Simon Lynen, Markus W Achtelik, Stephan Weiss, Margarita Chli, and Roland Siegwart. A robust and modular multi-sensor fusion approach applied to mav navigation. In *International Conference on Intelligent Robots and Systems (IROS) IEEE/RSJ*, pages 3923–3929, 2013.

[81] Robert Mahony and Tarek Hamel. A geometric nonlinear observer for simultaneous localisation and mapping. In *2017 IEEE 56th Annual Conference on Decision and Control (CDC)*, pages 2408–2415. IEEE, 2017.

[82] Robert Mahony, Tarek Hamel, and Jean-Michel Pflimlin. Nonlinear complementary filters on the special orthogonal group. *IEEE Transactions on Automatic Control*, 53(5):1203–1218, 2008.

[83] Robert Mahony, Jochen Trumpf, and Tarek Hamel. Observers for kinematic systems with symmetry. *IFAC Proceedings Volumes*, 46(23):617–633, 2013.

[84] Ezio Malis and Manuel Vargas. *Deeper understanding of the homography decomposition for vision-based control*. PhD thesis, INRIA, 2007.

[85] F Landis Markley. Attitude error representations for kalman filtering. *Journal of guidance, control, and dynamics*, 26(2):311–317, 2003.

[86] VM Matrosov. On the stability of motion. *Journal of Applied Mathematics and Mechanics*, 26(5):1337–1353, 1962.

[87] AP Morgan and KS Narendra. On the stability of nonautonomous differential equations, with skew symmetric matrix. *SIAM Journal on Control and Optimization*, 15(1):163–176, 1977.

[88] Anastasios I. Mourikis and Stergios I. Roumeliotis. A Multi-State Constraint Kalman Filter for Vision-aided Inertial Navigation. In *Proceedings 2007 IEEE International Conference on Robotics and Automation*, pages 3565–3572, Rome, Italy, apr 2007. IEEE.

[89] Raul Mur-Artal, Jose Maria Martinez Montiel, and Juan D Tardos. ORB-SLAM: a versatile and accurate monocular SLAM system. *IEEE Transactions on Robotics*, 31(5):1147–1163, 2015.

[90] Raúl Mur-Artal and Juan D Tardós. Fast relocalisation and loop closing in keyframe-based slam. In *2014 IEEE International Conference on Robotics and Automation (ICRA)*, pages 846–853. IEEE, 2014.

[91] Raúl Mur-Artal and Juan D Tardós. Visual-inertial monocular SLAM with map reuse. *IEEE Robotics and Automation Letters*, 2(2):796–803, 2017.

[92] José Neira and Juan D Tardós. Data association in stochastic mapping using the joint compatibility test. *IEEE Transactions on robotics and automation*, 17(6):890–897, 2001.

[93] David Nistér. An Efficient Solution to the Five-Point Relative Pose Problem. *IEEE transactions on pattern analysis and machine intelligence*, 26(6):756–770, 2004.

[94] Edwin Olson. AprilTag: A robust and flexible visual fiducial system. In *Proceedings of the IEEE International Conference on Robotics and Automation (ICRA)*, pages 3400–3407. IEEE, May 2011.

[95] Elena Panteley, Antonio Loria, and Andrew Teel. Relaxed persistency of excitation for uniform asymptotic stability. *IEEE Transactions on Automatic Control*, 46(12):1874–1886, 2001.

[96] Lina M Paz, Juan D Tardós, and José Neira. Divide and conquer: EKF SLAM in $O(n)$. *IEEE Transactions on Robotics*, 24(5):1107–1120, 2008.

[97] Siniša Šegvic, Gerald Schweighofer, and Axel Pinz. Performance evaluation of the five-point relative pose with emphasis on planar scenes. In *Proceedings of the workshop of the Austrian Association for Pattern Recognition, Schloss Krumbach, Austria*, pages 33–40, 2007.

[98] Jianbo Shi and Carlo Tomasi. Good features to track. Technical report, Cornell University, 1993.

[99] Leonard M Silverman and Brian D O Anderson. Controllability, observability and stability of linear systems. *SIAM Journal on control*, 6(1):121–130, 1968.

[100] Joan Sola. Quaternion kinematics for the error-state kf. *Laboratoire d'Analyse et d'Architecture des Systemes-Centre national de la recherche scientifique (LAAS-CNRS), Toulouse, France, Tech. Rep*, 2012.

[101] Riccardo Spica and Paolo Robuffo Giordano. A framework for active estimation: Application to structure from motion. In *Proceedings of the IEEE Conference on Decision and Control*, pages 7647–7653, 2013.

[102] Riccardo Spica, Paolo Robuffo Giordano, and François Chaumette. Active structure from motion: Application to point, sphere, and cylinder. *IEEE Transactions on Robotics*, 30(6):1499–1513, 2014.

[103] Hauke Strasdat, J Montiel, and Andrew J Davison. Scale drift-aware large scale monocular slam. *Robotics: Science and Systems VI*, 2(3):7, 2010.

[104] Hauke Strasdat, José MM Montiel, and Andrew J Davison. Visual slam: why filter? *Image and Vision Computing*, 30(2):65–77, 2012.

[105] HJ Sussmann and PV Kokotovic. The peaking phenomenon and the global stabilization of nonlinear systems. *IEEE Transactions on automatic control*, 36(4):424–440, 1991.

[106] Carlo Tomasi and Takeo Kanade. Detection and tracking of point features. 1991.

[107] Pieter van Goor, Robert Mahony, Tarek Hamel, and Jochen Trumpf. An equivariant observer design for visual localisation and mapping. *arXiv preprint arXiv:1904.02452*, 2019.

[108] José Fernandes Vasconcelos, Rita Cunha, Carlos Silvestre, and P Oliveira. A nonlinear position and attitude observer on SE(3) using landmark measurements. *Systems & Control Letters*, 59(3):155–166, 2010.

[109] Teresa Vidal-Calleja, Mitch Bryson, Salah Sukkarieh, Alberto Sanfeliu, and Juan Andrade-Cetto. On the observability of bearing-only SLAM. In *Proceedings 2007 IEEE International Conference on Robotics and Automation*, pages 4114–4119. IEEE, 2007.

[110] Stephan Weiss, Markus W. Achtelik, Margarita Chli, and Roland Siegwart. Versatile distributed pose estimation and sensor self-calibration for an autonomous MAV. In *International Conference on Robotics and Automation (ICRA)*, pages 31–38, 2012.

[111] Stephan Weiss, Roland Brockers, Sigurd Albrektsen, and Larry Matthies. Inertial optical flow for throw-and-go micro air vehicles. In *IEEE Winter Conference on Applications of Computer Vision (WACV)*, pages 262–269. IEEE, 2015.

[112] Stephan Weiss, Roland Brockers, and Larry Matthies. 4DoF drift free navigation using inertial cues and optical flow. In *IEEE International Conference on Intelligent Robots and Systems*, pages 4180–4186, 2013.

[113] Brian Williams, Mark Cummins, José Neira, Paul Newman, Ian Reid, and Juan Tardós. A comparison of loop closing techniques in monocular slam. *Robotics and Autonomous Systems*, 57(12):1188–1197, 2009.

[114] Zichao Zhang, Henri Rebecq, Christian Forster, and Davide Scaramuzza. Benefit of large field-of-view cameras for visual odometry. In *2016 IEEE International Conference on Robotics and Automation (ICRA)*, pages 801–808. IEEE, 2016.

[115] Liang Zhao, Shoudong Huang, and Gamini Dissanayake. Linear MonoSLAM: A linear approach to large-scale monocular SLAM problems. In *Proceedings of ICRA 2014*, pages 1517–1523. IEEE, 2014.